# Mixed ionic-electronic conductors in gas separation applications

A thesis submitted to the University of Manchester for the degree of Doctor of Philosophy in the Faculty of Engineering and Physical Sciences

**2016**

**Guannan Chen**

**School of Materials**

# Table of contents

Word count 53802

# List of figures

# List of tables

# Abstract

$Ba_{0.5}Sr_{0.5}Co_{0.8}Fe_{0.2}O_{3-\delta}$ (BSCF) and $SrCo_{0.48}Fe_{0.12}Ti_{0.4}O_{3-\delta}$ (SCFT) were synthesised by co-precipitation. BSCF was pressed and sintered at 1100℃ for 10 hours to pellets (relative density: 93%) from which X-ray diffraction (XRD) revealed single Pm-3m phase (a=3.9782 Å). Scanning electron microscopy (SEM) revealed clear equiaxed grains (grain size 33 ± 16 μm). The pellets were decomposed in 7±1 % $CO_2/N_2$ at 800℃ for 1 to 30 minutes. XRD confirmed secondary phases: R-3mH phase (a=b=5.1397 Å, c=9.4847 Å) and Fm-3m phase (a=4.2490 Å). Electron backscattered diffraction (EBSD) ascribed R-3mH and Fm-3m phases to the surface and part of the cross-section precipitates, respectively as revealed by SEM. Energy dispersive X-ray spectroscopy (EDX) revealed the compositions of R-3mH and Fm-3m phases to be $Ba_{0.65\pm0.03}Sr_{0.35\pm0.03}CO_3$ (BSC) and CoO, respectively. Transmission electron microscopy (TEM) and EDX revealed the structure (15R, R3m and R-3mH) and composition ($Ba_{0.20}Sr_{0.10}Co_{0.59}Fe_{0.10}O_x$) of lamellar precipitates in cross-section, suggesting Ba and Sr diffuse from the lamellae to BSC. A unique orientation relation (BSCF {111} // BSC {0001}) was uncovered by EBSD. TEM revealed high symmetry contact planes of lamellae and BSCF, suggesting nucleation energy governs decomposition. Fresh BSCF pellets were decomposed in $N_2$ at 800℃. Fm-3m and $P6_3$/mmc phases were confirmed by XRD and lamellae were observed by SEM, followed by decomposition in 7±1 % $N_2/CO_2$ at 800℃. XRD revealed higher weight % of BSC and CoO. SEM revealed BSC preferring lamellae, hence hexagonal phases accelerated BSC formation. BSCF pellets were dip coated in SCFT propan-2-ol suspension (3:10), followed by sintering at 1165℃ for 10 hours. XRD revealed a Pm-3m phase (a=3.885 Å) and SEM revealed a grain size of 65 ± 9 μm and open porosity of 1.6 ± 1 %. They were annealed in 7±1 % $CO_2/N_2$ at 800℃. XRD revealed no secondary phases, suggesting enhanced stability. However, oxygen permeability was reduced (1.2 ml/cm$^2$ to 0.8 ml/cm$^2$) because the coating composition changed to $Ba_{0.20}Sr_{0.27}Co_{0.40}Fe_{0.10}Ti_{0.04}O_x$; this was revealed by EDX.

**The University of Manchester**
**Guannan Chen**
**Doctor of Philosophy**
**Mixed ionic-electronic conductors in gas separation applications**
**January 2016**

# Declaration

No portion of the work referred to in the thesis has been submitted in support of an application for another degree or qualification of this or any other university or other institute of learning.

# Copyright statement

**i.** The author of this thesis (including any appendices and/or schedules to this thesis) owns certain copyright or related rights in it (the "Copyright") and s/he has given The University of Manchester certain rights to use such Copyright, including for administrative purposes.

**ii.** Copies of this thesis, either in full or in extracts and whether in hard or electronic copy, may be made **only** in accordance with the Copyright, Designs and Patents Act 1988 (as amended) and regulations issued under it or, where appropriate, in accordance with licensing agreements which the University has from time to time. This page must form part of any such copies made.

**iii.** The ownership of certain Copyright, patents, designs, trade marks and other intellectual property (the "Intellectual Property") and any reproductions of copyright works in the thesis, for example graphs and tables ("Reproductions"), which may be described in this thesis, may not be owned by the author and may be owned by third parties. Such Intellectual Property and Reproductions cannot and must not be made available for use without the prior written permission of the owner(s) of the relevant Intellectual Property and/or Reproductions.

**iv.** Further information on the conditions under which disclosure, publication and commercialisation of this thesis, the Copyright and any Intellectual Property and/or Reproductions described in it may take place is available in the University IP Policy (see http://documents.manchester.ac.uk/DocuInfo.aspx?DocID=487), in any relevant Thesis restriction declarations deposited in the University Library, The University Library's regulations (see http://www.manchester.ac.uk/library/aboutus/regulations) and in The University's policy on Presentation of Theses

# Acknowledgements

I appreciate my supervisor Dr Colin Leach for his support, guidance and inspiration during my PhD. I also gratefully thank my co-supervisor Dr David Hall for his help, advice and encouragement.

I would like to thank Dr Colin Norman for his support in various experiments and in accessing facilities outside of the university.

The members in the electron microscope centre are thanked for the training, help and encouragement they offered. In particular, I would like to thank Mike Faulkner, Dr Christopher Wilkins, Dr Alan Harvey, Matthew Smith, Dr Ali Gholinia and Teruo Hashimoto.

Gary Harrison and Dr John Warren are thanked for their help in the X-ray facilities.

Ivan Easdon and Ken Gyves are thanked for their help in research safety and the laboratories in the Materials Science Centre.

Finally, I would like to thank my family for their encouragement and support through my PhD.

# Sample nomenclature

The samples used in this study are named as follows.

The designation of the samples is that the capital letter, temperature and time indicate the annealing gas, temperature and time respectively, e.g. in C-800°C-1min, C indicates the gas environment ($CO_2/N_2$), 800 °C indicates the annealing temperature and 1 min indicates the annealing time.

| The annealing conditions | Designation |
|---|---|
| A BSCF pellet annealed in 7±1 % $CO_2/N_2$ at 800 °C for 1 min | C-800°C-1min |
| A BSCF pellet annealed in 7±1 % $CO_2/N_2$ at 800 °C for 2 min | C-800°C-2min |
| A BSCF pellet annealed in 7±1 % $CO_2/N_2$ at 800 °C for 5 min | C-800°C-5min |
| A BSCF pellet annealed in 7±1 % $CO_2/N_2$ at 800 °C for 15 min | C-800°C-15min |
| A BSCF pellet annealed in 7±1 % $CO_2/N_2$ at 800 °C for 30 min | C-800°C-30min |
| A BSCF pellet annealed in $N_2$ at 800 °C for 1 hour | N-800°C-1hour |
| A BSCF pellet annealed in $N_2$ at 800 °C for 6 hours | N-800°C-6hour |
| A BSCF pellet annealed in $N_2$ at 800 °C for 24 hours | N-800°C-24hour |
| A BSCF pellet annealed in air at 800 °C for 6 hours | A-800°C-6hour |

Three annealed samples were annealed again under different conditions and are named as follows. For example, in N6C2, N6 represents the annealed sample N-800°C-6hour, C2 represents the gas environment ($CO_2/N_2$) and annealing time (2 min) in which N-800°C-6hour was annealed again.

| Samples | The annealing conditions | Designation |
|---|---|---|
| N-800°C-6hour | 7±1 % $N_2/CO_2$ annealing 2 min 800 °C | N6C2 |
| N-800°C-1hour | 7±1 % $N_2/CO_2$ annealing 5 min 800 °C | N1C5 |
| A-800°C-6hour | 7±1 % $N_2/CO_2$ annealing 2 min 800 °C | A6C2 |

A BSCF pellet coated by $SrCo_{0.48}Fe_{0.12}Ti_{0.4}O_{3-\delta}$ powders is named SCFT coated BSCF pellet.

# Abbreviations

PO$_2$, P$_{O2}^1$ and P$_{O2}^2$  oxygen partial pressures

V$_O^{\bullet\bullet}$           positively charged oxygen vacancy

O$_i$''           oxygen interstitial site

O$^\chi$           neutral occupied oxygen site

e           electron

h           electron hole

$\sigma_t$           overall conductivity

$t_i$           ionic transfer number

$t_e$           electronic transfer number

$\mu_{O2}$           chemical potential of the hypothetical neutral oxygen in the oxide

L           oxide thickness

F           Faraday's constant

$\delta$           oxygen non stoichiometry

$\Delta Hm$           migration energy related to oxygen vacancy formation

$\Delta Hf$           enthalpy related to the oxygen vacancy formation

$L_c$           characteristic thickness of an oxygen separation membrane

D*           diffusion coefficient

k           surface exchange coefficient

$c_i$           concentration of the ions

n           concentration of the electrons

| | |
|---|---|
| p | concentration of the electron holes |
| q | charge of conducting species |
| μ | mobility of conducting species |
| $[V_O^{\bullet\bullet}]$ | concentration of oxygen vacancies |
| $[O_i'']$ | concentration of oxygen interstitial sites |
| nil | neutral charge |
| χ | magnetic susceptibility of materials |
| $n_1$ | density of magnetic moments |
| T | temperature |
| $D_{chem}$ | oxygen diffusion coefficient |
| $\sigma_{ion}$ | ionic conductivity |
| R | ideal gas constant |
| $D_V$ | oxygen diffusion coefficient |
| $V_m$ | perovskite molar volume |
| $v_r$ and $v_d$ | pre-exponential factors |
| R | universal gas constant |
| $E_r$ | activation energy of dissociation |
| $E_d$ | activation energy of desorption |
| $\delta_\infty$ | oxygen non stoichiometry at equilibrium |
| $x - 2\delta_\infty$ | hole concentration |
| Ea | activation energy of oxygen diffusion |

| | |
|---|---|
| $\sigma^0_{ion}$ | ionic conductivity at $PO_2 = 1$ atm |
| $J_{O2}$ | oxygen permeation flux |
| n | order of ambipolar conductivity |
| d or d-spacing | spacing between the lattice planes |
| $\theta$ | diffraction angle |
| $\lambda$ | wavelength of X-ray |
| n | order of diffraction |
| H | the depth of field |
| WD | working distance |
| A | aperture diameter |
| M | magnification |
| $N_{spec}$ | number of X-ray counts of an element in a spectrum of a specimen |
| $C_{spec}$ | concentration of an element in a specimen |
| $N_{std}$ | number of X-ray counts of an element in a spectrum of a standard sample |
| $C_{std}$ | concentration of an element in a standard sample |
| Z | atomic number corrector |
| A | absorption corrector |
| F | fluorescence corrector |
| $L\lambda$ | camera constant |
| L | camera length |
| $K_{AB}$ | scaling factor |

$\rho_b$        bulk density

$\rho_s$        apparent solid density

$\rho_s$        density of water

$m_1$        mass of ceramic pellet weighed in air

$m_2$        mass of ceramic pellet weighed in water

$m_3$        mass of ceramic pellet weighed in air after drying

$\alpha$        volume of the product of a reaction

$k_G$        reaction rate coefficient when nucleation happens rapidly and randomly

$t$        reaction time

$R$        average precipitate radius

# 1. Introduction

Ceramic-membrane based mixed ionic-electronic conductors (MIECs), operating at temperatures around 800°C - 850°C, have attracted much attention in recent years, as candidates for oxygen separation membranes [1-3] in technologies such as oxy-fuel combustion [4], and as a cathodes in solid oxide fuel cells (SOFCs) [5, 6].

For membrane applications, the cubic perovskite BSCF shows the highest oxygen permeation rate [1, 7] This is attributed to a remarkably high concentration of oxygen vacancies [8] caused by a reduction in the oxidation state of cobalt at elevated temperature [1, 8-10].

However, the performance of BSCF is compromised by reactions occurring during operation [11] which reduce the oxygen permeability [12-14] and the electrical conductivity [15]. There are two areas of issue; firstly a slow decomposition of the cubic BSCF phase to lower symmetry phases with slower permeation characteristics [13], and secondly a surface reaction forming Barium/Strontium carbonates in the presence of $CO_2$, which blocks oxygen surface exchange and diffusion [16].

The objectives of this study were to observe the microstructure changes using scanning electron microscope, to identify the secondary phases, to ascribe the phases to the features in the microstructure and to conduct a crystallographic study (using X-ray diffraction, electron backscatter diffraction and high resolution transmission electron microscopy) and a chemical analysis (using energy dispersive X-ray spectroscopy) to the secondary phases and neighbouring BSCF in a BSCF sample decomposed in $CO_2$ enriched atmosphere to establish a decomposition mechanism and to identify the governing process. This study focused on the initial decomposition which complements the previous studies focusing on the later decomposition. Subsidiary objectives were to synthesis BSCF, to optimise the synthesis process, to develop and optimise sample preparation techniques for electron microscopy, to relate the secondary phases due to the slow decomposition of cubic BSCF and the secondary phases due to the reaction with $CO_2$ to each other.

A second objective was to protect BSCF from the reaction with $CO_2$ using a cubic perovskite ceramic coating with higher thermal expansion than BSCF, similar lattice

parameters to BSCF and relatively high surface exchange coefficient. Subsidiary objectives were to synthesis the coating material and to study the $CO_2$ stability and oxygen permeability of the coated BSCF.

# 2. Literature review

## 2.1 Background knowledge

Ceramic-membrane based MIECs contain oxygen vacancies. Oxygen ions ($O^{2-}$) may diffuse through the membrane via the vacancies (Figure 1). The oxygen partial pressure ($PO_2$) of one side of the membrane ($P_{O2}^{1}$) needs to be higher than that of the other side of the membrane ($P_{O2}^{2}$) to create a $PO_2$ gradient across the membrane. The gradient is the driving force for the diffusion of the oxygen ions. Electrons (e) are released and transport back to the high $PO_2$ surface after oxygen ions arrive the low $PO_2$ surface. [1]
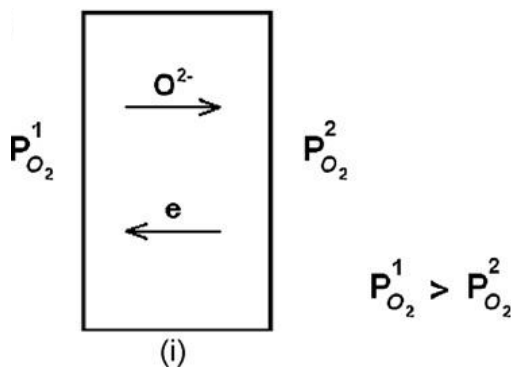


Figure 1. General working mechanism of a MIEC (From Sunarso et al. [1]).

There are three types of material which are able to separate oxygen [1]. They are the fluorite-based, perovskite-based and dual-phase materials. The perovskite-based materials are most popular because of their highest oxygen permeation rate. However, this type of material decomposes in $CO_2$ involved working environments [16, 17], which limits the commercialisation of this material. Therefore, this thesis focuses on this type of material to improve its stability without reducing its high oxygen permeation rate.

The following parameters are important for oxygen ion diffusion. The concentration of oxygen vacancies can be enhanced at high temperatures. The oxygen ion conductivity can be increased by increasing lattice parameter because the oxygen ion pathway can be larger in a large unit cell [18]. The activation energy of oxygen diffusion can be reduced by enhancing sintering temperature because of the decreasing in grain boundaries which limit the oxygen diffusion [19].

## 2.1.1 The applications of ceramic-membrane based MIECs

Since MIECs only allow oxygen ions to diffuse through them, $O_2$ can be separated by MIECs from air [8]. This is a lower energy penalty way of producing $O_2$, compared to the electrolysis of water and cryogenic distillation. The oxy-fuel combustion, which burns fuel and pure $O_2$, reduces nitrogen oxides pollution and captures and stores $CO_2$ [20]. The $O_2$ separation is important for the oxy-fuel combustion because an in-situ production of $O_2$ becomes possible. The capture and storage of $CO_2$ is made easier because of the removal of nitrogen oxides. Specifically, there is no need to separate $CO_2$ from a $CO_2$ and nitrogen oxides mixture and the volume of the gas condenser and container can be reduced. In addition, the heat taken by nitrogen and nitrogen oxides can be saved. [4]

SOFCs can reduce carbon emissions and nitrogen oxide pollutions because their flue gas contains only water when the fuel gas contains only $H_2$. The cathode of a SOFC transports oxygen ions and electrons when the SOFC produces electricity. A MIEC can function as the cathode because of its high oxygen ion conductivity and electronic conductivity. In addition, the rate of the oxygen dissociation reaction and that of the oxygen reduction reaction can be increased by a suitable catalyst which can be a MIEC due to the presence of variable valency transition metal cations. This is important because $O_2$ molecules have to be dissociated to ions before they diffuse in the cathode and the oxygen atoms are reduced in the dissociation process. [21]

Fossil fuels can be replaced by $H_2$ to reduce $CO_2$ emissions because the product of the combustion of $H_2$ and $O_2$ is $H_2O$. $H_2$ can be produced by water splitting [22]. There is a series of methods to split water [23-28]. The advantages of splitting water by MIECs are that $O_2$ can be removed from the split products and catalytic reactions can be coupled in the splitting process [22]. A water splitting process on a MIEC is shown in Figure 2. $H_2O$ reacts with electrons ($e^-$) to produce an oxygen ion ($O^{2-}$) and $H_2$. The oxygen ion diffuses through the MIEC under the driving force of a $PO_2$ gradient. Once the oxygen ion arrives on the other side of the MIEC, it reacts with CO or $H_2$ to produce $CO_2$ or $H_2O$ and electrons. As a result, the oxygen partial pressure on this side is reduced and the driving force is created. The electrons migrate back to the topside of the MIEC to react with water. Although $CO_2$ is produced in this process, it can be collected and stored in the $H_2$ production plant.

$$H_2O + 2e^- \longrightarrow O^{2-} + H_2$$

**MIEC Membrane**

$\uparrow e^-$ $\downarrow O^{2-}$

$$CO_2 + 2e^- \longleftarrow O^{2-} + CO$$
$$H_2O + 2e^- \longleftarrow O^{2-} + H_2$$
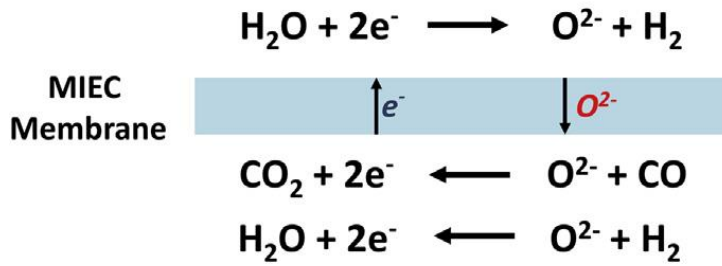
Figure 2. A water splitting process on a MIEC (from Li et al. [22]).

Syngas which consists of CO and $H_2$ is a raw material for the synthesis of methanol and a series of chemicals [29]. It is also a source of fuel [30]. It can be produced by the partial oxidation of methane on MIECs, which shows higher energy efficiency and emits less $CO_2$ than the steam reforming of methane [29]. The mechanism of partial oxidation of methane on a MIEC is shown in Figure 3. Oxygen vacancies which are shown as white spots are created on the top side of the MIEC, in order to offer oxygen ions shown as black circles. $CH_4$ is oxidized by the oxygen ions to produce CO and $H_2$. The vacancies are filled by the oxygen ions diffusing from the bottom side of the MIEC where $O_2/N_2$ is flowing. On the bottom side, the $O_2/N_2$ flow offers the oxygen ions which drop in the nearby oxygen vacancies caused by the upward oxygen ion diffusion. [29]

$CH_4$      $CO + H_2$

Generation/syngas production step

MIEC

Regeneration step

$O_2/N_2$
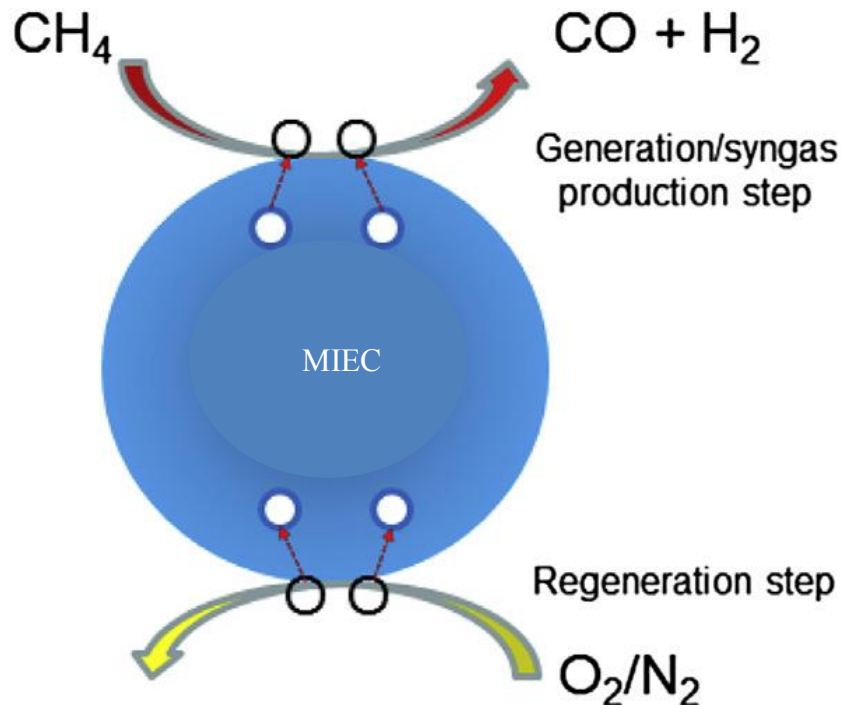
Figure 3. The mechanism of partial oxidation of methane on a MIEC (After Khine st al. [29]).

## 2.1.2 The perovskite structure

The perovskite structure is shown in Figure 4. Larger cations occupy the A-site, smaller cations occupy the B-site. The remaining sites are oxygen sites. [8]
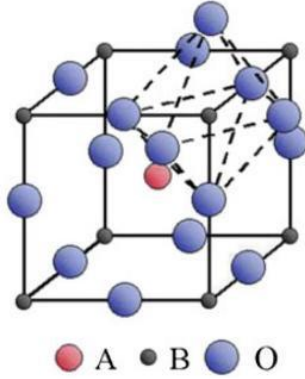


Figure 4. The cubic perovskite structure (from Manthiram et al. [8]).

### 2.1.2.1 The Goldschmidt tolerance factor

The perovskite structure can remain stable when the Goldschmidt tolerance factor t is between 0.75 and 1.1 [8]. The factor can be determined by the following equation, where $r_A$, $r_B$ and $r_O$ are the ionic radius of the A-site, B-site and oxygen ion respectively.

$$t = \frac{r_A + r_O}{\sqrt{2}(r_B + r_O)}$$
Equation 1

### 2.1.2.2 The charge neutrality

Once a perovskite MIEC doped by a foreign cation, the overall charge can be increased/reduced because the valence of the dopant may be different from that of the cation of the MIEC [8]. For a perovskite MIEC containing aliovalent cations, the high valence tends to be destabilised by higher temperatures or low $PO_2$ environments, hence the overall charge is reduced. The charge of the perovskite structure can be maintained by an ionic compensation and an electronic compensation [8]. The ionic compensation changes δ (oxygen non stoichiometry) to release/reclaim oxygen ions when the cation ion valence is decreased/increased. As a result, the oxygen vacancy concentration is changed. For example, an increase in temperature or a decrease in $PO_2$ can decrease the B-site cation valence [8]. As a result, the oxygen anions are released to keep the charge neutrality and oxygen vacancies are created. The electronic compensation changes the valence of

one cation to release/localise electrons when the valence of the other cation is reduced/increased. A n-type conductor compensates the extra positive charges created by extra oxygen vacancies or interstitial metal ions by releasing electrons [31]. A p-type conductor compensates the extra negative charges created by extra metal vacancies or interstitial oxygen ions by forming electron holes [31].

### 2.1.2.3 The transformation to the brownmillerite structure

However, too high an oxygen vacancy concentration may transform the cubic perovskite structure to the brownmillerite structure [32-34]. For example, the cubic perovskite structure of $SrFeO_{3-\delta}$ was transformed to brownmillerite structure when $\delta$ was increased from 0 to 0.5 [32]. In addition, the oxygen vacancy formation enthalpy can be reduced by Sr doping in $La_{0.98-x}Sr_xCo_{0.2}Fe_{0.8}O_{3-\delta}$ (x varies from 0.125 to 0.8) [35]. As a result, the oxygen permeation flux was increased.

### 2.1.2.4 The thermal expansion

Since the MIEC is an ideal material for the SOFC cathode which works at high temperatures. The thermal expansion of the cathode needs to match that of the electrolyte. Otherwise, the thermal strain mismatch can cause cracks or delaminations [8]. Unfortunately, the thermal expansion coefficient (TEC) of perovskite MIEC containing Co (TEC of $La_{1-x}Sr_xCoO_{3-\delta}$: $21.3*10^{-6}°C^{-1}$ [36]) can be higher than the TEC ($10.0*10^{-6}$ to $12.5*10^{-6}°C^{-1}$ [8]) of the electrolyte including yttria stabilized zirconia (YSZ), gadolinium-doped $CeO_2$ (GDC), and $La_{0.8}Sr_{0.2}Ga_{0.8}Mg_{0.2}O_{2.8}$ (LSGM). The spin state transition of Co can be one reason for the high TEC [36, 37]. The high TEC can also be attributed to oxygen loss because the $Co^{4+}$ cation becomes the larger $Co^{3+}$ cation to keep charge neutrality [38, 39]. In addition, the thermal expansion of ionic bonds is larger than that of covalent bonds, suggesting the variation in bonding covalency also affects TEC. [8] For example, the TEC of $Ln_{0.6}Sr_{0.4}CoO_{3-\delta}$ (Ln=La, Pr, Nd, Sm, and Gd) was reduced from $21.3*10^{-6}$ to $17.1*10^{-6}°C^{-1}$, when Ln was sequentially replaced by La, Pr, Nd. Sm and Gd. Meanwhile, the ionic character of the Ln-O bond decreased.

# 2.1.3 The conduction mechanism

### 2.1.3.1 The conducting species

The conduction is enhanced by the two types of conduction component in perovskite MIECs: the electronic component and structural component [1]. The electronic conductivity is affected by the electronic bandgap, while the ionic conductivity is affected by the crystal structure [40].

### 2.1.3.1.1 The electronic component

There are a negative and a positive electronic component. The negative electronic component is electrons excited from the valence band to the conduction band [41]. The electrons migrate between metal cations and oxygen anions via the metal-oxygen bond which is the overlap of a metal electron orbital and an oxygen electron orbital [36]. The electronic conductivity can be reduced when the overlap is reduced because the bond covalency is reduced and the electrons are more localised [36]. It can be increased by enhancing the metal cation valence to release more electrons and by increasing the metal-oxygen bond covalency [42]. The B-site aliovalent cations can receive/release electrons to vary electronic conductivity and charge transfer [18]. However, the A-site cations don't directly conduct electrons because they tend to have one valence state [18]. The positive electronic component is electron holes formed in the valence band after an electron is moved from the valence band to the neutral levels near the valence band [43, 44]. It migrates in the lattice by hopping, in which case a valence band electron can hop from one cation (creating a new hole) to another (filling an old hole) in the lattice [45].

## 2.1.3.1.2 The structural component

The structural component is point defects, line defects and plane defects [31]. Of the structural component, point defects are considered more important in this research. They are vacancies and interstitial sites in the lattice. Frenkel defects and Schottky defects are two types of common point defects, shown in Figure 5 [46]. For the former one, an atom/ion leaves its site creating a vacancy and become an interstitial site atom/ion. For the latter one, the same amount of cation vacancy and anion vacancy are created. Oxygen ions are conducted via oxygen vacancies [47-50].
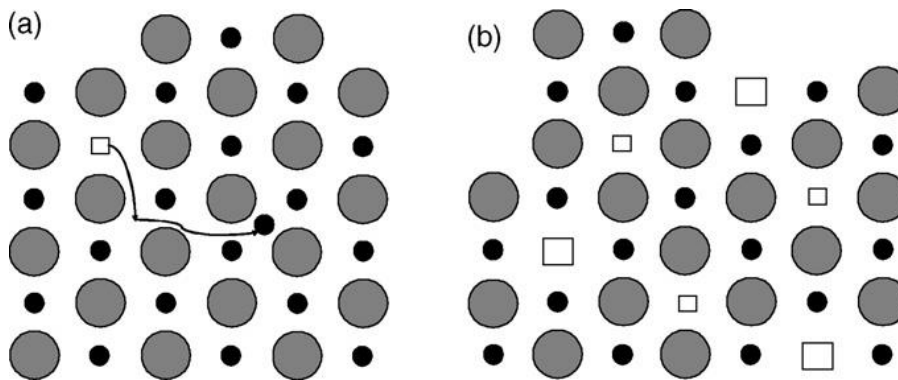


Figure 5 (a) Frenkel defects (b) Schottky defects (from Kingery et al. [46])

## 2.1.3.2 The transport of the species

### 2.1.3.2.1 Factors which affect the ionic conductivity

The Goldschmidt tolerance factor [8], the lattice free volume [51, 52] and the lattice stress [53] are some of the factors which affect the ionic conductivity. According to Kharton et al. [54], a decrease in the volume of the perovskite unit cell can decrease the oxygen ion conductivity because the oxygen ion transport channel size can be reduced.

### 2.1.3.2.2 The effect of bond bending on the electronic conductivity

For MIEC containing Co, the bending of the O-Co-O bond can affect the electronic conductivity [36, 55]. It may happen due to substitution of the A-site cations. If the O-Co-O bond was bent, the overlap between the $Co^{3+/4+}$: 3d and $O^{2-}$: 2p orbital would be reduced. The decrease in the overlap can reduce the bandwidth, which reduces the bond covalency. As a result, the electrons can be localised and the electronic conductivity can be reduced.

In a study of $La_{1-x}Sr_xCoO_{3-\delta}$ where x was increased from 0 to 0.15 [55], the bending in the Co-O-Co bond increased the bond angle from 164° to approximately 165.4°, the authors suggested that the bending also increased the spin state of Co from low spin $Co^{III}$ ($t_{2g}^6e_g^0$) to intermediate spin $Co^{iii}$ ($t_{2g}^5e_g^1$) and/or high spin $Co^{3+}$ ($t_{2g}^4e_g^2$) based on the conductivity behaviour change and spin state change at x=0.15, the increase in Co-O bond covalency accompanied by increasing in x and that the density of states was significantly affected by the bond angle.

### 2.1.3.2.3 A general description of the transport of the species

Figure 6 shows the charge carrier (oxygen ions and electrons) transport in a MIEC [56, 57]. At interface I, an oxygen molecule ($O_2$) becomes oxygen ions ($O^{2-}$) via a surface exchange (the electrons are provided by the MIEC). The oxygen ions ($O^{2-}$) diffuse through the bulk via oxygen vacancies. At interface II, the oxygen ions ($O^{2-}$) become an oxygen molecule ($O_2$) via a surface exchange and release electrons (e). The electrons (e) transport back to interface I. P'$O_2$ and P''$O_2$ are the $PO_2$ of the high $PO_2$ gas and the low $PO_2$ gas. The $PO_2$ gradient shown as the long dash line drives the $O^{2-}$s to diffuse.
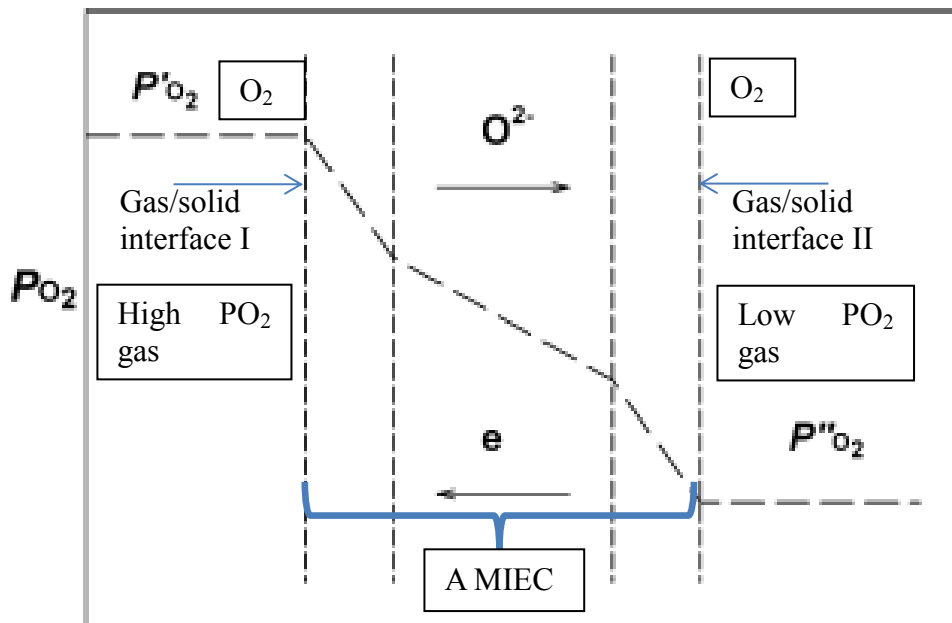


Figure 6. The charge carrier transport in a MIEC (after Sunarso et al. [1]).

2.1.3.2.4 The surface exchange reactions

An oxygen molecule in the gas phase becomes surface oxygen atoms on interface I (Figure 6). The surface oxygen atoms are combined with a surface oxygen vacancy to form an occupied oxygen site and electron holes on interface I. The process is defined as surface exchange and reversed on interface II after the occupied oxygen site and the electron hole are transported to interface II (Figure 6).

The surface exchange reactions can be described by the following equations [58] with Kröger-Vink notations [59, 60]. 'g' indicates $O_2$ in gas phase and 'W' indicates that the subscripted species is a surface species. Single and double prime indicate that the species is on interface I and II respectively. '$V_O^{\bullet\bullet}$' is a positively charged oxygen vacancy. '$O^{\chi}$' is a neutral occupied oxygen site. h is an electron hole.

The rate of surface exchange (the oxygen exchange flux through the surface) is associated with the kinetic parameter of oxygen surface exchange coefficient k [61] and is affected by the concentration of surface oxygen vacancies [5]. k was affected by $PO_2$, in one study of $La_{0.5}Sr_{0.5}CoO_{3-\delta}$ [62]. The coefficient can be measured by $^{18}O/^{16}O$ isotope exchange/depth-profiling (IEDP) [63, 64].

$$O_{2(g')} \leftrightarrow 2O_{(W')}$$

Equation 2

$$O_{(W')} + V_{O(W')}^{\bullet\bullet} \leftrightarrow O^{\chi}_{(W')} + 2h_{(W')}$$

Equation 3

$$O^{\chi}_{(W')} \leftrightarrow O^{\chi}_{(W'')}$$

Equation 4

$$h_{(W')} \leftrightarrow h_{(W'')}$$
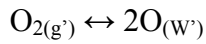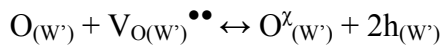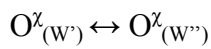
Equation 5

## 2.1.3.2.5 The oxygen permeation and the Wagner theory

The overall oxygen permeation rate tends to be restricted by the slowest step (surface exchange/diffusion) or the slowest conducting species (oxygen ions/electrons) [56, 65, 66].

Between the surface exchange and the bulk diffusion, the rate restricting step is mainly affected by the membrane thickness. In a recent study of $La_{0.1}Sr_{0.9}Co_{0.8}Fe_{0.2}O_{3-\delta}$ [67], the oxygen ion diffusion was converted from bulk diffusion predominant to surface exchange predominant, when the membrane thickness was reduced below $350 \pm 90$ μm, which can be considered as a critical thickness. However, when the membrane is relatively thicker, the bulk diffusion can limit the overall permeation rate. Hence, the oxygen flux can be calculated by the Wagner theory (Equation 6) [57]. In Equation 6, $\sigma_t$ is the overall conductivity, $t_i$ and $t_e$ are the ionic and electronic transfer number respectively, $\mu_{O2}$ is the chemical potential of the hypothetical neutral oxygen in the oxide, L is the oxide thickness, F is the Faraday's constant. The equation is valid, when the oxygen ions, electrons, electron holes and oxygen molecules maintain a local equilibrium. It can be changed according to the slowest step, the slowest species and the type of MIEC. For example, there is a Wagner equation developed for the case in which the surface exchange becomes the permeation rate limiting step.

$$J_{O_2} = \frac{1}{4^2 F^2 L} \int_{\mu_{O_2(II)}}^{\mu_{O_2(I)}} t_i t_e \sigma_t d\mu_{O_2}$$

Equation 6

## 2.1.3.2.6 Factors which affect the permeation rate

The rate of oxygen permeation can be affected by the working temperature, composition of the MIEC, decomposition during working, grain size, surface roughness, membrane thickness and $PO_2$ gradient, [18]. It can be measured in permeation experiments. The oxygen diffusion coefficient can be measured by isotope exchange/depth-profiling (IEDP).

*2.1.3.2.6.1 The composition effect*

It is difficult for the oxygen ions to leave the perovskite structure, when metal cations (e.g. Mn) form strong bond with the oxygen ions [48, 49, 68, 69]. In this case, the concentration of oxygen vacancies can be low, leading to low oxygen flux. For example, the oxygen flux of $La_{0.6}Sr_{0.4}Co_{0.8}Cu_{0.2}O_3$ at 900 ℃ was reduced from 1.9 ml/min*cm$^2$ to 0.5 ml/min*cm$^2$, after all Cu was replaced by Mn [48]. However, the stronger bonding may enhance the activation energy of oxygen diffusion, which may also be a reason for the permeation rate decrease.

*2.1.3.2.6.2 The phase effect*

Phase changes (perovskite to brownmillerite) due to the increase in δ leads to ordered oxygen vacancies, which reduces the permeation rate [32, 33]. In a $CO_2$ free environment, the cubic perovskite phase decomposes to secondary phases with hexagonal structures, which reduces the permeation rate [70]. In $CO_2$ involved environment, the MIECs containing alkaline earth elements (BSCF) may react with $CO_2$ and hence a carbonate phase grows on the MIEC surface to block oxygen permeation [16, 71].

*2.1.3.2.6.3 The thickness effect*

In a recent study of $La_{0.1}Sr_{0.9}Co_{0.8}Fe_{0.2}O_{3-\delta}$ [67], the permeation flux was increased from 0.6 ml cm$^{-2}$ min$^{-1}$ to 1.6 ml cm$^{-2}$ min$^{-1}$ when the membrane thickness was reduced from 2.65 mm to 0.8 mm. The other experimental conditions remained the same. The reason for the enhancement is that the rate limiting step is gradually converted from the bulk diffusion limiting to surface exchange limiting [72, 73]. The oxygen diffusion coefficient, the surface exchange coefficient and the surface oxygen vacancy concentration depend on $PO_2$ and temperature [18].

*2.1.3.2.6.4 The microstructure effect*

The microstructure affects the permeation rate by grain boundaries and the surface roughness. Since the grain boundaries can be responsible for the oxygen permeation flux [74, 75]. The amount of grain boundaries becomes important. It can be adjusted by changing the grain size because the larger the grains the fewer grain boundaries. The grain size is controlled by sintering temperatures. In one study [74, 75], the average grain size of the sample sintered at 1000 ℃, 1120 ℃ and 1150 ℃ were 10 μm, 30 μm and 45 μm, respectively. The oxygen flux measured at 900 ℃ of the 10 μm, 30 μm and 45 μm sample

were 1.25 $cm^3(STP)*cm^{-2}*min^{-1}$, 1.19 $cm^3(STP)*cm^{-2}*min^{-1}$ and 1.20 $cm^3(STP)*cm^{-2}*min^{-1}$ respectively. In the other study [9], the average grain size of the sample sintered at 1000 ℃, 1050 ℃ and 1100 ℃ were 3.32 μm, 6.86 μm and 18.25 μm, respectively. The oxygen flux measured at 900 ℃ of the 3.32 μm, 6.86 μm and 18.25 μm sample were 2.1 $Nml*min^{-1}*cm^{-2}$, 1.85 $Nml*min^{-1}*cm^{-2}$ and 2.0 $Nml*min^{-1}*cm^{-2}$, respectively. Both researches suggested that the grain size seemed to show limited effects on the oxygen flux because the resistance of the grain boundaries was similar to that of the grains [9]. The former research obtained larger grain size than the later research obtained after 1000 ℃ sintering because the sintering time of the former research (12 hours) is longer than that of the latter one (2 hours). The permeation rate can be increased by enhancing the surface roughness because the rougher the surface is the larger the surface area which the surface exchange reaction can take place, when surface exchange reaction is the rate limiting step [76].

### 2.1.3.2.6.5 The $PO_2$ gradient effect and the $PO_2$ effect

For the effect of the $PO_2$ gradient on the permeation rate, in a study of $La_{0.6}Sr_{0.4}Co_{0.2}Fe_{0.8}O_{3-\delta}$ [77], the permeation flux was decreased from 0.12 $ml/cm^2$ min to 0.05 $ml/cm^2$ min, when the $PO_2$ difference was reduced from 0.21 atm to 0.192 atm. However, the reason for this behaviour wasn't discussed. It was explained in one study of $La_{0.9}Sr_{0.1}FeO_3$ and $La_{0.9}Sr_{0.1}CoO_3$ [78]. Firstly, the permeation rate was positively correlated to the ionic conductivity, when the temperature and sample thickness were constant and the ionic conduction was the rate limiting step. Secondly, the ionic conductivity was positively correlated to the concentration of the oxygen vacancies, when the vacancy diffusion coefficient, the molar volume of perovskite and the temperature were constant. Thirdly, the concentration of the oxygen vacancy of the investigated materials showed a decrease of two orders when the $PO_2$ difference of the feed side and the permeate side decreased from 1 atm to 0 atm.

For the effect of the $PO_2$ on the ionic conductivity, in a study of $LaCoO_3$ [79], the ionic conductivity was reduced from $2*10^{-3}$ S $cm^{-1}$ to $0.4*10^{-3}$ S $cm^{-1}$, when $PO_2$ of the feed side was increased from 0.01 to 1 bar. The reason was that the ionic conductivity of $LaCoO_3$ was mainly affected by the oxygen vacancy concentration which was reduced by the increase in $PO_2$. The oxygen vacancy concentration of $LaCoO_3$ was strongly affected by

$PO_2$. Once $LaCoO_3$ was doped by Sr ($La_{0.4}Sr_{0.6}CoO_{3-\delta}$), the dependency of oxygen vacancy concentration on $PO_2$ became weaker. The doping level became the main faction that controls the oxygen vacancy concentration.

### 2.1.3.2.7 The activation energy of oxygen diffusion

The activation energy of the oxygen diffusion coefficient consists of the migration energy $\Delta Hm$ and the enthalpy $\Delta Hf$ related to the oxygen vacancy formation [80].

### *2.1.3.2.7.1 Factors which affect the activation energy*

In the study of $La_{1-x}Sr_xCoO_{3-\delta}$ [80], the diffusion coefficient of the material was studied by the conductivity relaxation technique. The $PO_2$ of the environment in which the material was studied was decreased from $1.1*10^{-2}$ bar to $4.0*10^{-4}$ bar. As a result, the activation energy of the oxygen diffusion coefficient was increased from 63 kJ $mol^{-1}$ to 91 kJ $mol^{-1}$. The increase is a result of the changes in $\Delta Hf$ because $\Delta Hm$ was considered to be constant, suggesting $PO_2$ changes the activation energy by changing $\Delta Hf$.

In the study of $Ba_xSr_{1-x}Co_yFe_{1-y}O_{3-\delta}$ [81], the activation energy of oxygen diffusion across the grain boundaries is higher than that across the bulk because the impurities in the boundaries may act as diffusion barriers. The boundaries may enhance $\Delta Hm$ to enhance the activation energy.

In one recent study of $La_{1-x}Sr_xCoO_{3-\delta}$ [55], the oxygen diffusion along the normal direction of the Co-O bond was relatively fast, compared to the other directions, suggesting the activation energy may depend on crystallographic orientations. The activation energy of oxygen ion diffusion was reduced because of the increased symmetry of the LSC lattice.

The activation energy of Li ion diffusion in $LiFePO_4$ is affected by the following factors [82] which may also affect the activation energy of oxygen ion diffusion in MIECs. The longer the metal-O bond is, the weaker the bonding. Hence, the diffusion activation energy is reduced. The larger the lattice parameter is, the larger the diffusion tunnel. Hence, the diffusion activation energy is reduced.

2.1.3.2.8 The characteristic thickness

When the membrane thickness is reduced to a characteristic thickness $L_c$ (Equation 7), the oxygen permeation is equally determined by the surface exchange and the bulk diffusion. In Equation 7, $D^*$ is the oxygen diffusion coefficient and k is the surface exchange coefficient. [73]

$$L_c = D^*/k$$

Equation 7

The surface exchange limited permeation flux of BSCF is higher than the bulk diffusion limited permeation flux of BSCF [72]. $L_c$ of BSCF was 1.1 mm at 900 °C [72]. In Figure 7, the permeation flux at 0.5 mm is higher than that at 1.5 mm.
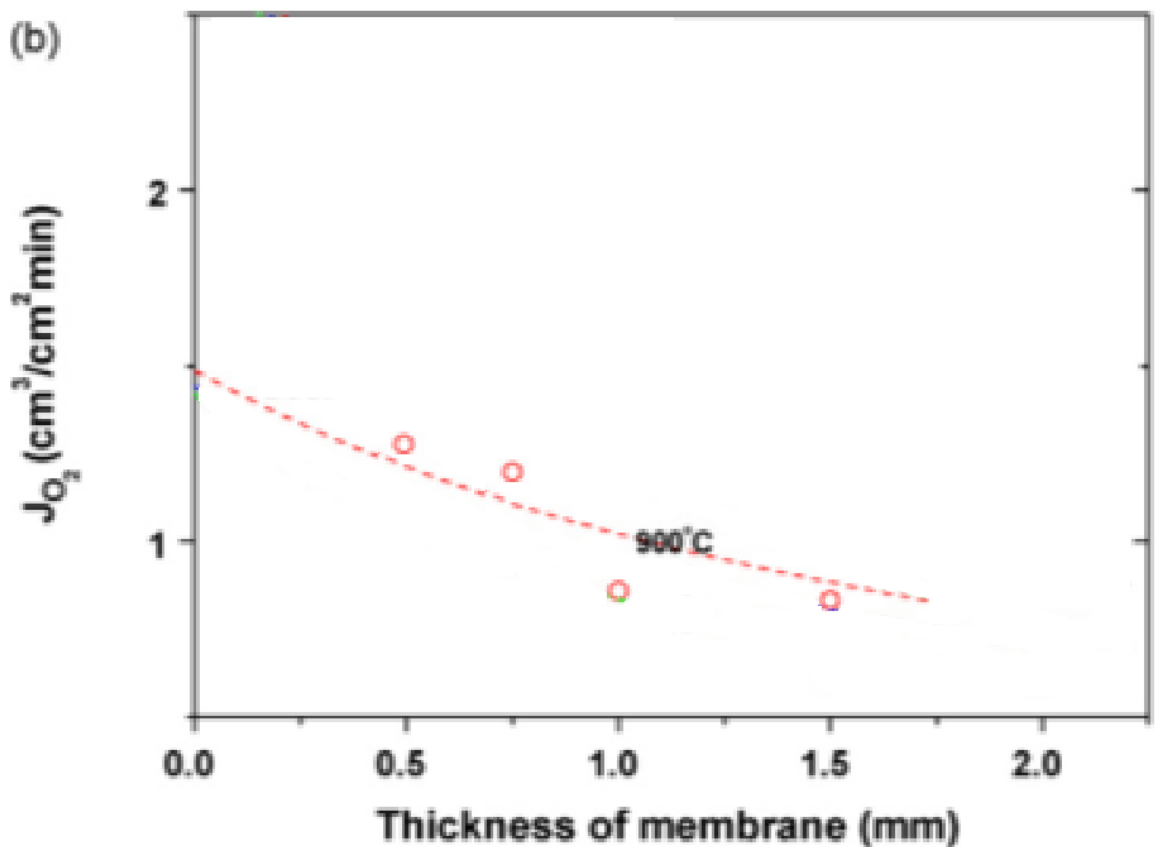


Figure 7. The permeation flux of BSCF plotted as a function of membrane thickness (After Hong and Choi [72]).

2.1.3.3 The overall conductivity

The overall conductivity can be determined by Equation 8 [1]. $c_i$, n, p are the

52

concentration of the ions, electrons and electron holes respectively. q and $\mu$ are the charge and mobility of the conducting species, respectively. The mobility of electronic defects is likely to be 100 or 1000 times higher than that of ions [1]. Therefore, electronic defects are likely to be the main contributor of the total conductivity. This is evidenced by a recent research [67] that the total conductivity of $La_{0.1}Sr_{0.9}Co_{0.8}Fe_{0.2}O_{3-\delta}$ was mainly contributed by electron hole conduction (localised holes hopping and delocalised holes conducting in the conduction band). In the study of $La_{1-x}Sr_xCoO_{3-\delta}$ [55], the Co spin state also seems to be important in terms of affecting the electronic conductivity because the spin state transition of Co converted semiconductor conduction to metal conduction. In addition, the O-Co-O bond bending and the electron density seem to outweigh $c_i$, p, q and $\mu$ [55].

$$\sigma = \sum_i c_i q_i \mu_i + n q_e \mu_e + p q_h \mu_h$$

Equation 8

2.1.3.3.1 The general Brouwer diagram

Figure 8 (a, b) show the logarithm of the defect concentration of four species (electrons, electrons holes, oxygen vacancies and oxygen interstitial sites) as a function of $PO_2$. $[V_O^{\bullet\bullet}]$ and $[O_i'']$ are the concentration of oxygen vacancies and oxygen interstitial sites respectively. Figure 8 (a) shows that the concentration of electronic defects is always higher than that of structural point defects. In Figure 8 (b), in the blue frame, the concentration of structural defects is higher than that of electronic defects. Outside the blue frame, the former concentration is lower than the latter concentration. However, these graphs are considered valid when the defect concentration is low because of the assumption that the interaction between defects is not involved [41].
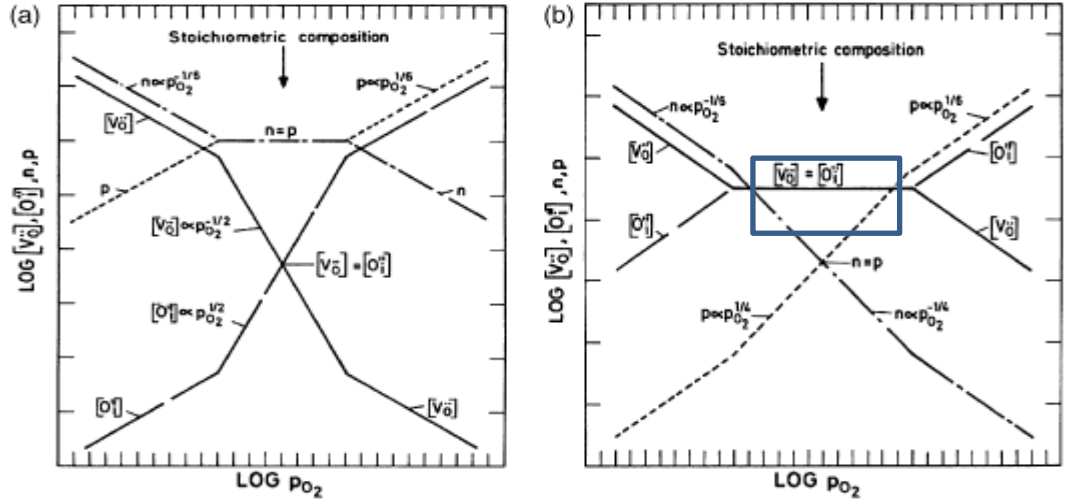
Figure 8. General Brouwer diagram for (a) Electronic defects concentration higher than structural point defect concentration (b) The blue frame highlights the opposite case to (a) (After Kofstad [83]).

2.1.3.3.2 The defect reactions

The defect reactions can be described by the following equations when the defect concentration is low [59, 60]. In Equation 9, an occupied oxygen site in a MIEC ($O_o^x$) becomes an oxygen vacancy ($V_O^{\bullet\bullet}$), half an oxygen molecule ($O_2$) and 2 electrons (e), and vice versa. In Equation 10, an oxygen atom becomes an oxygen interstitial site ($O_i''$) and two electron holes (h), and vise versa. In Equation 11, neutral charge becomes an electron and an electron hole, and vise versa. In Equation 12, the occupied oxygen site becomes an oxygen vacancy and an oxygen interstitial site, and vise versa.

$$O_O^x \leftrightarrow V_O^{\bullet\bullet} + \frac{1}{2}O_2 + 2e$$

Equation 9

$$\frac{1}{2}O_2 \leftrightarrow O_i'' + 2h$$

Equation 10

$$nil \leftrightarrow e + h$$

Equation 11

$$O_O^x \leftrightarrow O_i'' + V_O^{\bullet\bullet}$$
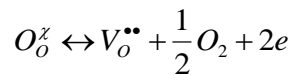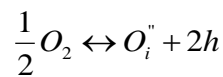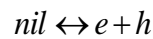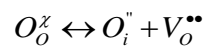
Equation 12

However, the defect concentration is not low in practice. Thus, defect interactions (point defect coulombic attractions and the defect ordering) have to be considered [41]. They can cause low conductivity. If the activation energy of one defect species is higher than that of the other one, the conductivity of this species tends to be increased faster when the temperature is increased [1].

## 2.1.4 The ceramic candidates for oxygen separation membranes

There are three types of ceramic oxide which are able to separate oxygen. They are the fluorite-based, perovskite-based and dual-phase materials [1]. The fluorite-based materials mainly include zirconia [58, 84] and bismuth oxide [66, 85]. The perovskite-based materials mainly include strontium cobaltite based compounds which are doped with alkaline-earth cations or rare-earth cations on the A-site [13, 47, 48, 86-91]. The dual-phase materials are composites which have a ceramic phase and a metal phase [2, 92-95]. Compared to the oxygen flux of the fluorite-based materials, the perovskite-based materials exhibit higher oxygen flux, especially BSCF (Figure 9). The dual-phase materials show lower oxygen flux, compared to the perovskite-based materials. Therefore, BSCF shows the highest oxygen flux over the temperatures in Figure 9. [1]

The perovskite based MIECs containing Co exhibit superior mixed electronic ionic conductivity, compared to the perovskite based MIECs containing other period 4 transition metal ions [8]. The increase in the number of oxygen vacancies in the perovskite structure can increase the oxygen flux. However, the perovskite structure may collapse to a brownmillerite structure when the amount of oxygen vacancies exceeds a limit [33, 96]. This collapse may reduce the oxygen flux because the oxygen vacancies tend to be ordered [8]. Barium and strontium are able to prevent the collapse when they occupy the A-site of the perovskite structure. [1]

The legend symbols correspond to:
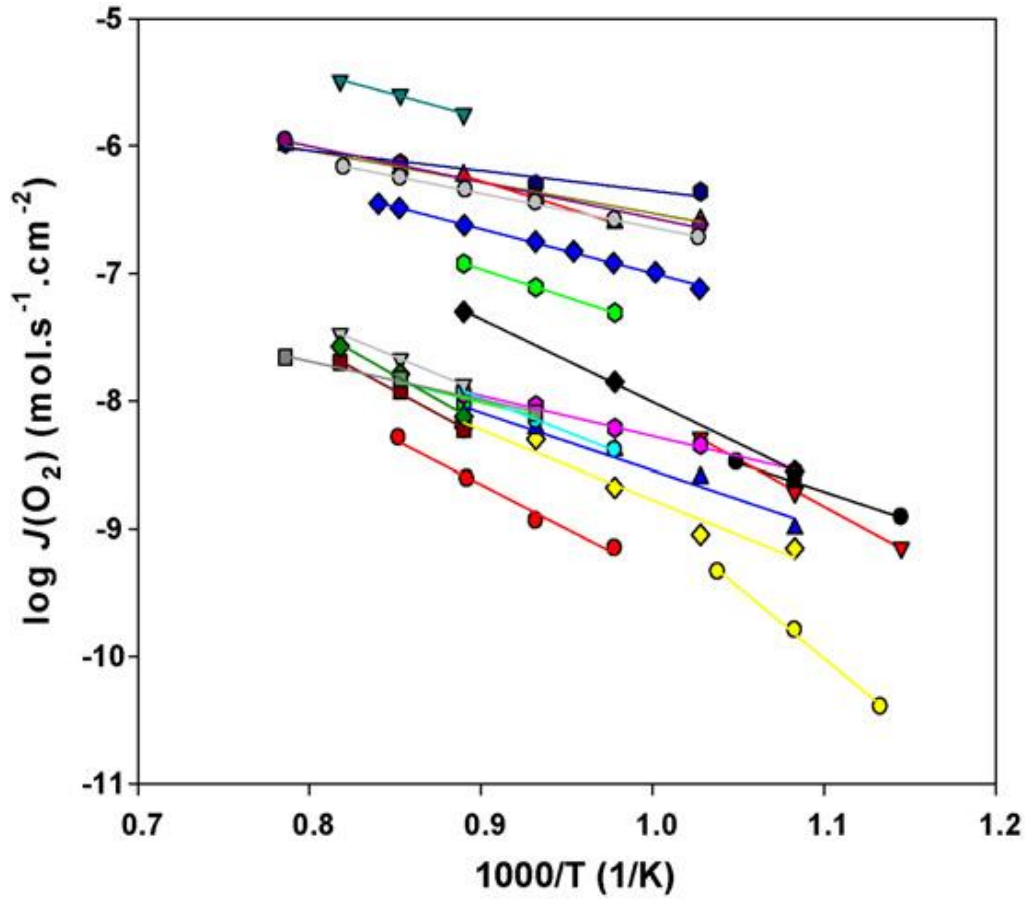
- $(Bi_2O_3)_{0.73}(CaO)_{0.27}$
- $(Bi_2O_3)_{0.75}(Er_2O_3)_{0.25}$
- $(Bi_2O_3)_{0.75}(Y_2O_3)_{0.25}$
- $Bi_{1.25}Y_{0.5}Cu_{0.25}O_3$
- $BiY_{0.5}Cu_{0.5}O_3$
- $Bi_{0.75}Y_{0.5}Cu_{0.75}O_3$
- $Bi_{1.5}Y_{0.3}Sm_{0.2}O_3$
- $Ce_{0.8}Pr_{0.2}O_{2-d}$
- $Gd_{0.15}Ce_{0.65}Pr_{0.2}O_{2-d}$
- $Gd_{0.2}Ce_{0.6}Pr_{0.2}O_{2-d}$
- $La_{0.8}Sr_{0.2}Ga_{0.7}Ni_{0.3}O_{3-d}$
- $La_{0.8}Sr_{0.2}Ga_{0.7}Fe_{0.3}O_{3-d}$
- $La_{0.8}Sr_{0.2}Ga_{0.7}Co_{0.3}O_{3-d}$
- $Ba_{0.5}Sr_{0.5}Co_{0.8}Fe_{0.2}O_{3-d}$
- $CaTi_{0.8}Fe_{0.2}O_{3-d}$
- $(ESB)_{0.6}$-$(Au)_{0.4}$
- $(BYS)_{0.6}$-$(Ag)_{0.4}$
- $(BYS)_{0.7}$-$(Ag)_{0.3}$
- $(BICOVOX)_{0.6}$-$(Au)_{0.4}$
- $(Zr_{0.8}Y_{0.2}O_{1.9})_{0.6}$-$(La_{0.8}Sr_{0.2}CrO_{3-d})_{0.4}$

Figure 9. The oxygen flux of the MIEC candidates plotted against temperature (from Sunarso et al. [1]).

The following works [72, 97-104] show the most recent oxygen permeation data from the three types of material described above. The data measured at 900 °C or 850 °C were chosen for comparison because the permeation flux is relatively higher than that

measured at lower temperatures. 900 ℃ is the highest measurement temperature in most works reviewed here hence no data measured at a temperature higher than 900 ℃ is included.

### 2.1.4.1 The perovskite candidates

### 2.1.4.1.1 The hollow fibre membranes

Table 1 shows permeation and geometry data from recent studies of hollow fibre membranes. The highest values of permeation flux obtained from the geometry are for BSCF [97].

Table 1 Oxygen permeation flux data for perovskite MIECs (hollow fibres)

| Material | BSCF | $La_{0.6}Sr_{0.4}Co_{0.2}Fe_{0.8}O_{3-\delta}$ |
|---|---|---|
| Permeation flux | 1.6 ml/min*cm$^2$ | 0.35 ml/min*cm$^2$ |
| Temperature | 900 ℃ | 900 ℃ |
| Thickness | 500 μm | 400 μm |
| Feed gas | Air | Air |
| Sweep gas | He | He |
| Shape | Hollow fibre | Hollow fibre |
| References | [98] | [99] |

### 2.1.4.1.2 The multichannel hollow fibre membranes

Figure 10 shows a schematic cross section of a multichannel hollow fibre. The portion shaded in blue is solid, while the portions shaded in white are hollow. Table 2 shows permeation and geometry data from recent studies of multichannel hollow fibre membranes. The highest values of permeation flux obtained from the geometry are for BSCF [99].
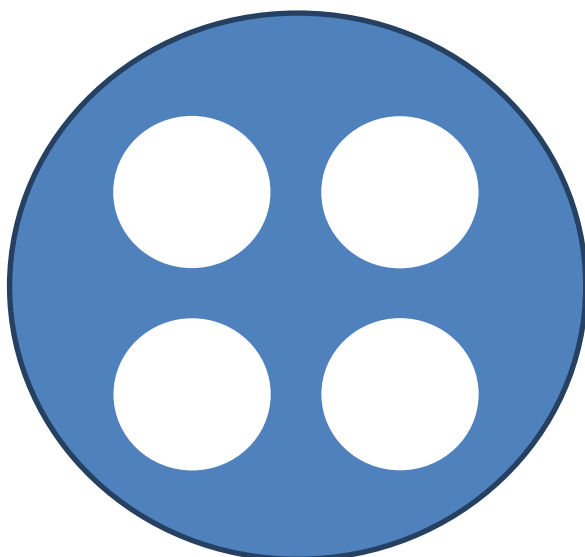
Figure 10. The cross section of a multichannel hollow fibre.

Table 2 Oxygen permeation flux data for perovskite MIECs (multichannel hollow fibres)

| Material | BSCF | $SrFe_{0.8}Nb_{0.2}O_{3-\delta}$ |
|---|---|---|
| Permeation flux | 2.5 ml/min*cm$^2$ | 1.2 ml/min*cm$^2$ |
| Temperature | 900 ℃ | 900 ℃ |
| Outer diameter | 3.31 mm | 2.48 mm |
| Inner diameter of every channel | 0.69 mm | 0.71 mm |
| Feed gas | Air | Air |
| Sweep gas | He | He |
| Shape | Multichannel hollow fibre | Multichannel hollow fibre |
| References | [100] | [101] |

## 2.1.4.2 A fluorite candidate

Table 3 shows permeation and geometry data from recent studies of ceramic pellet membranes. The highest values of permeation flux obtained from the geometry are for BSCF [72].

Table 3 Oxygen permeation flux data for a fluorite MIEC (The data of BSCF was shown as a standard)

| Material | BSCF | $Ce_{0.8}Tb_{0.2}O_{2-\delta}$ |
|---|---|---|
| Permeation flux | 1 ml/min*cm$^2$ | 0.01 ml/min*cm$^2$ |
| Temperature | 850 ℃ | 850 ℃ |
| Thickness | 1000 μm | 1000 μm |
| Feed gas | Air (PO$_2$ 0.21 atm) | Unknown gas (PO$_2$ 0.21 atm) |
| Sweep gas | He (PO$_2$ 0.002 atm) | Unknown gas (PO$_2$ 0.05 atm) |
| Shape | pellet | pellet |
| References | [73] | [102] |

### 2.1.4.3 The composite candidates (coated pellet)

#### 2.1.4.3.1 Dense base + coating

Row 1 and 3 in Table 4 show permeation and geometry data from recent studies of a $Ba_{0.95}La_{0.05}FeO_{3-\delta}$ (BLF) dense pellet coated by a $La_{0.9}Sr_{0.1}FeO_{3-\delta}$ (LSF91) porous layer [102] and a BSCF dense pellet coated by $La_{0.7}Sr_{0.3}CoO_3$ (LSC73) [72]. The highest values of permeation flux obtained from the geometry are for LSF91 coated BLF [102].

In the work of LSF91 coated BLF [102], x in $La_{1-x}Sr_xFeO_{3-\delta}$ varies from 0.1 to 1. As a result, the oxygen non stoichiometry, amount of open voids and surface area are all changed. The oxygen non stoichiometry wasn't strongly associated with the permeation rate. The increase in the amount of open voids reduced the permeation rate because an open void may cause coating free areas on the BLF pellet [102]. The increase in the surface area increased the permeation rate.

In Table 4, the coated BSCF shows higher permeation rate than BSCF, suggesting the coating layer improved the permeation [72]. The improved permeation rate was attributed to better surface exchange [72]. The factors which affect the surface exchange are the coating microstructure (particle size, porosity and surface area) and the different coating composition [72].

#### 2.1.4.3.2 Complex base + coating

In one study [103], a sandwich pellet consists of a dense BSCF layer (thickness: 20 μm), a porous BSCF layer (thickness: 40 μm) and the other porous BSCF layer (thickness: 940 μm) (Figure 11). Both surfaces of the pellet were infiltrated by $Gd_{0.1}Ce_{0.9}O_{1.95}$ (GDC) particles followed by sintering. The cross section of one surface is shown in Figure 12 (a), showing the particles are on the surface. The oxygen permeation flux of this sample is shown in Table 4. However, which side is fed/swept wasn't mentioned.

This work was nice for measuring the permeation rate of a sandwich pellet without GDC infiltration under exactly the same condition (shown in Table 4), suggesting the GDC layer improves the permeation rate by 25%. The surface exchange was investigated by measuring the surface exchange coefficient of a dense BSCF sample and a GDC infiltrated dense BSCF sample which was sintered after infiltration. At 600 ℃, the surface exchange coefficient of the dense BSCF pellet and the GDC infiltrated dense BSCF pellet are 2.5

*$10^{-4}$ cm s$^{-1}$ and 6.6 * $10^{-3}$ cm s$^{-1}$ respectively, suggesting the higher permeation rate can be a result of better surface exchange. In addition, the activation energy of BSCF surface exchange was reduced from 129 kJ mol$^{-1}$ to 82.4 kJ mol$^{-1}$ due to GDC infiltration, suggesting easier surface exchange.

The permeation rate of a BSCF dense pellet was also measured under the same condition (shown in Table 4), suggesting the sandwich structure improve the permeation rate by 17% because the sandwich structure reduced the dense layer thickness which is inversely related to the permeation rate.



The 940 µm porous layer

The 20 µm dense layer

The 40 µm dense layer
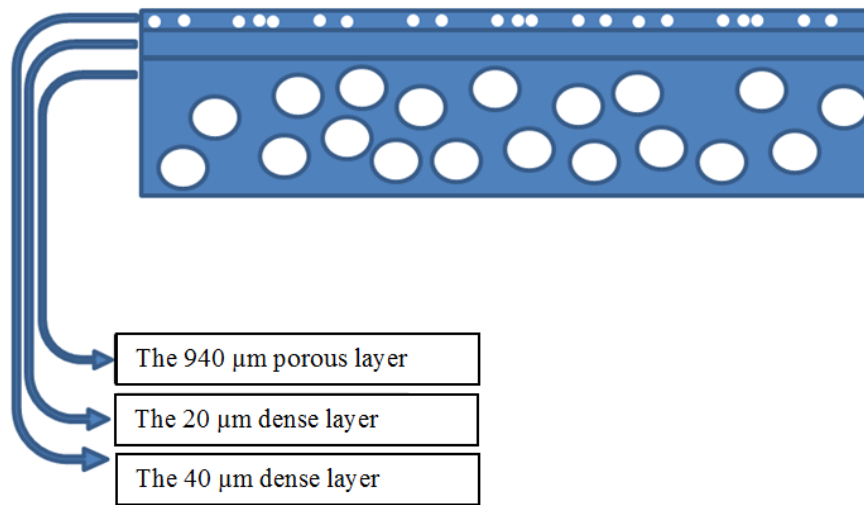
Figure 11. The schematic drawing of the multilayer BSCF pellet with thickness of each layer indicated (After He et al. [103]).



The GDC particles

BSCF

100 nm
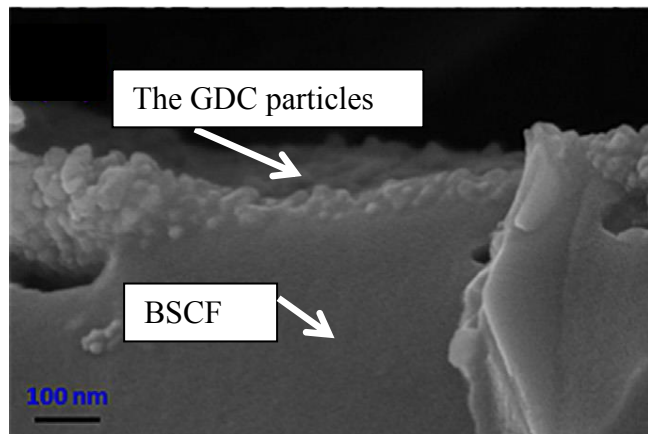
Figure 12. The GDC infiltrated porous BSCF cross section with arrows indicating both phases (After He et al. [103]).

Table 4 Oxygen permeation flux data for composite MIECs

| The base material | The coating material | Permeation flux | Temperature | Thickness | Coating layer thickness | Feed gas | Sweep gas | Shape | References |
|---|---|---|---|---|---|---|---|---|---|
| $Ba_{0.95}La_{0.05}FeO_{3-\delta}$ | $La_{0.9}Sr_{0.1}FeO_{3-\delta}$ | 2.4 ml/min*cm$^2$ | 900 ℃ | 670 μm | 8 – 10 μm | Air | He | pellet | [102] |
| $Ba_{0.95}La_{0.05}FeO_{3-\delta}$ | | 1.6 ml/min*cm$^2$ | 900 ℃ | 670 | | Air | He | pellet | [104] |
| BSCF | $La_{0.7}Sr_{0.3}CoO_3$ | 1.9 ml/min*cm$^2$ | 900 ℃ | 625 μm | 20 μm | Air | He | pellet | [72] |
| BSCF | | 1.15 ml/min*cm$^2$ | 900 ℃ | 670 μm | | Air | He | pellet | [72] |
| BSCF (sandwich) | $Gd_{0.1}Ce_{0.9}O_{1.95}$ | 5 ml/min*cm$^2$ | 900 ℃ | 1000 μm | 0.03-0.17 μm | Air | He | pellet | [103] |
| BSCF (sandwich) | | 4 ml/min*cm$^2$ | 900 ℃ | 1000 μm | | Air | He | pellet | [103] |
| BSCF | | 3.4 ml/min*cm$^2$ | 900 ℃ | 1000 μm | | Air | He | pellet | [103] |

## 2.1.5 The ceramic preparation methods

The conventional powder method, the co-precipitation method and the EDTA/citrate complexation method are widely used to prepare ceramics [1].

For the conventional mixed-oxide powder method [1], the powders of the starting chemicals are thoroughly mixed and fired at a high temperature (higher than 2/3 of the melting point) for up to 10 hours [105]. The disadvantages are high energy penalty, low homogeneity of powder, low purity of powder and wide range of particle size [1]. In addition, chemicals can vaporize during firing [105]. For the co-precipitation method [1], the initial chemicals are dissolved in water and a precipitation agent is added to the solution. The pH and the temperature of the solution can be changed to tune the stoichiometry of the product. The mixing rate and the cation concentration can control the product physical properties. The precipitates are filtered, dried and heated to obtain the required material. The advantages of this method are good morphology, purity and composition control of products.

For the EDTA/citrate complexation method, the starting chemicals are dissolved in an ethylenediaminetetraacetic acid (EDTA) and $NH_3 \cdot H_2O$ solution [13]. $NH_3 \cdot H_2O$ can adjust the pH (6) of the solution [13]. EDTA can prevent partial segregation [1]. After dissolving, citric acid is added (EDTA/citric acid/total metal ions mole ratio: 1/1.5/1) [13]. Gel can be obtained after water is vaporised. Initial powders can be obtained by heating the gel at 120 ℃ - 150 ℃ for hours. The product is carbonate free and chemically homogeneous and shows high density. Its composition is well controlled.

A study [106] investigated the effects of the conventional mixed-oxide powder (CP) method and the EDTA/citrate complexation (EC) method on the material properties. The powders prepared by these two methods showed similar distributions of the particle size. However, the EC method produced smaller grains (0.1 μm grain size) than the CP method did (0.3 – 0.5 μm grain size). The CP method produced denser ceramics (92.3%) than the EC method did (88.6%). In addition, the products prepared by the CP method showed higher oxygen flux ($11.0 * 10^{-7}$ mol*cm$^{-2}$*s$^{-1}$) than those prepared by the EC method ($6.6 * 10^{-7}$ mol*cm$^{-2}$*s$^{-1}$).

# 2.1.6 The properties of BSCF

## 2.1.6.1 The structural properties

### 2.1.6.1.1 The structure

BSCF shows the perovskite structure. Ba and Sr occupy the A-site. Co and Fe occupy the B-site. The Goldschmidt tolerance factor of BSCF varies between 1.043 and 1.062 [107]. The variation is caused by the valence changes of Co and Fe (changes between 3+ and 4+) [107].

### 2.1.6.1.2 The charge neutrality

*2.1.6.1.2.1 Charge neutralisation caused by temperature variation*

In one study [108], $Co^{3+}$ was partially reduced to $Co^{2+}$ when temperature was increased from room temperature to 500 ℃. More $Co^{3+}$ would be expected to be reduced if the temperature is further increased to 800 ℃. The decrease in the overall charge may be compensated ionically because it has been reported the oxygen stoichiometry (3-δ) reduced from approximately 2.9 to 2.85 when temperature was increased from 600 ℃ to 800 ℃ [109].

*2.1.6.1.2.2 Charge neutralisation caused by PO$_2$ variation*

In another study [110], $Co^{3.36+}$ and $Fe^{3.36+}$ cations of $La_{0.6}Sr_{0.4}Co_{0.2}Fe_{0.8}O_{3-\delta}$ (LSCF6428) were reduced to $Co^{2.82+}$ and $Fe^{3.10+}$ identified by X-ray absorption near-edge structure (XANES), when PO$_2$ was decreased from 1 atm to $10^{-4}$ atm at 727 ℃. According to extended X-ray absorption fine structure (EXAFS), the oxygen stoichiometry (3-δ) associated to Co was reduced from 2.98 to 2.66, while that associated to Fe was reduced from 2.98 to 2.86, suggesting the oxygen concentration is strongly associated to the B-site cation valence.

## 2.1.6.1.3 The transformation to the brownmillerite structure

In one study [10], no transformation to the brownmillerite structure was observed by high temperature X-ray diffraction (HT-XRD), when temperature was increased from 300 °C to 1000 °C in $N_2$ ($PO_2 = 1*10^{-3}$ atm). According their neutron diffraction results, no transformation was observed when the temperature was increased from 600 °C to 900 °C in four different gas environments the $PO_2$ of which are 1 atm, 0.1 atm, 0.01 atm and 0.001 atm. For BSCF, the periodic potential of the A-site was not uniform because Ba and Sr occupy the A-sites [10]. Hence the transformation cannot happen.

## 2.1.6.1.4 The thermal expansion

One of the contributors to the thermal expansion is the spin state transition of $Co^{3+}$ [111] in which electrons are activated from the $t_{2g}$ orbital to the higher energy $e_g$ orbital. A non-magnetic material becomes magnetic after such spin state transition, as was observed in a study of $La_{1-x}Sr_xCoO_{3-\delta}$ [112]. The transition can be characterised by a Quantum Design Physical Property Measurement System (PPMS) which measures the magnetic susceptibility ($\chi$) of materials [113]. In Equation 13, $\chi$ is proportional to $n_1$ (the density of magnetic moments) and inversely proportional to T (temperature), $C_1$ and $\Delta$ are positive constants. $\chi$ may increase with raising temperature when $n_1$ increase with temperature rapidly. In Figure 13, $\chi$ of BSCF is plotted as a function of temperature and a maximum of $\chi$ is seen at 250 °C, indicating a spin state transition [111].

$\chi = n_1 C_1/(T-\Delta)$

Equation 13

Figure 13. χ of BSCF is plotted as a function of temperature (from Huang et al. [114]).

In another study [115], the TEC of BSCF was measured in air and was found to be higher at temperatures above 382 ℃, compared to the TEC measured at temperatures below 382 ℃. The formation of oxygen vacancies may increase the TEC [116-118] because a portion of the B-site cations are reduced. The B-O bond strength is then reduced according to Pauling's second rule [115], giving rise to larger $BO_6$ octahedra which increases the TEC [117].

2.1.6.2 The conduction properties

2.1.6.2.1 The Electronic component

*2.1.6.2.1.1 The conducting species*

In one study [119], the total electronic conductivity at 700 ℃ was mainly contributed by electron hole conduction. In another study [115], p-type polaron hopping was found to be the electrical conductivity mechanism.

*2.1.6.2.1.2 The transport of the species*

An electron hole may hop from a B-site cation to a neighbouring O ion followed by hopping to another B-site cation via the B-O-B bond [119]. Electrons also move via the B-O-B bond [119]. A higher degree of B-O-B bond overlapping and a shorter B-O bond distance were found to increase the total conductivity [119]. For the polaron hopping in $La_{1-x}Sr_xB_{1-x}B_xO_3$ [120], an electron hole hops from the B-site cation I to the neighbouring

oxygen (the valence of BI and O is hence changed), followed by hopping to the B-site cation II (the valence of BII and O is hence changed), shown in Equation 14.

$$B_I^{4+} - O^{2-} - B_{II}^{3+} \quad \rightarrow \quad B_I^{3+} - O^- - B_{II}^{3+} \quad \rightarrow \quad B_I^{3+} - O^{2-} - B_{II}^{4+}$$
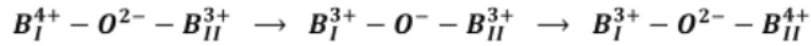
Equation 14

### 2.1.6.2.1.3 The B-O-B bond

In one study [121], x in $Ba_{1-x}Sr_xCo_{0.8}Fe_{0.2}O_{3-\delta}$ was increased from 0.2 to 0.8. As a result, the B-O-B bond angle was changed, along with the attraction/repulsion of the B 3d electrons and the O 2p electrons. The hybridization of the B 3d orbital and the O 2p orbital can be increased by reducing the B-O-B bond length or by increasing the B-O-B bond angle to $180°$, e.g. tilting adjacent $BO_6$ octahedra [121]. The bandwidth is increased when the hybridization is increased.

### 2.1.6.2.1.4 The PO2 effects on electron holes

In one study [119], oxygen vacancies were created after a decrease in $PO_2$ at 700 °C (from approximately 0.2 atm to 0 atm) hence the concentration of electron holes was decreased to maintain charge neutrality. The decrease in the hole concentration caused the reduction in the total electronic conductivity (from approximately 30 S/cm to 10 S/cm) [119].

### 2.1.6.2.1.5 The temperature effects

The conductivity was increased with increasing temperature because the electron holes are thermally created and B-O-B bonds return to $180°$ [121].

### 2.1.6.2.1.6 The unoccupied states in oxygen ions

In one study [121], the total conductivity of $Ba_{1-x}Sr_xCo_{0.8}Fe_{0.2}O_{3-\delta}$ was increased from 44.43 to 57.77 to 253.9 S*cm$^{-1}$ when x was increased from 0.2 to 0.5 to 0.8. The oxygen 2p orbitals were investigated by soft X-ray absorption spectroscopy (XAS). The normalised total electron yield of the peak at 527eV in the spectra was increased from 0.23 to 0.32 to 0.55, suggesting the concentration of unoccupied states in oxygen 2p orbitals was increased. Hence, a high concentration of unoccupied states gives rise to a high total conductivity [121].

## 2.1.6.2.2 The ionic component

Oxygen ions are delivered into the surface of BSCF via surface exchange and diffuse via oxygen vacancies through the bulk [122].

### 2.1.6.2.2.1 The oxygen non stoichiometry δ

In Figure 14, the oxygen non stoichiometry is decreased when $PO_2$ is increased, while it is increased when temperature is increased at various different $PO_2$.
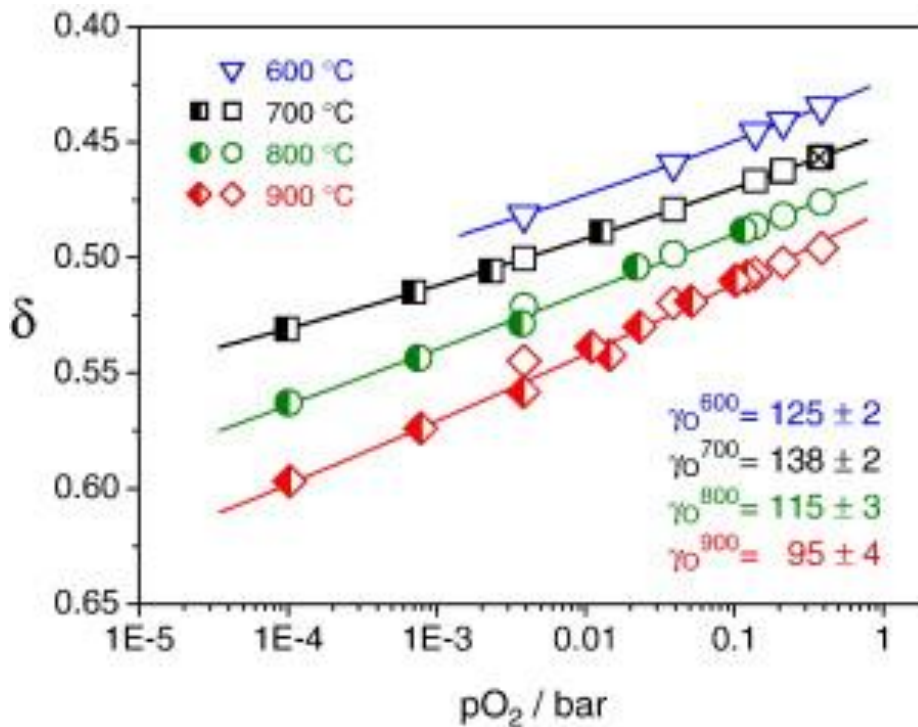


Figure 14. The oxygen non stoichiometry δ is plotted as a function of $PO_2$ at different temperatures (from Bucher et al. [123]).

In another study [109], the oxygen non-stoichiometry (δ) of BSCF was decreased from approximately 0.19 to 0.14 when $PO_2$ was increased from approximately 0 atm to 0.33 atm.

### 2.1.6.2.2.2 The factors affecting the oxygen diffusion coefficient

### 2.1.6.2.2.2.1 The PO₂ effect on the diffusion coefficient

The oxygen diffusion coefficient decreased from $7.5*10^{-7}$ to $6*10^{-7}$ cm$^2$/s, when $PO_2$ was increased from 0.001 bar to 0.01 bar at 800 ℃ [122].

In Figure 15, at 600 ℃, oxygen diffusion coefficient increased slowly from approximately

$6*10^{-6}$ to $10^{-5}$ cm$^2$*s$^{-1}$ when PO$_2$ increased from $10^{-6}$ atm to 0.05 atm. This is followed by a faster increase from approximately $10^{-5}$ to $4*10^{-5}$ cm$^2$*s$^{-1}$ when PO$_2$ is increased from 0.05 atm to 0.2 atm.
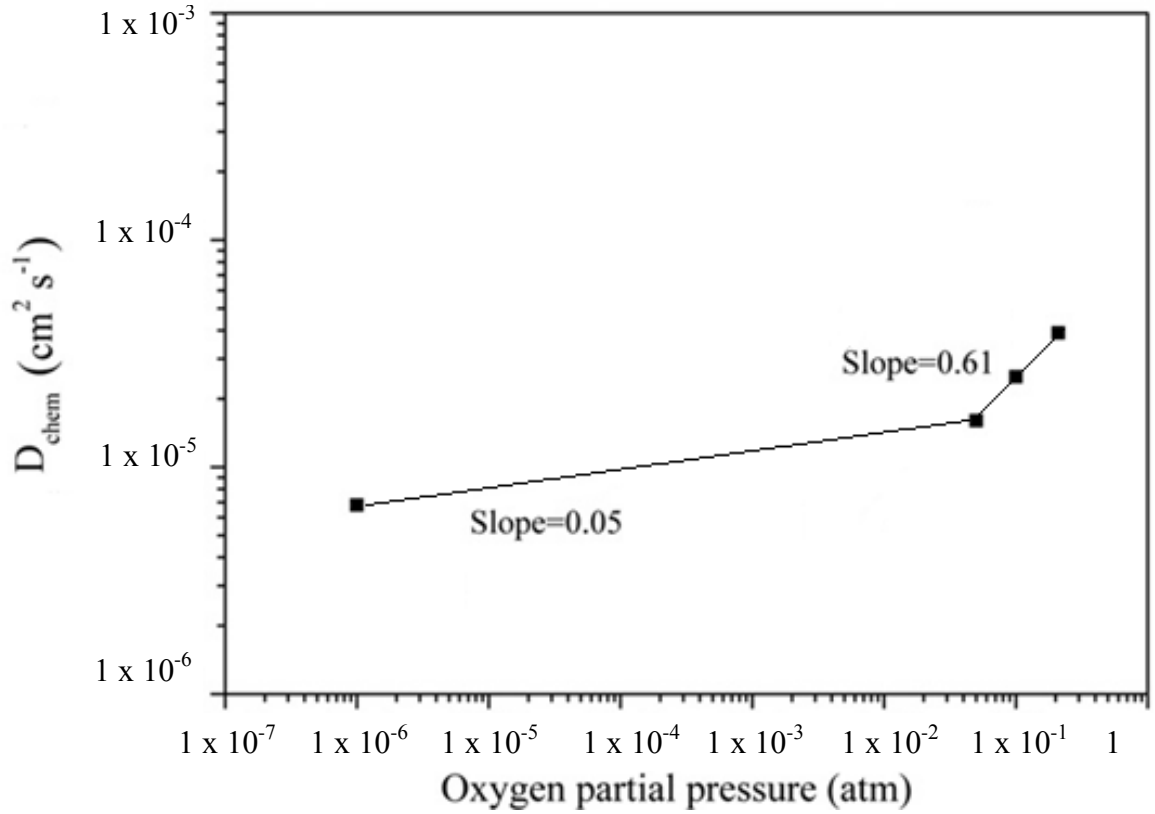


Figure 15. Oxygen diffusion coefficient is plotted as a function of PO$_2$ (after Chen and Shao [124]).

*2.1.6.2.2.2.2 The microstructure effect on the diffusion coefficient*

In one study [122], three samples A, C and B of progressively increasing porosity (4%, 6% and 8%) and decreasing grain size (57±8 μm, 9±1 μm and 6±2 μm) showed a progressive increase in diffusion coefficient. The increase in diffusion coefficient was caused by the variations in the porosity and grain size [122]. The reason can be that smaller grains cause more grain boundaries which diffuse oxygen faster than grains.

*2.1.6.2.2.2.3 The temperature*

In Figure 16, oxygen diffusion coefficients are increased when temperature is increased. D$_{chem}$$^{[ox]}$ and D$_{chem}$$^{[red]}$ are the chemical diffusion coefficient measured at PO$_2$ = 0.02 bar and 0.009 bar, respectively. D$_O$ is the self-diffusion coefficient.
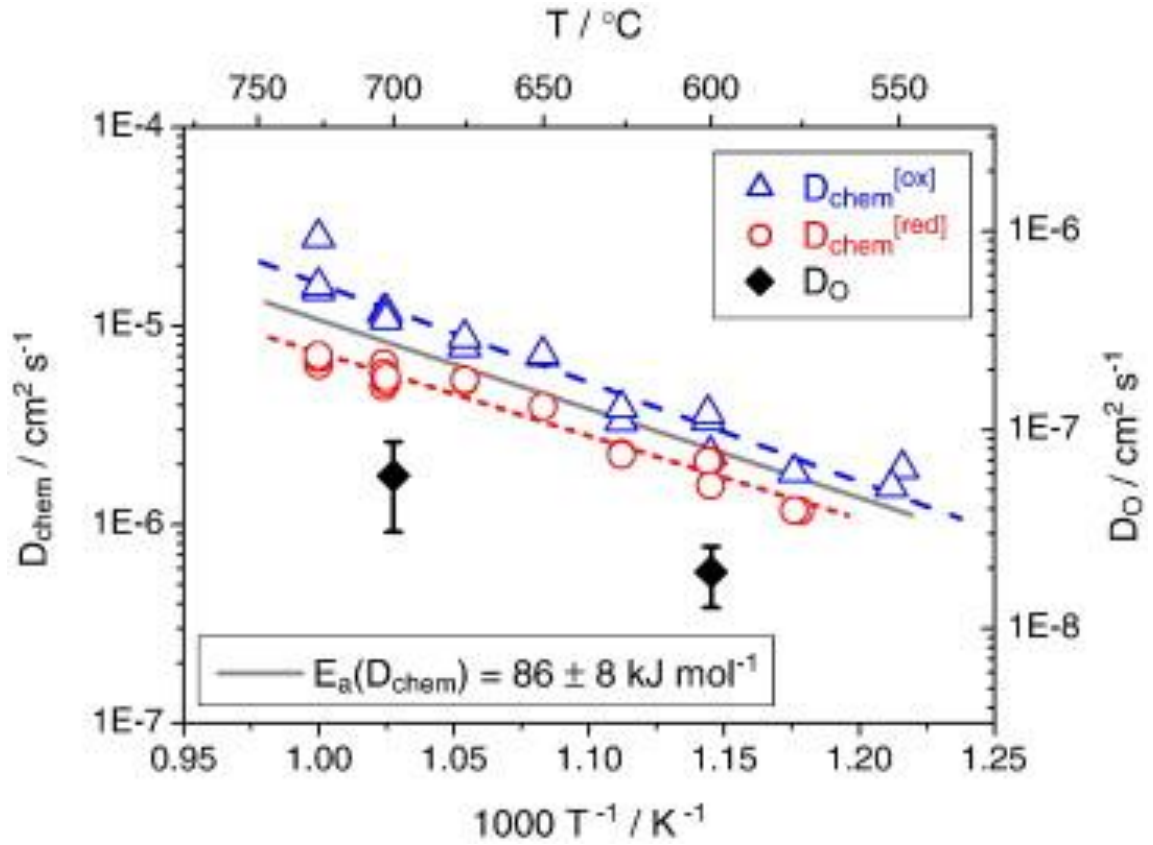
Figure 16. Oxygen diffusion coefficients are plotted as a function of 1000/T (from Bucher et al. [123]).

### 2.1.6.2.2.2.4 Other factors

$D_V$ (oxygen vacancy diffusion coefficient) of BSCF decreases with B-O bonding energy and increases with the channel size in the lattice for oxygen diffusion and the phase of the material also affects $D_V$ [119].

### 2.1.6.2.2.3 The ionic conductivity

In one study [119], the ionic conductivity of BSCF was calculated by Equation 15. $\sigma_{ion}$ is the ionic conductivity, F is the Faraday constant, R is the ideal gas constant [125], $[V_o^{\bullet\bullet}]$ is the oxygen vacancy concentration, $V_m$ is the perovskite molar volume, T is temperature.

$$\sigma_{ion} = \frac{4F^2[V_O^{\bullet\bullet}]D_V}{RTV_m}$$

Equation 15

2.1.6.2.3 The surface exchange

*2.1.6.2.3.1 The microstructure effects on surface exchange*

In one study [126], chemical surface exchange coefficient k was increased after the sample was coated by a porous BSCF layer (in Table 5). It was measured at 400 ℃.

The cross section of the coated sample is shown in Figure 17. The coating and the dense BSCF are indicated by white arrows.

Table 5 Chemical surface exchange coeffcient $k_{chem}$ of coated sample and sample without coating (after Hayamizu et al. [126])

| Sample | $k_{chem}/\mathrm{cm\,s^{-1}}$ |
|---|---|
| Without coating | $6.3 \times 10^{-6}$ |
| Porous layer coated | $2.0 \times 10^{-5}$ |
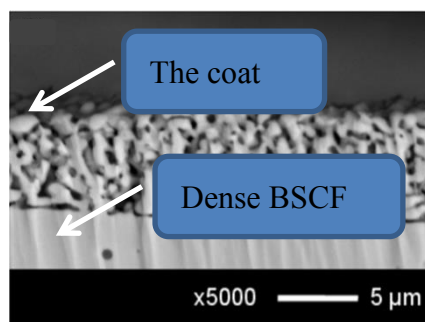


Figure 17. The cross section of the coated sample with arrows indicating the coating and substrate (after Hayamizu et al. [126]).

*2.1.6.2.3.2 The temperature effects on surface exchange*

In Figure 18, k is increased when the temperature is increased from 400 ℃ to 700 ℃ because there are more oxygen vacancies in BSCF at higher temperatures [119] and k is affected by the concentration of oxygen vacancies [5]. A similar trend is also found in another study [123].
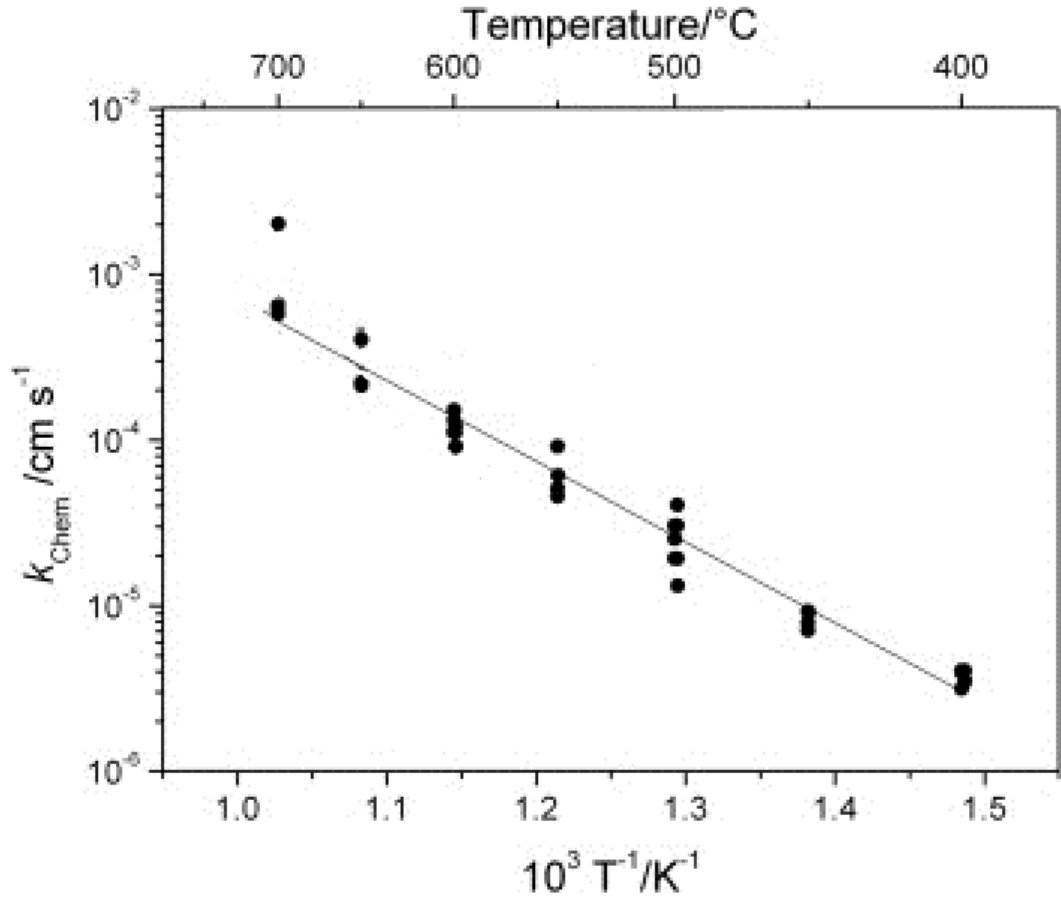
Figure 18. The surface exchange coefficient is plotted as a function of temperature. It was measured multiple times at each temperature (after Burriel et al. [127]).

In one study [128], an equation was developed for $LaMnO_{3+\delta}$, $LaCoO_3$, $La_{0.6}Sr_{0.4}FeO_{3-\delta}$ and $La_{0.6}Sr_{0.4}Co_{0.2}Fe_{0.8}O_{3-\delta}$ to calculate the surface exchange coefficient k. In Equation 16, $v_r$ and $v_d$ are pre-exponential factors, R is the universal gas constant, T is the temperature, $E_r$ is the activation energy of dissociation, $E_d$ is the activation energy of desorption. Once an oxygen molecule is absorbed on a MIEC surface, it may desorb and return to the gas or may dissociate to oxygen atoms on the surface. The surface exchange coefficient k raises with increasing temperature, when $E_r$ is higher than $E_d$.

$$k = \frac{v_r}{v_d} exp \frac{-(E_r - E_d)}{RT}$$

Equation 16

### 2.1.6.2.3.3 The PO₂ effects on surface exchange

The surface exchange coefficient of BSCF increases with increasing $PO_2$ [122, 124, 129].

In Figure 19, k is increased from $2*10^{-6}$ to $2*10^{-5}$ cm/s at 800 °C, when PO$_2$ is increased from approximately 0.001 bar to 0.03 bar.
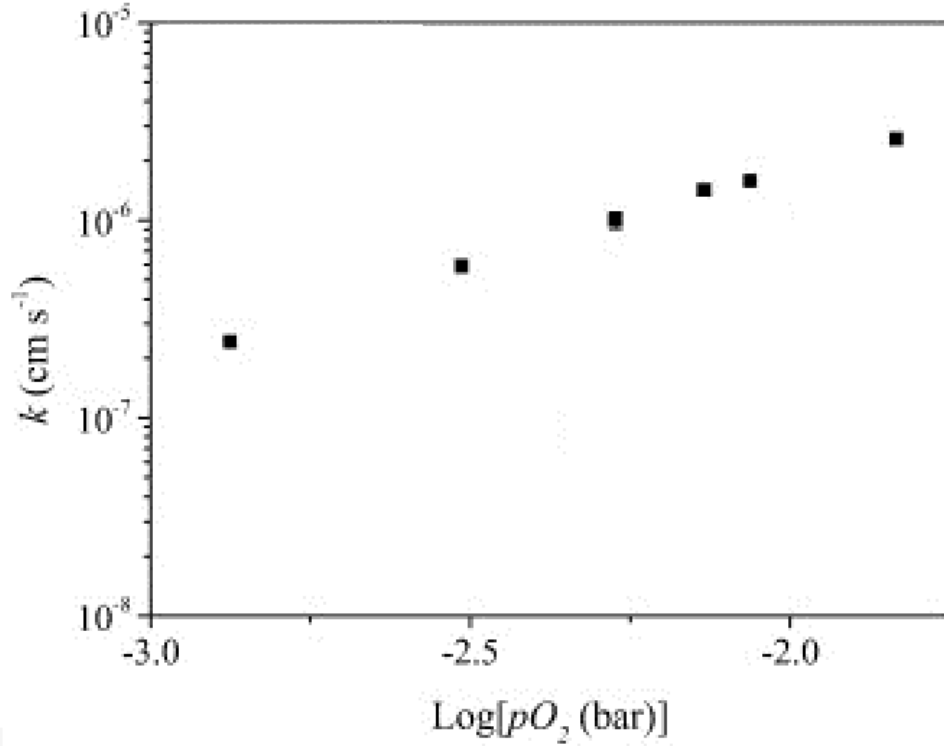


Figure 19. The surface exchange coefficient of BSCF is plotted as function of log(PO$_2$) (after Berenov et al. [122]).

In Equation 17 [130], $k_V$ is the surface oxygen vacancy exchange coefficient, L is the sample thickness, $\delta_\infty$ is the oxygen non stoichiometry at equilibrium (k was measured as a function of PO$_2$, the system was allowed to reach an equilibrium every time after the PO$_2$ was changed.), m, n, t are exponents which can be determined by curve fitting of experimental data, x-2$\delta_\infty$ is the hole concentration. This equation was developed for La$_{0.6}$Fe$_{0.4}$O$_{3-\delta}$. Hence, it has to be used tentatively in the analysis of BSCF.

$$\frac{k_V}{L} \propto P_{O_2}^m \delta_\infty^n (x - 2\delta_\infty)^t$$

Equation 17

2.1.6.2.4 The activation energy of diffusion and surface exchange

The activation energy (Ea) of diffusion and surface exchange are shown in Table 6 [122]. The defect concentration variations caused by PO$_2$ variation might be responsible for this behaviour [122].

Table 6 The activation energy of diffusion and surface exchange measured at different $PO_2$ (After Berenov et al. [122])

| | Ea of D | Ea of k | $PO_2$ |
|---|---|---|---|
| Sample A | $0.72 \pm 0.05$ eV | $1.10 \pm 0.15$ eV | 0.207 atm |
| Sample C | $1.15 \pm 0.21$ eV | $0.99 \pm 0.12$ eV | $6.6 \times 10^{-3}$ atm |

2.1.6.2.5 Permeation

*2.1.6.2.5.1 The permeation flux equation*

The permeation flux of BSCF can be determined by Equation 18 [119]. The equation holds when the electronic conductivity overwhelms hence the permeation flux is limited by the ionic conductivity [119]. L is the sample thickness. P''$O_2$ and P'$O_2$ are the oxygen partial pressures on the permeate side and the feed side respectively. $\beta$ is shown in Equation 19 [119]. In Equation 19 [119], $\sigma^0_{ion}$ is the ionic conductivity at $PO_2 = 1$ atm [72] and changes with temperature [131], R is the ideal gas constant [125], T is temperature, F is the Faraday constant and n is the order of ambipolar conductivity [89]. The ambipolar conductivity shows the ability of a MIEC to transport ionic and electronic charge carriers simultaneously [132]. Surface exchange was taken into account by changing n [119], e.g. n has a positive value if the permeation is limited by both surface exchange and bulk diffusion, n has a negative value if the permeation is limited by bulk diffusion only.

$$J_{O_2} = \frac{\beta}{L}[P''^n_{O_2} - P'^n_{O_2}]$$

Equation 18

$$\beta = -\frac{\sigma^O_{ion}RT}{4^2F^2n}$$

Equation 19

*2.1.6.2.5.2 The feed flow rate effect and the feed pressure effect on permeation flux*

In Figure 20, the increase in air flow rate at constant feed pressure increases the permeation flux rapidly followed by a plateau because the permeation reduces the $PO_2$ gradient at low air flow rate [4]. However, the reduction in $PO_2$ gradient is negligible at high air flow rate [4]. The increase in feed pressure at constant air flow rate also increases the permeation flux.
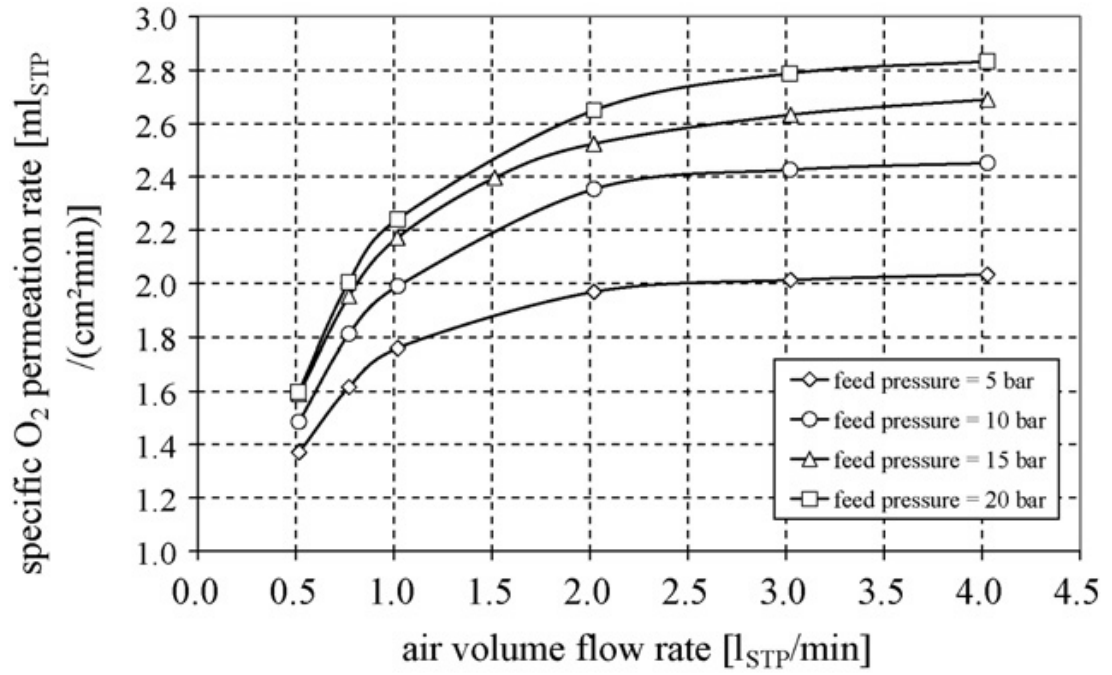
Figure 20. The feed flow rate effect and the feed pressure effect on permeation flux, measured at 900 °C (from Engels et al. [4]).

*2.1.6.2.5.3 The sweep flow rate effect and the feed pressure effect on permeation flux*

In Figure 21, the permeation flux is increased when the sweep flow rate is increased at constant feed pressure. Since the $PO_2$ of the permeate side is reduced [4]. At constant sweep flow rate, the permeation flux is increased when the feed pressure is increased.
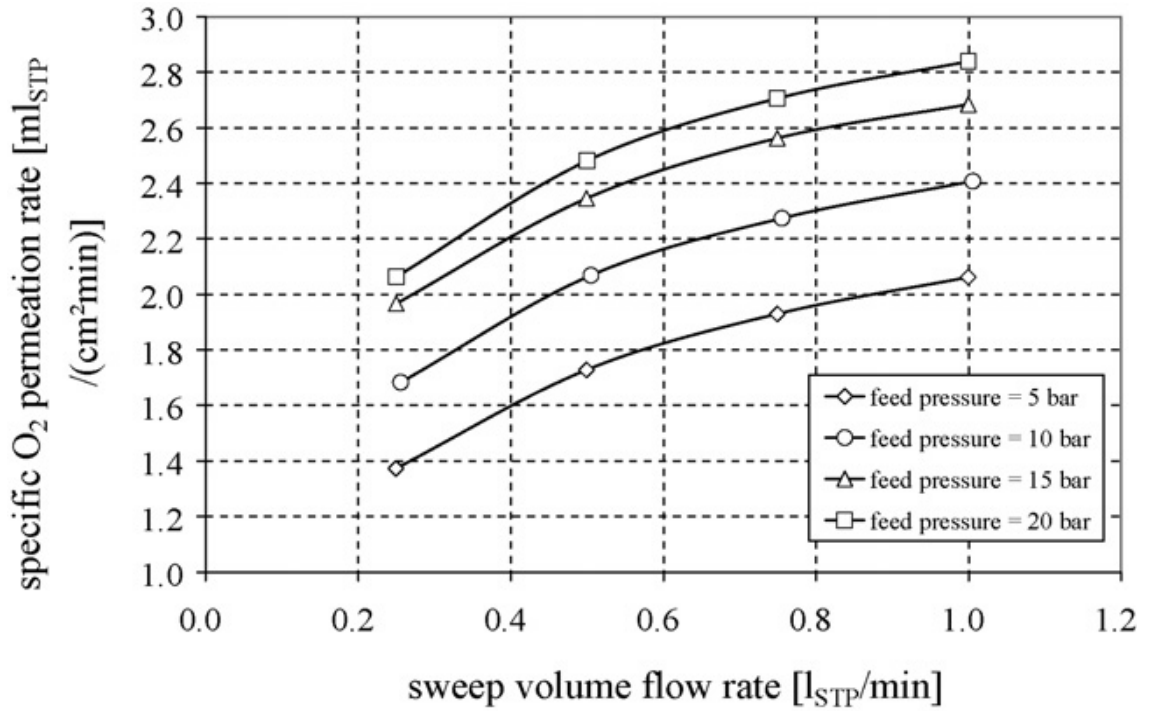
Figure 21. The sweep flow rate effect and the feed pressure effect on permeation flux, measured at 900 °C (from Engels et al. [4]).

2.1.6.3 The surface chemistry of BSCF

In one X-ray photoelectron spectroscopy (XPS) study [108], BSCF pellets were heated to high temperatures to study the surface chemical bonding concentration variation. The binding energy of Ba was not changed after one sample was heated to 500 °C, indicating there was no valence change. However, one quarter of the $Co^{3+}$ cations were reduced to $Co^{2+}$ cations, which was not observed after heating to 300 °C. Before heating, the bonding between the A/B-site cation of BSCF and oxygen (A-O/B-O), the bonding between carbon and oxygen (C-O) and the absorbed oxygen were found by XPS. After heating, the amount of the A-O bond was increased from approximately 7% to 27%, indicating the concentration of BSCF was increased. This suggests that the A-site cations may be associated to other phases before heating.

The other BSCF pellet was heated to between 500 °C and 800 °C. XPS data were acquired before all the heat treatments and after each heat treatment. The binding energy of Sr was not changed, suggesting there was no valence change. Meanwhile, the desorption of carbon was observed and the A-O bond concentration was increased from approximately 7% (before heating) to 31% (after heating at 800 °C). The sample was exposed to air for 48

hours after it was cooled. The A-O bond concentration was reduced to approximately 12% and the $CO_3^{2-}$ concentration was increased from approximately 12% (after heating at 800 ℃) to 30% (after air exposure).

In summary, surface carbonates seem to be decomposed on heating to 800°C, indicated by the carbon desorption and the increase in the A-O bond concentration. After the air exposure, carbonates formed again and the A-site cations were drawn to the carbonates (A-O bond concentration decreased). The changes of the surface cation concentration tend to be facilitated by diffusion, surface relaxation and reconstruction.

# 2.2 The decomposition of BSCF

## 2.2.1 The $CO_2$ affected decomposition

### 2.2.1.1 Surface microstructure and composition changes

In one study [17], a BSCF membrane was degraded as a result of being annealed in pure $CO_2$ at 800 ℃. A series of precipitates were observed on the surface of the degraded sample by scanning electron microscopy (SEM). The grain boundaries are more vulnerable to $CO_2$ attack, compared to the grains. The precipitates gradually formed a continuous dense layer with grain boundaries covered by precipitates, as the annealing duration was increased to 24 hours. Another sample was observed at 800 ℃ under vacuum by SEM, after it was annealed at 800 ℃ in pure $CO_2$ for 3 hours. Precipitates were observed on grains. The grain boundaries were widened and sunk below the surface. The precipitates consist of $(Ba,Sr)CO_3$, characterised by energy dispersive X-ray spectroscopy (EDX). The annealing conditions affected the composition of $(Ba,Sr)CO_3$ (Table 7).

Table 7 The atomic concentration ratio of Ba/(Ba+Sr) measured under different conditions (After Yi and Schroeder [17])

| Ba/(Ba+Sr) ratio | Time | Temperature | Gas |
|---|---|---|---|
| 0.55 to 0.6 | 0 to 250 hours | 900 ℃ | 33% $CO_2$/Ar |
| | | | Pure $CO_2$ |
| 0.5 to 0.53 | | | 33% $CO_2$/$O_2$ |

In another study [133], the sample surface after reaction with $CO_2$ was characterised by atomic force microscopy (AFM). The contrast in the AFM images indicated that the surface was not even. However, the difference in surface morphology arising as a result of the reaction is unclear because the surface wasn't observed before the reaction.

The surface potential variations of a reference sample and the samples reacted with $CO_2$ were characterised by electrostatic force microscopy (EFM) and Kelvin probe force microscopy (KPFM) [133]. The average surface potential (ASP) of the samples is shown in Table 8. The reference was treated to decompose all secondary phases. The increase in ASP indicates composition changes as a result of the reaction with $CO_2$.

Table 8 ASP of different samples and associated conditions (After Schmale et al. [133])

| Sample | ASP | Condition(s) |
|---|---|---|
| Reference | 0V | 1000 ℃, air and 10 hours |
| Annealed 1 | 0.55V | 900 ℃, pure $CO_2$ and 24 hours |
| Annealed 2 | 0.6V | 900 ℃, pure $CO_2$ and 240 hours |

2.2.1.2 Cross section microstructure and composition changes

In one study [17], a (Ba, Sr)$CO_3$ surface layer (Figure 22) was found from a cross section of a BSCF sample after a reaction with $CO_2$. Its composition was changed by the reaction conditions. Below the surface layer, a decomposed zone (Figure 22) which consists of (Ba, Sr)$_x$(Co, Fe)$_y$O$_z$, CoO and (Ba, Sr)$CO_3$ was observed. However, no picture was taken from a fresh sample hence whether the surface layer and the decomposed zone were caused by the reaction is unclear. The longer the $CO_2$ attack, the thicker the surface layer and the decomposed zone. This process is controlled by diffusion because the thickness growth of both layers follows a parabolic rate law. Ba and Sr were found to diffuse from BSCF to the carbonate surface layer. The lamellar phase wasn't studied hence its composition and structure aren't clear.
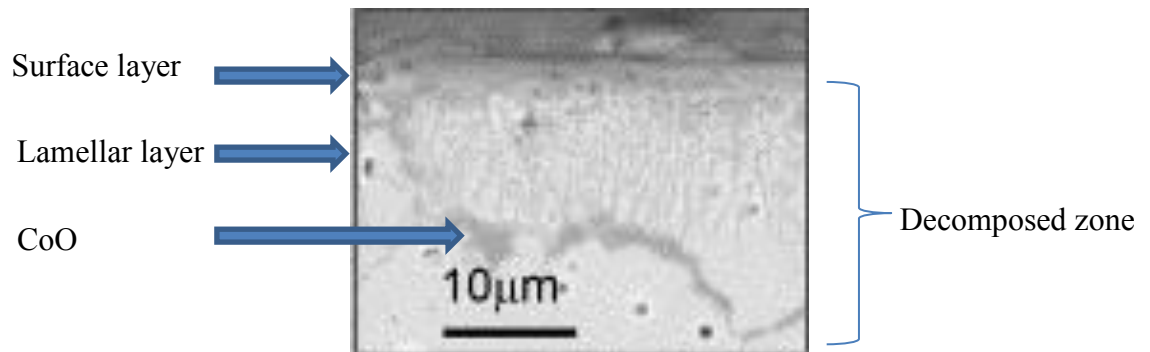


Figure 22. A BSE image of the cross section of a sample annealed in pure $CO_2$ at 900 ℃ for 24 hours with arrows indicating decomposed areas (after Yi and Schroeder [17]).

In another study [16], the thickness of the decomposed BSCF (layer ii and iii in Figure 23) reached a maximum of $40 - 50$ μm, after a reaction with $CO_2$ of 4320 minutes. Layer ii consists of mainly a Sr enriched (Ba, Sr)$CO_3$ phase and a (Ba, Sr)$_x$(Co, Fe)$_y$O$_z$ phase, characterised by SEM and transmission electron microscopy (TEM). The lamellar phase seen in layer ii is associated to the (Ba, Sr)$_x$(Co, Fe)$_y$O$_z$ phase which was characterised by EDX and electron-loss near-edge structures (ELNES). However, its structure is unclear,

although it was characterised by selected area electron diffraction (SAED). A CoO precipitate was characterised in layer ii by SAED. The (Ba, Sr)CO$_3$ phase was characterised by SAED and ELNES. Layer iii contains the Sr enriched (Ba, Sr)CO$_3$ phase. Layer i is not decomposed. However, no picture was taken from a fresh sample hence whether layer ii and layer iii were caused by the reaction is unclear.
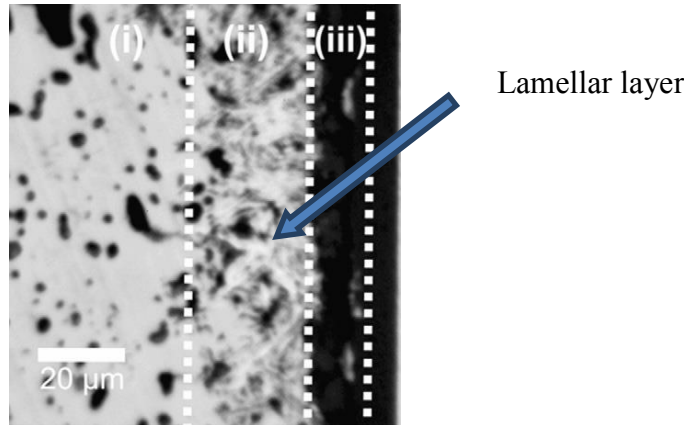


Figure 23. Optical microscope image of a cross section of a sample annealed in pure CO$_2$ at 875 °C for 4320 minutes with an arrow indicating lamellar layer (after Arnold et al. [16]).

In another study [133], neither a dense top layer nor a decomposed layer containing lamellar structures was observed from a BSCF cross section before CO$_2$ attack (Figure 24 (a)), although there are hexagonal BSCF. A top layer containing (Ba,Sr)CO$_3$ and a decomposed layer containing a series of phases (CoO, BSCF, BSCF*, (Ba,Sr)O) were observed from cross sections after CO$_2$ attack (Figure 24 (b, c)). BSCF* which is Ba and Co depleted BSCF shows lamellar morphology. Hence the layers were caused by CO$_2$ attack. The lamellar morphology is seen in the decomposed layer, which agrees with other studies [16, 17]. The thickness of the dense top layer was increased from 2.2 μm ± 0.8 μm to 6 μm ± 1 μm when the annealing duration was increased from 24 hours to 240 hours [133] (Figure 24 (b, c)). However, this relation was not described in the study [133] hence whether and how the thickness is affected by the duration is not clear. The relation was summarised by the author of this review.

The formation of the (Ba,Sr)CO$_3$ layer and the ASP variation (Table 8) indicated that KPFM and EFM are sensitive techniques to study a thin reaction layer on a solid surface after chemical reactions of gas and the surface. The advantage of KPFM and EFM over

TEM is that the samples can be observed without sample preparation.



(a)



(b)
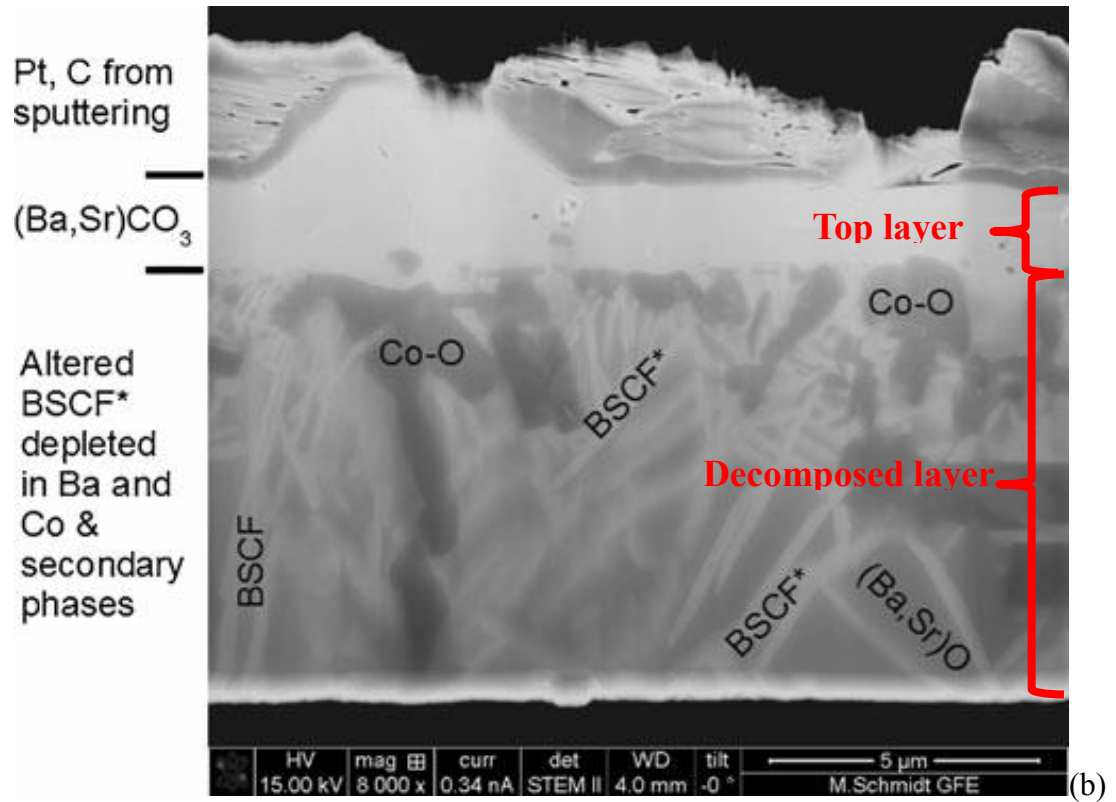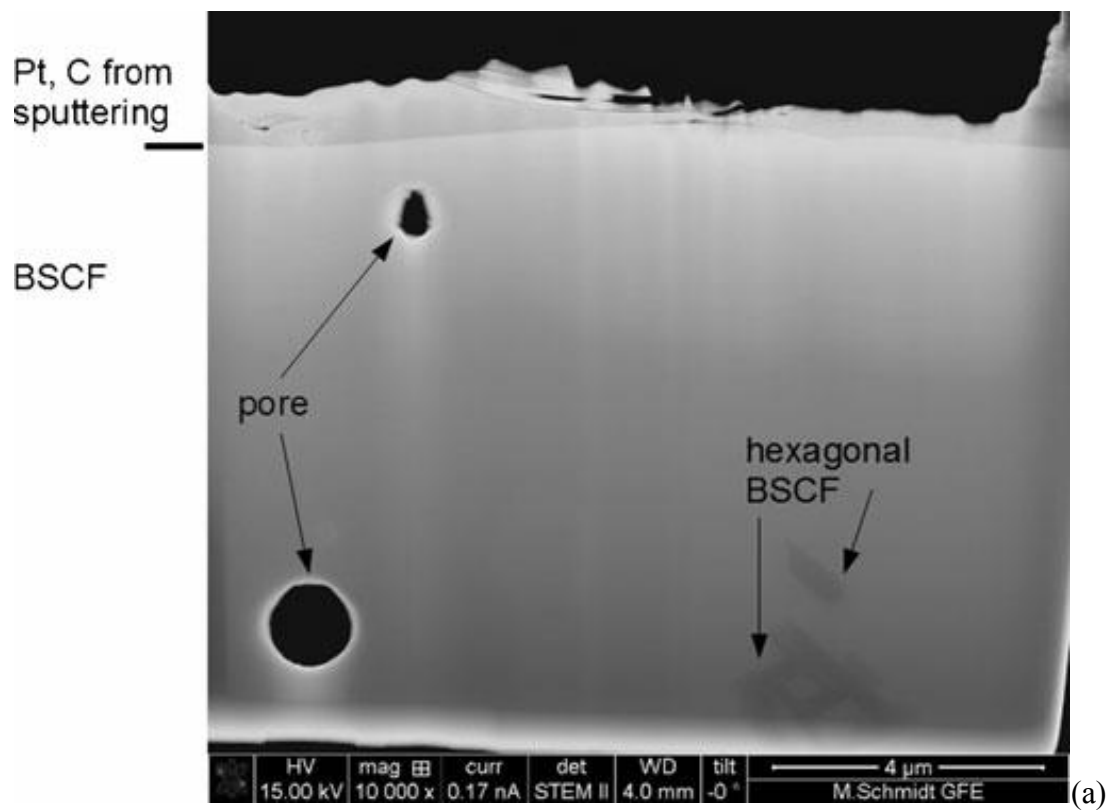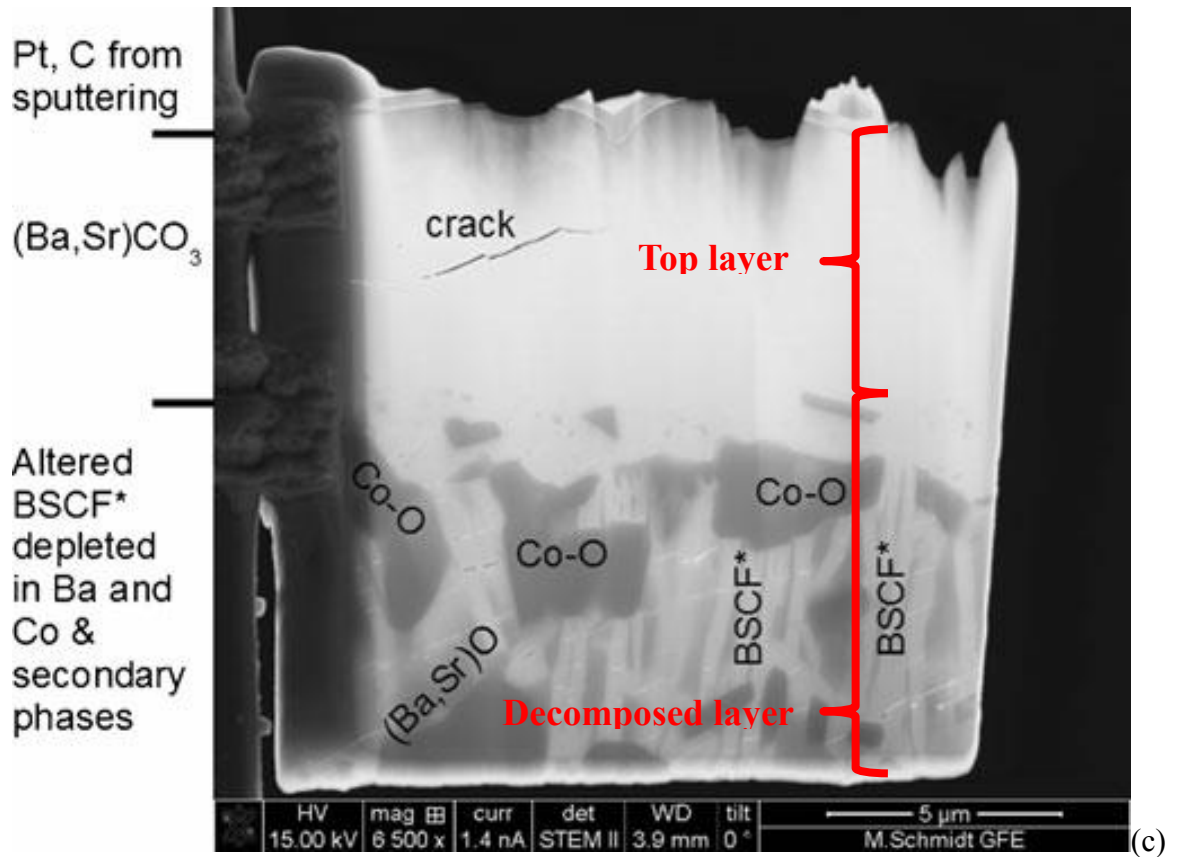
Figure 24. Scanning TEM (STEM) image of a cross section of (a) a sample annealed in air at 1000 ℃ for 10 hours, (b) a sample annealed in 99.9% $CO_2$ at 900 ℃ for 24 hours and (c) a sample annealed in 99.9% $CO_2$ at 900 ℃ for 240 hours with secondary phases and decomposed zones indicated (from Schmale et al. [133]).

In another study [134], the sweep side (swept by 10% $CO_2$/He) of a BSCF membrane was observed after a permeation measurement. It showed a (Ba,Sr)$CO_3$ layer (Figure 25) which was found to reduce the permeation flux. The lamellar phase adjacent to the (Ba,Sr)$CO_3$ layer contains Ba, Sr, Co and Fe. However, no more results were obtained from the lamellae hence structure and composition of the lamellae are unclear.
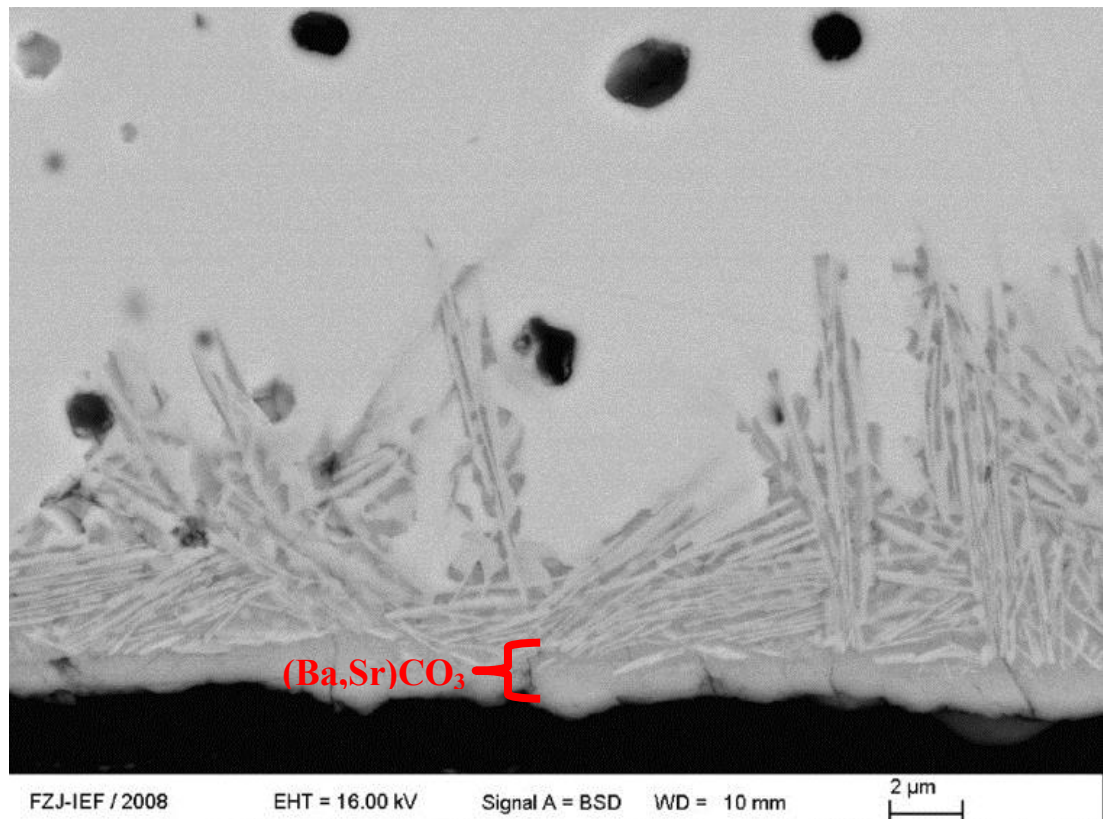
Figure 25. SEM image of a cross section of the sweep side of a BSCF membrane after a permeation measurement with the carbonate layer indicated (from Engels et al. [134]).

## 2.2.1.3 The phase identification

In one study [17], the phases after annealing under various conditions were identified by X-ray diffraction (XRD) and are shown in Table 9. Crystallographic information and composition of the phases can be found in Table 10. Hence the annealing condition changes the composition and structure of the carbonates. It also affects the outcome of the reaction with $CO_2$.

Table 9 Secondary phases obtained after different annealing experiments (Temperature 900 ℃) (from Yi and Schroeder [17])

| Sample | Atmosphere | Time (h) | Phase composition |
|---|---|---|---|
| Pellet | $CO_2$ | 24 | OP 1, OP 2, P, CoO |
| Pellet | $CO_2$ | 240 | OP 2 |
| Pellet | 33% $CO_2$/Ar | 24 | OP 1, OP 2, P, CoO |
| Pellet | 33% $CO_2$/$O_2$ | 24 | OP 3, P |
| Powder | $CO_2$ | 24 | OP 1, P, CoO, $Fe_3O_4$ |
| Powder | $CO_2$ | 165 | OP 1, CoO, $Fe_3O_4$ |
| Powder | 33% $CO_2$/Ar | 24 | OP 1, OP 2, P, CoO, $Fe_3O_4$ |
| Powder | 33% $CO_2$/$O_2$ | 24 | OP 2, OP 3, unknown phase |

Table 10 Crystallographic information of the phases (After Yi and Schroeder [17])

| Phase | Composition | Structure | Lattice parameters |
|---|---|---|---|
| OP1 | $Ba_{0.5}Sr_{0.5}CO_3$ | Orthorhombic | a = 8.7687 Å, b = 5.1789 Å c = 12.7365 Å |
| OP2 | $Ba_{0.42}Sr_{0.58}CO_3$ | Orthorhombic | a = 8.6809 Å, b = 5.2244 Å c = 6.3004 Å |
| OP3 | $Ba_{0.49}Sr_{0.51}CO_3$ | Orthorhombic | a = 10.2823 Å, b = 8.7214 Å c = 6.9650 Å |
| P | BSCF | Cubic | |
| CoO | CoO | Cubic | PDF 43-1004 |
| $Fe_3O_4$ | $Fe_3O_4$ | Cubic | PDF 65-3107 |

In another study [16], the phases of the permeate side of a sample after a permeation experiment were identified by XRD and are shown in Table 11. The permeation was conducted at 875 ℃ for 4320 minutes and the sample was swept by pure $CO_2$. The crystallographic information of the CoO phase agreed to the SAED results. The d-spacings determined from the unknown phase matched that determined from the SAED results of the $(Ba, Sr)_x(Co, Fe)_yO_z$ phase. Hence the sweep side of BSCF was decomposed to these phases after permeation.

Table 11 Crystallographic information of the phases (After Arnold et al. [16])

| Phase | Structure | Lattice parameters |
|---|---|---|
| $Ba_{0.4}Sr_{0.6}CO_3$ | Orthorhombic | a = 6.2262 Å, b = 5.1957 Å and c = 8.6190 Å |
| CoO | Cubic | a = 4.25 Å |
| Unknown phase | Unknown | Unknown |

Table 12 shows the secondary phases after $CO_2$ attack in the other studies. Hence carbonates and various other secondary phases formed after annealing BSCF in $CO_2$ involved gas [109, 135-138]. For Table 12 row 3, a sample was heated for 480 min at each temperature in one of the atmospheres.

Table 12 The secondary phases after $CO_2$ attack and corresponding experimental conditions

| Secondary phase(s) | Atmosphere | Temperature | Time | References |
|---|---|---|---|---|
| $SrCO_3$, $BaCO_3$ and $CoO$ | 10% $CO_2/Ar$ | 900 °C | 20 min | [135] |
| $Ba_{0.4}Sr_{0.6}CO_3$ and BaO | 1% $CO_2/He$ | 700 °C | 120 min | [136] |
| $Ba_{0.4}Sr_{0.6}CO_3$ | 1% $CO_2/O_2$ | 400 °C, 500 °C, 600 °C and 700 °C. | 480 min | [109] |
|  | 10% $CO_2/O_2$ |  |  |  |
|  | 100% $CO_2/O_2$ |  |  |  |
| $Ba_{0.4}Sr_{0.6}CO_3$, BaO and an unknown phase | 1% $CO_2/O_2$ | 450 °C | 1440 min | [137] |
| (Ba, Sr)$CO_3$ | $CO_2$ | 600 °C | 600 min | [138] |

2.2.1.4 The chemical reaction

Compared to BSCF, the lower Co atomic concentration in $(Ba,Sr)_x(Co,Fe)_yO_z$ gives rise to higher $CO_2$ resistance, which may be a result of a reduction in the barium and strontium chemical potential [17]. The higher resistance makes $(Ba,Sr)_x(Co,Fe)_yO_z$ an intermediate product in an incomplete reaction between BSCF and $CO_2$ (Equation 20). Equation 21 shows the complete reaction where the intermediate phase is decomposed. In the first equation, m equals 0.5, 0.58 or 0.51 depending on the annealing conditions, suggesting the annealing condition affects the carbonate composition. For x, y and z, they are still unclear because no quantitative results were obtained from the $(Ba,Sr)_x(Co,Fe)_yO_z$ phase. For α, β and γ, they vary depending on the reaction mass balance.

$$Ba_{0.5}Sr_{0.5}Co_{0.8}Fe_{0.2}O_{3-\delta} + \alpha CO_2$$
$$\rightarrow (Ba,Sr)_x(Co,Fe)_yO_z + \beta CoO + \alpha Ba_{1-m}Sr_mCO_3 + \gamma O_2$$

Equation 20

$$Ba_{0.5}Sr_{0.5}Co_{0.8}Fe_{0.2}O_{3-\delta} + CO_2 \rightarrow Ba_{0.5}Sr_{0.5}CO_3 + 0.8CoO + \frac{0.2}{3}Fe_3O_4 + (\frac{1.4}{3} - \frac{\delta}{2})O_2$$
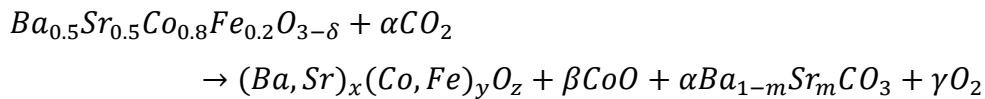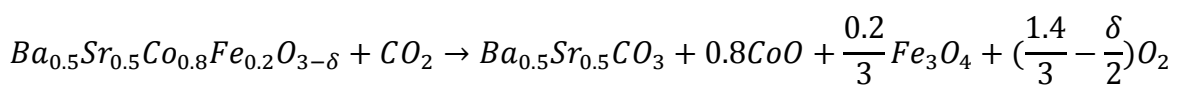
Equation 21

2.2.1.5 The permeation flux reduction induced by $CO_2$ attack

In one study [16], the permeation flux was reduced from 2.7 ml/min*cm$^2$ to 1.5 ml/min*cm$^2$ at 875 ℃, 150 minutes after 5% $CO_2$ was introduced into the sweep gas (He), suggesting the poisoning effect of $CO_2$ on the oxygen permeation. The permeation can be recovered after $CO_2$ was removed from the sweep gas though. The permeation flux was reduced from 2.7 ml/min*cm$^2$ to 2.2 ml/min*cm$^2$ when 10% $CO_2$ was applied in the feed gas, suggesting BSCF can endure $CO_2$ attack from the feed side.

In another study [71], the $CO_2$ concentration was changed in the sweep gas at 900 ℃, the reduced permeation flux is shown in Table 13, suggesting the poisoning effect of $CO_2$ on the oxygen permeation.

Table 13 Permeation flux change as a result of sweep gas change (After Schulz et al. [71])

| Permeation flux | Reduced permeation flux | $CO_2$ concentration in $CO_2/N_2$ | How long after changing the sweep gas was the flux measured |
|---|---|---|---|
| 0.12 ml(STP)/cm/min | 0.104 ml(STP)/cm/min | 10% | 4 hours |
| 0.12 ml(STP)/cm/min | 0.004 ml(STP)/cm/min | 60% | 4 hours |
| 0.12 ml(STP)/cm/min | 0 ml(STP)/cm/min | 100% | A few seconds |

# 2.2.2 The $CO_2$ free decomposition

BSCF also gradually decomposes at working temperatures without $CO_2$ attack [11, 15, 70, 139-158].

### 2.2.2.1 Microstructure and composition changes

Mueller et al. [139] suggested that the decomposition reached an equilibrium state where crystallites and BSCF co-exist. In their study, a BSCF sample was annealed in air for 192 hours at 800 ℃, its grain boundaries decomposed to crystallites. Compared to BSCF, the crystallites are Ba and Co enriched, Sr partially depleted and Fe completely depleted, suggested by EDX on STEM. The crystallites with lamellar morphology stretching across grains are Ba enriched and Sr and Fe depleted. The chemical formula of the crystallites is $Ba_{0.5+x}Sr_{0.5-x}CoO_{3-\delta}$. The parental BSCF became $Ba_{0.5-x}Sr_{0.5+x}Co_{0.6}Fe_{0.4}O_{3-\delta}$. The difference in composition was also characterised by Z-contrast.

In another study [140], BSCF was found to decompose to a $Ba_{0.6}Sr_{0.4}CoO_{3-\delta}$ phase, a $Ba_{1-x}Sr_xCo_{2-y}Fe_yO_{5-\delta}$ phase, a $Ba_{0.4}Sr_{0.6}O$ phase and a $Ba_{0.5-x}Sr_{0.5+x}Co_{0.8-y}Fe_{0.2+y}O_{3-\delta}$. The BSCF sample was annealed in air for 180 hours at 800 ℃. Observed by high resolution TEM (HRTEM), the $Ba_{0.6}Sr_{0.4}CoO_{3-\delta}$ phase shows hexagonal lattice. A-site and B-site cations of BSCF were assigned to the atom columns in the high resolution scanning TEM (HRSTEM) image of the $Ba_{1-x}Sr_xCo_{2-y}Fe_yO_{5-\delta}$ phase with lamellar morphology, according to the Z-contrast, giving rise to a chemical formula of $(A_3B_6O_{15})_3$. The Co and Ba atomic concentrations are 63% and 30% respectively, characterised by EDX. The $Ba_{0.4}Sr_{0.6}O$ phase was observed next to the lamellar phase. The parental BSCF became $Ba_{0.5-x}Sr_{0.5+x}Co_{0.8-y}Fe_{0.2+y}O_{3-\delta}$.

In another study [141], a series of BSCF samples were annealed in ambient air for 100 hours at 700 ℃, 800 ℃, 900 ℃ and 1000 ℃, respectively. BSCF was decomposed and secondary phases were formed and characterised by electron microscopy and EDX. The formation temperatures and locations of the secondary phases are shown in Table 14. The plate-like phase consists of cubic phase lamellae, hexagonal phase lamellae and $Ba_{n+1}Co_nO_{3n+3}(Co_8O_8)$ (BCO) lamellae, revealed by HRTEM. For the hexagonal phase, it is Fe deficient because Fe cations are large for the hexagonal lattice. The formation rate of the hexagonal phase is restricted by the interdiffusion of Fe and Co ions. The composition

of such plate-like phase varies depending on the concentration of each component. A model developed by Sun et al. [159] of the BCO phase suggested that this phase consists of cubic perovskite structure layers and $CdI_2$ structure layers. The atomic concentration of Ba, Sr, Co and Fe of the identified phases are shown in Table 15.

Table 14 The secondary phases and their formation temperatures and locations (After Muller et al. [141])

| Phase | Formation temperature | Location in sample |
|---|---|---|
| CoO | 700 ℃, 800 ℃, 900℃, 1000 ℃ | Grains |
| Plate-like phase | 700 ℃, 800 ℃, 900 ℃ | Grain boundaries or close to CoO |
| Hexagonal phase | 700 ℃, 800 ℃ | Grain boundaries or close to the plate-like phase |

Table 15 The atomic concentration of the elements of the phases in a decomposed sample (from Muller et al. [141])

| phase | Ba [atom %] | Sr [atom %] | Co [atom %] | Fe [atom %] |
|---|---|---|---|---|
| $Ba_{0.5}Sr_{0.5}Co_{0.8}Fe_{0.2}O_{3-d}$ | 25 | 25 | 40 | 10 |
| cubic phase | 26 ± 1 | 25.5 ± 1.5 | 40 ± 1.5 | 8.5 ± 1 |
| hexagonal phase | 30 ± 1 | 27 ± 1.5 | 42 ± 1 | 1 ± 0.5 |
| BCO-type phase | 21.5 ± 3 | 3 ± 1 | 67.5 ± 2.5 | 8 ± 1 |

[a]The errors are the standard deviations of the average values of up to 200 spectra recorded for the same phase.

In another study [70], the cross-section of a BSCF tube membrane was characterised by backscattered electron channelling contrast after permeating at 950 ℃ for 100 hours and 750 ℃ for 120 hours. $O_2$ enriched air (50 Vol %) with a pressure of 1 bar to 5 bar was fed in the feed side, while the permeate side was vacuumed. Hence, there was only $O_2$ in the permeate side with a pressure of 0.1 bar. The BSCF tube was found structurally unstable and a partial decomposition was responsible for the instability. After decomposition, a $Ba_{0.5\pm x}Sr_{0.5\pm x}CoO_{3-\delta}$ phase with lamellar morphology and a $Ba_{1-x}Sr_xCo_{2-y}Fe_yO_{5-\delta}$ phase with plate-like morphology were formed, characterised by TEM and EDX. The secondary phases are restricted to grain boundaries on the permeate side. The $Ba_{0.5\pm x}Sr_{0.5\pm x}CoO_{3-\delta}$ phase was found on grains and grain boundaries on the feed side, while the $Ba_{1-x}Sr_xCo_{2-y}Fe_yO_{5-\delta}$ phase was rarely seen.

2.2.2.2 The crystallography of the secondary phases

The crystallographic information of the phases after decomposition in the studies [15, 70, 139-141, 143] are shown in Table 16.

Table 16 Crystallographic information of the phases after decomposition

| References | Special morphology | Composition | Structure | Space group | Lattice parameter |
|---|---|---|---|---|---|
| [139] | No | $Ba_{0.5+x}Sr_{0.5-x}CoO_{3-\delta}$ | Hexagonal | $P6_3/mmc$ | a = 5.63 Å<br>c = 4.38 Å |
| | No | $Ba_{0.5-x}Sr_{0.5+x}Co_{0.6}Fe_{0.4}O_{3-\delta}$ | Cubic | Pm-3m | a= 4.00 Å |
| [140] | No | $Ba_{0.6}Sr_{0.4}CoO_{3-\delta}$ | Hexagonal | Not mentioned | Not mentioned |
| | Lamellae | $Ba_{1-x}Sr_xCo_{2-y}Fe_yO_{5-\delta}$ | 15R hexagonal | Not mentioned | a ≈ 5.6 Å, c ≈ 35.7 Å |
| | Plate-like | $Ba_{0.4}Sr_{0.6}O$ | Not mentioned | Not mentioned | Not mentioned |
| [141] | Lamellae | $Ba_{0.5}Sr_{0.5}Co_{0.8}O_{3-\delta}$ | Hexagonal | Not mentioned | Not mentioned |
| | Plate-like | BSCF | Cubic perovskite | | |
| | | Hexagonal in Table 15 | Hexagonal | | |
| | | $Ba_{n+1}Co_nO_{3n+3}(Co_8O_8)$ (BCO) | Cubic lamellae | | |
| | | | CdI$_2$ lamellae | | |
| | Particle | CoO | Not mentioned | | |
| [70] | Lamellae | $Ba_{0.5\pm x}Sr_{0.5\pm x}CoO_{3-\delta}$ | Hexagonal | Not mentioned | Not mentioned |
| | Plate-like | $Ba_{1-x}Sr_xCo_{2-y}Fe_yO_{5-\delta}$ | Trigonal | R – 3 m | Not mentioned |

## 2.2.2.3 The crystallographic orientation relation

The interface of the lamellar/plate-like phase and cubic BSCF phase was investigated [70, 140, 141, 143]. Muller et al. [143] suggested that the crystallographic orientation relation between the cubic BSCF phase and the lamellar phase is well-defined. However, this is not agreed by Efimov et al. [140] because the reconstruction of lattice (from cubic to lamellae) during decomposition is complex, giving rise to complex structures, complex pathways and complex orientation relations [140]. The complex reconstruction is the result of the high mobility of the cations in BSCF [140]. The complex orientation relation cannot be explained by the decomposition mechanism which attributed the reconstruction to the stacking sequence change of the $AO_3$ planes in BSCF [140]. The mechanism was suggested by Mueller et al. [139]. The complex orientation relations from a series of studies [70, 140, 141, 143] are shown in Table 17.

Table 17 The lamellae and BSCF crystallographic orientation relation

| Interface | The cubic BSCF plane is parallel with the lamellae | The cubic BSCF zone axis is parallel with the zone axis on the right | Hexagonal lamellar zone axis | References |
|---|---|---|---|---|
| 1 | {111} | <011> | <100> | [141] |
| 2 | | | Not mentioned | [140] |
| 3 | | | Not mentioned | [143] |
| 4 | {001} | | [-110] | [140] |
| 5 | | | [-110] | |
| 6 | (3-11) | | Not mentioned | |
| 7 | (2-11) | | Not mentioned | |
| 8 | {011} | <001> | [-110] | |
| 9 | (1-2-1) | [11-1] | [00-1] | [70] |

The crystallographic orientation relation of the hexagonal phase without lamellar morphology and the BSCF phase is shown in Table 18, indicating that the hexagonal phase grows on certain sites on BSCF grains.

Table 18 The hexagonal phase and BSCF crystallographic relation (After Mueller et al. [139])

| Interface | Cubic BSCF plane | Hexagonal plane | Cubic BSCF zone axis | Hexagonal zone axis |
|-----------|------------------|-----------------|----------------------|---------------------|
| 1 | {-121} | {-110} | [111] | [001] |

2.2.2.4 The decomposition mechanism

Muller et al. [141] suggested a two steps decomposition mechanism where the fast growing lamellar phase forms first followed by the hexagonal phase. Muller et al. [143] suggested that the lamellar phase is an intermediate structure when cubic BSCF was decomposed to hexagonal BSCF.

The lamellar phase showed higher $Co-L_3/Ba-M_5$ edge intensity ratio, compared to the cubic BSCF phase, characterised by electron energy loss spectroscopy (EELS), suggesting the lamellar phase had higher Co concentration. The $Co-L_3$ edge of the lamellar phase was moved by 0.7eV to the right of that of BSCF, suggesting the average Co valence of the lamellar phase was higher. This higher Co valence led to smaller Co cation which is unstable in cubic BSCF [70, 140], which is the reason for the decomposition of BSCF [70]. The Co valence and spin state and the corresponding ionic radius [160] is shown in Table 19.

Table 19 Co valence and spin state and its ionic radius (after Shannon [160])

| Valence | Spin state | Ionic radius |
|---------|-----------|--------------|
| $Co^{2+}$ | High spin | 74.5 pm |
| $Co^{3+}$ | High spin | 61 pm |
| $Co^{3+}$ | Low spin | 54.5 pm |
| $Co^{4+}$ | High spin | 53 pm |

2.2.2.5 The decomposition effects on permeation

Muller et al. [141] suggested that all secondary phases reduce the oxygen conduction and the negative impact of the lamellar phase on oxygen conduction may have been lower estimated in earlier studies. Efimov et al. [140] suggested that the lamellar phase is a barrier of oxygen permeation because the concentration of oxygen vacancy in the lamellar phase is lower than that in cubic BSCF. The geometry and low crystal symmetry also contribute to the barrier effect. Liang et al. [70] suggested that the oxygen permeation flux reduction they measured is a result of the partial decomposition of BSCF.

# 2.3 The stabilisation of BSCF and other MIEC

## 2.3.1 The stabilisation in $CO_2$ enriched environment

BSCF and some other MIEC suffer from decomposition in normal use when exposed to $CO_2$. A number of researchers have attempted to stabilise these materials [1, 161-174]. Their methods are described in this section, and fall into three categories: doping, coating and compositing.

### 2.3.1.1 BSCF and other MIEC stabilised by doping

2.3.1.1.1 Control the Goldschmidt tolerance factor by doping

In MIEC containing Co, the ionic radius of Co can change when its valence changes at high temperatures [1, 161, 162]. As a result, the Goldschmidt tolerance factor can move away from the stable range to destabilise the perovskite structure [162]. The unstable structure may be ideal for the reaction between MIEC and $CO_2$. Therefore, researchers have attempted to restrict the variation of the tolerance factor by doping [163, 164].

One work [164] doped Zr into $BaCo_{0.4}Fe_{0.6}O_{3-\delta}$, to obtain $BaCo_xFe_yZr_zO_{3-\delta}$ (BCFZ, x+y+z=1). The ionic radius of $Zr^{4+}$ is similar to that of $Co^{2+}$ and does not change at high temperatures. Hence, the tolerance factor may remain the same. However, a large amount of carbonate was formed in the BCFZ sample exposed to $CO_2$ at 800 °C. As a result, the oxygen permeation flux was reduced significantly when $CO_2$ concentration was increased in the sweep gas. Therefore, Zr doping cannot enhance the stability of MIEC to prevent carbonate formation and to maintain oxygen permeation in a high $CO_2$ concentration environment.

In the work [163], $La_{0.6}Sr_{0.4}CoO_{3-\delta}$ (LSC) was doped with Ga, to obtain $La_{0.6}Sr_{0.4}Co_{0.8}Ga_{0.2}O_{3-\delta}$ (LSCG). Ga does not change its radius at high temperatures and may therefore improve the stability of LSC. The permeation flux remained constant (0.6 ml/min $cm^2$), after a pure $CO_2$ swept permeation test for 80 hours, suggesting the stability of LSCG is good. However, the stability of LSC was not shown. Therefore, how much the stability was improved was not clear. The oxygen permeation flux of LSCG was reported, while the oxygen permeation flux of LSC was not given. Therefore, the doping effect on

oxygen permeation flux of LSC was not clear.

2.3.1.1.2 Restrict the alkaline-earth and $CO_2$ reaction by doping

The alkaline-earth elements in MIEC tend to react with $CO_2$ due to basicity [165, 166]. As a result, the stability of MIEC in $CO_2$ is low. Recent research has attempted to improve the stability by reducing the basicity of the material [165, 166, 169].

Since the alkaline-earth element in $SrCo_{0.8}Fe_{0.2}O_{3-\delta}$ (SCF) was likely to react with $CO_2$ [165], and a rare-earth element is less reactive in $CO_2$, compared to the alkaline-earth element [165], $La_2(CO_3)_3$ was less stable, compared to $SrCO_3$ [167]. T. Klande et al. [165] doped SCF with La to obtain LSCF. However, the oxygen permeation flux of LSCF was lower than 60% of that of SCF at 900 ℃. The stability of LSCF was better than that of SCF, although oxygen permeation stopped approximately 220 hours after the sweep gas was switched to pure $CO_2$ at 900 ℃.

It was noted the alkaline earth element in $BaCo_{0.4}Fe_{0.4}Nb_{0.2}O_{3-\delta}$ (BCFN) reacts readily with $CO_2$ [166]. The concentrations of Fe and Nb in BCFN were increased to produce $BaFe_{0.55}Nb_{0.45}O_{3-\delta}$, in order to increase the acidity of BCFN. However, the oxygen permeation flux of BCFN was reduced to 0.01 ml/min $cm^2$ at 900 ℃. The $CO_2$ stability of BCFN was improved and permeation flux remained stable in pure $CO_2$.

In another study, $SrCoO_{3-\delta}$ was doped with Nb and Fe, to obtain $SrCo_{1-2x}(Fe,Nb)_xO_{3-\delta}$ (SCFN) x=0.05, x=0.10 [169]. The stability of SCFN was compared to that of BSCF. The weight gain due to reaction with $CO_2$ of BSCF (14.9%) was higher than that of SCFN x=0.10 (11.1%), suggesting the $CO_2$ stability of the latter was better than the former. The oxygen permeation flux of both materials was not measured in this work.

In summary, the stability of MIEC in $CO_2$ rich atmosphere can be improved by increasing the acidity or reducing the basicity of MIEC. Unfortunately, the oxygen permeation flux was significantly reduced after the stability improvement.

### 2.3.1.1.3 Restrict the MIEC and $CO_2$ reaction by Ti doping

Strong Ti - O bonding can reduce basicity, which can be provided if BSCF is doped with Ti.

The ionic radius of $Ti^{4+}$ (60.5 pm) is close to that of $Co^{3+}$ (61 pm) and $Fe^{3+}$ (64.5 pm) [170]. In one study, Co and Fe in BSCF were partially substituted by Ti [170], to obtain BSCFT. The stability of BSCF was enhanced, since the doped sample showed fewer carbonates after exposure to $CO_2$ at high temperatures, compared to BSCF. The area specific resistance (ASR) was measured for both BSCF and BSCFT. The ASR of BSCF was the same as that of BSCFT at 700 ℃.  However, the oxygen permeation flux of both types of sample wasn't measured, and so the doping effect on oxygen permeation was not obtained.

In another study SCFO was doped with Ti [168]. The doped material functioned continuously for 200 hours, in a pure $CO_2$ sweep gas, although the oxygen permeation flux was reduced by approximately 23% due to $CO_2$ attack. Such performance is better than SCFO which stopped permeation after approximately 75 hours of exposure to $CO_2$ sweep gas [171]. The reduction is lower than that reported by other researchers [164-166]. The oxygen permeation flux of SCFT is comparable with that of BSCF, when there is no $CO_2$ attack. However, the oxygen permeation flux of SCFO wasn't measured, and so the doping effect on oxygen permeation flux is unclear.

In summary, Ti was able to enhance the stability of BSCF and SCFO. The oxygen permeation flux of SCFO under $CO_2$ attack appeared to be good. However, the doping effect on oxygen permeation flux wasn't obtained.

## 2.3.1.2 BSCF stabilised by coating

In this section, the results of attempts to stabilise BSCF by coating are described.

W. Zhou et al. [172] coated BSCF with $La_2NiO_{4+d}$ (LN). A $La(NO_3)_3$ and $Ni(NO_3)_2$ solution was infiltrated on a BSCF substrate followed by heating at 850 °C for 5 hours. Citric acid was added to the solution, which was infiltrated into the heated substrate followed by heating at 850 °C for 5 hours. The sample was sintered by microwave plasma treatment (MP), to densify the coating layer. A BSCF sample and the LN coated BSCF (BSCF-LN) sample were exposed to a 10% $CO_2$ air environment for 1hr at 600 °C. A significant amount of carbonate was formed on the BSCF sample, as characterised by Fourier transform infrared (FT-IR) spectroscopy. However, carbonates were not found on the BSCF-LN sample. Thus, the LN coating layer protected BSCF. The ASR of BSCF and BSCF-LN was measured. The ASR of BSCF-LN is 40% of that of BSCF at 653 °C, which may give rise to better electricity conduction than BSCF. Unfortunately, the oxygen permeation flux of BSCF-LN was not measured in this work. However, the oxygen permeation flux (0.4 ml/min cm2) of LN was measured by one work [175] in a $CO_2$ free environment. It was lower than the oxygen permeation flux of BSCF (1.2 ml/min cm2 [13]) under similar conditions (900 °C, sample thickness 1.8 mm, feed side: 150 ml/min synthetic air, sweep side: 30 ml/min He [13]). It was reduced nearly by half when the concentration of $CO_2$ reached 96.7% in the sweep side of the permeation rig, suggesting that LN cannot survive high concentrations of $CO_2$.

In another study, BSCF was coated by $La_{0.6}Sr_{0.4}Ti_{0.3}Fe_{0.7}O_{3-\delta}$ [173]. The coated sample (tube membrane, wall thickness: 1 mm) worked continuously for 400 hours and the oxygen permeation flux was high (2.14 ml/min $cm^2$) at 900 °C with ambient air feeding. However, the $CO_2$ concentration was as low as 500 ppm in the feed side and $PO_2$ of the feed side was above one atmosphere. This experimental condition restricts the formation of carbonates, compared to a $CO_2$ enriched low $PO_2$ environment and so this material should be tested in a $CO_2$ enriched environment.

In summary, both types of coating material were able to survive low concentration $CO_2$ attack. The former material did not survive pure $CO_2$. Whether the latter material can survive pure $CO_2$ or not is not clear. The former coating did not affect permeability significantly. Whether the latter one affects permeability significantly or not is not clear.

### 2.3.1.3 BSCF stabilised by forming a composite

In this section the outcomes of experiments where BSCF and another material were mixed and sintered, to produce a composite material are described. The rationale for this approach is that while the oxygen permeation flux of BSCF can be significantly reduced under $CO_2$ attack, the oxygen permeation flux of the other phase may remain constant, if this phase is more stable than BSCF in $CO_2$ [174].

In one study $Ce_{0.9}Gd_{0.1}O_{2-\delta}$ (CGO) was introduced to BSCF by mixing the powder of both phases [174]. The mixed powder was pressed and sintered, to produce a CGO-BSCF membrane. The oxygen permeation flux of CGO-BSCF was approximately half that of BSCF, in a $CO_2$ free atmosphere. The oxygen permeation flux of BSCF (membrane thickness: 0.5 mm) was reduced by 84% and that of CGO-BSCF was reduced by 54% under $CO_2$ attack at 950 °C (Feed side: air 150 ml/min, sweep side: 80% $CO_2$/He 100 ml/min). Therefore, the stability of CGO-BSCF is better than that of BSCF.

## 2.3.2 The stabilisation in $CO_2$ free environment

In MIEC containing Co, the ionic radius of Co can change when its valence changes at high temperatures [1, 161, 162]. As a result, the Goldschmidt tolerance factor can move away from the stable range [162]. This may destabilise the perovskite structure or give rise to a cubic to hexagonal phase transition [140].

In one study La was introduced to the A-site of BSCF to produce $Ba_{0.2}La_{0.3}Sr_{0.5}Co_{0.6}Fe_{0.4}O_{3-\delta}$ [161], to keep the tolerance factor in the stable range. The doped material showed better stability, compared to unmodified BSCF. However, the oxygen permeation flux wasn't measured, and so the effect of doping on the oxygen permeability was not obtained.

In the work [162], the B-site of BSCF was doped with Zr 4+ to produce $Ba_{0.5}Sr_{0.5}Co_{0.79}Fe_{0.2}Zr_{0.01}O_{3-\delta}$. The ionic radius of Zr 4+ is similar to that of Co 2+ and does not change at high temperatures. Hence, the tolerance factor may remain the same. The doped BSCF showed higher permeation flux (0.51 ml/cm min) than BSCF (0.43 ml/cm min) at 800 °C (feed side: synthetic air 150 ml/min, sweep side: He 29 ml/min and Ne 1 ml/min, membrane thickness 1 mm) after 180 hours of permeation, suggesting the

stability of the doped BSCF is better than BSCF in a $CO_2$ free environment. However, it showed lower oxygen permeation flux (0.9 ml/cm min) than BSCF (1.2 ml/cm min) prior to the decompositions.

Other researchers have developed Co free MIEC, e.g. $Ba_{0.5}Sr_{0.5}Zn_{0.2}Fe_{0.8}O_{3-\delta}$ [176] and $BaCe_xFe_{1-x}O_{3-\delta}$ [177]. However, none of these two studies compared the stability and permeability of the new material with those of BSCF.

# 3. Experimental methods

## 3.1 Sample preparation

### 3.1.1 Synthesis of BSCF

BSCF pellets were prepared by the co-precipitation method. The details of the starting materials are shown in Table 20. Barium, strontium, cobalt and iron nitrates were weighed according to the required amount and were dissolved in water. The dissolution was accelerated by heating to 60 °C and stirring. The mass concentration was 8% which could not be reduced further. The solution was added to a sodium carbonate solution by dripping to precipitate the metal cations. It also maintained stable pH because pH of the metal nitrate solution increased when the sodium carbonate solution was added to the metal nitrate solution [18]. The increase in pH caused the insufficient precipitation of Co which was evidenced by pink filtrates [18]. The sodium carbonate solution was stirred during dripping. The mixing rate needed to be optimised because a high mixing rate may produce fine particles which can pass through a filter paper and a low mixing rate may produce large particles in which the sodium carbonate solution cannot react completely. Further, large particles tend to be inhomogeneous. The suspension was diluted by water and filtered by filtration papers (Whatman 541 paper) to remove sodium cations and reduce pH to remove excess sodium carbonates.

The wet precipitates were dried at 100 °C overnight, followed by calcination for 4 hours at 850 °C in air in an alumina crucible (heating and cooling rate: 3 °C min$^{-1}$). The calcined powders (10 g) were vibration milled with 10 cm$^3$ propan-2-ol and 10 g zirconia milling balls for 24 hours, followed by overnight drying at 85 °C. The milled powders were uniaxially pressed to form pellets (diameter: 1 cm) at 100 MPa. The pressed pellets were sintered under different conditions shown in Table 21 (heating and cooling rate: 3 °C min$^{-1}$) to obtain optimised density. Table 21 shows the sample nomenclature adopted after each step. Only 1100°CS-BSCF pellets were ground using SiC paper (Grade: P400) to remove the rough surface and secondary phases on the surface. They were polished with diamond paste (grit diameter: 6 μm and 1 μm). After polishing, they were named BSCF pellets and were washed with soap and industrial methylated spirits.

Table 20 Details of the starting materials

| Powder name | Chemical formula | Supplier | Purity (wt%) |
|---|---|---|---|
| Barium nitrate | $Ba(NO_3)_2$ | Fisher Scientific | 99% |
| Strontium nitrate | $Sr(NO_3)_2$ | Fisher Scientific | 99% |
| Iron(III) nitrate nonahydrate | $Fe(NO_3)_3 \cdot 9H_2O$ | Fisher Scientific | 99% |
| Cobalt(II) nitrate hexahydrate | $Co(NO_3)_2 \cdot 6H_2O$ | Merck Millipore | 99% |
| Sodium carbonate | $Na_2CO_3$ | Fisher Scientific | 99.7% |
| Titanium tetrachloride | $TiCl_4$ | Sigma Aldrich | 99.9% |
| Commercial BSCF | $Ba_{0.5}Sr_{0.5}Co_{0.8}Fe_{0.2}O_{3-\delta}$ | Treibacher Industrie AG | 99% |

Table 21 Sample names and corresponding processes

| Processes | Sample name |
|---|---|
| Co-precipitation, drying. | CP-BSCF |
| Co-precipitation, drying, calcination at 850 ℃ for 4hr. | CP-850℃4hrC-BSCF |
| Co-precipitation, drying, calcination at 850 ℃ for 4hr, milling for 24hr. | CP-850℃4hrC-24hrM-BSCF |
| Co-precipitation, drying, calcination at 850 ℃ for 4hr, milling for 24hr, sintering at 1100 ℃ for 10hr in air. | 1100℃CS-BSCF |
| Co-precipitation, drying, calcination at 850 ℃ for 4hr, milling for 24hr, sintering at 1100 ℃ for 24hr in air. | 1100℃CS24hr-BSCF |
| Co-precipitation, drying, calcination at 850 ℃ for 4hr, milling for 24hr, sintering at 1125 ℃ for 10hr in air. | 1125℃CS-BSCF |
| Co-precipitation, drying, calcination at 850 ℃ for 4hr, milling for 24hr, sintering at 1100 ℃ for 10hr, grinding, polishing. | BSCF pellet |

A series of additional calcinations were applied to CP-850°C4hrC-BSCF to discover an optimised condition eliminating precursor phases and are shown in Table 22. The corresponding sample names are also shown in Table 22.

Table 22 Processes applied to CP-850°C4hrC-BSCF and associated sample names

| Processes | Sample name |
|---|---|
| Calcination at 930 °C for 4.5hr. | CP-850°C4hrC-930°C4.5hrC-BSCF |
| Calcination at 930 °C for 4.5hr followed by calcination at 950 °C for 5hr. | CP-850°C4hrC-930°C4.5hrC-950°C5hrC-BSCF |
| Calcination at 950 °C for 5hr. | CP-850°C4hrC-950°C5hrC-BSCF |

## 3.1.2 Decomposition of BSCF

### 3.1.2.1 $CO_2$ enriched decomposition

An annealing rig was designed and built to decompose BSCF pellets (thickness 1 mm, diameter 10 mm) in various gas environments (Figure 26). Sample surfaces were cleaned before annealing. Samples were placed in a quartz tube which endures the experimental temperatures (600 °C - 850 °C). The sample was positioned in the hot zone of the furnace. The tube was pulled out of the furnace after annealing to quench the samples. A type-K thermocouple was used to measure the sample temperature. A gas composition from Table 23 was introduced into the quartz tube, depending on the purpose. The quartz tube was flushed by the gas for 2 hours before annealing to expel ambient air. The incoming gas flow rate was measured by an electronic gas flowmeter (EFM17, Aalborg, Orangeburg, NY, USA). For the gas mixture in Table 23, the composition was controlled by changing the flow rate of each component. The flow rate was controlled by the valve attached to the gas regulator.
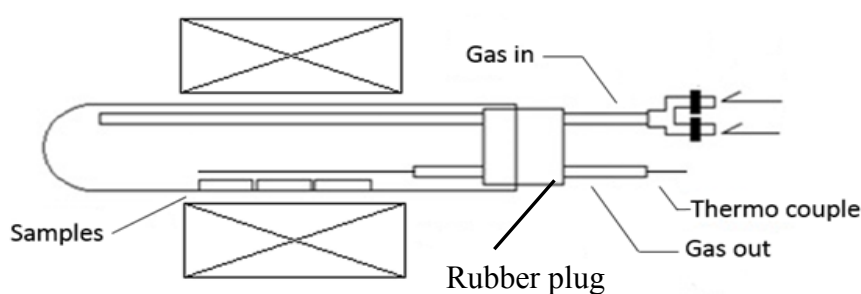


Figure 26. A schematic diagram of the annealing rig.

Table 23 Gas environments for various annealing experiments

| Gas | Flow rate |
|---|---|
| $N_2$ | $100 \pm 1$ ml.min$^{-1}$ |
| $7 \pm 1$ % $CO_2/N_2$ | $100 \pm 3.3$ ml.min$^{-1}$ |
| Air without $CO_2$ | $100 \pm 1$ ml.min$^{-1}$ |

A series of BSCF pellets were annealed in a $CO_2/N_2$ atmosphere (Table 23), allowing the effects of $CO_2$ on the decomposition to be studied. So was commercial BSCF powder (Table 20) with cubic structure (Treibacher Industrie AG, Austria). The annealing conditions and corresponding sample names are shown in Table 24. 800 ℃ was chosen because this is close to the normal BSCF operating temperature [17]. The annealing times were chosen to study the initial stage of the decomposition. The $CO_2$ concentration ($7\pm1$ %) was chosen to provide a slow rate of reaction. Higher concentrations (33%, 100%) were used in another study and the decomposition progressed too fast to observe the initial stage [17]. Higher temperatures (900 ℃ and 950 ℃) and higher $CO_2$ concentration ($16 \pm 1.6$ %) were also used to establish whether these factors affect the decomposition products.

To test oxide polishing suspension (OPS) effects on decomposition, one BSCF pellet was polished by OPS, while another BSCF pellet was not. After the polishing, the sample was washed thoroughly to remove any remaining OPS. Methylated spirit is applied to the sample to accelerate drying. The two pellets were annealed in $7 \pm 1$ % $CO_2/N_2$ at 900 ℃ for 30 min. The sample names and procedures are shown in Table 24.

Table 24 Annealing conditions and corresponding sample names

| The annealing conditions | The sample names |
|---|---|
| A BSCF pellet annealed in $7 \pm 1$ % $CO_2/N_2$ at 800 ℃ for 1 min | C-800℃-1min |
| A BSCF pellet annealed in $7 \pm 1$ % $CO_2/N_2$ at 800 ℃ for 2 min | C-800℃-2min |
| A BSCF pellet annealed in $7 \pm 1$ % $CO_2/N_2$ at 800 ℃ for 5 min | C-800℃-5min |
| A BSCF pellet annealed in $7 \pm 1$ % $CO_2/N_2$ at 800 ℃ for 15 min | C-800℃-15min |
| A BSCF pellet annealed in $7 \pm 1$ % $CO_2/N_2$ at 800 ℃ for 30 min | C-800℃-30min |
| Commercial BSCF powder annealed in $7 \pm 1$ % $CO_2/N_2$ at 800 ℃ for 30 min | C-800℃-30min-p |
| A BSCF pellet annealed in $16 \pm 1.6$ % $CO_2/N_2$ at 900 ℃ for 15 min | C-900℃-15min |
| A BSCF pellet annealed in $16 \pm 1.6$ % $CO_2/N_2$ at 950 ℃ for 15 min | C-950℃-15min |
| A BSCF pellet annealed in $16 \pm 1.6$ % $CO_2/N_2$ at 950 ℃ for 30 min | C-950℃-30min |
| A BSCF pellet annealed in $7 \pm 1$ % $CO_2/N_2$ at 900 ℃ for 30 min | C-900℃-30min |
| A BSCF pellet was polished by OPS then annealed in $7 \pm 1$ % $CO_2/N_2$ at 900 ℃ for 30 min | OPS-C-900℃-30min |

### 3.1.2.2 $CO_2$ free slow decomposition

A series of BSCF pellets were annealed in gas environments where no $CO_2$ was involved to study the $CO_2$ free decomposition and to prepare sample for the decomposition relation study. The annealing rig is shown in Figure 26. The annealing conditions and sample names are shown in Table 25. Various annealing times were chosen to observe microstructure changes from the initial decomposition to the later decomposition and to ensure that the secondary phases can be detected by XRD. The chosen temperature is consistent with the $CO_2$ enriched decomposition study.

Table 25 Annealing conditions and corresponding sample names

| The annealing conditions | The sample names |
|---|---|
| A BSCF pellet annealed in $N_2$ at 800 °C for 1 hour | N-800°C-1hour |
| A BSCF pellet annealed in $N_2$ at 800 °C for 6 hours | N-800°C-6hour |
| A BSCF pellet annealed in $N_2$ at 800 °C for 24 hours | N-800°C-24hour |
| A BSCF pellet annealed in air at 800 °C for 6 hours | A-800°C-6hour |

### 3.1.2.3 Relating two types of decomposition

In this stage, the samples in column one of Table 26 were annealed under the conditions listed in column two to prepare samples to study the decomposition relation. The annealed sample names are shown in column three. The annealing conditions are the same as those of sample C-800°C-2min and C-800°C-5min. C-800°C-2min and C-800°C-5min will be compared with N6C2 and N1C5 respectively, to observe the differences induced by the annealing in $N_2$ or air. The differences may reveal the interrelations between the cubic to hexagonal decomposition and the reaction between BSCF and $CO_2$.

Table 26 Annealing conditions and corresponding sample names

| Samples used | The annealing conditions | Sample names |
|---|---|---|
| N-800°C-6hour | $7 \pm 1$ % $N_2/CO_2$ annealing 2 min 800 °C | N6C2 |
| N-800°C-1hour | $7 \pm 1$ % $N_2/CO_2$ annealing 5 min 800 °C | N1C5 |
| A-800°C-6hour | $7 \pm 1$ % $N_2/CO_2$ annealing 2 min 800 °C | A6C2 |

### 3.1.3 Coating of BSCF

3.1.3.1 $SrCo_{0.48}Fe_{0.12}Ti_{0.4}O_{3-\delta}$ (SCFT414) synthesis and BSCF coating

Strontium, cobalt and iron nitrates were weighed according to the required amounts and dissolved in deionised (DI) water. Titanium tetrachloride was weighed in cold DI water because it is soluble in cold water but reacts with warm water to produce $TiOCl_2$ and HCl [178]. The details of the starting materials are shown in Table 20. The $TiCl_4$ solution was mixed with the tri-cation solution and dripped to the sodium carbonate solution via a dripping funnel. The sodium carbonate solution was stirred during dripping. The mixing rate needed to be optimised because a high mixing rate may produce fine particles which can pass through a filter paper and a low mixing rate may produce large particles in which the sodium carbonate solution cannot react completely [18]. Further, large particles tend to be inhomogeneous [18]. The suspension was diluted by water and filtered by filtration papers (Whatman 541 paper) to remove ions that were not precipitated ($Na^+$, $Cl^-$, $NO_3^{2-}$, $CO_3^{2-}$) and to reduce pH. The wet precipitates were dried at 100 ℃ overnight, followed by calcination for 10 hours at 950 ℃ (heating and cooling rate: 3 ℃ $min^{-1}$) to decompose the precursor phases which were still present for calcination conditions of 850 ℃ 4 hours. The calcined powders (3.5 g) were vibration milled with 10 ml propan-2-ol and 3 g zirconia milling balls for 48 hours, followed by overnight drying at 85 ℃. Table 27 shows sample names after corresponding processes.

A series of BSCF pellets were dip coated in a suspension (3.5 g CP-950℃10hrC-48hrM-SCFT414 powder and 10 ml propan-2-ol). The coated pellets were dried at room temperature overnight and sintered at 1165 ℃ to avoid cracking at higher temperatures and to decompose precursor phases observed at lower temperatures. The heating rate was 3 ℃ $min^{-1}$ (20 ℃ to 950 ℃) and 1 ℃ $min^{-1}$ (950 ℃ to 1165 ℃). The cooling rate was as low as 1 ℃ $min^{-1}$ to avoid cracking. Table 27 shows sample names after corresponding processes.

Table 27 Sample names and corresponding processes

| Processes | Sample name |
|---|---|
| Co-precipitation, drying | CP-SCFT414 |
| Co-precipitation, drying, calcination at 950 ℃ for 10hr | CP-950℃10hrC-SCFT414 |
| Co-precipitation, drying, calcination at 950 ℃ for 10hr, milling for 48hr. | CP-950℃10hrC-48hrM-SCFT414 |
| BSCF pellet coated by CP-950℃10hrC-48hrM-SCFT414 and sintered | SCFT coated BSCF pellet |

No entire SCFT414 pellets were obtained because the pellets cracked extensively after sintering at 1230 ℃ or 1250 ℃. In one study [179], the sintered Co-Cr alloy cracked due to over densification after sintering at a temperature of 1400 ℃ which is higher than normal sintering temperature (1200 ℃). This may be the reason why the pellets cracked extensively, hence lower sintering temperatures were attempted. After sintering at 1165 ℃, a single phase pellet with just one crack was obtained, suggesting lower sintering temperature can mitigate the collapsing problem due to over densification. For lower sintering temperature (1100 ℃), precursor phases were observed and there was still a crack on the pellet.

SCFT414 green pellets were obtained and remained intact after pressing, suggesting the collapsing and cracking problem is less likely to be caused by pressing when the pressing did not cause inhomogeneous density and cup and cone fractures. A portion of the green pellets were obtained by uniaxial pressing at 100 MPa because BSCF green pellets can be obtained after such pressing. Another portion of the green pellets were obtained by isostatic pressing at 207 MPa because SCFT414 green pellets were obtained and remained entire after isostatic pressing in one study [171]. This suggests that both techniques can produce useful SCFT414 green pellet.

### 3.1.3.2 For $CO_2$ stability study

Commercial BSCF powder (Treibacher Industrie AG, Austria) was uniaxially pressed to pellets (diameter: 1 cm, mass: 0.5 g) at 100 MPa. The pressed pellets were sintered at 1100 ℃ for 10 hours (heating and cooling rate: 3 ℃ $min^{-1}$). The sintered pellets were ground by SiC paper (Grade: P400) to remove the rough surface and secondary phases on the surface. They were polished by diamond compound (grit diameter: 6 μm and 1 μm).

After polishing, the pellets were washed with soap and industrial methylated spirits and were denoted as c-BSCF pellets. The details of the starting materials are shown in Table 20.

A SCFT coated BSCF pellet, c-BSCF pellet and a BSCF commercial powder were annealed at 800 ℃ in 7±1 % $CO_2/N_2$ for 30 minutes to understand the coating effect on decomposition. They were denoted as SCFTBSCF-CO2 pellet, c-BSCF-CO2 pellet and c-BSCF-CO2 powder.

### 3.1.3.3 For oxygen permeability study

C-BSCF pellet (thickness: 0.310 mm) and SCFT coated BSCF pellet (thickness: 0.495 mm) were chosen for this study. Both pellets have the same diameter (10 mm) and were ground by P400 SiC paper then polished using 1 μm diamond paste. The coated surface was not ground or polished to maintain the coating. The oxygen permeation flux was measured under the same conditions to understand the effects of coating on the oxygen permeability of BSCF.

## 3.1.4 Sample preparation for characterisation

### 3.1.4.1 X-Ray diffraction (XRD)

The pellet samples and powder samples were directly mounted on XRD sample holders to be ready for investigation, except 1100℃ S-BSCF which was ground using grade P400 SiC paper before mounting to remove surface carbonates induced by sintering.

### 3.1.4.2 Scanning electron microscope (SEM)

The surface of BSCF pellet was ground by P400 SiC paper and polished by 1 μm diamond compound, while the surfaces of decomposed pellets were not treated in anyway before SEM sample preparation. The pellet samples were coated by carbon on a precision etching and coating system (PECS) I system (Gatan, UK). The pellet base was stuck on an alumina SEM stub using a conductive carbon adhesive. The surface was connected to the stub by silver paint. This procedure was conducted to reduce charging effects to enhance image quality.

Powder sample was sprinkled on a carbon adhesive stuck to a SEM stub, followed by blasting away excess powders using an air duster in a fume cardboard to protect the SEMs

because free powder can cause damage during vacuuming. The assembly was coated by carbon on a PECS I system (Gatan, UK).

The cross-section of C-800℃-1min was exposed by focused ion beam milling (FIB) because the precipitate layer is thin and would be damaged or removed during mechanical grinding and polishing. A platinum layer with a thickness of $0.4 \pm 0.08$ μm and an area of $50 \pm 5$ μm$^2$ was deposited on the surface of C-800℃-1min to protect the precipitates. FIB was conducted on a FEI Nova NanoLab 600 system (FEI, UK). The platinum deposition, FIB and SE imaging at 5 kV were performed by Dr Ali Gholinia.

The cross section of C-800℃-30min and SCFT coated BSCF pellet were prepared by a mechanical grinding (P400, P800, P1200 and P2500 SiC paper) and polishing route (diamond paste with grit diameter of 6 μm and 1 μm), followed by carbon coating, silver painting and stub mounting. OPS was used for SCFT coated BSCF pellet for enhanced orientation contrast.

### 3.1.4.3 Transmission electron microscope (TEM)

Cross section TEM samples were prepared from C-800℃-5min and C-800℃-30min. Two identical pellets were mounted surface to surface in resin epoxy. The assembly was ground to expose the cross section using P400 and P1200 SiC papers. It was then thinned to a 100 μm slice followed by copper grid mounting. The slice was further thinned in a Gatan model 691 precision ion polishing system (Gatan, UK) to reduce the thickness to below 100 nm allowing the sample to be studied in a TEM.

Powder TEM sample was prepared from C-800℃-30min-p. The powder was dispersed in acetone to produce a suspension where copper grid with carbon film can be coated. Acetone allows fast drying of coated grids.

### 3.1.4.4 Electron backscatter diffraction (EBSD)

The surface of C-800℃-1min and cross-section of C-800℃-30min were coated by carbon on a PECS I system (Gatan, UK). The sample back was stuck on an alumina SEM stub using silver paint to reduce charging effects to achieve stable image.

### 3.1.4.5 Permeation

The back of SCFT coated BSCF pellet and c-BSCF pellet were ground by P400 SiC paper and polished by 1 μm diameter diamond paste to ensure gas tight after sealing.

### 3.1.4.6 Density

The density of 1100°CS-BSCF, 1100°CS24hr-BSCF and 1125°CS-BSCF were measured as sintered.  Three pellets of each kind were measured.

# 3.2 Characterisation techniques

## 3.2.1 XRD

### 3.2.1.1 Theory

#### 3.2.1.1.1 Bragg's law

The atoms of a crystalline material are ordered in a 3D structure; hence there are planes of atoms which are called lattice planes. X-ray diffraction occurs when an X-ray hits a crystalline material and Bragg's law is satisfied. Equation 22 describes Bragg's law, where d is the spacing between adjacent lattice planes (d-spacing), θ is the diffraction angle, λ is the wavelength of X-ray, n is the order of diffraction. When the angle θ between the incident beam and the lattice plane satisfies Bragg's law, the X-rays which are scattered by the electrons of the atoms are in phase and constructively interfere to produce high intensity to become visible to the detectors. When θ does not satisfy Bragg's law, the X-rays interfere destructively hence cannot be detected. [180]

$$2d\sin\theta = n\lambda$$

Equation 22

#### 3.2.1.1.2 The instrument

The XRD goniometer measures the diffraction angle θ and the X-ray intensity, rotates the sample and moves the detector precisely (Figure 27). The incident beam is generated from a tube on the left. The angle between the incident beam and the specimen lattice plane and the angle between the diffracted beam and the lattice plane are θ. The diffracted beam is then received by a detector. The detected angle is 2θ. The direct beam slit produces a line source of X-ray. The detector slit reduces the range of X-ray wavelength that enters. [180]
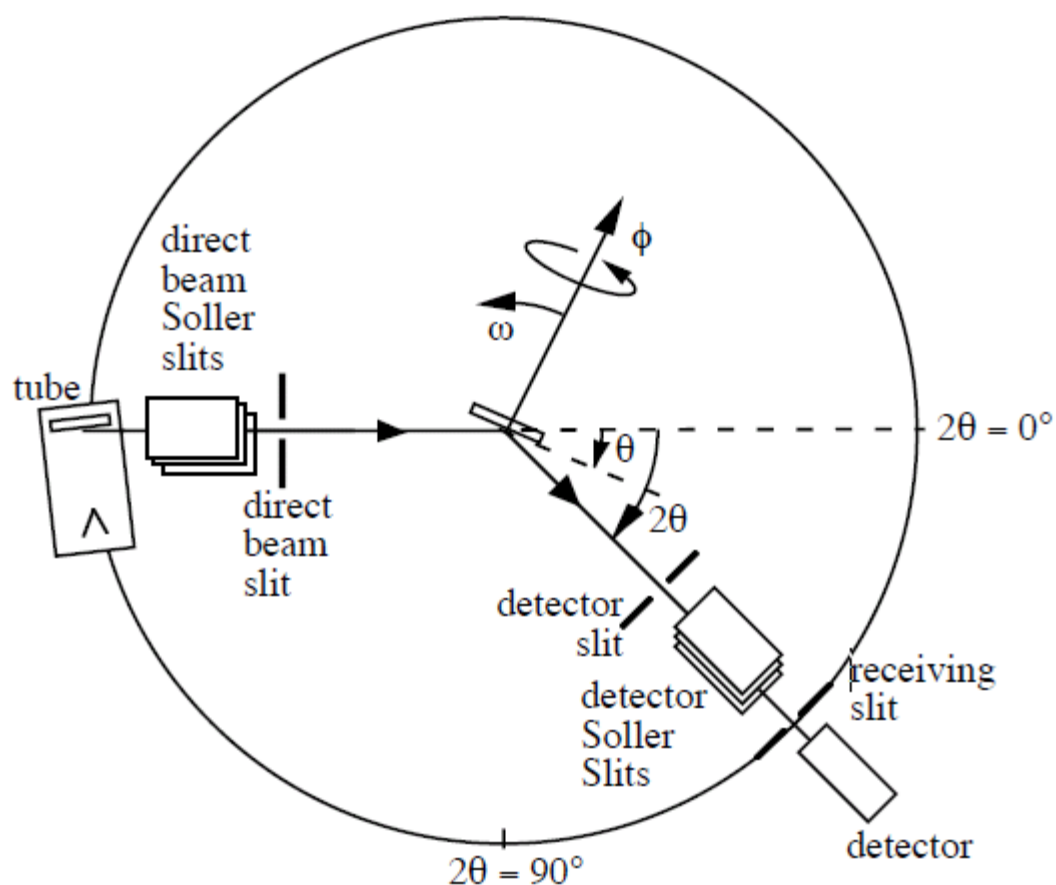
Figure 27. A schematic diagram of the XRD goniometer (from Fultz and Howe [180]).

### 3.2.1.1.3 The XRD pattern

The measured X-ray intensity is plotted as a function of $2\theta$ (Figure 28). A d-spacing can be determined from a peak by Bragg's law. The crystal structure can be identified by a series of d-spacings and the associated peak intensity on HighScore plus (Philips software). The Miller indices of the lattice planes are then assigned to the peaks (Figure 28). [180]
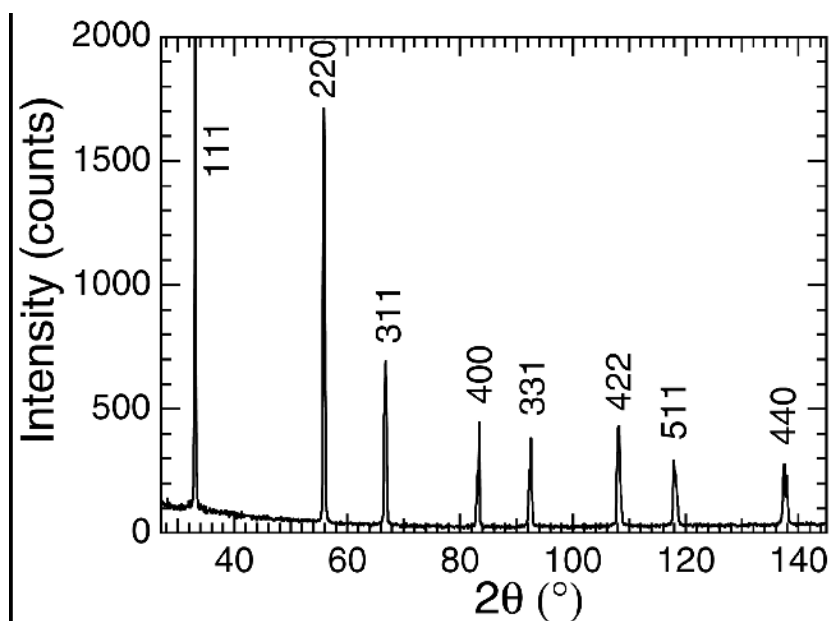
Figure 28. An XRD pattern of an face-centred cubic crystal (from Fultz and Howe [180]).

### 3.2.1.2 The characterisation procedures

The samples were characterised in a Philips Automatic Powder Diffractometer for phase determination, using a Cu X-ray tube. The wavelength of X-ray beam was 1.54060 Å. The instrument operated at 40 kV and 40 mA. The scanning step size was 0.020° and the scanning range was 5° - 85° 2θ. The scan step time was 22 seconds. The detection limit is 3% of the specimen.

The spectra were refined to determine lattice parameters and phase concentration on TOPAS software (Bruker, UK) and were indexed on HighScore Plus software (PANalytical, Netherlands) against reference cards the reference number of which was stated with indexed patterns.

### 3.2.1.3 Determination of XRD penetration depth

This is calculated by the mass attenuation coefficient (MAC) calculator in HighScore plus (Philips). The depth is affected by the sample packing factor (experimental density), theoretical density, incident angle and composition [181].

## 3.2.2 SEM

### 3.2.2.1 Theory

#### 3.2.2.1.1 Image formation

A SEM focuses, accelerates and delivers electrons to a specimen which is inside a vacuum chamber. The focused electron beam scans across the specimen surface line by line and a detector detects the emitted or scattered electrons from the surface. Meanwhile, the brightness and contrast of the pixels on the monitor are adjusted according to the detected intensity. Hence an image is obtained to show the microstructure of the specimen. The specimen pixel size equals the monitor pixel size divided by the magnification. [182]

#### 3.2.2.1.2 The image resolution

The shortest distance between the centres of two adjacent pixels is the resolution of a SEM, when the two pixels are distinguishable. The probe diameter is 2 to 10 nm. A smaller probe diameter is available with a field emission gun (FEG). The probe diameter needs to match the pixel size. The resolution becomes worse when the probe diameter is larger than the specimen pixel size. The noise in an image may be increased when the probe diameter is smaller than the specimen pixel size. The ultimate resolution is determined by the beam specimen interaction volume. However, when the probe diameter decreases, the beam current is decreased. The low beam current may lead to a low signal/noise ratio hence the resolution can be reduced. Longer scanning time can prevent such reduction. [182]

#### 3.2.2.1.3 The depth of field

The depth of field H can be determined from Equation 23, where WD is the working distance, A is the aperture diameter, M is the magnification. [182]

$$H = 0.2WD / AM$$

Equation 23

### 3.2.2.1.4 The beam and specimen interaction

Figure 29 shows the electron beam and specimen interaction volume. The region which produces the secondary electrons (SE) is the smallest and matches the dimension of the incident beam best. The SEs are generated from the specimen after inelastic interactions of the beam and the specimen. The energy of these electrons are approximately 50eV [182] hence they can be detected only when they are very close to the surface (approximately 1 nm at a beam energy of 3 keV). Therefore, the SEs are topography sensitive and contribute to topographic contrast. [18, 182]

An electron of the beam which is reflected from the specimen after an elastic interaction is called a backscattered electron (BSE or BE). An atom with higher atomic number has higher chance to have such an interaction because the electron beam interacts with the electrons of the atom. Hence BSEs are sensitive to the average atomic number changes and contribute to compositional contrast. [18]
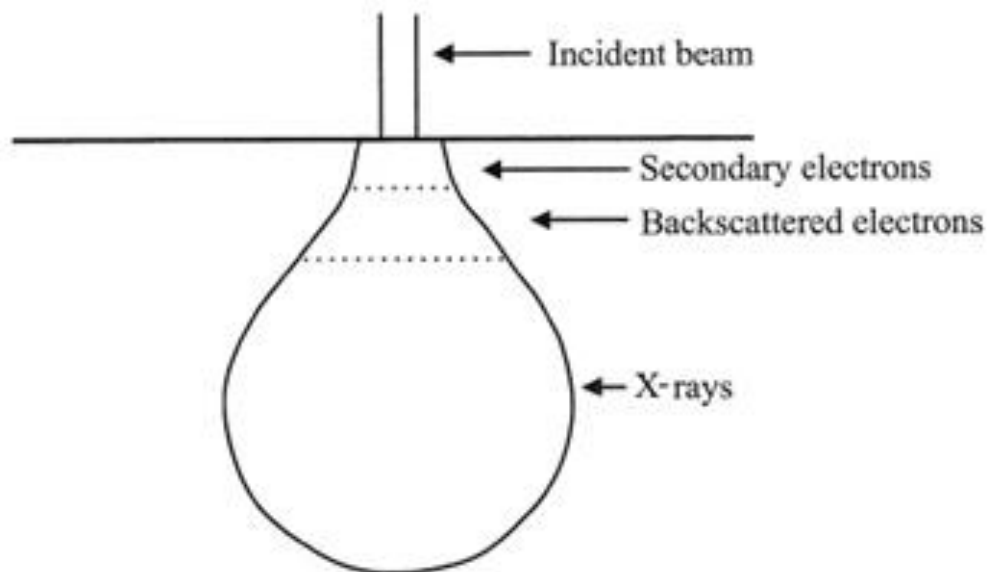


Figure 29. The incident beam interacts with specimen within a certain volume and produces electron and X-ray emissions (from Goodhew et al. [182]).

Figure 30 shows the set-up of a SEM detector. The BEs and SEs go through a scintillator, a light guide and a photomultiplier.
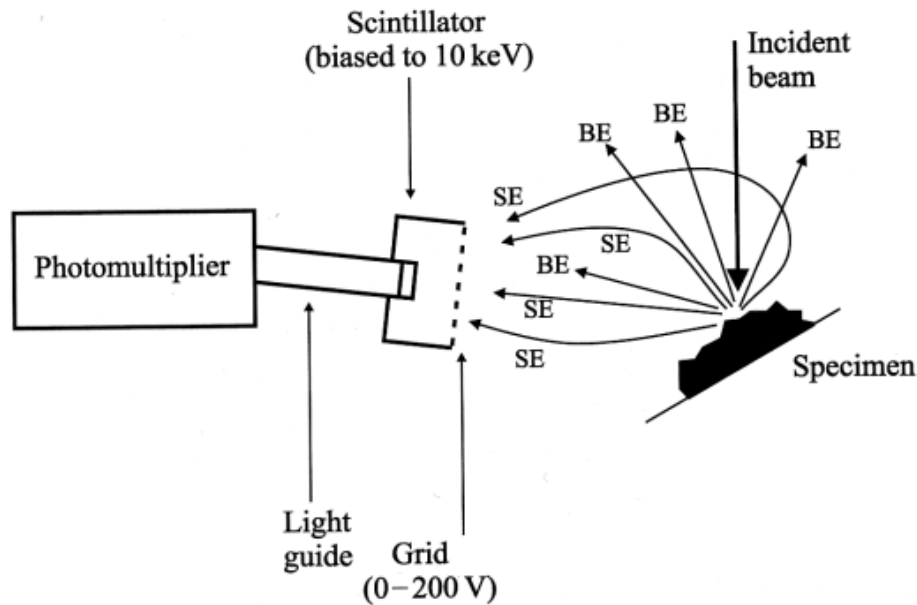


Figure 30. A schematic diagram of a SEM detector and how SE and BE reach the detector (from Goodhew et al. [182]).

3.2.2.1.5 Energy dispersive X-ray spectroscopy (EDX)

*3.2.2.1.5.1 The principle*

When an electron beam interacts with an atom, an electron of the atom may be excited and leave its orbital. Another electron from a higher energy orbital may fill in the vacancy, emitting an X-ray. The amounts of energy of the emitted X-rays from different elements are distinguishable. Hence they are called characteristic X-rays and elements are identified by measuring the energy of the emitted X-ray. The amount of emitted X-rays (intensity) can also be measured and plotted as a function of energy, giving rise to an EDX spectrum with peaks (Figure 31). Such peaks are called characteristic lines. The measurement was conducted on an EDX detector. [182]
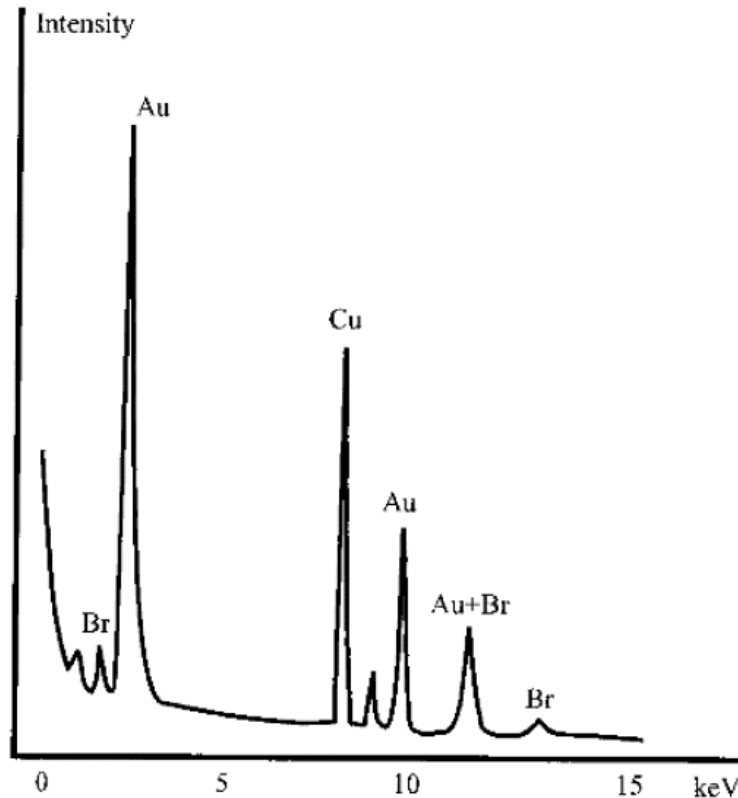
Figure 31. An EDX spectrum with characteristic lines of Au, Cu and Br (from Goodhew et al. [182]).

### 3.2.2.1.5.2 The characteristic lines

A characteristic line, caused by electrons jumping from inner shells to the K/L/M shell, is called a K/L/M line. For an element, the K line is more intense than the other lines, hence it is better to quantify the element by the K line. A higher beam energy is required to excite a K line compared with other lines, giving rise to a larger specimen interaction volume and higher fluorescence effect. In this case, L lines are used. [182]

### 3.2.2.1.5.3 The beryllium window

A beryllium window covers the X-ray entrance on the EDX detector to prevent contamination. Light elements are hard to detect because the window absorbs a large proportion of low energy X-rays. [182]

### 3.2.2.1.5.4 The fluorescence effect

When an X-ray escapes from the specimen, atoms on its path can be excited and hence emit X-rays at a lower energy. This is called fluorescence. It may change the apparent

concentration of elements, especially when the atomic numbers of the elements in the specimen are similar. [182]

### 3.2.2.1.5.5 The shadow effect

An X-ray can be stopped by an obstacle on its path because it travels in a straight line, losing chemical information. This is called the shadow effect which happens on rough sample surfaces and has to be avoided because the EDX map intensity variation may be caused by the shadow effect rather than chemical composition changes. [182]

### 3.2.2.1.5.6 When the bulk and surface composition are different

Care should be taken when X-rays are acquired from such a sample because X-rays are mainly emitted below the surface (Figure 29). The chemical information of the bulk may be mistaken as that of the surface. [182]

### 3.2.2.1.5.7 Quantification

When a spectrum can be acquired from an unknown specimen, the number of X-ray counts of an element in the spectrum is $N_{spec}$ and the concentration of this element is $C_{spec}$. A series of samples which consist of the elements of the unknown specimen have to be made and the compositions have to be known to generate standard EDX spectra. The number of counts of an element in a spectrum is $N_{std}$ and the concentration of this element is $C_{std}$. $C_{spec}$ can be determined by Equation 24 under an ideal condition. [182]

$$C_{spec} = \frac{N_{spec}}{N_{std}} * C_{std} = k * C_{std}$$

Equation 24

However, the density and average atomic number of the unknown specimen can be different from that of the standard sample. Hence Equation 24 is modified to Equation 25 by a ZAF correction. Z is the atomic number corrector and depends on the X-ray emission efficiency. Before the electron beam is too weak to excite X-rays, it penetrates into the specimen for a certain depth which affects the X-ray emission efficiency. The number of backscattered electrons also affects the efficiency. A is the absorption corrector and depends on the mass absorption coefficient of the specimen and the standard. F is the fluorescence corrector and can be important when the atomic numbers of the elements are similar. [182]

$$C_{spec} = k * Z * A * F$$

Equation 25

## 3.2.2.2 The characterisation procedures

The samples were imaged on a Philips XL30 FEGSEM operating at 8 kV - 20 kV or on a Zeiss EVO60 operating at 20 kV. The former one with resolution of 3.5 nm at 30 kV worked in secondary (SE) and backscattered (BE) electron imaging modes for topographic constrast and orientational contrast respectively. The latter one with resolution of 2nm at 30 kV worked in SE mode.

All dimensions in the SE/BE images were measured using ImageJ software (Wayne Rasband, USA). The measurement precision was pixel side lengh (0.01 μm at 10000x magnification) and the tolerance interval was half the precision. The grain size was measured by the linear intercept method [183]. 5 lines were randomly drawn across an image. The number of intercepts of a line and grain boundaries was counted and the line length was divided by this number. The average of quotients of all lines becomes the grain size and the uncertainty is contributed by standard deviation. Uncertainties of all measurements were reported with measured data.

EDX element mapping was carried out on a FEI Magellan FEG-SEM operating at 10 keV along a cubic grid with a step size of 0.1 μm using Aztec software (Oxford Instruments, UK). The diameter of beam and specimen interaction area is 500 nm at 5 kV. Dr Ali Gholinia was acknowledged for conducting the mapping.

# 3.2.3 TEM

## 3.2.3.1 Theory

### 3.2.3.1.1 The resolution of TEMs

The resolution of microscopes is inversely proportional to the wavelength of the imaging radiation. The wavelength of an electron beam is between approximately 0.001nm and 0.01nm. Visible light is between 400nm and 700nm in wavelength. Hence the resolution of a TEM is better than that of the light microscopes, giving rise to the wide application of the electron microscopes in material studies. Diffraction at the lenses and the specimen ultimately limits the TEM resolution. Spherical and chromatic aberration also limit the resolution of TEMs. The effect of aberrations can be minimized by aligning the electron beam along the optical axis of each lens, although aberration correctors are required for further correction. The lens astigmatism also affects the resolution. Hence it should be carefully adjusted before imaging. [182]

### 3.2.3.1.2 Imaging mechanisms

#### 3.2.3.1.2.1 Beam and specimen interaction and ray diagrams

The imaging mechanism of a TEM is based on the interaction between the beam and the specimen. This interaction changes the beam by scattering the electrons, which produces contrast in the image. Images formed by the elastically scattered electrons are dark field (DF) images. Images formed by the unscattered and inelastically scattered electrons are bright field (BF) images. Figure 32 (a) shows the ray diagram of the electron beam. The beams with the same order focus on the back focal plane (BFP) after they are diffracted by the specimen. A diffraction pattern is hence formed on the BFP. An image can be formed after the beams arrive at the image plane of the objective lens. Both the image and diffraction pattern can be projected to a screen by the intermediate lens. Figure 32 (a) and (b) show electron beams in the imaging model and diffraction model, respectively. The imaging (contrast) mechanisms of TEMs are introduced in the following paragraphs. [182]
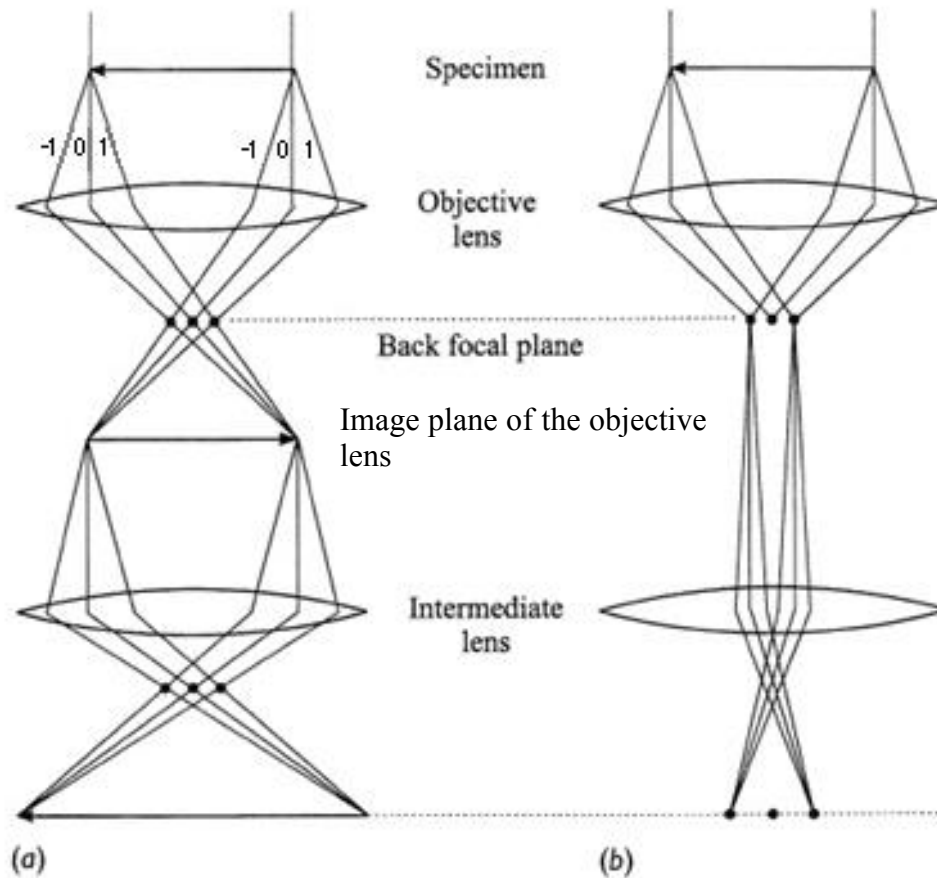
Figure 32. Ray diagram of the electron beam in TEM: (a) Imaging model, (b) Diffraction pattern model. (after Goodhew et al. [182])

### 3.2.3.1.2.2 Mass-thickness contrast

The mass-thickness contrast mechanism suggests that the changes in the sample thickness and density produce different brightness in the image. [182]

### 3.2.3.1.2.3 Diffraction contrast

In a buckled crystalline thin specimen, if some lattice planes satisfy Bragg's law, and the electron beam can be diffracted away without contributing brightness to the image. Hence dark bands (extinction contours) are formed below these lattice planes, as shown in Figure 33. For a wedge shaped thin specimen, dark bands (thickness fringe) can also be seen in the image due to diffraction. Both types of dark bands are produced by the diffraction contrast mechanism which is useful for detecting planar defects (stacking faults, grain boundaries and phase boundaries). [182]
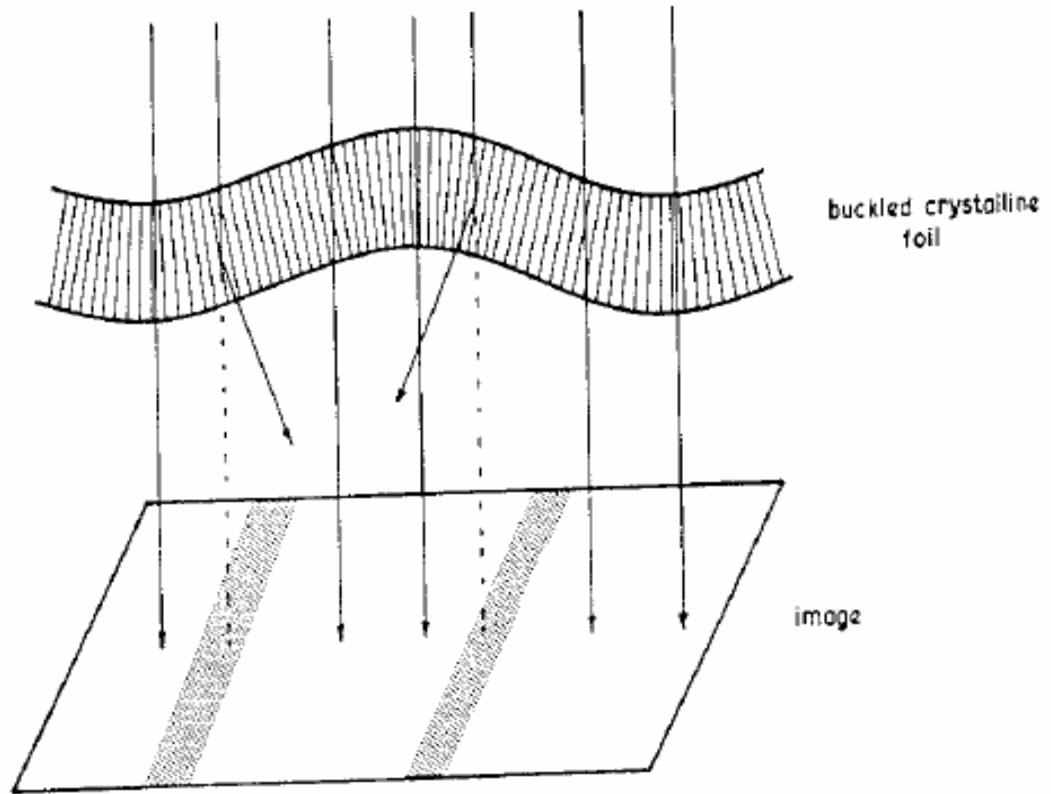
Figure 33. A schematic diagram of the formation of extinction contours (from Goodhew et al. [182]).

### 3.2.3.1.2.4 Phase contrast

Thickness-mass contrast and diffraction contrast are forms of amplitude contrast because they use only the amplitude of the beams to form images. The phase contrast mechanism produces an image by the interference of beams with different phases. It occurs in many images because phase changes occur during most electron scattering. [182]

When a specimen is tilted so that one zone axis in the observed area is parallel with the incident beam, a series of strongly diffracted beams are formed. A high resolution TEM (HRTEM) image is formed when the beams are allowed to interfere. It is also called structure image or lattice image because it shows dark or bright spots corresponding to atom columns. However, the spots can also be associated with the spaces between the columns or two columns, depending on the thickness of specimen and the defocus and resolution of the microscope. Hence experimental images have to be compared to simulated images produced according to likely structures. [182]

All the above mechanisms may contribute to an image. The objective aperture selects which electron beam(s) contributes to the image hence the dominant contrast mechanism of an image is mainly determined by the objective aperture. [182]

### 3.2.3.1.3 The electron diffraction pattern

Study of the electron diffraction pattern (DP) constitutes another important characterization technique. Figure 34 (a) shows a DP of a single crystal specimen. The spots surrounding the big one in the centre are caused by electrons diffracted by a set of lattice planes which are nearly parallel to the electron beam in directions that satisfy Bragg's law. Figure 34 (b) shows a DP of a polycrystal specimen, more diffraction spots are seen. If there are many crystals with different lattice plane orientations, a large amount of diffraction spots form rings outside the central spot caused by the incident beam (Figure 34 (c)). [182]
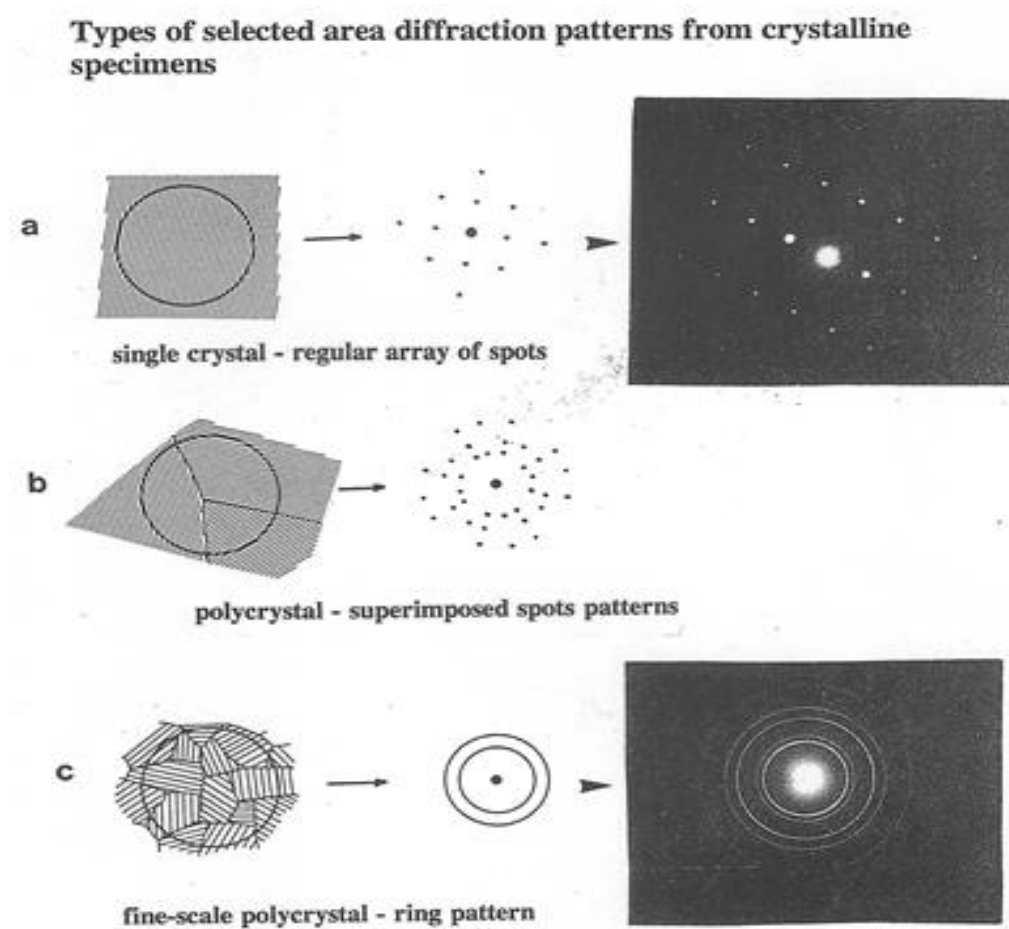


Figure 34. Electron diffraction patterns of (a) single crystal (b) polycrystal and (c) fine-scale polycrystal. (from Goodhew et al. [182])

Using the diffraction geometry in Figure 35, where point A is a diffraction spot, Equation 26 can be derived. $\theta$ is the Bragg angle. By combining Equation 26 and Equation 22, Equation 27 can be obtained. The d-spacing of the set of lattice planes forming the diffraction spot can be determined by Equation 27 in which $L\lambda$ is the camera constant. L is the camera length and $\lambda$ is the wavelength of electron beam. [182]
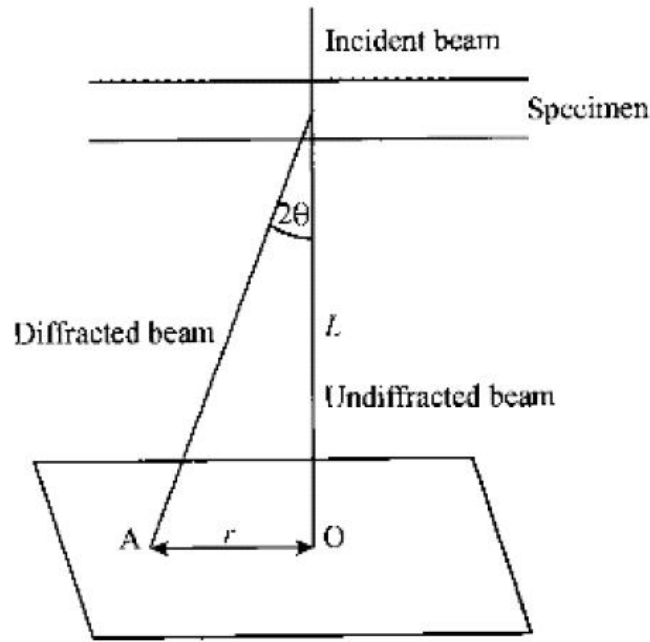


Figure 35. A schematic diagram of the diffraction pattern formation geometry (from Goodhew et al. [182]).

$$\frac{r}{L} = 2\theta$$

Equation 26

$$rd = L\lambda$$

Equation 27

The crystallographic orientation of the specimen can be determined from the corresponding single crystal DP. Each point in a single pattern represents a set of lattice planes in real space. A reciprocal lattice can be drawn by scaling the single crystal DP by the camera constant. [182]

3.2.3.1.4 EDX on a TEM (The advantages over SEM-EDX)

*3.2.3.1.4.1 Higher beam energy*

The beam energy of TEMs (100kV to 300kV) is higher than that of SEMs (10kV to 30kV) hence some K lines of certain elements which cannot be excited by SEMs can be excited by TEMs. [182]

*3.2.3.1.4.2 Smaller probe diameter*

In Figure 36, the beam and specimen interaction volume of a TEM is smaller than that of a SEM because the thickness of a TEM sample (approximately 100 nm or thinner) is thinner than that of a SEM sample [182]. A smaller interaction volume gives rise to a smaller probe diameter which is between 1 to 10 nm on a field emission gun (FEG) TEM depending on the probe current and beam convergent semi-angle [184]. However, the probe diameter of a SEM can be as large as 2 μm [182].



(a)                    (b)
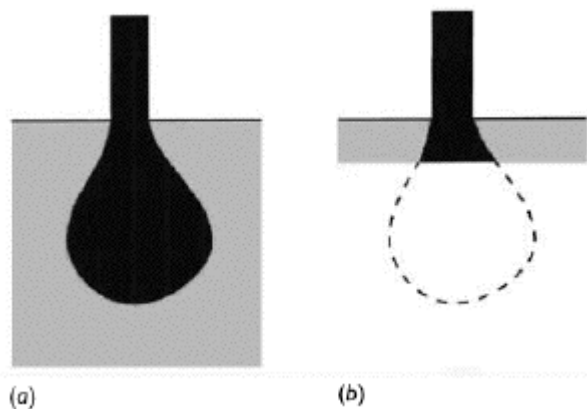
Figure 36 The beam and specimen interaction volume of (a) SEM and (b) TEM (from Goodhew et al. [182])

*3.2.3.1.4.3 Detecting light elements*

One of the EDX detectors (T20) in this research has no beryllium window hence it is able to detect light elements like oxygen and carbon.

*3.2.3.1.4.4 Easier quantification*

The absorption corrector (A) and the fluorescence corrector (F) can be removed from Equation 25 without introducing significant error because the path for X-rays to escape from a specimen is shorter in a TEM specimen than in a SEM specimen, leading to fewer interactions. Equation 25 is hence simplified to Equation 28, suggested by Cliff and

Lorimer [185]. In this equation, $k_{AB}$ is a scaling factor which depends on the sample, detector and operation and can be determined from experiments. Equation 28 holds when the sample thickness is between 50 - 100 nm. [182]

$$\frac{C_A}{C_B} = k_{AB} \frac{N_A}{N_B}$$

Equation 28

### 3.2.3.1.5 Scanning TEM (STEM)

In STEM mode, the beam is focused and scans across a specimen, forming a stable diffraction pattern on the following detectors (Figure 37). A bright field (BF) detector is placed under the direct beam. Another beam is scanning the computer screen synchronously to generate a BF image, with intensity controlled by the BF detector. A DF image is generated in a similar way except that the signal comes from the annular dark field (ADF) detector shown in Figure 37. Also in Figure 37, the high angle annular dark field (HAADF) detector collects scattered electrons from higher angles. HAADF image shows atomic number contrast (Z-contrast) and maximises Rutherford scattering, while diffraction contrast is minimised. [184]
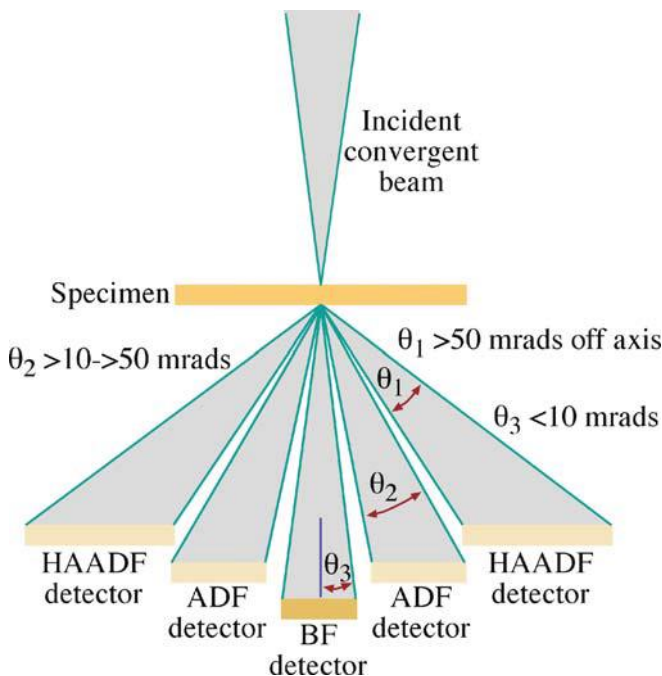


Figure 37. A schematic diagram of the detection angles of BF, ADF and HAADF detectors in STEM (from Williams and Carter [184]).

### 3.2.3.2 The characterisation procedures

HRTEM was carried out using a FEI Tecnai TF30 TEM operating at 300 keV with spatial resolution of 2 Å on the cross section TEM samples. The raw images were processed to remove noise by Fourier filtering and reconstruction [184] on Digital Micrograph (DM) software (Gatan, UK). Diffraction patterns were produced by fast Fourier transform (FFT) [184] based on raw images using DM software and were indexed after matching simulated patterns from PDF-4+ 2013 software (ICDD, US). Dimensions and d-spacing were measured on DM software and the measurement precision is the side length of a pixel. Uncertainties were reported with measured data.

EDX analysis was conducted on the same instrument to cross section TEM samples and powder TEM samples. A FEI Tecnai TF20 TEM operating at 200 keV was also used for EDX. Both microscopes had an EDX probe diameter below 10 nm. This probe diameter was smaller than the areas of interest therefore the chemical information was obtained exclusively from the selected phases. The energy resolution of the EDX detector was 126 eV for Mn Kα. All point analysis, linescan and element mapping were performed on AztecTEM (Oxford Instruments NanoAnalysis, UK) to generate composition or element map of the phases. The acquisition time for point analysis was 30 s. The uncertainty in reported compositions are typically ± 1 % or 2 %.

## 3.2.4 EBSD

### 3.2.4.1 Theory

#### 3.2.4.1.1 The formation of an EBSD pattern

When a lattice plane is irradiated by an electron beam, the elastically scattered electrons which satisfy Bragg's law can form Kikuchi lines on a nearby phosphor screen, as shown in Figure 38. The lines correspond to the lattice plane. Therefore, they can be indexed by Miller indices of the parental lattice plane. An EBSD pattern is formed when all the lattice planes that satisfy Bragg's law and are hit by an electron beam generate a series of Kikuchi bands on a screen. Figure 39 shows an EBSD pattern, all the bright bands are Kikuchi bands. [186]
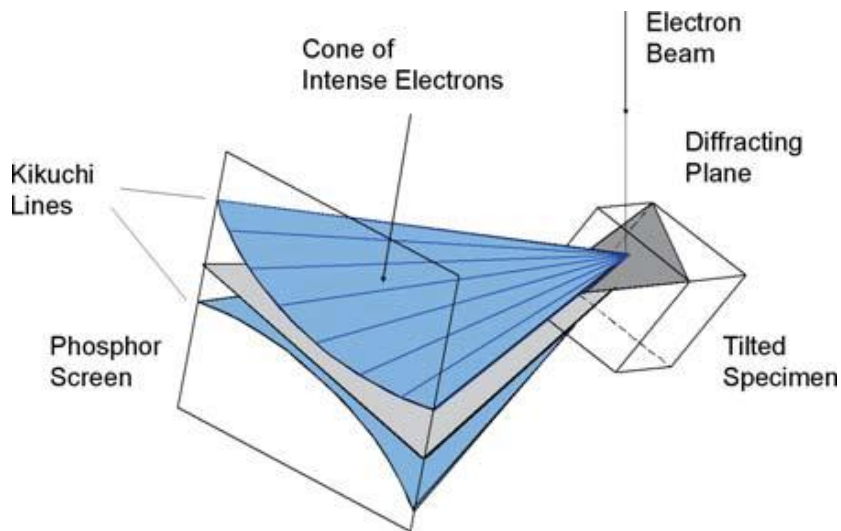
Figure 38. A schematic diagram of formation mechanism of Kikuchi band in SEM with EBSD (from Schwartz [186]).
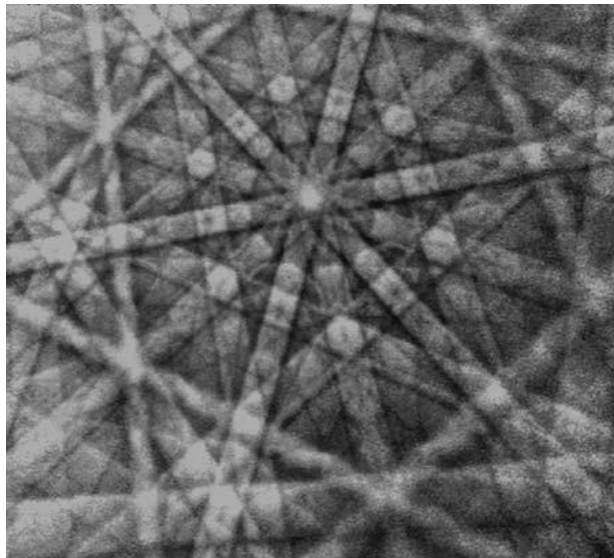


Figure 39. An EBSD pattern with Kikuchi bands (from Schwartz [186]).

3.2.4.1.2 The EBSD set-up

Figure 40 shows an EBSD set-up inside a SEM. A detector is on the left of the picture with a phosphor screen faces the sample (brown) and shows a few Kikuchi bands. The sample is tilted 70° from horizontal position to maximise the intensity and contrast of the EBSD pattern. An electron beam (black) is impinging on the sample. [186]
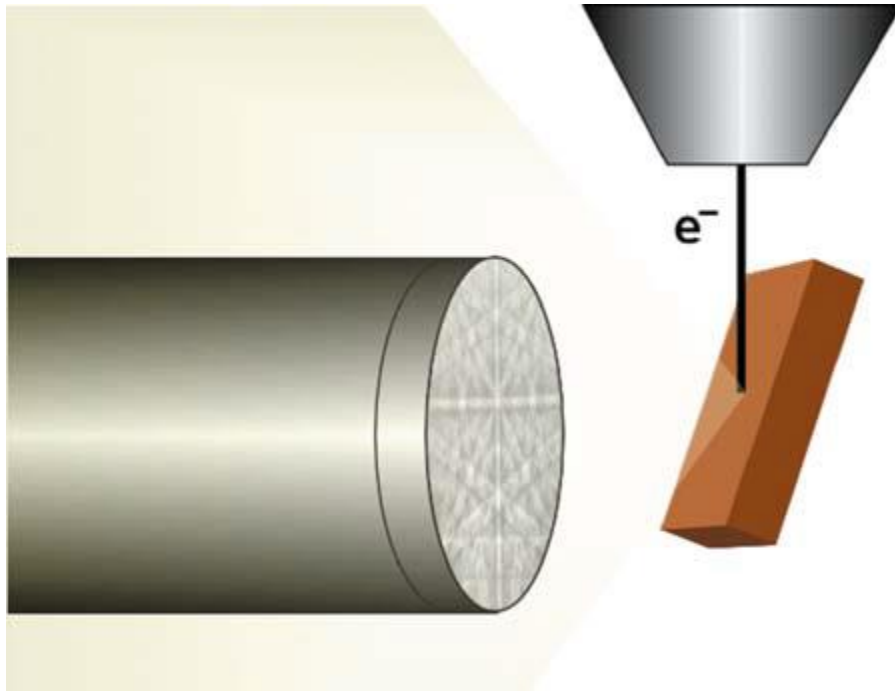
Figure 40. A schematic diagram of the relative location of EBSD detector, specimen and electron beam in SEM (from Schwartz [186]).

3.2.4.1.3 The Hough transform

An EBSD pattern can be indexed automatically by a computer using the Hough transforms. In Figure 41 (a), the perpendicular distance ρ from a line to the origin and the angle θ between the line normal and the x axis are shown. A point indicated by an arrow can represent this line in Hough space where x axis shows θ and y axis shows ρ (Figure 41 (b)). In fact, any line in Figure 41 (a) can be represented by a point in Hough space. All the lines through point 1 in Figure 41 (a) can be represented by points in Hough space. These points form a sinusoidal curve labelled by '1' in Hough space. Similarly, all lines through point 2 and 3 are represented by sinusoidal curve labelled by '2' and '3' respectively in Hough space. The curves are of constant intensity. Point 1, 2 and 3 are in a line, as a result, the sinusoidal curve 1, 2 and 3 intersect on a point indicated by an arrow in Hough space. At the intersection point, the intensity of each curve contributes to the overall intensity. Hence this point becomes brighter as the points on the line are all transformed to Hough space. Hence the task of detecting a fragmentary band with noise becomes a task of detecting a point in Hough space. [186]
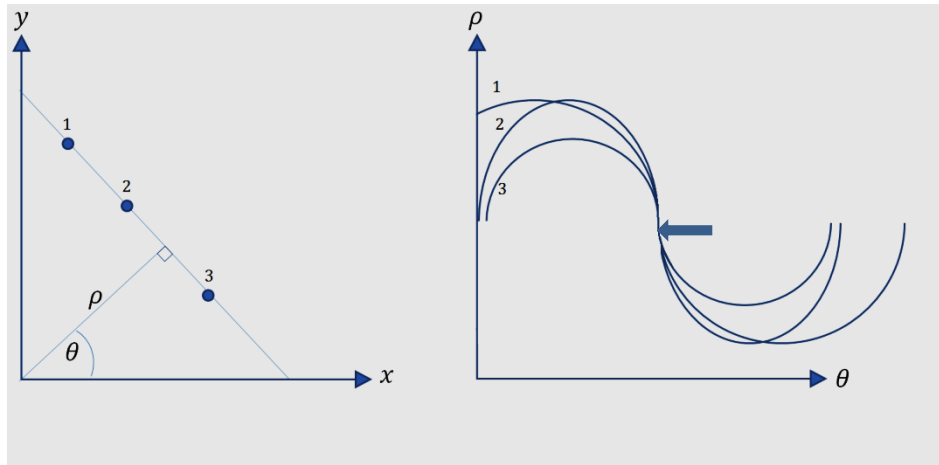
(a)                                    (b)

Figure 41. Schematic diagrams of (a) a line in Cartesian coordinate system and (b) the Hough space with points 1, 2 and 3 on the line transformed. The arrow indicates a point which is the line after Hough transform.

### 3.2.4.1.4 The indexing

Once the interplanar angles and the interplanar spacings are measured from an EBSD pattern, they are compared with theoretical values calculated for the crystal structure of the sample. The angles are measured from the angles between Kikuchi bands. The spacings are calculated from the Kikuchi band widths. Miller indices of lattice planes are assigned to Kikuchi bands according to the comparison. The crystallographic zone axes can be assigned to the intersections of the indexed Kikuchi bands. Hence the crystallographic orientation of the sample can be determined. [186]

### 3.2.4.1.5 The formation of a pole figure

A Pole figure reveals the orientations of lattice planes with a particular miller index in a crystalline material. Figure 42 shows a lattice plane the normal direction of which intersects a sphere at a point p. The origin of the sphere is located on the plane (superimposed by the origin of the plane normal). Point p and the south pole Q of the sphere are linked by a line which intersects a shaded projection plane at point p'. Point p' is the pole of the normal direction of the lattice plane. A pole figure consists of the projection plane and poles of particular lattice planes. [186]
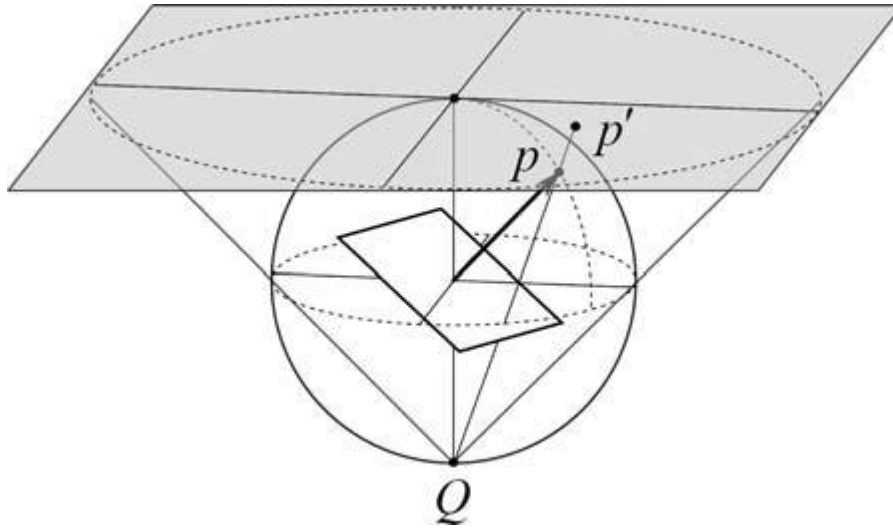
Figure 42. A schematic diagram of the EBSD pole figure formation (from Schwartz [186]).

3.2.4.2 The characterisation procedures

EBSD study was carried out on a FEI Magellan FEG-SEM equipped with an EBSD detector and AZtecHKL software (Oxford, UK). The SEM operated at an accelerating voltage of 10 keV. The spatial resolution of EBSD is 10 nm and the orientation accuracy is 0.2°. The specimen was tilted 70° from horizontal position. Automatic EBSD data collection was performed along a cubic grid with a step size of 0.05 μm after the feasibility of rough surface EBSD analysis was ensured. The phase maps and pole figures were produced using the HKL Channel 5 software (Oxford, UK) based on the diffraction data.

## 3.2.5 Density and porosity measurements

### 3.2.5.1 Theory

The sintered pellet density was measured by the Archimedes technique [183] which measured the pellet mass in air and in water. The pellet weighed less in water: the difference being equal to the mass of the displaced water. The pellet volume can be determined from the measured values and the density of water. Hence the pellet density can be calculated.

However the pellets are porous and may have a cross section similar as Figure 43 (b). A series of pores shaded in white connect to the outside (open pores). The rest of the pores shaded in yellow do not connect to the outside (closed pores). Assuming a porosity free pellet (Figure 43 (a)), the pellet volume is called the bulk volume. Taking all the pores into account (Figure 43 (b)), the remaining pellet volume is called true volume [18]. Taking only the open pores into account (Figure 43 (c)), the remaining pellet volume is called apparent solid volume [18]. The bulk and apparent solid density can be calculated according to the bulk and apparent solid volume, respectively. [18]
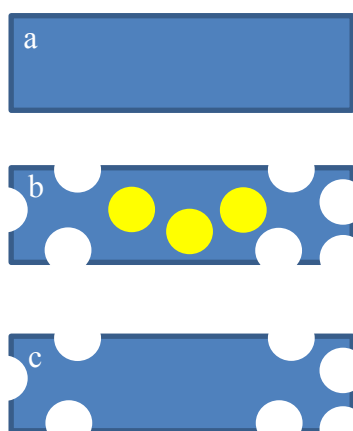


Figure 43. Schematic diagrams of the (a) bulk volume, (b) true volume and (c) apparent solid volume.

### 3.2.5.2 The characterisation procedure

Pellet samples were measured on a laboratory electronic balance (precision: 0.0001g) with density determination kits. A pellet was weighed in air to obtain mass $m_1$. It was then weighted in water to obtain mass $m_2$ and was vibrated in water to lose attached observable bubbles. It was then dried by a paper towel and weighed to obtain $m_3$. The bulk density ($\rho_b$) can be calculated by Equation 29. $\rho_{water}$ is the density of water. $\rho_b$ was divided by theoretical density (5.52 g/cm$^3$) to determine the relative density. Theoretical density was obtained through dividing unit cell mass (3.5 x 10$^{-22}$ g) of BSCF by unit cell volume (63.39 Å$^3$). The lattice parameter in volume calculation was refind by TOPAS. For each type of sample (1100℃S-BSCF, 1100°CS24hr-BSCF and 1125°CS-BSCF), the density was measured three times to extablish an uncertainty (standard deviation). The uncertainty in reported densities is from ± 0.3 % to ± 0.8 %.

$$\rho_b = \frac{m_1}{m_3 - m_2} \times \rho_{water}$$

Equation 29

## 3.2.6 The permeation

### 3.2.6.1 The permeation rig

Figure 44 shows the experimental rig used to measure the oxygen permeability of BSCF pellets and coated BSCF pellets. The grey, blue and orange tubes are alumina tubes. Both the alumina and quartz tubes can endure the temperatures of this study (20 °C - 850 °C). The rubber plugs are at least 10 cm away from the furnace to avoid damage. The sample is a 1 mm thick, 10 mm diameter disk. To the left of the pellet, the alumina tube is minimized in size hence the time for equilibrium can be minimized. Re-equilibrium is necessary after temperature variations, gas flow rate variations, etc. The gas flow is more likely to be described by a plug flow model [187] as a result of the minimization. The temperature of the pellet is measured by a thermo couple. The pellet and tube are sealed by cement (Aron Ceramic D, Toagosei Chemical Industry Co. Ltd., Tokyo, Japan). The $N_2$ flow rate was controlled by an outlet valve on the gas regulator. For the "air in" tube (Figure 44), it was measured by a tube flow meter. The flow meters were calibrated by a bubble flow rate indicator.
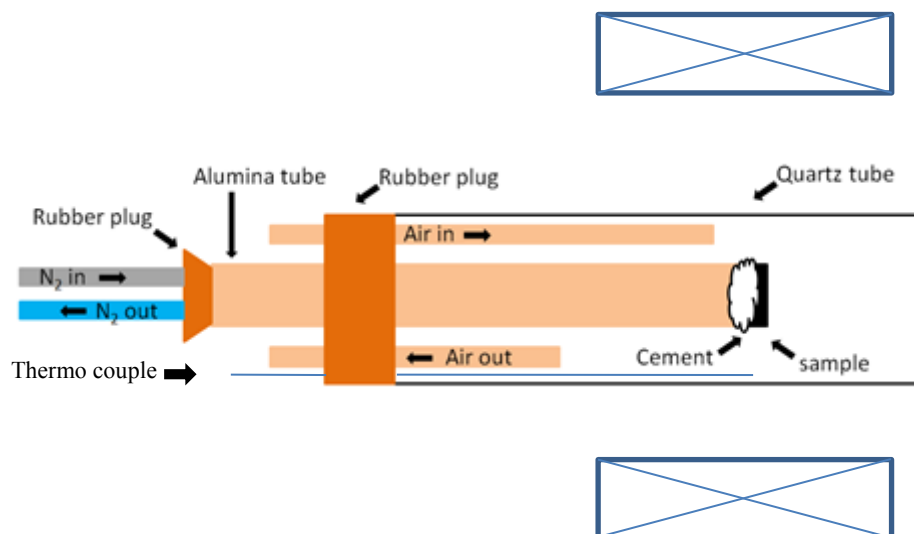
Figure 44. A schematic diagram of the permeation rig.

3.2.6.2 The sealing procedure

Before sealing, the alumina tube (Figure 44) end was ground using P400 SiC paper and was attached to the polished sample back (Figure 44). After painting the interface of the tube and sample (Figure 44), the cement was dried for 16 hours at room temperature then heated at 90 °C for 1 hour and 150 °C for 1 hour. During drying and heating, the sealed tube was blown by $N_2$ to expel air. The flow rate of $N_2$ was approximately 10 cm$^3$ min$^{-1}$ and that of air was approximately 50 cm$^3$ min$^{-1}$. The $N_2$ flow was slow because high flow rate cooled down the tube, cement and pellet, leading to a thermal shock at high temperatures causing crack and leakage.

3.2.6.3 The leakage detection and corresponding solution

The leakage from the sweep side (the left side of the pellet in Figure 44) to the feed side (the right side of the pellet in Figure 44) was detected from the flow rate difference between "$N_2$ in" and "$N_2$ out" (Figure 44). Before the difference was eventually reduced to 0 cm$^3$ min$^{-1}$, it indicated leakage. The flow rate of "air out" (Figure 44) was also measured because leaked gas may escape from the "air out" tube (Figure 44). Leakages were confirmed when the flow rate of "air out" (Figure 44) can be changed by the flow rate of "$N_2$ in" (Figure 44). They were minimised by using a slow $N_2$ flow rate (10 cm$^3$ min$^{-1}$).

The leakage from the feed side to the sweep side was checked by changing "air in" (Figure 44) flow rate. The flow rate of "$N_2$ out" (Figure 44) would be significantly affected by that

of "air in" (Figure 44) if there was a leakage. No such leakage was detected.

Both types of leakage were checked for at room temperature and 850 ℃.

### 3.2.6.4 The characterisation procedure

For the "$N_2$ out" tube (Figure 44), it was measured by a mass flow meter (EFM17, Aalborg, Orangeburg, NY, USA) with accuracy of $\pm$ 1.5% of reading to generate a flow rate. The permeated oxygen concentration (volume fraction in percentage) was measured by an oxygen analyzer (G1010 Mark 2 oxygen analyser, Hitech Instruments Ltd., Luton, England) with precision of 0.01% from the "$N_2$ out" tube (Figure 44). The analyser was calibrated using air (BOC, UK) whose oxygen concentration is known. The oxygen permeation flux is the product of the flow rate and the oxygen concentration. The uncertainty in reported permeation flux is typically $\pm$ 3 %.

The temperature was increased to 850 ℃ and was held for 30 minutes for equilibrium of temperature and oxygen concentration. Reading was taken, followed by reducing temperature by 40 ℃ steps. Equilibirum needs to be achieved after each step. The last reading was taken at 600 ℃ where there is no permeation.

# 4. Results

## 4.1 Basic characterisation

### 4.1.1 Basic characterisation of BSCF

#### 4.1.1.1 The characterisation of BSCF synthesis

##### 4.1.1.1.1 XRD analysis

Figure 45 shows an XRD pattern of CP-BSCF with peak positions for a $Ba_{0.5}Sr_{0.5}CO_3$ (ICSD: 04-014-5883) phase indicated. A number of indexed peaks at angles lower than 60° fit the $Ba_{0.5}Sr_{0.5}CO_3$ phase. Hence the $Ba_{0.5}Sr_{0.5}CO_3$ phase was assigned to the fitted peaks. No other phases were identified from the pattern. Unknown peaks are labelled by 'U'.
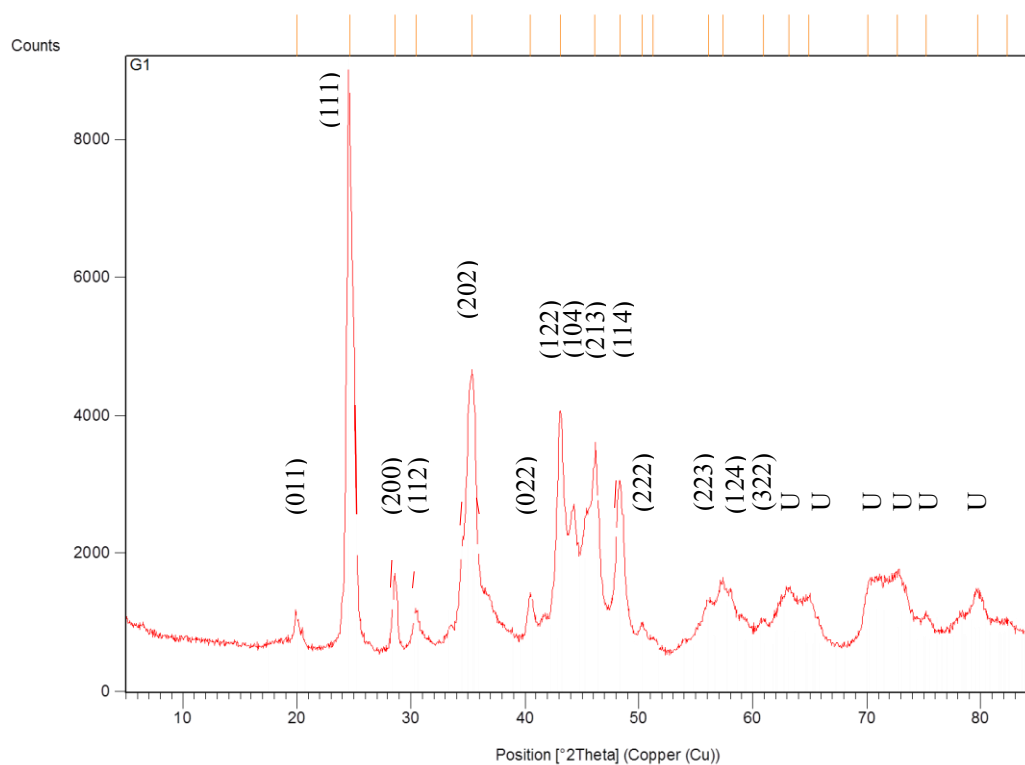


Figure 45. The indexed XRD pattern of CP-BSCF over 5 - 85° 2θ range with 'U' indicating unknown peaks.

Figure 46 shows an XRD pattern of CP-850°C4hrC-BSCF with peak positions for a $Ba_{0.5}Sr_{0.5}Co_{0.8}Fe_{0.2}O_{3-\delta}$ phase (ICSD: 00-055-0563) labelled by 'B', a $Ba_{0.5}Sr_{0.5}CO_3$ phase

(ICSD: 04-014-5883) labelled by 'CA', a $Ba_{0.5}Sr_{0.5}CoO_3$ phase (ICSD: 04-007-0067) labelled by 'BSCO' and unidentified phases labelled by 'U'. Hence the $Ba_{0.5}Sr_{0.5}Co_{0.8}Fe_{0.2}O_{3-\delta}$ phase, $Ba_{0.5}Sr_{0.5}CO_3$ phase and $Ba_{0.5}Sr_{0.5}CoO_3$ phase were assigned to the fitted peaks. No other phases were identified from the pattern.
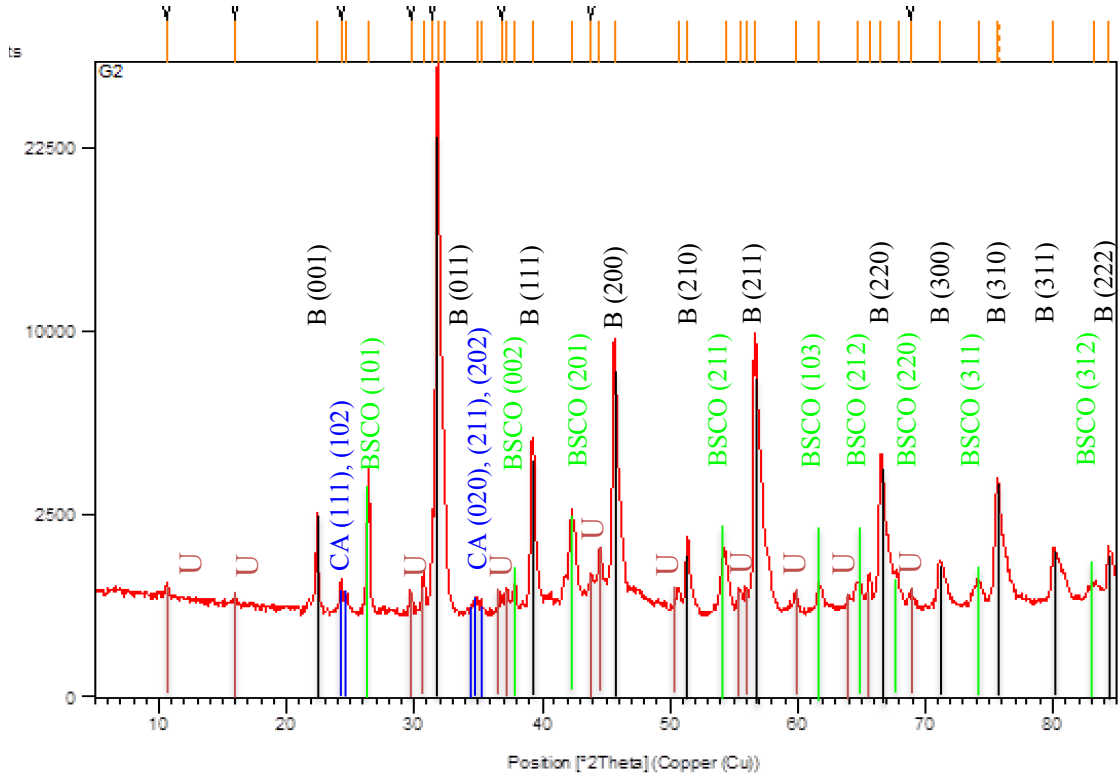


Figure 46. The indexed XRD pattern of CP-850°C4hrC-BSCF over 5 - 85° 2θ range. The $Ba_{0.5}Sr_{0.5}Co_{0.8}Fe_{0.2}O_{3-\delta}$ phase is indicated by 'B' and black indicators. The $Ba_{0.5}Sr_{0.5}CoO_3$ phase is indicated by 'BSCO' and green indicators. The $Ba_{0.5}Sr_{0.5}CO_3$ phase is indicated by 'CA' and blue indicators. The unidentified peaks are indicated by 'U' and orange indicators.

### 4.1.1.1.2 SEM investigation

Figure 47 (a) shows the microstructure of CP-BSCF. There are a number of isolated particles with an average radius of $1.8 \pm 0.8$ µm. Three of the particles are indicated by three white arrows. A few large agglomerates can be seen with the isolated particles. The outline of one agglomerate is shown in white. Figure 47 (b) shows the microstructure of CP-850°C4hrC-BSCF. A number of agglomerates with an average radius of $7.7 \pm 1.7$ µm are seen. The agglomerates consist of a number of tiny particles with an average radius of $0.75 \pm 0.33$ µm. Figure 47 (c) shows the microstructure of CP-850°C4hrC-24hrM-BSCF. A number of agglomerates are seen in the image. The average agglomerate radius is $1.5 \pm 0.5$

µm and the average particle radius is $0.51 \pm 0.29$ µm. Both the agglomerate radius and the particle radius were reduced after milling.



(a)



(b)

(c)
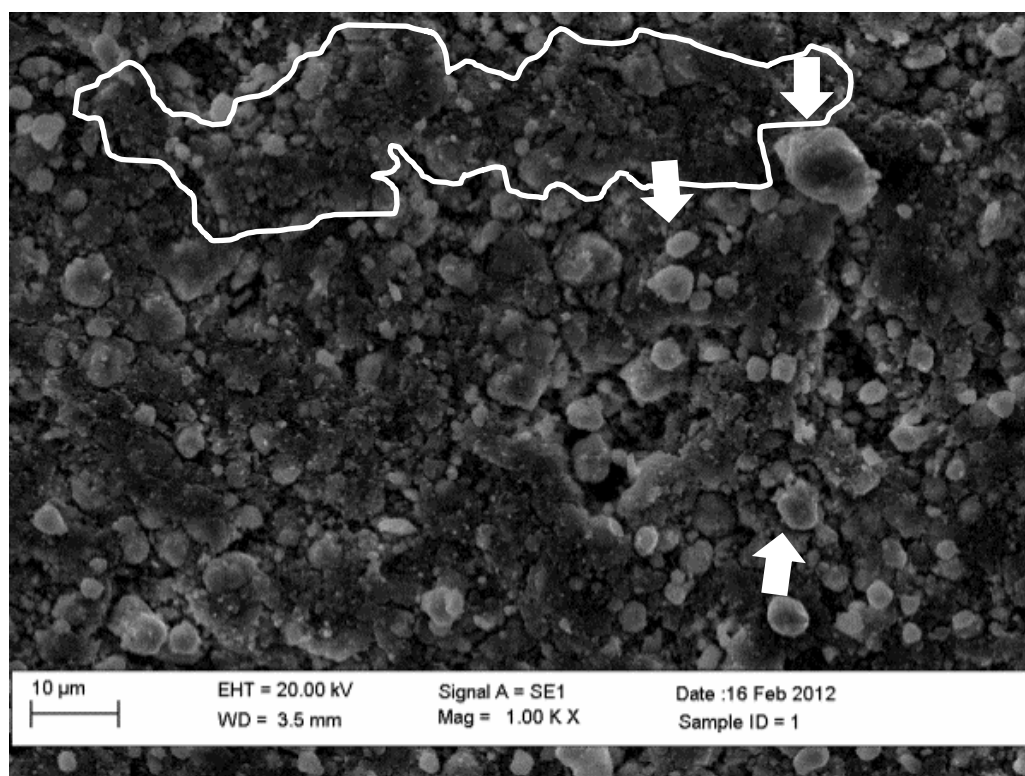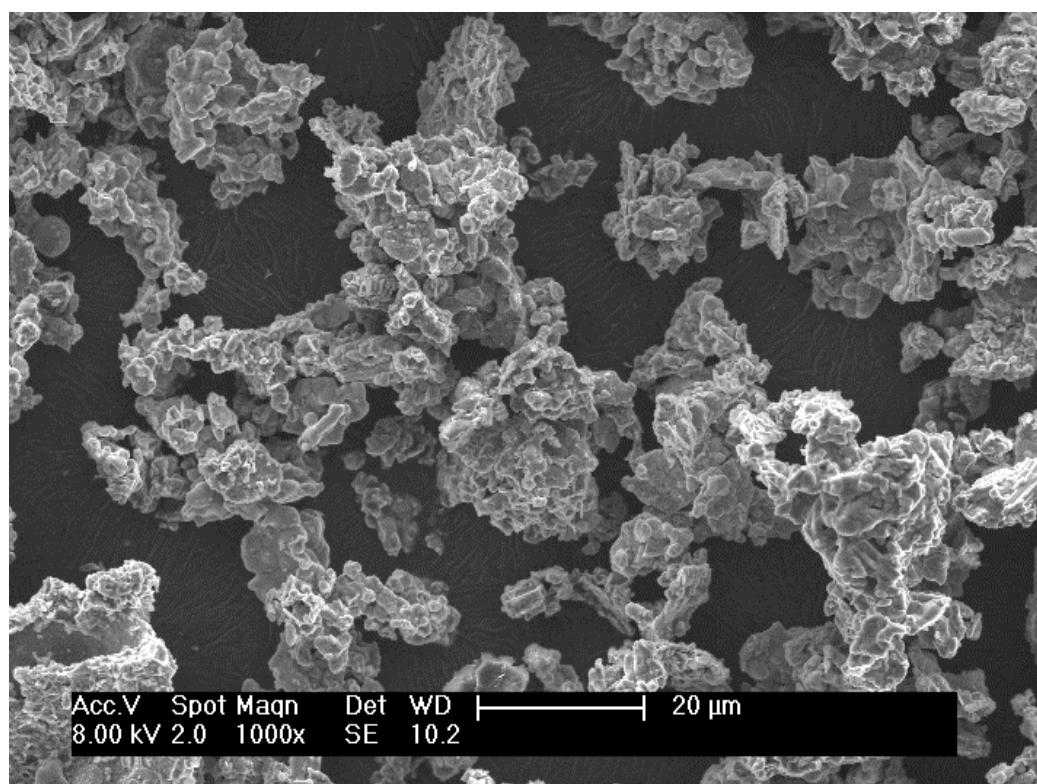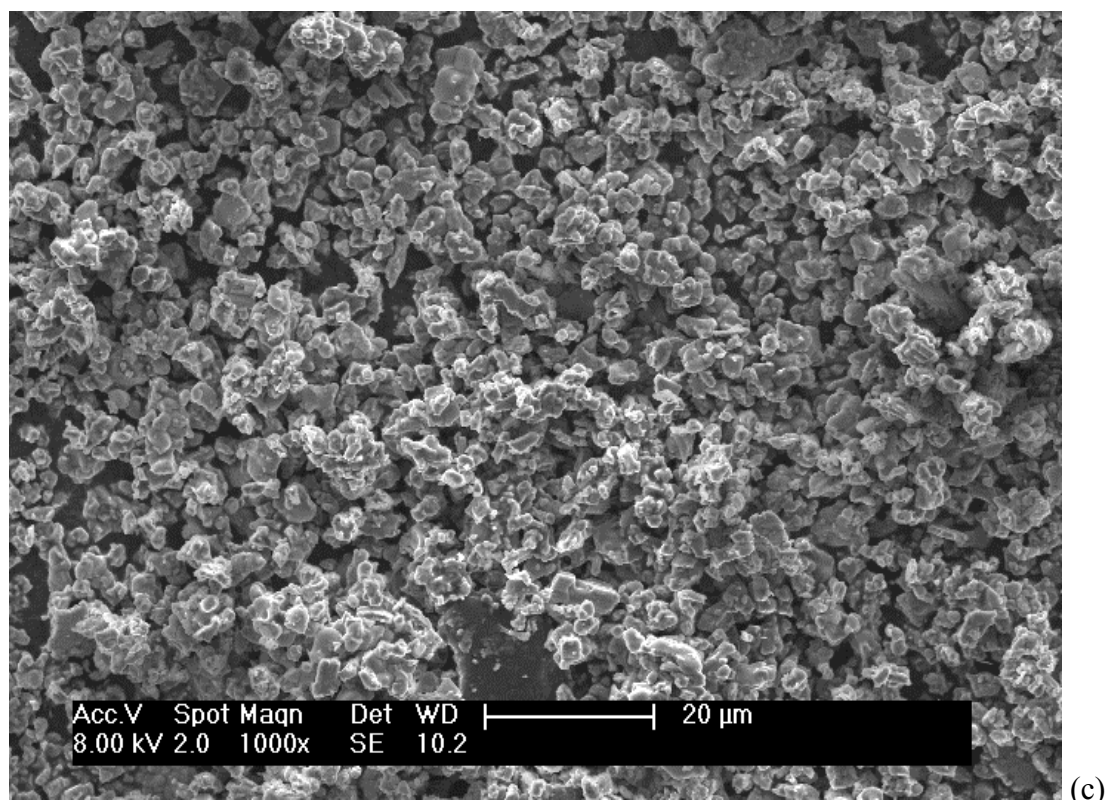
Figure 47. The SE image of (a) CP-BSCF with arrows indicating isolated particles and large agglomerate outlined, (b) CP-850°C4hrC-BSCF and (c) CP-850°C4hrC-24hrM-BSCF.

### 4.1.1.1.3 Discussion and conclusion

After the co-precipitation, the $Ba_{0.5}Sr_{0.5}CO_3$ phase was formed by the reaction between the alkaline earth metal nitrates and the sodium carbonate. According to the study of another worker [18], the cobalt and iron cations may not be fully crystallised at this stage, suggesting they are XRD amorphous. This may be the reason why no phases containing cobalt or iron were identified. Peak overlapping (the carbonate peaks overlap other phases containing Co/Fe: FeOOH, (Fe,Co)O(OH), $Co_3O_4$, $Fe_3O_4$ etc.) may also account for this. Theoretically, Co and Fe cations can be precipitated by sodium carbonate to form cobalt carbonate and iron carbonate [18]. Such carbonates can convert to Co/Fe hydroxides because they react with the $OH^-$ in the sodium carbonate solution [18]. Oxidation can happen to cobalt hydroxides to form cobalt oxyhydroxides [18]. The valence state of cobalt is thus increased from 2+ to 3+ [18]. The hydroxides can be changed to oxyhydroxides or oxides, during the 100 °C overnight drying [18].

After the calcination, the alkaline earth metal carbonates were partially decomposed. The

138

carbonate phase reacted with the Co/Fe oxides and oxyhydroxides [18] to produce the BSCF phase and the $Ba_{0.5}Sr_{0.5}CoO_3$ phase.

After sintering, the carbonate phase and the $Ba_{0.5}Sr_{0.5}CoO_3$ phase were fully decomposed and the cubic perovskite BSCF5582 phase was obtained, demonstrating the synthesis was successful.

In conclusion, dense BSCF pellet with cubic perovskite structure can be produced according to this synthesis route.

4.1.1.2 The characterisation of sintered pellet

4.1.1.2.1 Density measurement

The relative density of 1100℃S-BSCF, 1100℃S24hr-BSCF and 1125℃S-BSCF are shown in Table 28. 1100℃S-BSCF has the highest density, suggesting 1100 ℃ 10 hr is the optimised sintering condition.

Table 28 Relative density of sample 1100℃S-BSCF, 1100℃S24hr-BSCF and 1125℃S-BSCF

| Sample | Density |
|---|---|
| 1100℃S-BSCF | 93.4 ± 0.8 % |
| 1100℃S24hr-BSCF | 91.1 ± 0.3 % |
| 1125℃S-BSCF | 90.6 ± 0.4 % |

1100℃S-BSCF shows open porosity of 1.9 ± 0.4 % and closed porosity of 5.4 ± 1.3 %. The low proportion of open (surface connected) porosity means the ceramic is sufficiently dense for membrane applications.

4.1.1.2.2 XRD analysis

Figure 48 shows a XRD pattern of 1100℃S-BSCF. All the red peaks can be ascribed to the $Ba_{0.5}Sr_{0.5}Co_{0.8}Fe_{0.2}O_{3-\delta}$ phase (ICSD: 00-055-0563). There is no secondary phase identified although the peaks indicated by "V" are not known due to low intensity. The low intensity suggests a less than 3% concentration which is the detection limit. The reasonable phase purity suggests the synthesis of BSCF is successful.
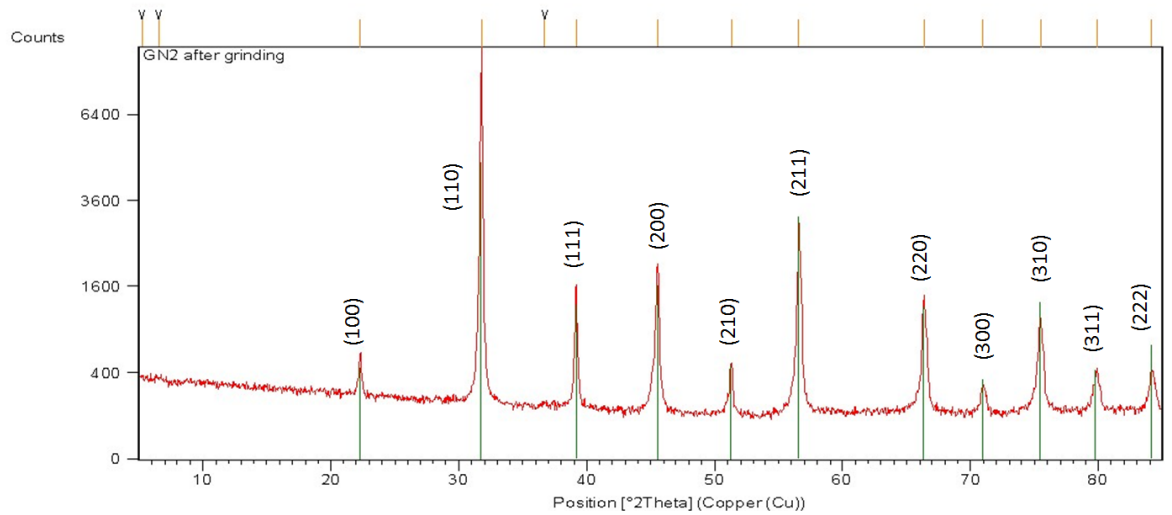
Figure 48. The indexed XRD pattern of 1100°CS-BSCF after grinding over 5 - 85° 2θ range. The green sticks indicate peaks of the $Ba_{0.5}Sr_{0.5}Co_{0.8}Fe_{0.2}O_{3-\delta}$ phase.

### 4.1.1.2.3 SEM investigation

Figure 49 shows a BSE image of the surface of a BSCF pellet. The grains are equiaxed: pores are distributed both at grain boundaries and within grains. The grain size was found to be $33 \pm 16$ μm using the linear intercept method [188]. The porosity measured from the image is $7.9 \% \pm 0.1 \%$ agreeing to that measured by the Archimedes immersion method [183].
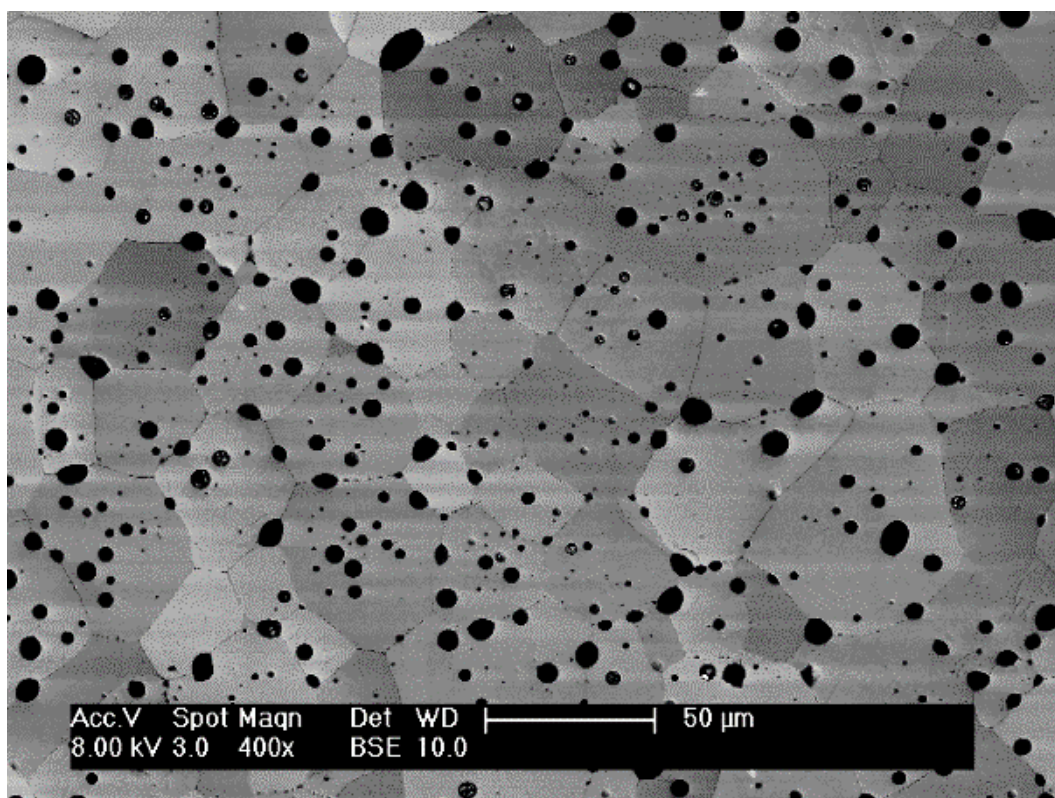
Figure 49. A BSE image shows orientation contrast of a BSCF pellet surface.

### 4.1.1.3 Additional calcination

The phases matched by the powder diffraction file of the $Ba_{0.5}Sr_{0.5}CoO_3$ phase and the $Ba_{0.5}Sr_{0.5}CO_3$ phase have to be removed from CP-850°C4hrC-BSCF to enhance phase purity. Additional calcinations were performed to discover a treatment for this purpose.

### 4.1.1.3.1 XRD characterisation

Figure 50 (a) shows an XRD pattern of a BSCF pellet. All the peaks were matched by the powder diffraction file of the cubic perovskite $Ba_{0.5}Sr_{0.5}Co_{0.8}Fe_{0.2}O_{3-\delta}$ (ICSD: 00-055-0563) phase, labelled by 'B'.

Figure 50 (b) shows an XRD pattern of CP-850°C4hrC-BSCF. Green indicators indicate peaks of the $Ba_{0.5}Sr_{0.5}CoO_3$ (ICSD: 04-007-0067) phase, labelled by 'BSCO'. Blue indicators indicate peaks of the $Ba_{0.5}Sr_{0.5}CO_3$ phase (ICSD: 04-014-5883), labelled by 'CA'. Black indicators indicate peaks of BSCF, labelled by 'B'. The unknown peaks were labelled by 'U'.

Figure 50 (c) shows an XRD pattern of CP-850°C4hrC-930°C4.5hrC-BSCF with peak

positions for a $Ba_{0.5}Sr_{0.5}Co_{0.8}Fe_{0.2}O_{3-\delta}$ phase labelled by 'B', a $Ba_{0.5}Sr_{0.5}CO_3$ phase labelled by 'CA', a $Ba_{0.3}Sr_{0.7}CoO_3$ phase (ICSD: 04-016-5546) labelled by 'BSCO37' and unidentified phases labelled by 'U'. Hence the $Ba_{0.5}Sr_{0.5}Co_{0.8}Fe_{0.2}O_{3-\delta}$ phase, $Ba_{0.5}Sr_{0.5}CO_3$ phase and $Ba_{0.3}Sr_{0.7}CoO_3$ phase were assigned to the fitted peaks. No other phases were identified from the pattern.

Figure 50 (d) shows an XRD pattern of CP-850°C4hrC-930°C4.5hrC-950°C5hrC-BSCF with peak positions for a $Ba_{0.5}Sr_{0.5}Co_{0.8}Fe_{0.2}O_{3-\delta}$ phase labelled by 'B'. Hence the $Ba_{0.5}Sr_{0.5}Co_{0.8}Fe_{0.2}O_{3-\delta}$ phase was assigned to the fitted peaks. No other phases were identified from the pattern.

Figure 50 (e) shows an XRD pattern of the CP-850°C4hrC-950°C5hrC-BSCF sample with peak positions for a $Ba_{0.5}Sr_{0.5}Co_{0.8}Fe_{0.2}O_{3-\delta}$ phase labelled by 'B' and unidentified phases labelled by 'U'. Hence the $Ba_{0.5}Sr_{0.5}Co_{0.8}Fe_{0.2}O_{3-\delta}$ phase was assigned to the fitted peaks. No other phases were identified from the pattern.
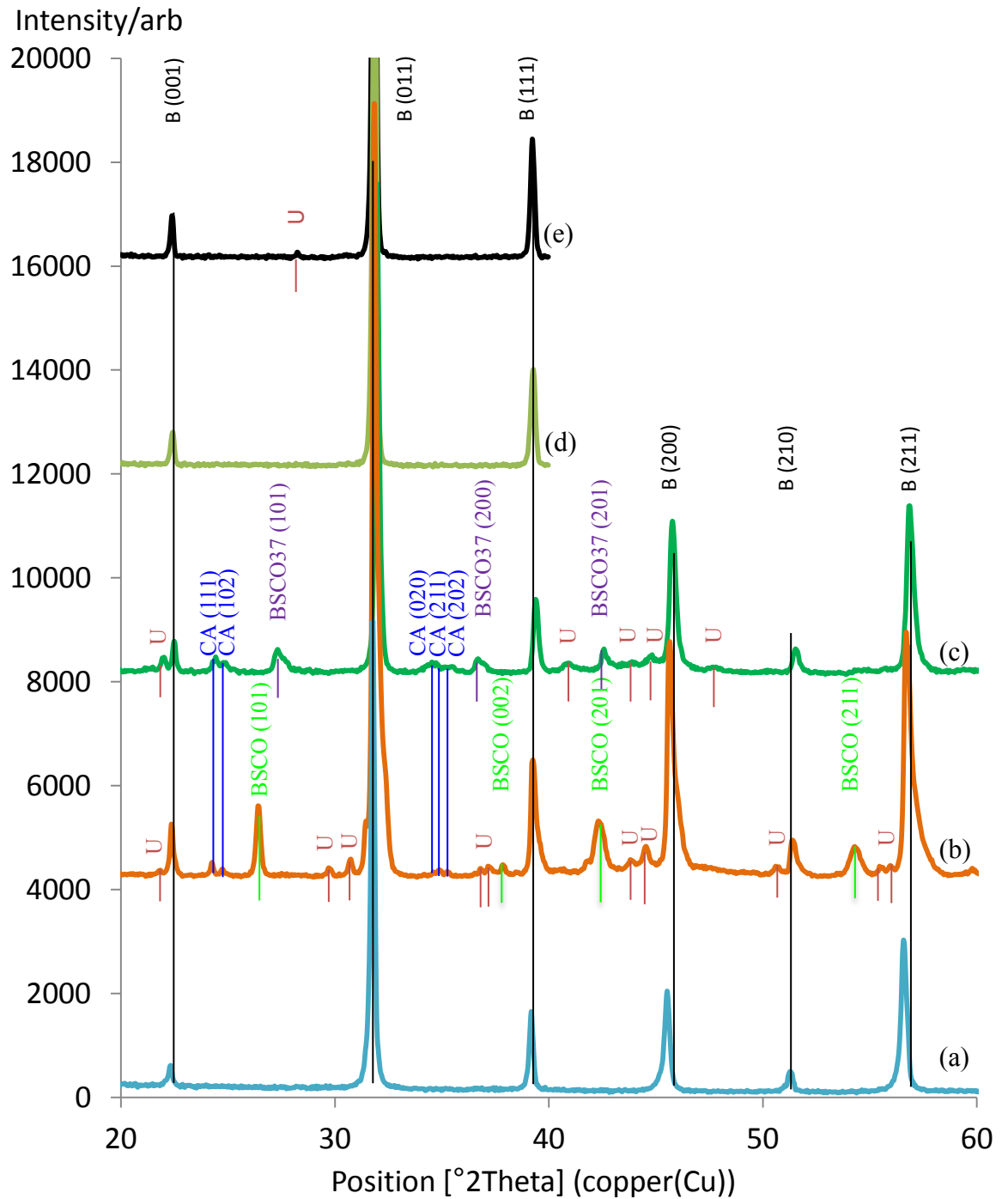
Figure 50. Indexed XRD pattern over 20 - 60º 2θ range of (a) BSCF pellet, (b) CP-850℃ 4hrC-BSCF sample, (c) CP-850℃4hrC-930℃4.5hrC-BSCF sample, (d) CP-850℃4hrC-930℃4.5hrC-950℃5hrC-BSCF sample and (e) CP-850℃4hrC-950℃5hrC-BSCF sample. The $Ba_{0.5}Sr_{0.5}Co_{0.8}Fe_{0.2}O_{3-\delta}$ phase is indicated by 'B' and black indicators. The $Ba_{0.5}Sr_{0.5}CoO_3$ phase is indicated by 'BSCO' and green indicators. The $Ba_{0.5}Sr_{0.5}CO_3$ phase is indicated by 'CA' and blue indicators. The $Ba_{0.3}Sr_{0.7}CoO_3$ is indicated by 'BSCO37' and purple indicators. The unidentified peaks are indicated by 'U' and orange indicators.

### 4.1.1.3.2 Discussions

Table 29 shows the phases identified from the samples and corresponding XRD pattern number. Only CP-850°C4hrC-930°C4.5hrC-950°C5hrC-BSCF shows single cubic BSCF phase, suggesting only the calcination condition of this sample can decompose all the precursor phases, although it consumes more energy and spend more time.

The $Ba_{0.5}Sr_{0.5}CoO_3$ phase is absent in patterns (c, d, e) but present in pattern (b), which agrees to the findings of Mueller et al. [143] that this phase is stable at temperatures between 700 °C - 900 °C. The carbonate phases are absent in patterns (d, e) but present in patterns (b, c), which agrees to the findings of Maitra et al. [189] that such phases are stable at temperatures below 950 °C.

Table 29 Summary of the identified phases in BSCF pellet, CP-850°C4hrC-BSCF, CP-850°C4hrC-930°C4.5hrC-BSCF, CP-850°C4hrC-930°C4.5hrC-950°C5hrC-BSCF and CP-850°C4hrC-950°C5hrC-BSCF

| XRD pattern | Sample | Phases identified |
|---|---|---|
| (a) | BSCF pellet | $Ba_{0.5}Sr_{0.5}Co_{0.8}Fe_{0.2}O_{3-\delta}$ |
| (b) | CP-850°C4hrC-BSCF | $Ba_{0.5}Sr_{0.5}CoO_3$<br>$Ba_{0.5}Sr_{0.5}CO_3$<br>$Ba_{0.5}Sr_{0.5}Co_{0.8}Fe_{0.2}O_{3-\delta}$<br>Unknown phase |
| (c) | CP-850°C4hrC-930°C4.5hrC-BSCF | $Ba_{0.5}Sr_{0.5}Co_{0.8}Fe_{0.2}O_{3-\delta}$<br>$Ba_{0.5}Sr_{0.5}CO_3$<br>$Ba_{0.3}Sr_{0.7}CoO_3$<br>Unknown phase |
| (d) | CP-850°C4hrC-930°C4.5hrC-950°C5hrC-BSCF | $Ba_{0.5}Sr_{0.5}Co_{0.8}Fe_{0.2}O_{3-\delta}$ |
| (e) | CP-850°C4hrC-950°C5hrC-BSCF | $Ba_{0.5}Sr_{0.5}Co_{0.8}Fe_{0.2}O_{3-\delta}$<br>Unknown phase |

# 4.1.2 Basic characterisation of SCFT414

### 4.1.2.1 The characterisation of SCFT414 synthesis and coating

#### 4.1.2.1.1 XRD analysis

Figure 51 (a) shows an XRD pattern of the CP-SCFT414. The peaks labelled by 'O' match the powder diffraction file peaks for $SrCO_3$. The rest of the peaks were not identified

(labelled by 'U'). The orthorhombic $SrCO_3$ phase has the space group Pmcn and lattice parameters of a=5.1070 Å, b=8.4140 Å and c=6.0290 Å. The crystallographic information was obtained from the powder diffraction file of $SrCO_3$ (Reference code: 00-005-0418).

Figure 51 (b) shows the XRD pattern of the CP-950°C10hrC-SCFT414. The peaks labelled by 'STF' and 'SF' match the powder diffraction file peaks for $SrTi_{0.2}Fe_{0.8}O_{2.6}$ and $Sr_2FeO_{4-x}$, respectively. The rest of the peaks were not identified (labelled by 'U'). The cubic $SrTi_{0.2}Fe_{0.8}O_{2.6}$ phase has the space group Pm-3m and a lattice parameter of a=3.885 Å. The tetragonal $Sr_2FeO_{4-x}$ phase has the lattice parameters of a=b=3.8680 Å and c=12.4100 Å. The crystallographic information was obtained from the powder diffraction file of $SrTi_{0.2}Fe_{0.8}O_{2.6}$ (Reference code: 04-013-9876) and $Sr_2FeO_{4-x}$ (Reference code: 00-022-1428).

Figure 51 (c) shows the XRD pattern of the SCFT coated BSCF. The peaks labelled by 'B' match the powder diffraction file peaks for cubic perovskite BSCF. The cubic perovskite BSCF phase has the space group Pm-3m and a lattice parameter of 3.983 Å. The crystallographic information was obtained from the powder diffraction file of BSCF (Reference code: 00-055-0563). No other phases were observed in this pattern, suggesting the precursor phases were decomposed.

Figure 52 shows the XRD pattern of the SCFT414 pellet sintered at 1165°C. All peaks match the powder diffraction file peaks for a $SrTi_{0.2}Fe_{0.8}O_{2.6}$. The cubic $SrTi_{0.2}Fe_{0.8}O_{2.6}$ phase has the space group Pm-3m and a lattice parameter of a=3.885 Å. The crystallographic information was obtained from the powder diffraction file of $SrTi_{0.2}Fe_{0.8}O_{2.6}$ (Reference code: 04-013-9876). No other phases were observed in this pattern and the lattice parameter (3.885 Å) is close to 3.90 Å obtained from a previous study of SCFT414 [171], suggesting SCFT414 may be obtained and the synthesis may be successful in terms of crystal structure, space group, lattice parameter and phase purity.
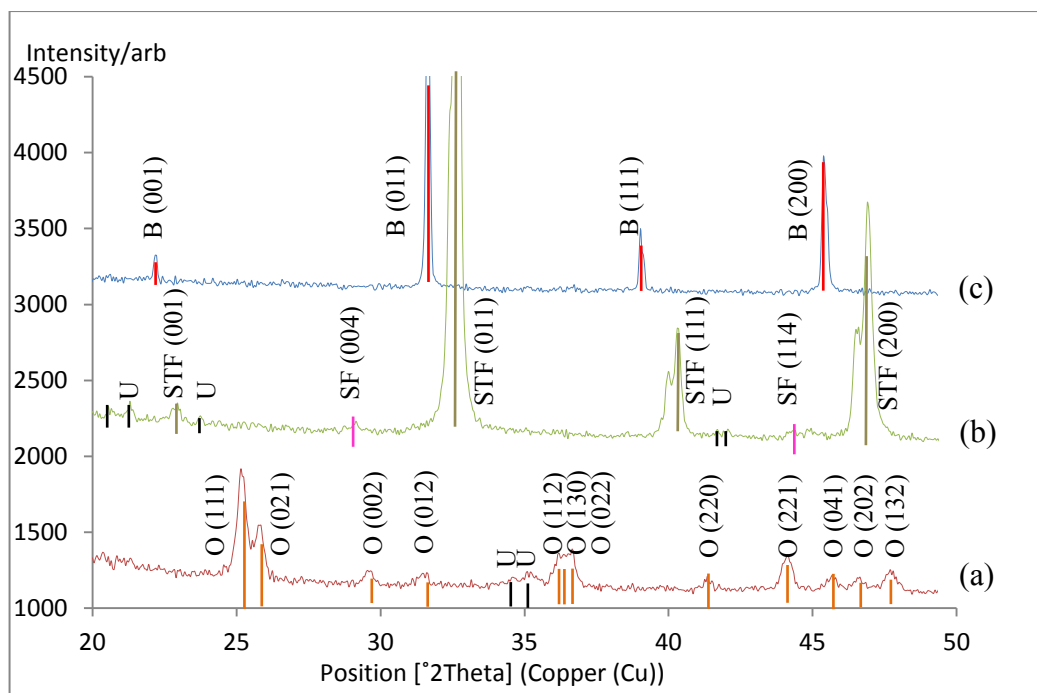
Figure 51. The indexed XRD pattern of (a) CP-SCFT414, (b) CP-950°C10hrC-SCFT414 and (c) SCFT coated BSCF with peak indicators. O: $SrCO_3$, STF: $SrTi_{0.2}Fe_{0.8}O_{2.6}$, SF: $Sr_2FeO_{4-x}$, B: BSCF, U: unknown phase.
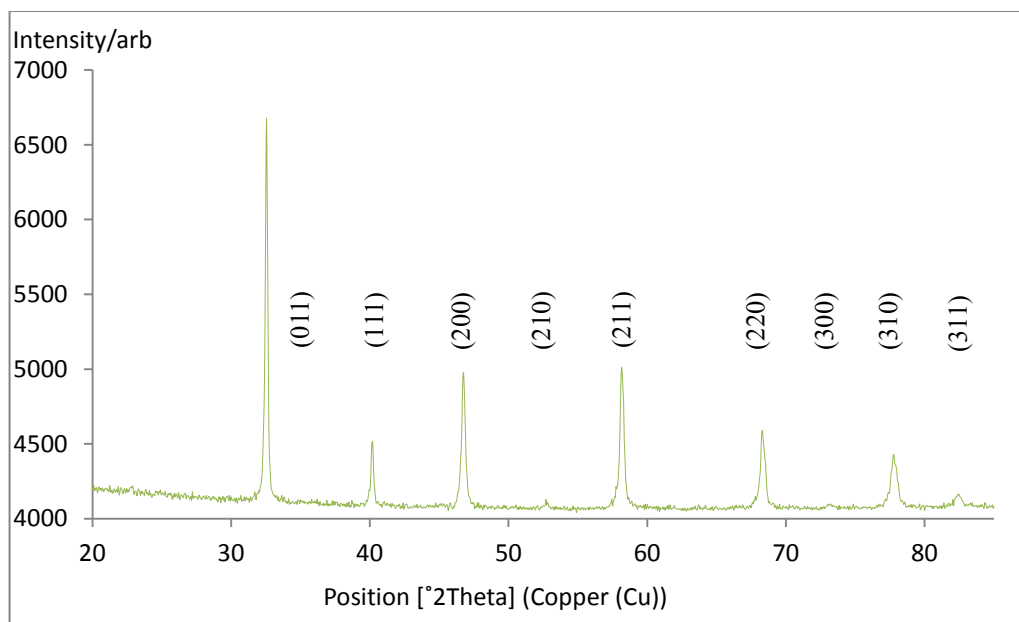


Figure 52. The indexed XRD pattern of the SCFT414 pellet sintered at 1165°C.

## 4.1.2.1.2 SEM investigation

Figure 53 shows the microstructure of the CP-SCFT414 sample. Agglomerates with an average radius of $0.99 \pm 0.52$ µm are seen. One agglomerate is outlined in the figure.
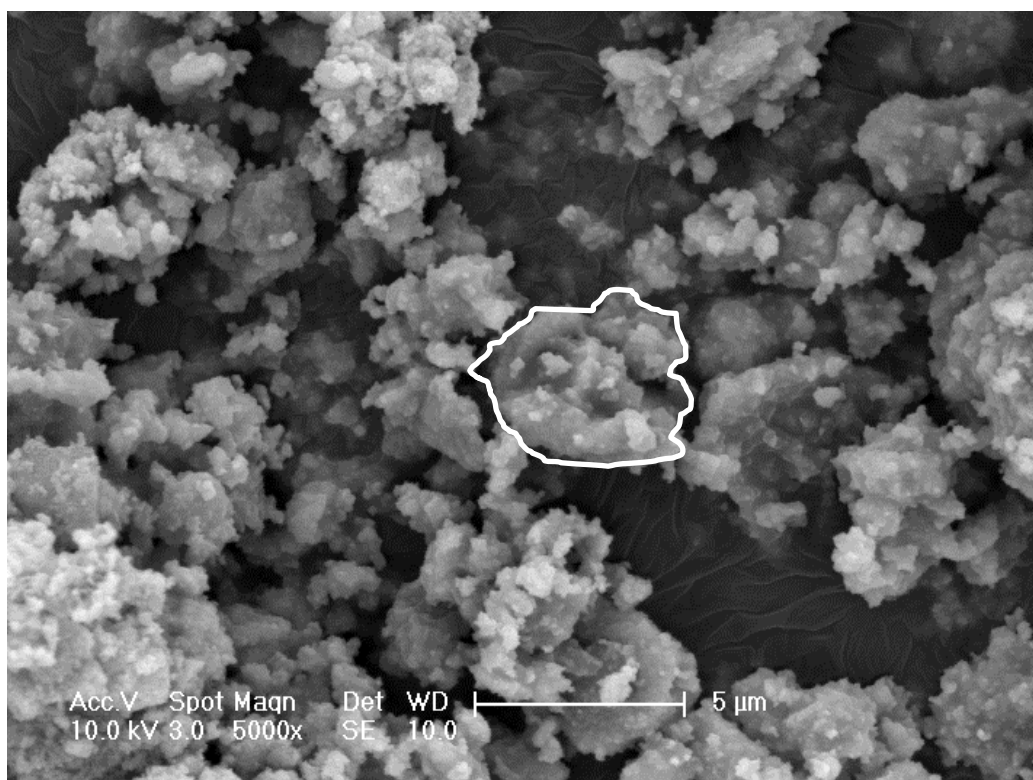
Figure 53. SE image shows the microstructure of the CP-SCFT414 with agglomerate outlined.

Figure 54 shows the microstructure of the CP-950°C10hrC-SCFT414. No cracks are seen in Figure 54 (a), suggesting the calcination did not induce defects which may cause inhomogeneous pressing leading to the extensive cracking of the sintered pellets. The average agglomerate radius ($0.50 \pm 0.80$ µm) was measured from Figure 54 (b).
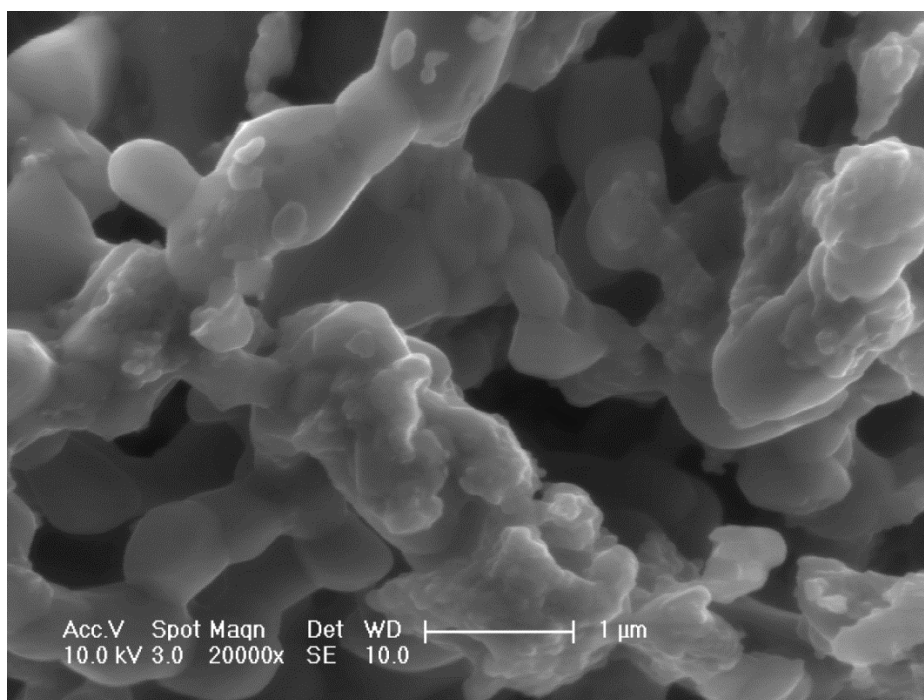
(a)
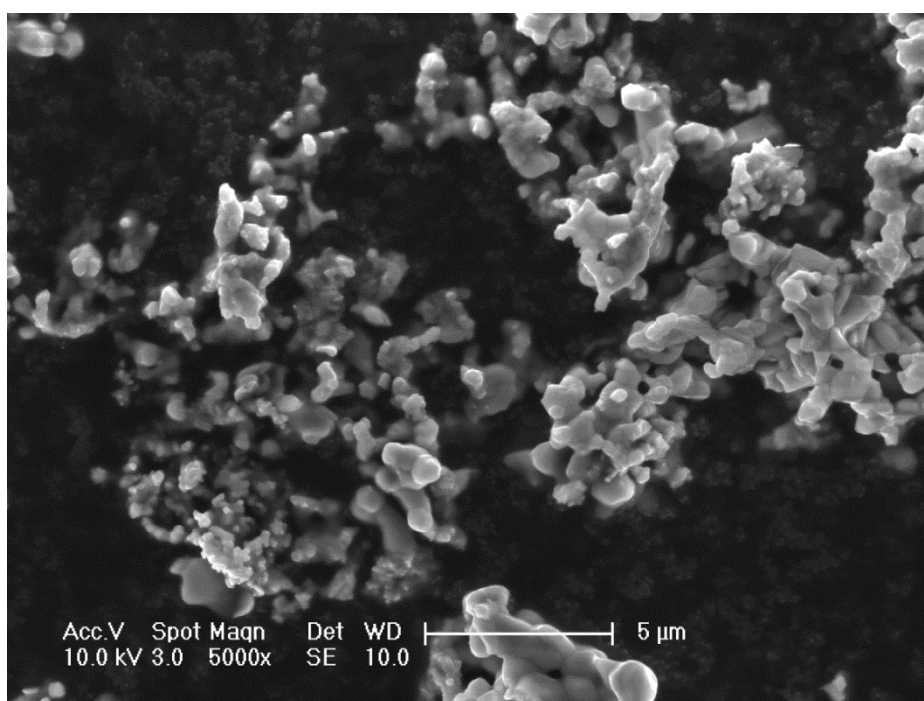


(b)

Figure 54. (a – b) SE images show the microstructure of the CP-950°C10hrC-SCFT414.

Figure 55 shows the microstructure of the CP-950°C10hrC-48hrM-SCFT414. The average radius of the agglomerates is $0.41 \pm 0.40$ µm. Both the average radius and SD were reduced by milling. The reduction in SD suggests a more uniform particle size which allows homogeneous pressing to reduce fractures in green pellets.
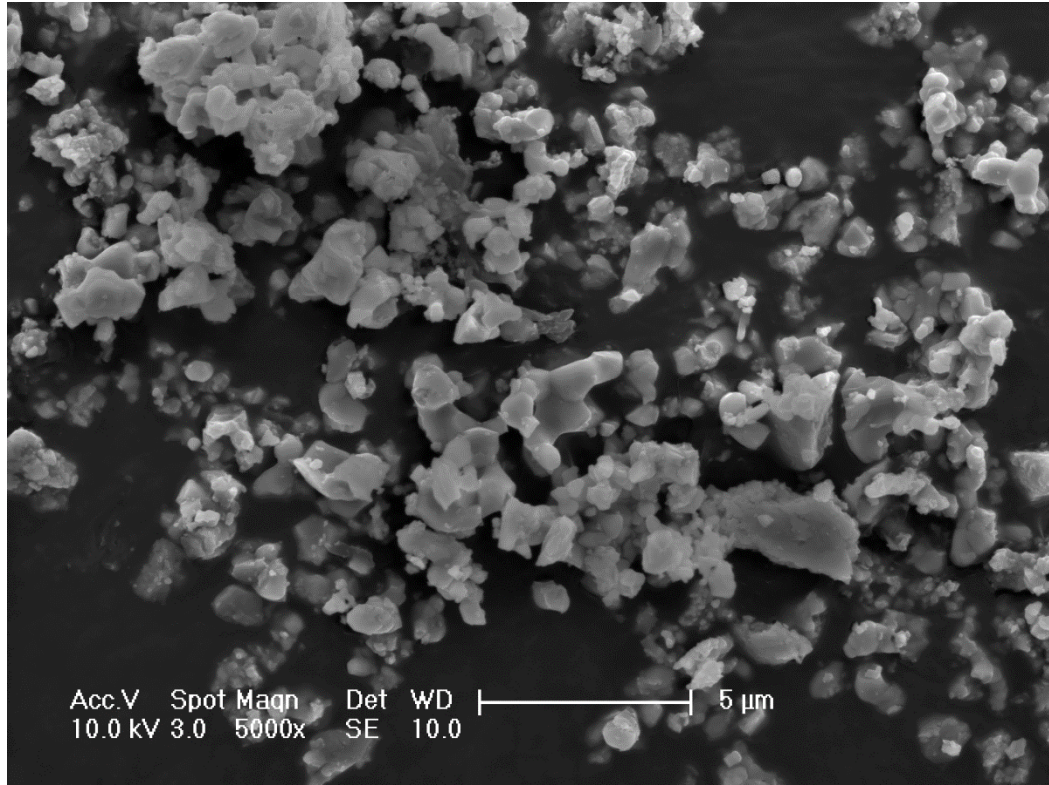


Figure 55. SE image shows the microstructure of the CP-950°C10hrC-48hrM-SCFT414.

Figure 56 shows the microstructure of the SCFT coated BSCF pellet. The pellet was not ground or polished to keep the coating layer entire. The grains are equiaxed: pores are distributed both at grain boundaries and within grains. The grain size was found to be $65 \pm 9$ µm using the linear intercept method [188]. The open porosity measured from the image is $1.6 \pm 1$ %. The low proportion of open (surface connected) porosity means the ceramic is sufficiently dense for membrane applications.
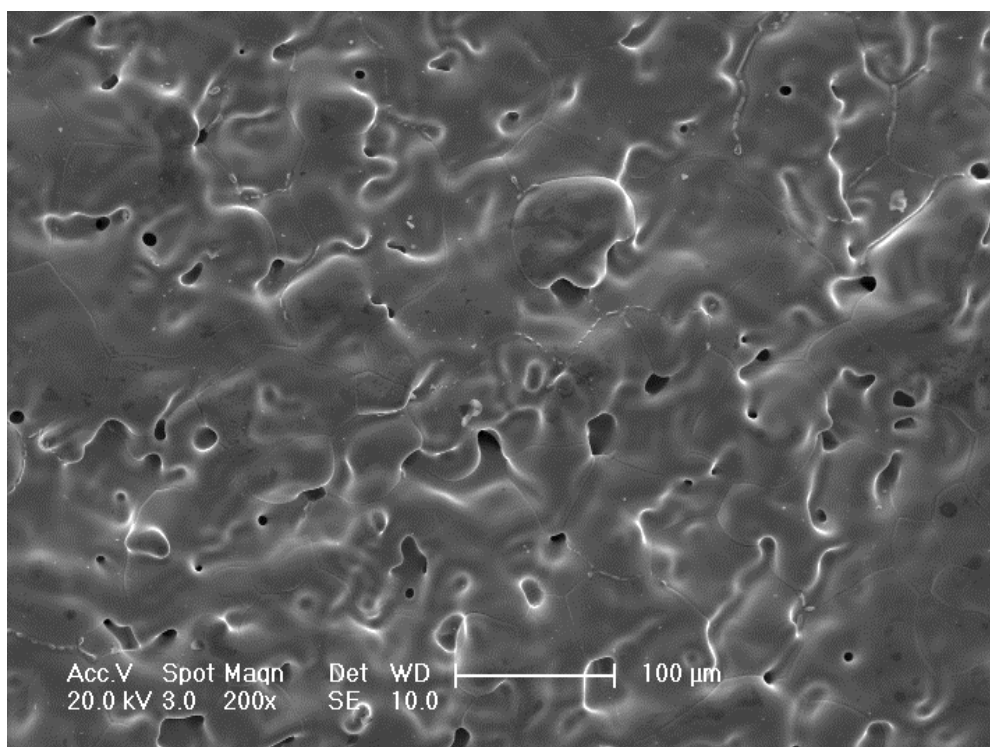
Figure 56. SE image shows the microstructure of the SCFT coated BSCF pellet.

4.1.2.2 Discussion

The composition of the phases is not clear at this stage. The phases are temporarily denoted as the corresponding peak labels. The composition will be studied in the future.

# 4.2 The $CO_2$ decomposition study

## 4.2.1 Surface preparation

### 4.2.1.1 Surface preparation

Colloidal silica, which is also known as OPS, is often used in the final polishing (after diamond polishing) to reveal orientation contrast under SEM in backscattered electron imaging mode (BS). It removes scratches and damages from a sample surface to create a flat surface [190]. This may be how OPS reveals the orientation contrast. Backscattered electrons travel in straight lines [182]. Hence they cannot reach the detector when they are scattered to a direction leading to a destination that is not the detector [182]. An uneven surface can scatter backscattered electrons in all directions to prevent a portion of them from arriving at the detector hence to reduce the orientation contrast [182].

However, OPS was suspected to damage the grain boundaries because it is an acidic suspension (pH = 3 − 3.5) [191] and acid is often used to etch grain boundaries [192]. Grain boundaries have higher interfacial energy than grains and the bonding in grain boundaries is relatively weaker than those in grains hence grain boundaries often become preferred sites of heterogeneous nucleation (precipitation) [193]. The damaged grain boundaries might have higher interfacial energy and lower bonding strength than undamaged grain boundaries hence the damaged boundaries might have more chance to become preferred sites of precipitation during annealing runs. The research in this section was conducted to address this issue.

4.2.1.2 Surface characterisation

The microstructure of the OPS-C-900℃-30min and C-900℃-30min are shown in Figure 57 and Figure 58, respectively. Both show porosity, and surface precipitates (four of them are outlined in red) formed during the annealing. There are significantly more rows of precipitates following grain boundaries in Figure 57 (five of them are indicated by a red arrow) than in Figure 58, suggesting the grain boundaries become preferred sites of precipitation after an OPS polish. Hence OPS polishing was not used for the annealing experiment samples.
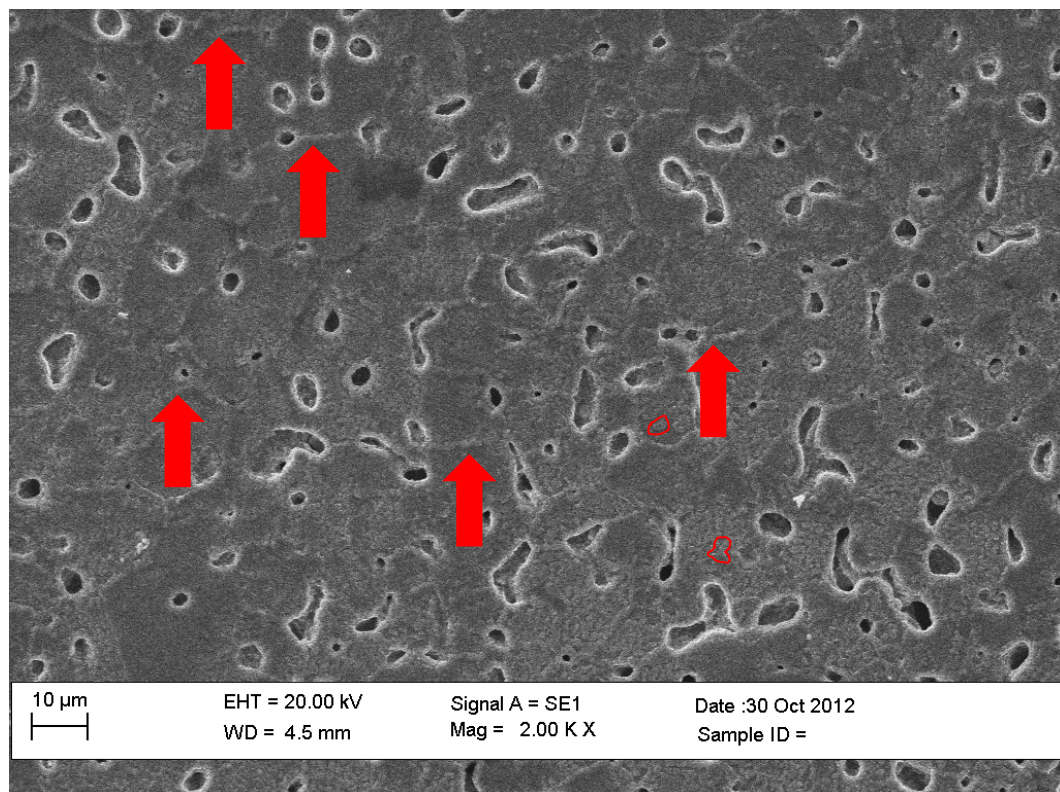


Figure 57. SE image of the OPS-C-900℃-30min sample with arrows indicating precipitates on grain boundaries and circles indicating precipitates on grains.
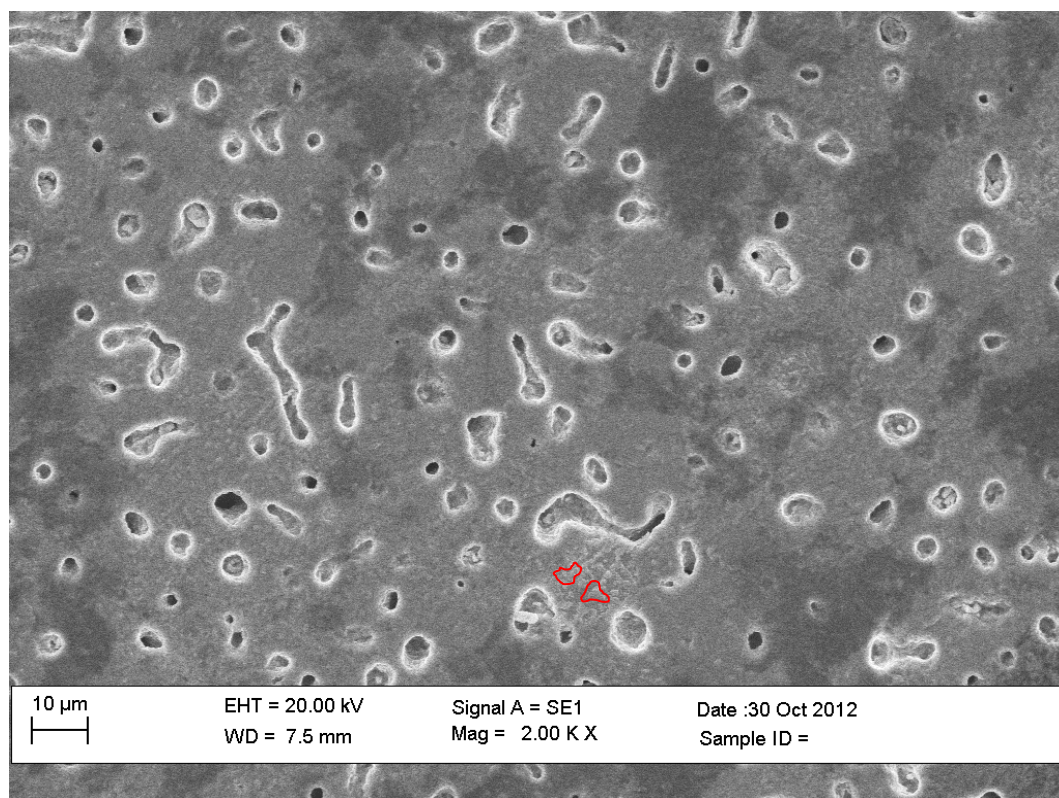
Figure 58. SE image of the C-900℃-30min sample with circles indicating precipitates on grains.

## 4.2.2 The phase identification after decomposition

### 4.2.2.1 Results

Figure 59 shows XRD patterns of C-800℃-1min, C-800℃-2min, C-800℃-5min, C-800℃-15min and C-800℃-30min. In the patterns, the peaks labelled by 'B', 'S' and 'C' match the powder diffraction file peaks for BSCF, $SrCO_3$ and CoO, respectively. The labelled peaks were indexed according to the matched phases. The rest of the peaks were not identified (labelled by 'U'). The cubic perovskite BSCF phase has the space group Pm-3m and a lattice parameter of $3.9782 \pm 0.0002$ Å refined by TOPAS. The rhombohedral $SrCO_3$ phase has the space group R-3mH and lattice parameters of a=b=$5.1397 \pm 0.0070$ Å, c=$9.4847 \pm 0.0177$ Å refined by TOPAS. The cubic CoO phase has the space group Fm-3m and a lattice parameter of $4.2490 \pm 0.0045$ Å refined by TOPAS. The crystallographic information was obtained from the powder diffraction files of BSCF (ICSD: 109462), $SrCO_3$ (ICSD: 27445) and CoO (ICSD: 9865).
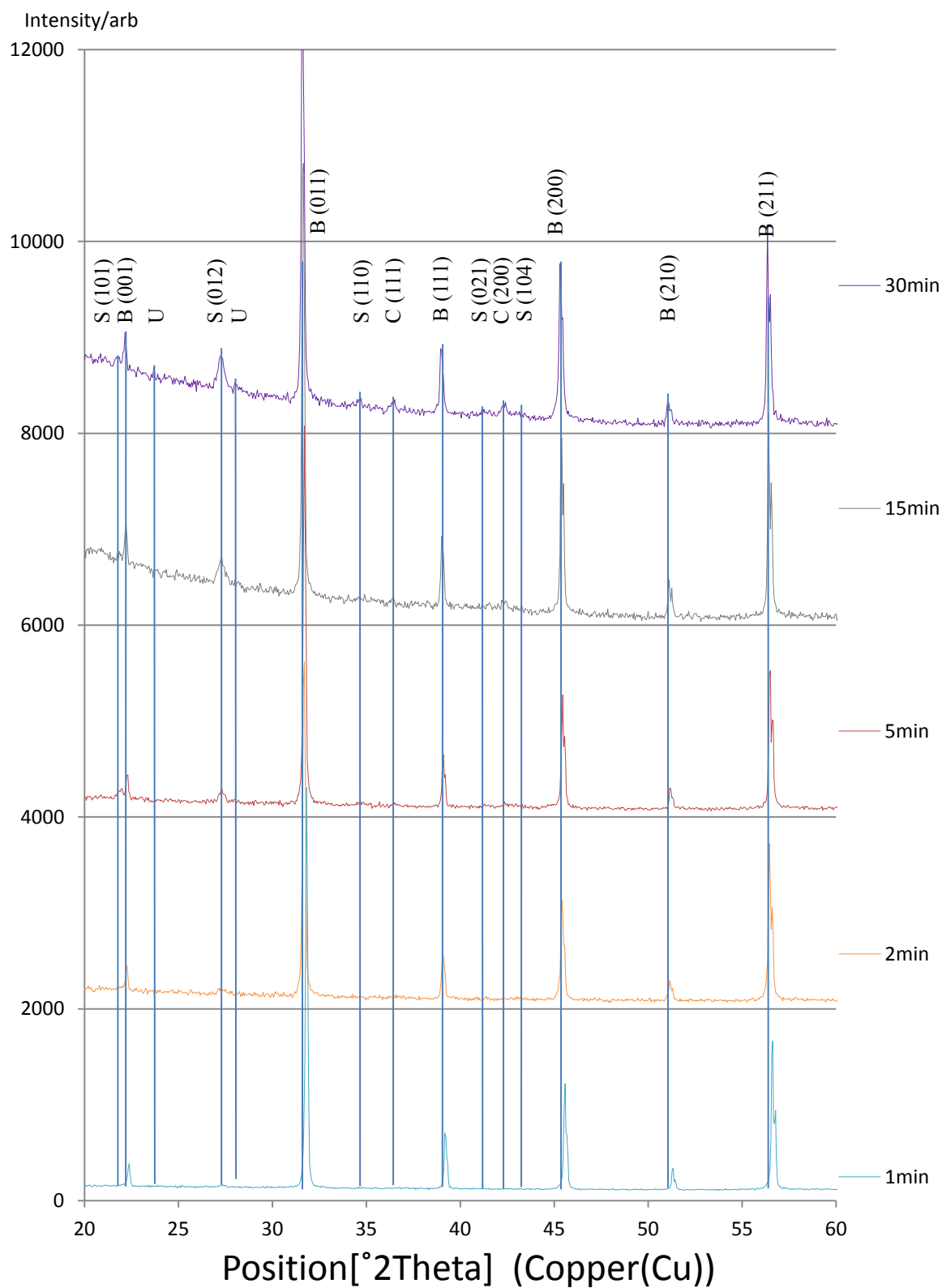
Figure 59. Indexed XRD patterns with peak indicators over 20 - 60º 2θ range of the C-800℃-1min sample, C-800℃-2min sample, C-800℃-5min sample, C-800℃-15min sample and C-800℃-30min sample. B indicates BSCF. S indicates $SrCO_3$. C indicates CoO. U indicates unknown peaks.

The Wt% with corresponding error of the SrCO$_3$ phase and CoO phase were determined on TOPAS from the XRD patterns and are plotted as a function of the annealing time in Figure 60 (a) and (b), respectively. Both data series were fitted by a logarithmic curve to show and predict the behaviour.
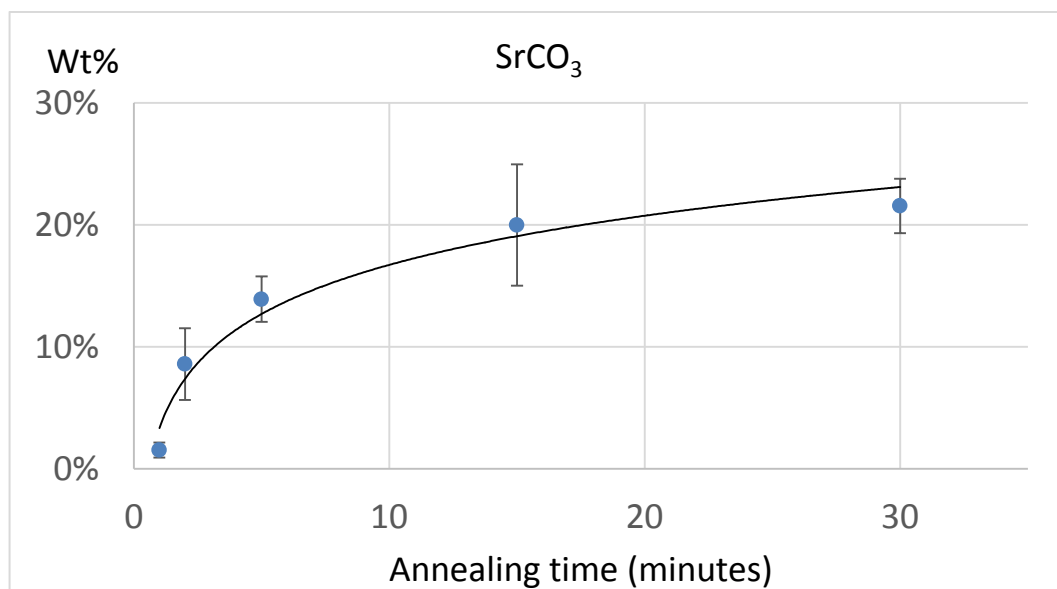


(a)
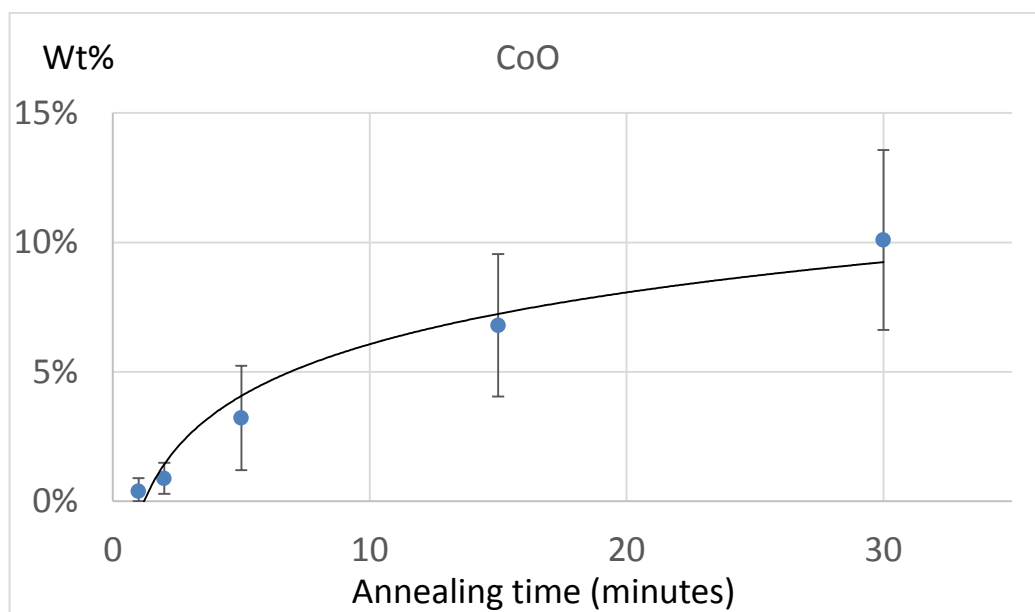


(b)

Figure 60. Wt% of (a) SrCO$_3$ and (b) CoO plotted as a function of time. The logarithmic curves fit the data series.

Figure 61 shows XRD patterns of the C-900℃-15min, C-950℃-15min and C-950℃-30min sample. In the patterns, the peaks labelled by 'B', 'S' and 'C' match the powder diffraction file peaks in BSCF, $SrCO_3$ and CoO, respectively. The rest of the peaks were not identified (labelled by 'U'). The phase assemblage is the same as that of the C-800℃-1min sample, C-800℃-2min sample, C-800℃-5min sample, C-800℃-15min sample and C-800℃-30min sample, suggesting higher temperatures did not introduce new secondary phases or decompose existing secondary phases. The structure, lattice parameter and space group of the secondary phases are the same as those of the secondary phases in the C-800℃-1min sample, C-800℃-2min sample, C-800℃-5min sample, C-800℃-15min sample and C-800℃-30min sample, suggesting higher temperatures do not change the crystallographic features of the secondary phases.
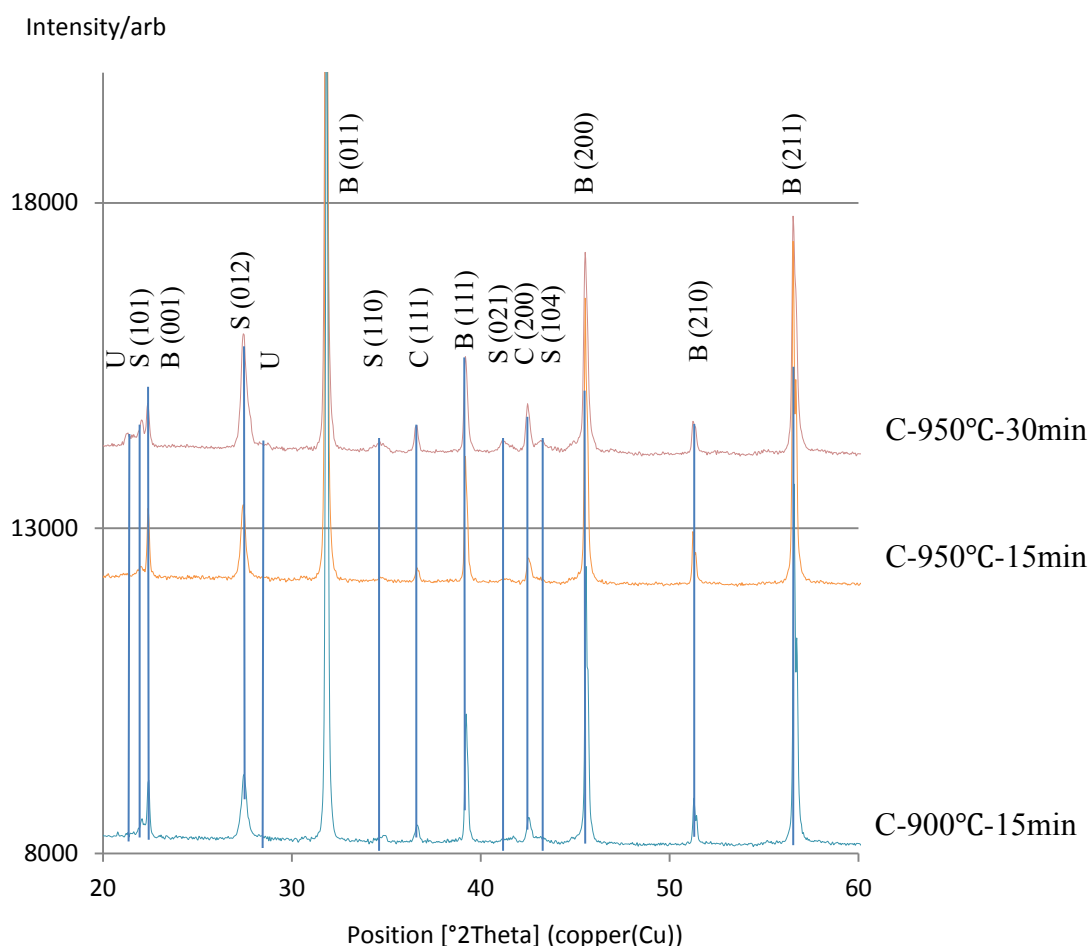


Figure 61. Indexed XRD pattern with peak indicators over 20 - 60º 2θ range of the C-900℃-15min, C-950℃-15min and C-950℃-30min sample. B: BSCF, S: $SrCO_3$ and C: CoO. U indicates unknown peaks.

## 4.2.2.2 Discussion

### 4.2.2.2.1 The composition of the secondary phases

The composition of the secondary phases is not clear at this stage. The secondary phases are temporarily denoted as the $SrCO_3$ phase and the $CoO$ phase. The real composition will be studied and the secondary phase names will be updated.

### 4.2.2.2.2 The structure of the secondary phases

The rhombohedral structure of the $SrCO_3$ in this study is different from the orthorhombic structure of the $(Ba, Sr)CO_3$ phases reported in previous studies [16, 17]. Other workers have noted that the inclusion of Co or Fe in the $(Ba, Sr)CO_3$ phase transformed the orthorhombic structure to the rhombohedral structure because the average cation radius was reduced [194]. Hence the rhombohedral carbonate phase in this study might be caused by the inclusion of Co and Fe. Another study suggested that the orthorhombic $BaCO_3$ and $SrCO_3$ were transformed to rhombohedral $BaCO_3$ and $SrCO_3$ at 810 ℃ and 950 ℃, respectively [195]. Hence the rhombohedral carbonate phase in this study may be caused by the annealing temperature. The structure and lattice parameter of the $CoO$ is the same as those observed in previous studies [16, 17].

### 4.2.2.2.3 The pattern noise effects

In Figure 59, the peaks of both secondary phases can be clearly seen in the 5 min, 15 min and 30 min patterns. However, for the 2 min and 1 min patterns, only the (012) $SrCO_3$ peak can be clearly seen. The reason is that the signal to noise ratio of those unclear peaks is low due to the relatively low amount. The ratio may be improved by an extended collection time.

The error bars in Figure 60 were mainly caused by the noise of the XRD patterns.

### 4.2.2.2.4 The exposure of BSCF to X-ray

For Figure 60, the X-ray penetration depth varies between 3 μm to 20 μm which is thicker than the carbonate layer. Hence the carbonate coverage does not affect the exposure of BSCF to X-rays.

## 4.2.3 Surface microstructural changes

Figure 62 (a) shows a SE image of the surface of a BSCF pellet. Figure 62 (b-f) show SE images of the surface of the C-800℃-1min, C-800℃-2min, C-800℃-5min, C-800℃-15min and C-800℃-30min samples, respectively. For (b-d), the grain and grain boundary regions are covered by secondary phase precipitates (some of them are indicated by white arrows). The grain boundaries are clearly differentiated and the precipitate morphology appears similar within each grain although there are differences in appearance between grains. For (e-f), the precipitates form a continuous layer. The pores are not taken into account because they cannot be polished.
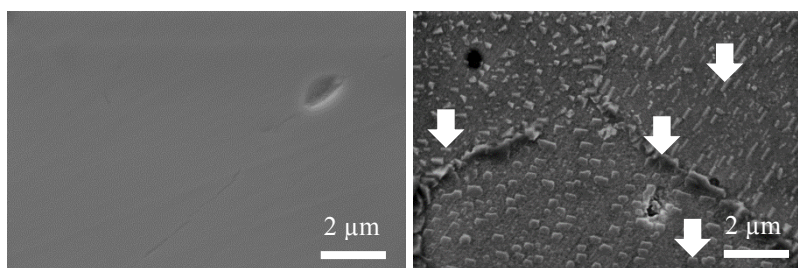


(a)



(b)
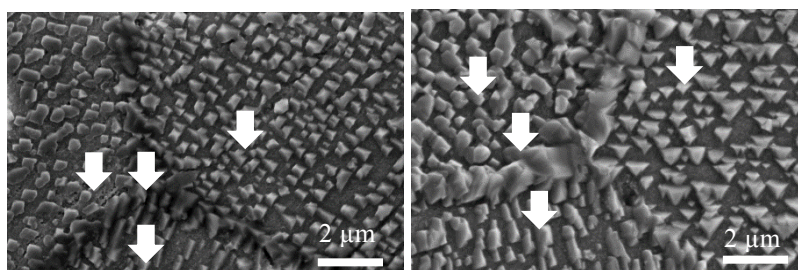


(c)



(d)
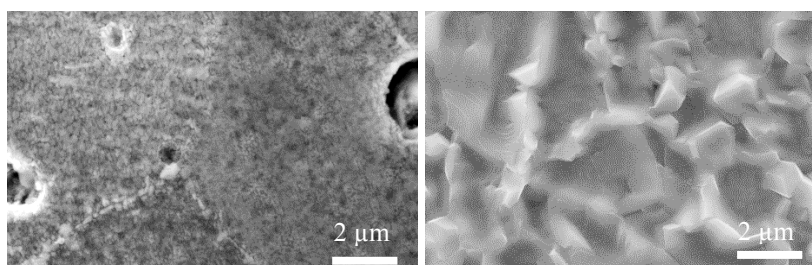


(e)



(f)

Figure 62. (a) SE image of the surface of a BSCF pellet. (b-f) SE images of the surface of the C-800℃-1min, C-800℃-2min, C-800℃-5min, C-800℃-15min and C-800℃-30min sample, respectively. The arrows indicate precipitates.

## 4.2.4 Phase distribution of surface

### 4.2.4.1 Results

Figure 63 (a-c) show EBSD patterns collected from the C-800℃-1min sample. The 'B', 'S' and 'C' phase identified by XRD were assigned to pattern (a), (b) and (c), respectively, after matching theoretical patterns of the 3 phases with each experimental pattern. The pattern (a), (b) and (c) were indexed according to structure and shown as (d), (e) and (f), respectively. The patterns are clear and indexed, suggesting the precipitate causing uneven surface is not an issue in obtaining patterns. Hence EBSD study can be applied on this sample.

A series of EBSD patterns were collected from various points on the sample surface. One of the 3 phases was assigned to each area, after pattern matching. All the areas are indicated by spots, (Figure 64a,b). Figure 64 (a) shows holes due to pores and surface precipitates introduced by the annealing. Figure 64 (b) shows similar with a row of precipitates following a grain boundary. Yellow and blue spots indicate the 'B' and 'S' phase respectively. The 'C' phase is indicated by a green spot.

A number of 'S' phase precipitates can be seen on the BSCF surface. Some of them are seen on the grains. The others are seen on the grain boundaries. The grain boundaries are highlighted by white lines. However, the 'C' phase was observed in only one area. The pattern from the green spot is obscured, as shown in Figure 63 (c), suggesting the CoO precipitates may form below the surface. Therefore, all investigated surface precipitates were ascribed to the 'S' phase, suggesting the surface precipitates are 'S' phase precipitates. In addition, the successful phase ID study of individual points provided a base for phase mapping an entire area.
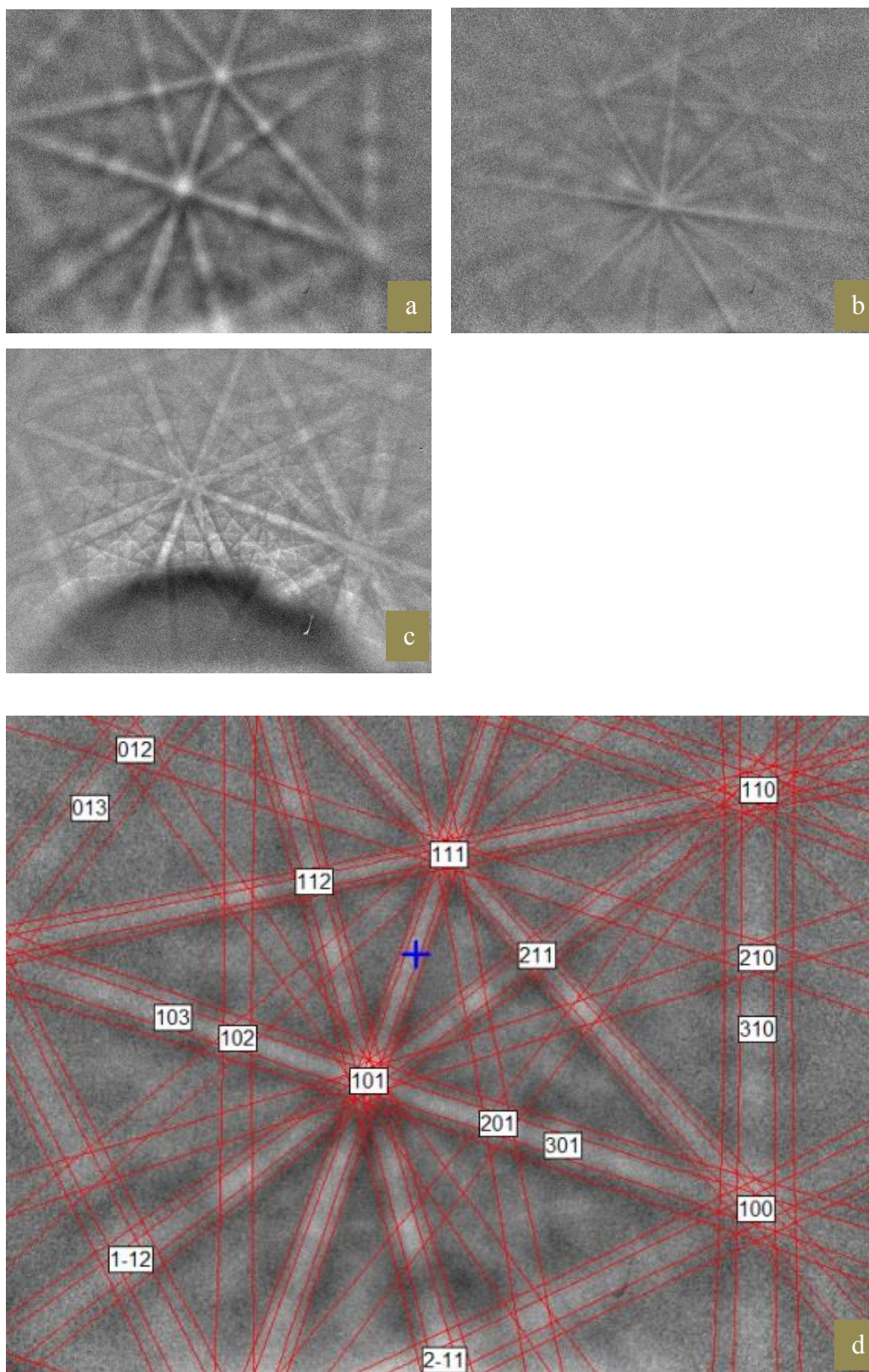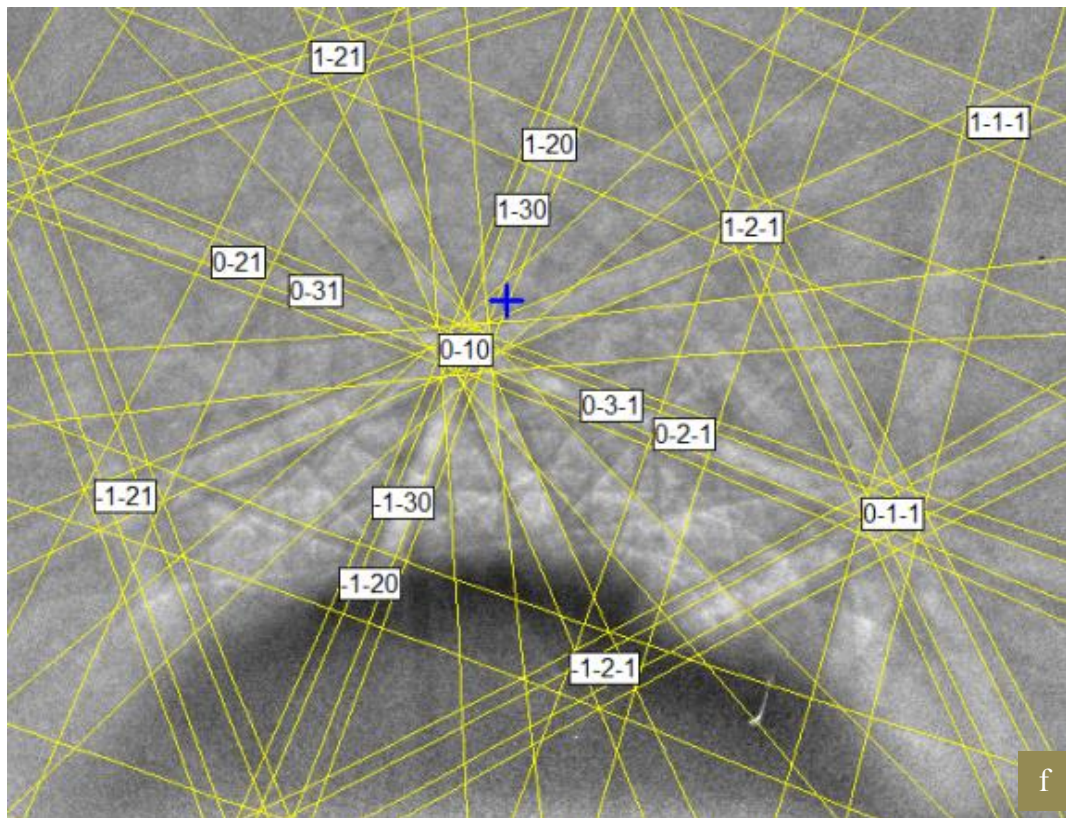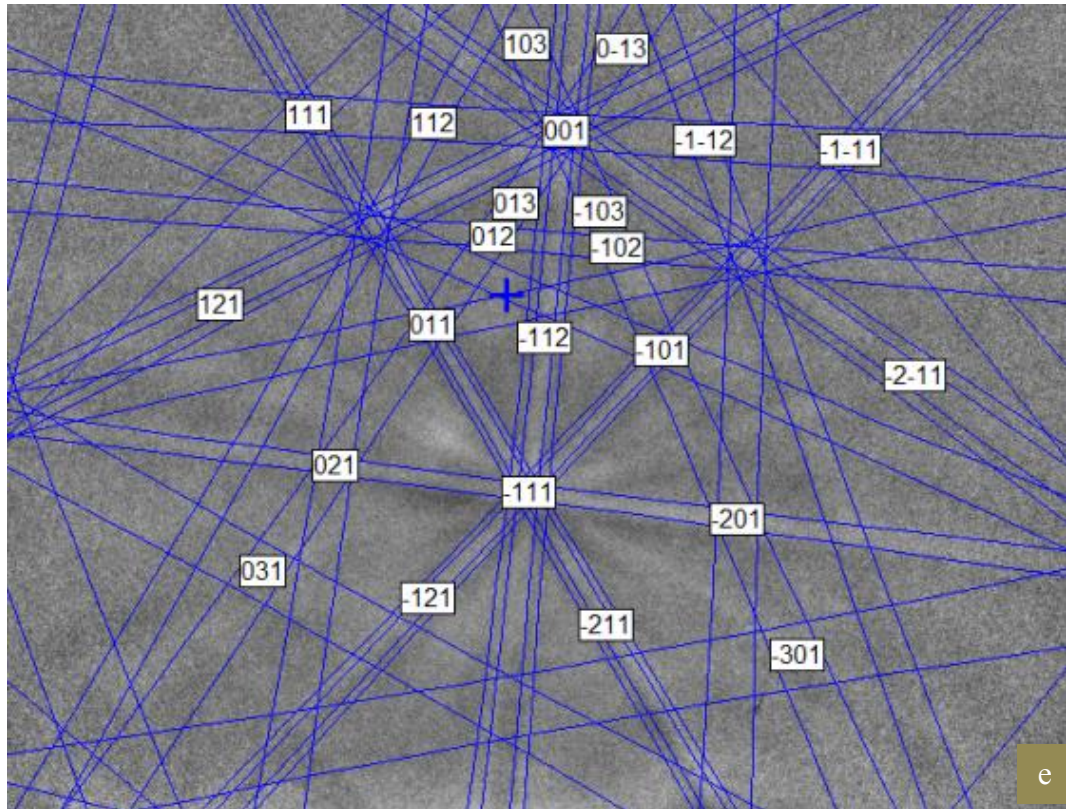
Figure 63. EBSD pattern of the (a) 'B', (b) 'S' and (c) 'C' phase acquired from C-800℃-1min. (d): the indexed pattern (a). (e): the indexed pattern (b). (f): the indexed pattern (c).
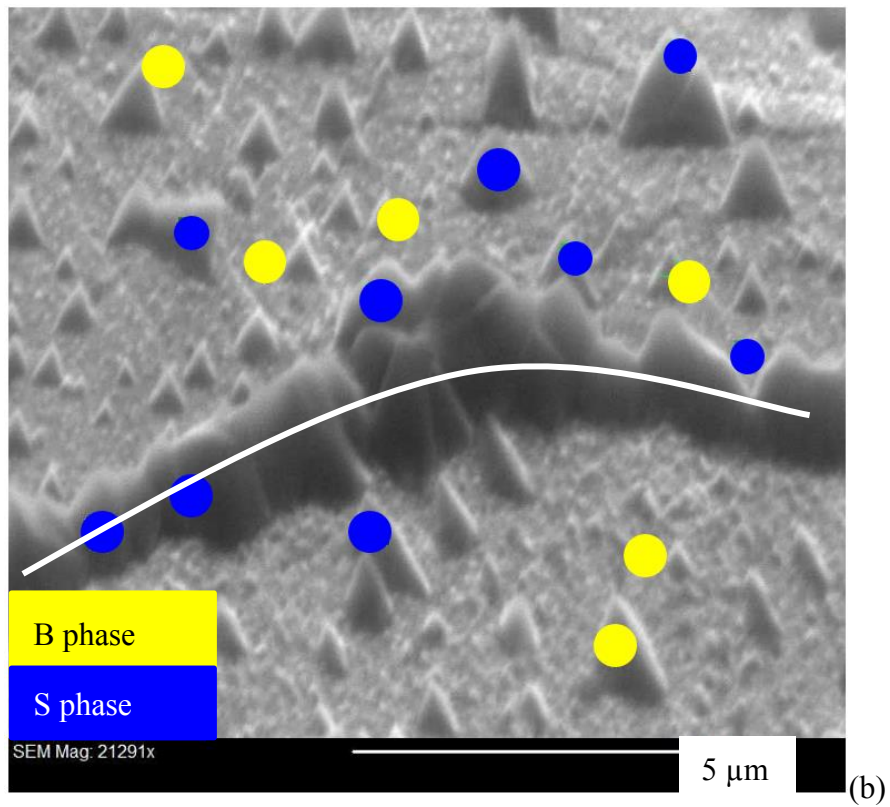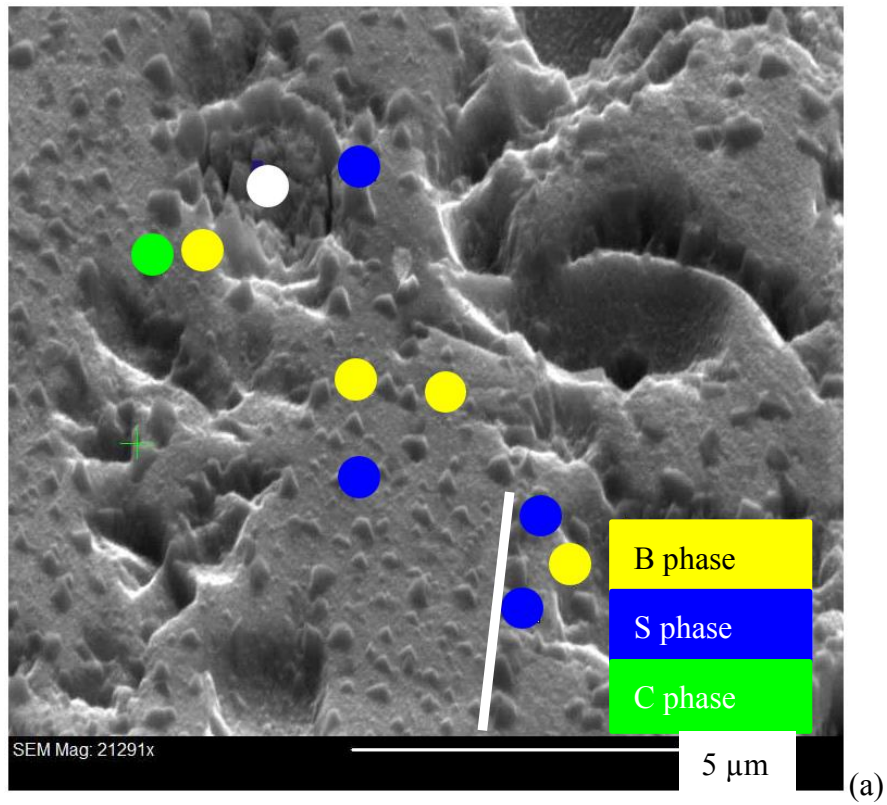
Figure 64. SE images of C-800℃-1min. The yellow, blue and green spots indicate the 'B', 'S' and 'C' phase respectively.

Figure 65 (a) shows the microstructure of the C-800℃-1min sample surface. The grain boundaries in the figure are highlighted by white lines. Grey precipitates can be seen on the surface. Those on the grain boundaries are connected. Those on the grains are separated. Figure 65 (b) is a phase distribution map of Figure 65 (a). In the map, the 'B' phase is shown in green and the 'S' phase is given in yellow. Therefore, all precipitates in the imaged area were ascribed to the 'S' phase, suggesting the surface precipitates are 'S' phase precipitates. In addition, EBSD phase map can be conducted in such surface precipitate study. The EBSD phase mapping on an uneven surface was performed on a SEM for the first time.



(a)                                          (b)
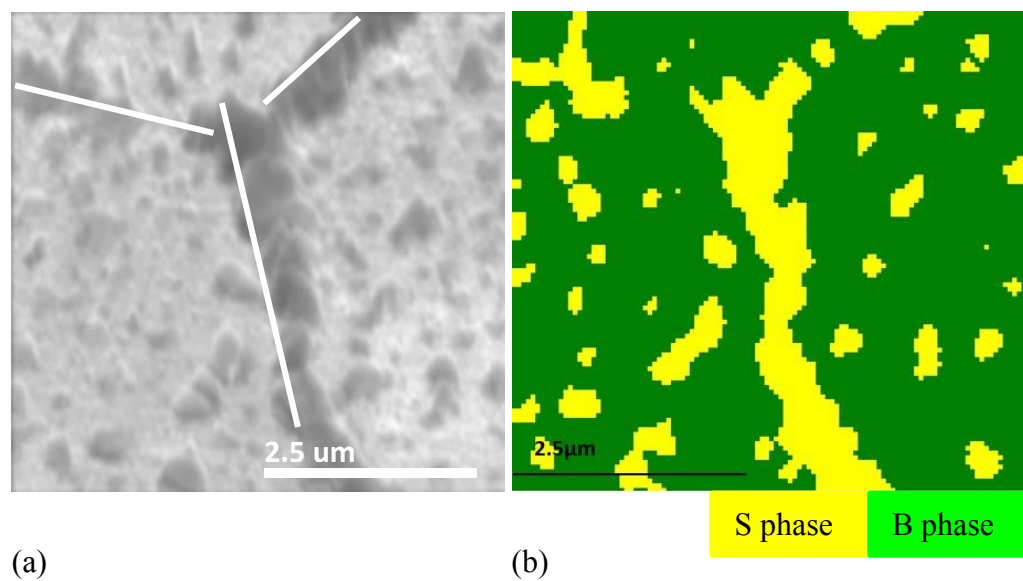
Figure 65. (a) A SE image of the C-800℃-1min sample surface. (b) an EBSD phase map of (a). Yellow: the 'S' phase. Green: the 'B' phase.

Figure 66 shows the X-ray penetration depth as a function of 2θ, determined for BSCF. As the incident angle increases, the depth is increased.
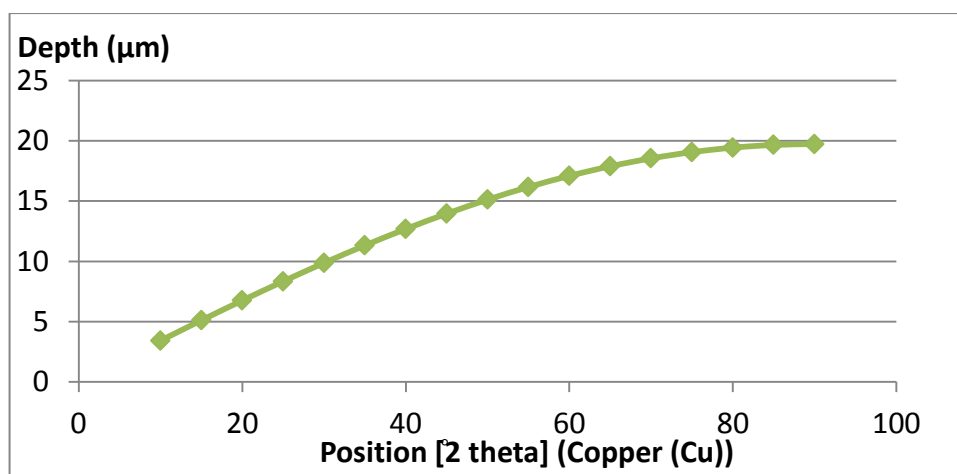
Figure 66. The X-ray penetration depth determined for BSCF plotted against 2θ.

4.2.4.2 Discussion

The surface precipitates are isostructural because the EBSD patterns generated from the precipitates can be fitted by the EBSD patterns of the 'S' phase without modifying the structure of the 'S' phase.

The 'C' phase was rarely observed in the EBSD maps of the sample surface. However, the 'C' phase was identified by XRD which obtained information from both the surface and bulk. For a BSCF sample, the penetration depth of X-ray is between 3 and 20 μm (Figure 66). Therefore, the 'C' phase is likely to be found underneath the sample surface.

The advantage of investigating the precipitates by EBSD is that EBSD signals are generated a few nm below the precipitate surface. In this research, the precipitates expand downwards at least 30 nm underneath their own surface. Thus, EBSD signals can be generated from the precipitates only. This is better than EDX signals which are generated from both BSCF and the precipitates. The other advantage is that the spatial resolution of EBSD under optimised microscope conditions can be 10 nm which is smaller than the average radius of the precipitates. As a result, signals can be generated from the precipitates only. By contrast, the spatial resolution of EDX is larger than the average radius of the precipitates. As a result, EDX signals are generated from both the precipitates and BSCF.

A sample needs to be tilted 70˚ with respect to the horizon, so that the angle between the sample surface and the horizon is 70˚. This angle affects the EBSD pattern contrast. The

best contrast can be obtained, when the angle is 70˚. However, the angle between a precipitate facet and the sample surface is rarely 0˚. Therefore, the angle between a precipitate facet and the horizon is rarely 70˚. As a result, the contrast of the EBSD pattern from a facet is likely to be less clear. This is why the precipitate pattern in Figure 63 (b) shows unclear contrast.

## 4.2.5 The composition of the surface precipitates

### 4.2.5.1 Introduction

Following the EBSD phase characterisation, the 'S' phase identified by XRD was assigned to the surface precipitates. The composition of the precipitates has to be investigated by EDX on a TEM due to their small radius. The thin TEM sample allows high spatial resolution of the EDX probe (almost the same as the STEM probe) [182]. This high spatial resolution allows the chemical information to be acquired from precipitate only. However, preparing a thin slice TEM sample that exposes the precipitates to a TEM proved impossible and so C-800℃-30min-p was prepared as a compromised sample.

A C-800℃-30min-p particle was expected to be covered by a continuous precipitate layer because the C-800℃-30min pellet was covered by a continuous precipitate layer. The former layer was expected to be equivalent to the latter layer in terms of composition and crystal structure because of the same treatments and parental material. Hence the composition obtained from the former layer was considered to match the composition of the latter layer and that of the surface precipitates.

Figure 67 shows a schematic drawing of the cross section of a C-800℃-30min-p particle. The edge of a powder particle was thinner than 100 nm because it was possible to take HRTEM images from the edges. The precipitate layer can be studied by a TEM without thinning because it was thinner than 100 nm.

HRTEM images were also taken from where chemical information was obtained to match the crystallographic information of the area to that of the surface precipitates to ensure the composition from the particle is equivalent to the composition of the surface precipitates.
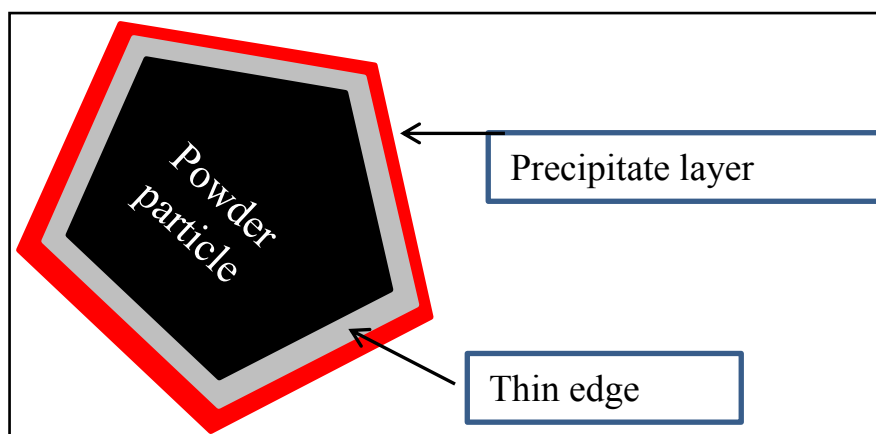
Figure 67. A schematic drawing of the cross-section of a C-800℃-30min-p particle with the thin edge and precipitate layer indicated. This is observed along the observation direction of a TEM study.

4.2.5.2 Results

Prior to TEM the C-800℃-30min-p was analysed by XRD and only the 'B', 'S' and 'C'

phases in the C-800℃-30min were identified. The indexed pattern is shown in Figure 68.
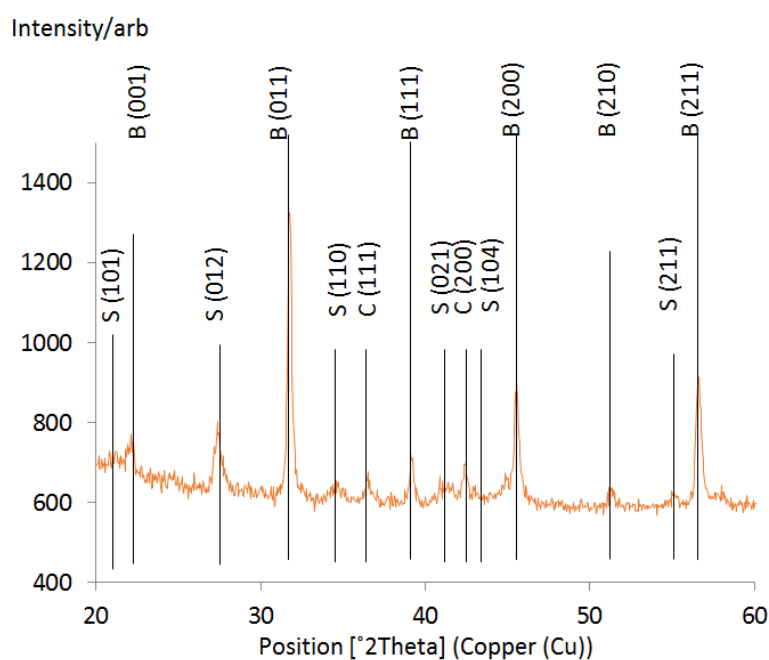


Figure 68. The indexed XRD pattern of C-800℃-30min-p with the peaks of the 'B', 'S' and 'C' phase indicated. B indicates BSCF. S indicates $SrCO_3$. C indicates CoO.

A composition of $Ba_{0.65\pm0.03}Sr_{0.35\pm0.03}CO_3$ was obtained from the very outer layer of a C-800℃-30min-p particle by EDX. The errors were contributed by the standard deviation (SD) of measurements from 6 areas. The HRTEM image (Figure 69) shows a set of lattice

planes indicated by double lines from which a d-spacing of 3.16 ± 0.11 Å was measured in DM software (Gatan, UK). The d-spacing can only be associated with the (003) peak of the 'S' phase with d-spacing of 3.1767 Å (Reference code: 04-011-6008). Hence the 'S' phase was in the area where the composition of $Ba_{0.65\pm0.03}Sr_{0.35\pm0.03}CO_3$ was obtained. No Co or Fe was identified by EDX hence the 'B' phase and the 'C' phase did not present in this area, and the area contained only the 'S' phase, to which the composition of $Ba_{0.65\pm0.03}Sr_{0.35\pm0.03}CO_3$ can be ascribed. This composition can be assigned to the surface precipitates, confirming the surface precipitates are the product of the reaction between BSCF and $CO_2$.
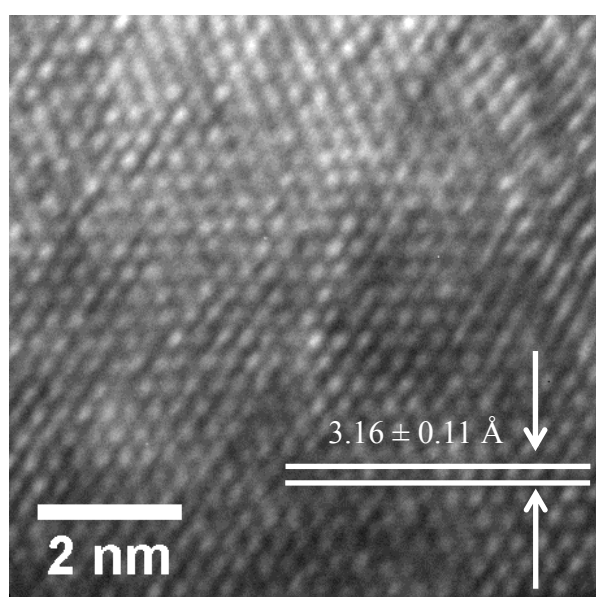


Figure 69. HRTEM image of the BSC phase in the C-800℃-30min-p with a set of lattice planes with d-spacing of 3.16 ± 0.11 Å indicated.

4.2.5.3 Discussion

In three previous studies [16, 17, 133], (Ba, Sr)$CO_3$ phases were assigned to the surface precipitates they found because only Ba, Sr, C and O were found in the precipitates by EDX. Thus, this study and the previous studies [16, 17, 133] suggest that the precipitates are carbonates. This and another study [133] suggest that the (Ba, Sr)$CO_3$ phase is Ba enriched. In one study [17], the Ba/Sr ratio of the carbonate phase also varied (1 to 0.67), supporting the variation of Ba/Sr ratio in this study.

## 4.2.6 The growth of the surface precipitates

### 4.2.6.1 Results

The precipitate coverage and radius were measured from SE images (Figure 62) using ImageJ to quantify the growth. The tolerance interval of ImageJ contributed a fractional error of 0.11, 0.07 and 0.07 to the coverage of C-800℃-1min, C-800℃-2min and C-800℃-5min. It did not contribute to the error in the 15 min and 30 min samples because coverage was 100%. For each of C-800℃-1min, C-800℃-2min and C-800℃-5min, the coverage was measured from 3 different areas. The averaged values were plotted in Figure 70 (a). The SD of each averaged value was calculated to show a range in which two thirds of the measured values should fall.  The SD and the fractional error contribute to the magnitude of the error bars in Figure 70 (a).

The average coverage increased from 0 to 100% in 15 minutes, Figure 70 (a). The average coverage from 0 min to 15 min was fitted by a power law curve. The equation of the fitted curve was shown in Equation 30.

For precipitate radius measurement, the tolerance interval was also 0.005 μm. The radius was only measured from the 1 min, 2 min and 5 min samples because the 15 min and 30 min samples did not show separated precipitates. The radius was measured from 352, 428 and 382 precipitates on the 1 min, 2 min and 5 min samples, respectively. For each sample, the measured radii were averaged and the averaged radius (R) is shown in Figure 70 (b). The SD of the average value of the 1 min, 2 min and 5 min samples were 0.06 μm, 0.07 μm and 0.10 μm, respectively. Both the SD and the tolerance interval contributed to the error bars in Figure 70 (b).

The averaged radius increased from 0 to 0.17 μm in 5 minutes, Figure 70 (b). The averaged radii were fitted by a power law curve. The equation of the curve is shown in Equation 31.
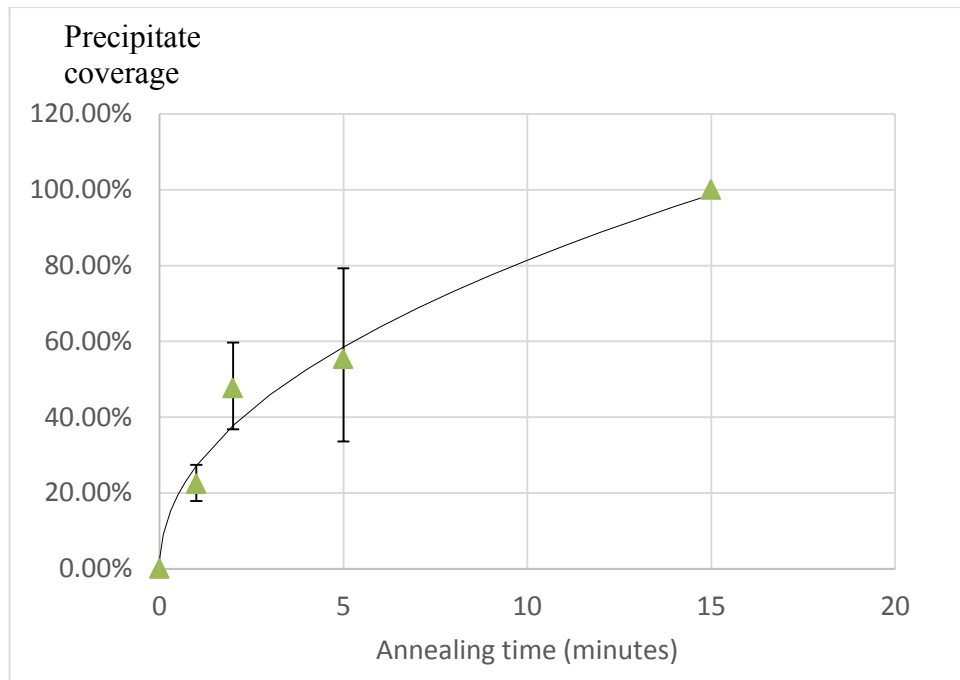
(a)
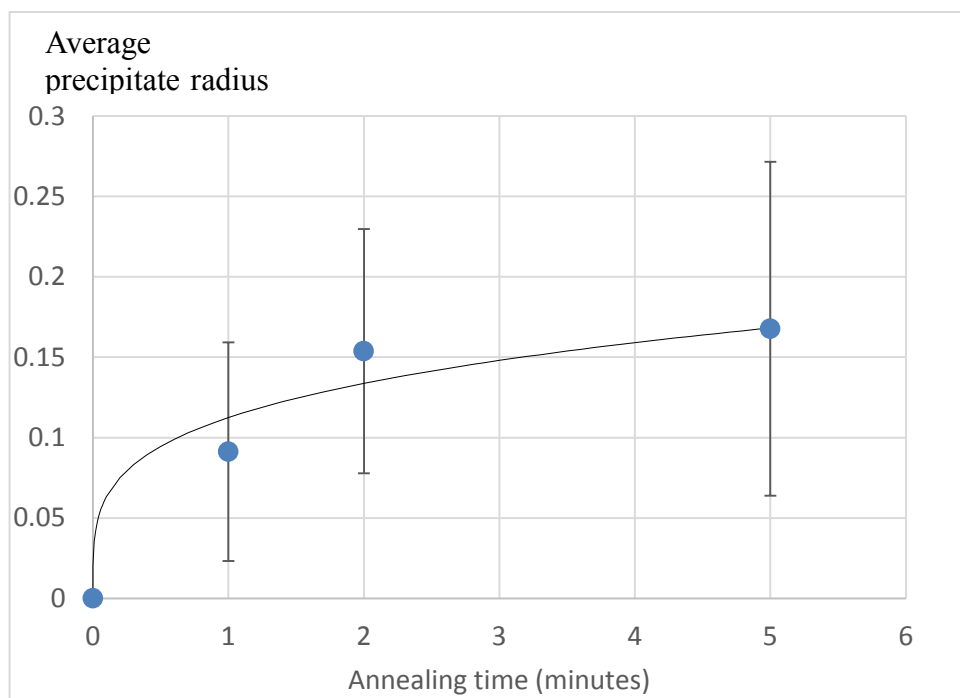


(b)

Figure 70. (a) The precipitate coverage (C-800°C-1min, C-800°C-2min, C-800°C-5min and C-800°C-15min) plotted as a function of annealing time. (b) The average precipitate radius (C-800°C-1min, C-800°C-2min and C-800°C-5min) plotted as a function of annealing time. Both plots were fitted by a power law curve.

$$Coverage = 0.272 * t^{0.47619}$$

Equation 30

$$R = 0.112 * t^{0.25}$$

Equation 31

4.2.6.2 Discussion

Equation 32 (the parabolic law) was derived for diffusion limited gas-solid chemical reactions [196]. In the equation, α is proportional to the volume of the product of a reaction, $k_G$ is the reaction rate coefficient when nucleation happens rapidly and randomly, t is the reaction time [196]. The similar exponents in Equation 30 and Equation 32 indicate that the growth of the precipitates is a diffusion controlled process.

$$\alpha = (k_G t)^{1/2}$$

Equation 32

In reactions which can be described by Equation 32, the reaction rate is reduced because of a barrier layer, formed as the reaction product between the reactants, reduces the contact area of the reactants [196]. Since the reaction between BSCF and $CO_2$ can be described by Equation 30 which is similar to Equation 32, the reduction in the rate of increase of coverage in Figure 70 (a) can be explained by a similar mechanism that the precipitate layer (the reaction product) between BSCF and $CO_2$ reduces the contact area between BSCF and $CO_2$.

Equation 33 was obtained after both sides of Equation 31 were squared. $R^2$ indicates the average precipitate area and the exponent of time t is 0.5 which is the same as that of Equation 32. This suggests again that the precipitate growth is a diffusion controlled process. It also suggests that the radius growth rate reduction in Figure 70 (b) was caused by that of the precipitate layer reducing the contact area between BSCF and $CO_2$.

$$R^2 = 0.112^2 * t^{0.5}$$

Equation 33

Figure 70 (a) and (b) were plotted in log-log form and shown in Figure 71 (a) and (b) respectively. The straight lines in (a) and (b) suggest a one stage reaction because the constant slope indicating that the reaction is governed by a single mechanism.
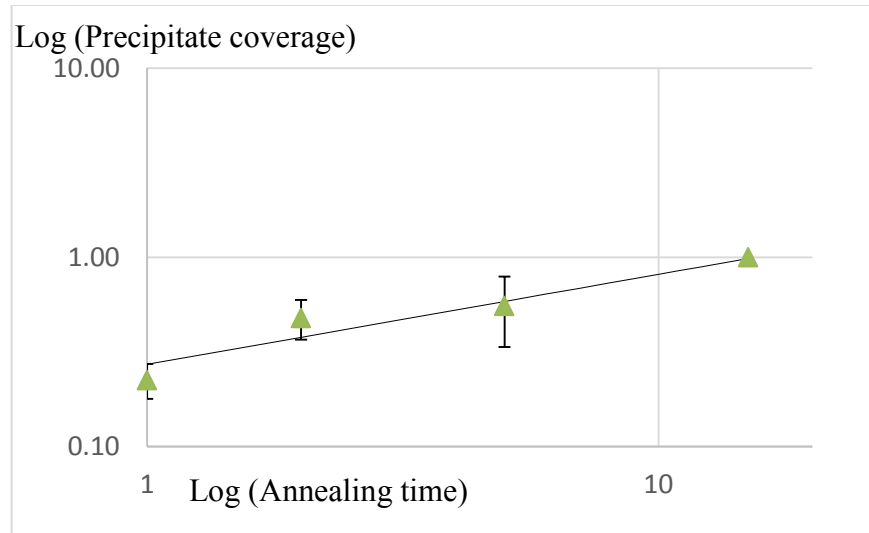


(a)
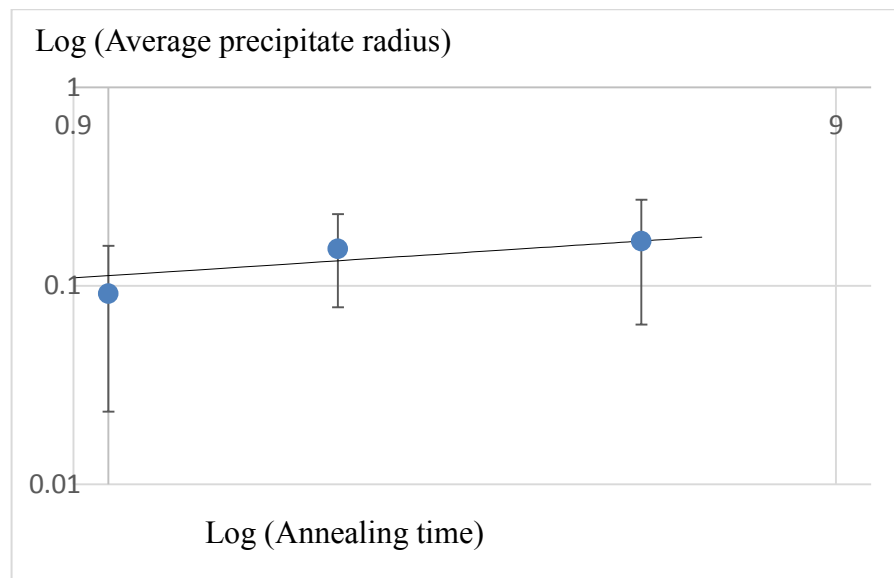


(b)

Figure 71 (a) The log-log plot of the precipitate coverage vs time plot (C-800℃-1min, C-800℃-2min, C-800℃-5min and C-800℃-15min). (b) The log-log plot of the average radius vs time plot (C-800℃-1min, C-800℃-2min and C-800℃-5min).

It was suggested that Ba and Sr diffuse to the sample surface to form carbonate precipitates [17]. The diffusion of cations via grain boundaries is typically faster than that via grains [197]. Hence the reason why the precipitates on grain boundaries are larger than those on grains can be that the former precipitates obtain more cations per second than the latter precipitates.

## 4.2.7 The crystallographic orientation relation

### 4.2.7.1 Results

The pole figures in Figure 72 (a) and (b) were acquired from two grains of the C-800°C-1min sample to study the crystallographic relationship between the precipitates and BSCF grains. Each one of (a) and (b) shows {001}, {110} and {111} pole figures of a BSCF grain (they were acquired from grain centres) and {0001}, {11-20} and {10-10} pole figures of 20 $Ba_{0.65\pm0.03}Sr_{0.35\pm0.03}CO_3$ (BSC) precipitates on the grain. In each case the blue circle highlighted BSCF {110} poles are aligned to the blue circle highlighted BSC {11-20} poles and the green circle highlighted BSCF {111} poles are aligned to the green circle highlighted BSC {0001} poles, suggesting the {110} and {111} BSCF planes are parallel with the {11-20} and {0001} BSC planes respectively, which is the crystallographic orientation relation between the two phases. The relation is well defined hence the precipitate orientation is affected by the orientation of BSCF.

In Figure 72 (a), the BSC precipitates show one orientation, indicated by the green poles. In Figure 72 (b), the BSC precipitates show two orientations, indicated by the pink poles and the green poles in the {10-10} pole figure, the rest of the poles are noise. Hence all precipitates on a BSCF grain can have one or two orientations (governed by the underlying BSCF grain).
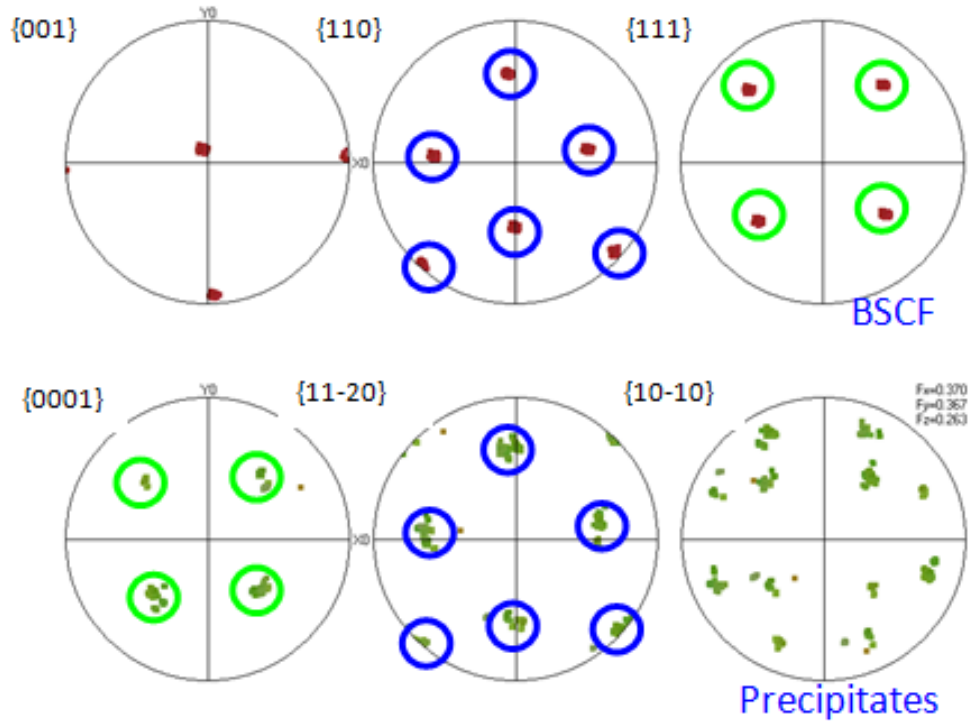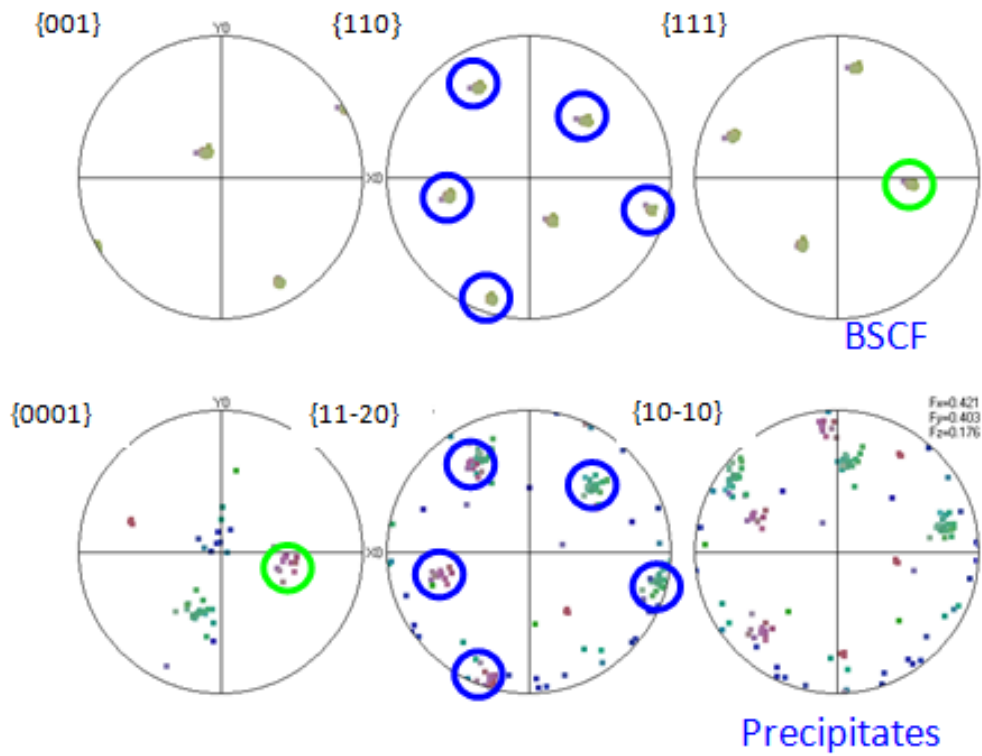
Figure 72. (a, b) {001}, {110} and {111} Pole figures of a BSCF grain on C-800°C-1min and {0001}, {11-20} and {10-10} pole figures of the BSC precipitates on the grain.

BSC precipitate orientation in a grain boundary was also studied. Figure 73 (a) and (b) each show {001}, {110} and {111} pole figures of two BSCF grains on either side of a grain boundary. The poles of two grains are plotted in different colours (green and red) to distinguish. Each of Figure 73 (a, b) also show {0001}, {11-20} and {10-10} pole figures of a series of the BSC precipitates growing along the grain boundary. The blue circle highlighted {110} poles of BSCF are aligned to the blue circle highlighted BSC {11-20} poles and the green circle highlighted {111} poles of BSCF are aligned to the green circle highlighted BSC {0001} poles, suggesting the {110} and {111} BSCF planes are parallel with the {11-20} and {0001} BSC planes respectively, which is the crystallographic orientation relation between the two phases on a grain boundary. The relation is the same as the one found from grains (Figure 72), suggesting the relation is the same for grains and grain boundaries. Hence on a grain boundary, the precipitate orientation is also affected by the orientation of BSCF.

In Figure 73 (b), the orientation of a portion of precipitates is parallel to one BSCF grain, while the rest is parallel to another grain. This suggests that the orientation of precipitates on a grain boundary can be affected by either grain forming the boundary.
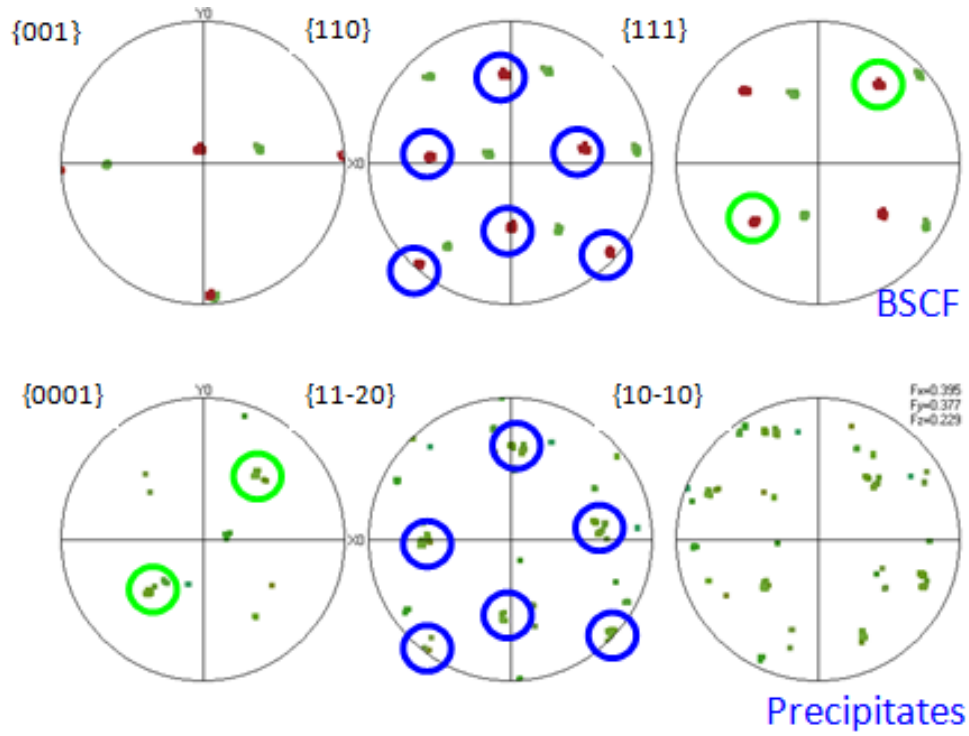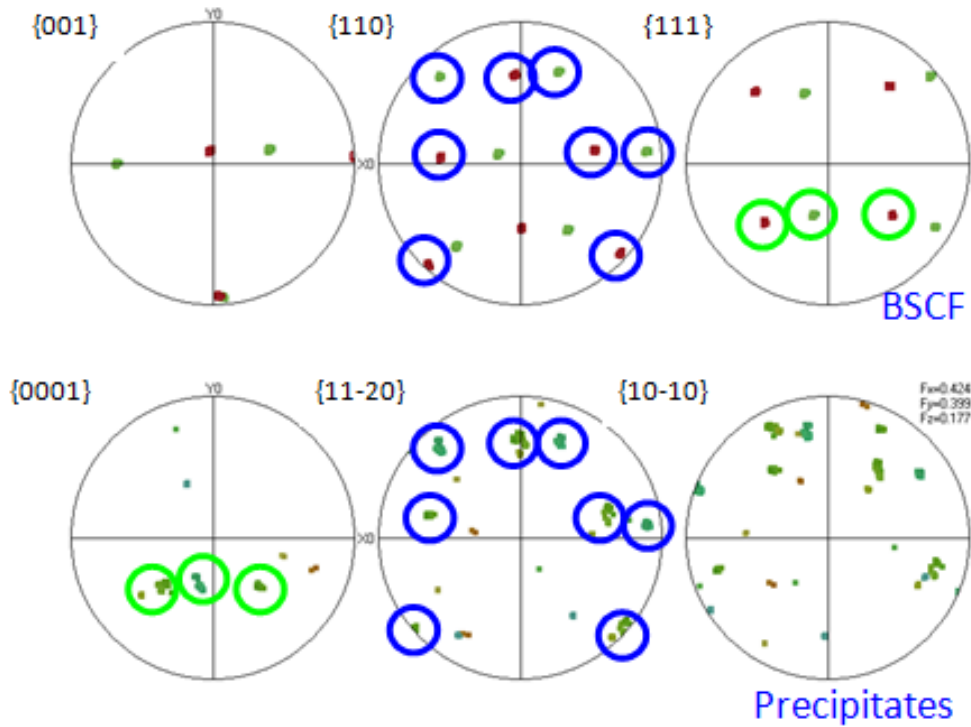
Figure 73. (a - b) {001}, {110} and {111} Pole figures of neighbour BSCF grains on C-800°C-1min and {0001}, {11-20} and {10-10} pole figures of the BSC precipitates on the grain boundary. (a, b) were acquired from different parts of one boundary.

### 4.2.7.2 Discussion

### 4.2.7.2.1 The precipitate morphology and the orientation relation

The precipitate crystallographic orientation is aligned with the orientation of the underlying BSCF grains, which explains why the precipitate morphology appears similar within each grain although there are differences in appearance between grains.

### 4.2.7.2.2 The d-spacing matching at the interface

The pole figure alignment indicates that {110} planes of BSCF are parallel to BSC {11-20} planes. The d-spacing of BSCF {110} and BSC {11-20} planes are 2.817 Å (ICSD: 109462) and 2.546 Å (ICSD: 27445), respectively. They are closely matched, giving rise to good crystallographic matching at the interface. {111} planes of BSCF are parallel to BSC {0001} planes. The d-spacing of {111} and {0001} planes are 2.300 Å (ICSD: 109462) and 9.530 Å (ICSD: 27445), respectively. The latter is approximately 4 times as large as the former. The d-spacings may also give rise to good crystallographic matching at the interface.

### 4.2.7.2.3 Why are the precipitates oriented this way

Figure 74 (a) shows the BSC (0001) plane, observed along the [0001] zone axis. The BSC (11-20) plane is highlighted in red. Figure 74 (b) shows the (111) plane of BSCF, observed along the [111] zone axis. The (-110) plane is highlighted in red. In Figure 73 (a) and (b), the green spots indicating Sr atoms and the unit cell of each phase are drawn in white. Figure 73 (a) and (b) are oriented according to the pole figure alignments. Figure 74 (c) shows that when the two structures are overlaid there is minimal mismatch between the Sr atoms of the two phases. Minimising mismatches can reduce the interfacial energy [198], and may explain why the two phases are oriented this way.
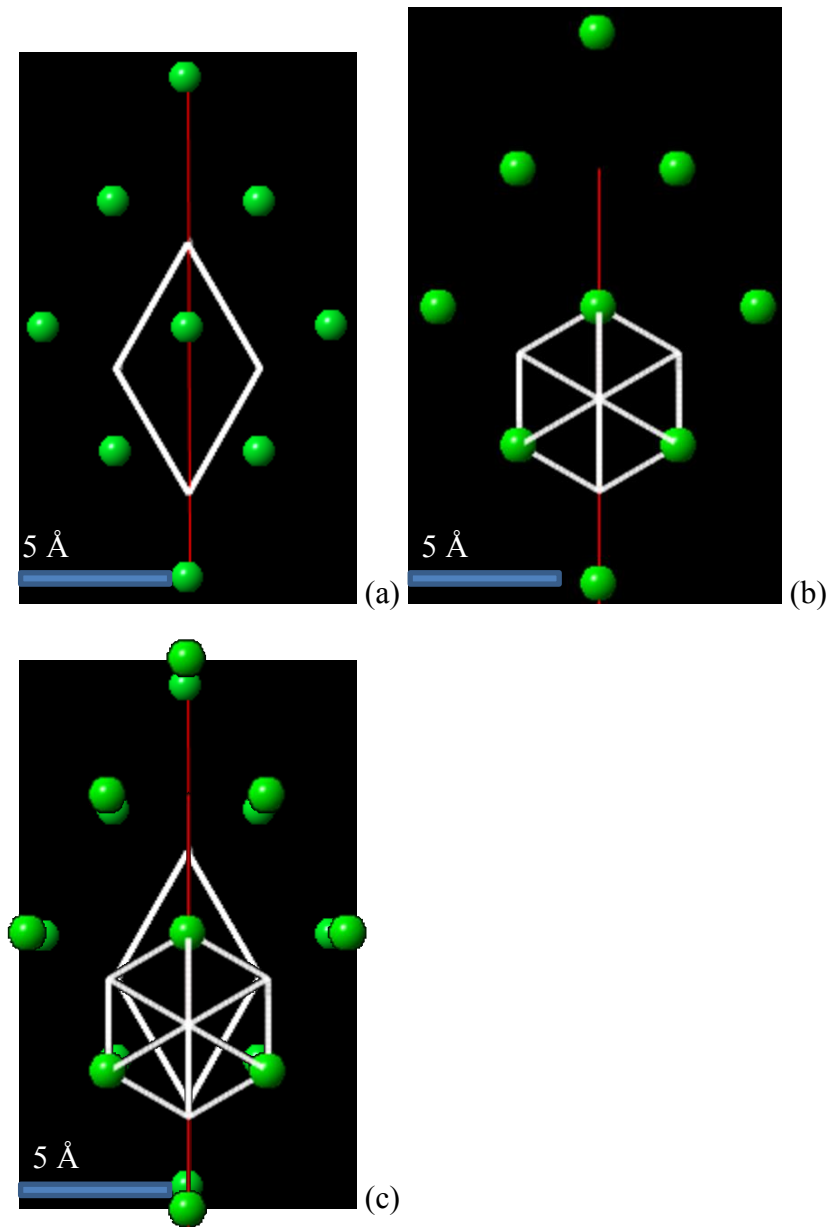
Figure 74. (a) The (0001) plane of the BSC precipitates, observed along the [0001] zone axis with hexagonal unit cell indicated in white and the (11-20) plane indicated in red. (b) The (111) plane of BSCF, observed along the [111] zone axis with cubic unit cell indicated in white and the (-110) plane indicated in red. (c) The (111) plane is overlaid with the (0001) plane.

4.2.7.2.4 The noise in the pole figures

The sample needs to be tilted 70° from horizontal position to maximise the intensity and contrast of the EBSD pattern [186]. However, the surfaces of the precipitates are rarely parallel with the sample surface. Such surfaces are not 70° from the horizontal position, which can reduce the intensity and contrast of the EBSD patterns. Based on such patterns, the orientation of the precipitates can be indexed incorrectly, hence noises are created in

178

the pole figures. Evidence is shown in Figure 75. Figure 75 (a) shows BSC precipitates on BSCF grains and grain boundaries indicated by a red curve and Figure 75 (b) shows the orientation mapping of (a). The mapping of the left grain was highlighted in a quadrilateral and the remaining area was shaded. The circled precipitate in (a) shows two colours (brown and green) in (b), suggesting two orientations were ascribed to the precipitate. The green orientation is aligned to BSCF and the brown orientation is noise which gives rise to noise in pole figures.
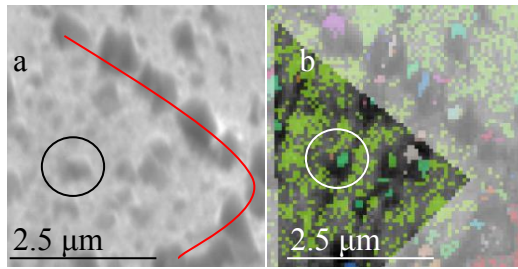


Figure 75. (a) SE image of the C-800°C-1min sample with a red curve indicating grain boundary and a circle outlining a precipitate. (b) EBSD orientation map of (a) with a circle outlining the precipitate. Except the left grain, the map is shaded.

4.2.7.2.5 The orientation of BSCF grains

Figure 76 (a, b) show EBSD orientation maps of two areas on the cross section of the C-800°C-30min. For both maps, the surface is on the right. The colour and orientation scheme is shown on the right. The maps reveal no preferred grain orientation.



(a)                    (b)
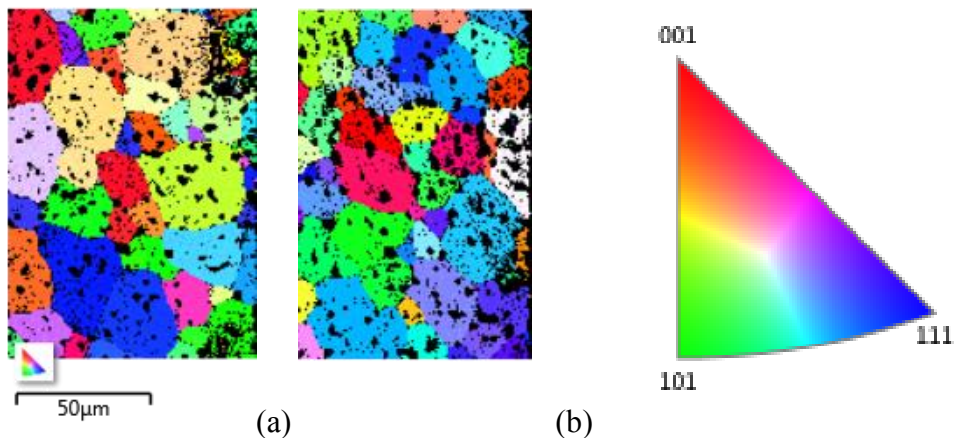
Figure 76. (a, b) EBSD orientation maps of two areas on the cross section of the C-800°C-30min with orientation and colour scheme shown on the right.

## 4.2.8 Microstructure changes of cross section

### 4.2.8.1 Results

The cross section of C-800°C-1min is prepared by FIB and shown in Figure 77 (a). A grain boundary covered by a row of BSC precipitates is highlighted by a line. The row is intercepted by the platinum layer indicated in the figure. The cross section can be seen below the platinum layer. The area which shows dark contrast is highlighted by a frame and is shown in Figure 77 (b). A plate-like phase and a dark phase indicated by arrows can be seen in this area, there is a discontinuous layer (highlighted in the white frame) just below the platinum layer. The surface BSC precipitates were assigned to this layer. A few plates extend into the precipitate layer, (highlighted in the red frame). Other precipitates in the layer are highlighted in the blue frame. The integration of the secondary phases suggested a complex decomposition mechanism.

Figure 77 (c) shows the cross section of C-800°C-30min. There is a continuous surface layer (highlighted in the green frame). The plate-like phase can be seen in the white frame below the surface layer. In previous studies [17, 133], a carbonate layer was noted to form on top of a plate-like phase layer. Hence the surface BSC precipitates were tentatively assigned to the layer in the green frame. On this basis the layer thickness was increased from $101 \pm 70$ nm to $1130 \pm 160$ nm with increasing annealing time from 1 min to 30 min.

Figure 77 (d) shows a TEM image of one of the plate-like phase precipitates, a lamellar structure is seen in the plate, and is consistent with that observed in previous studies [140, 141].

Platinum layer

HV: 5.00 kV | curr: 98 pA | mag ⊞: 12 500 x | tilt: 52 ° | WD: 4.8 mm | HFW: 10.2 μm | 3 μm | Electron Beam

(a)



Platinum layer

HV: 5.00 kV | curr: 98 pA | mag ⊞: 60 000 x | tilt: 52 ° | WD: 4.9 mm | HFW: 2.13 μm | 500 nm | Electron Beam

(b)
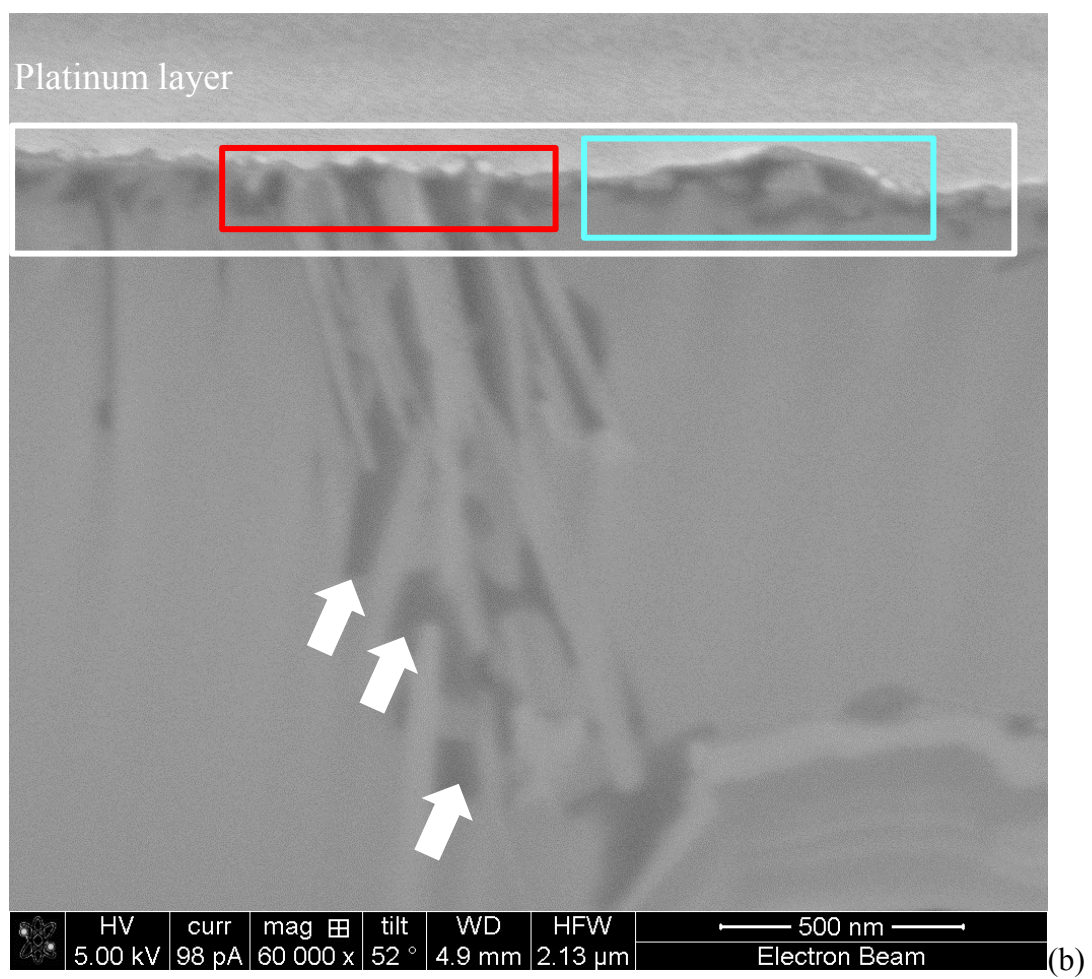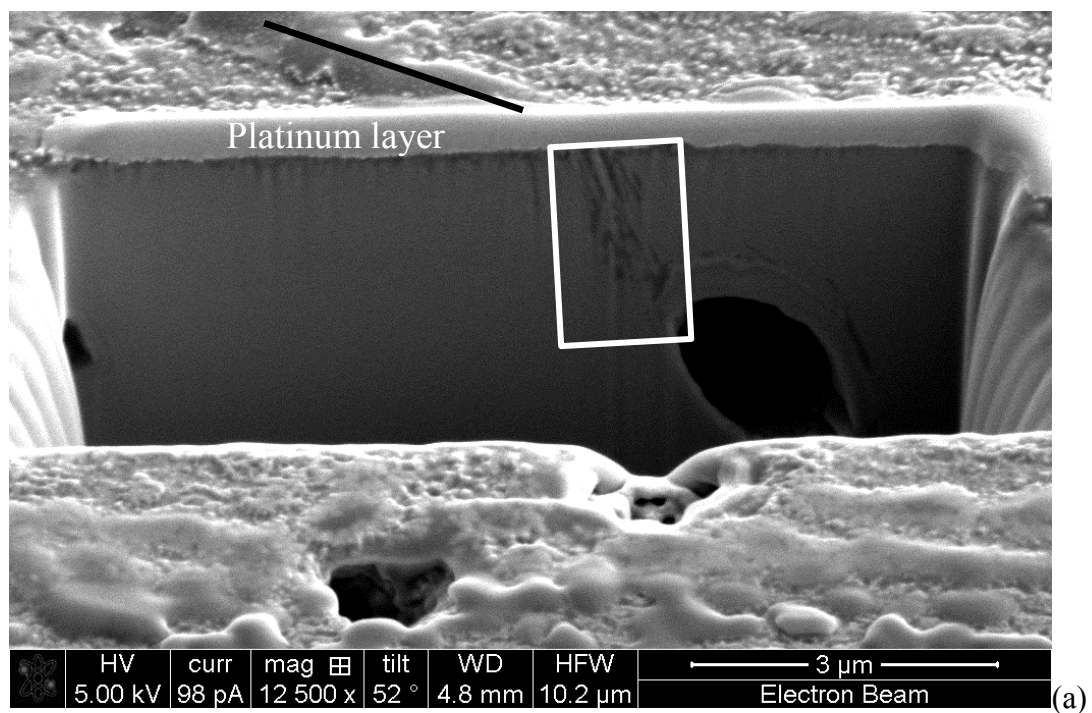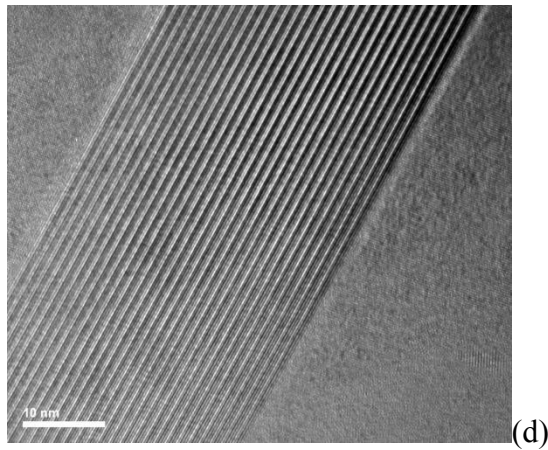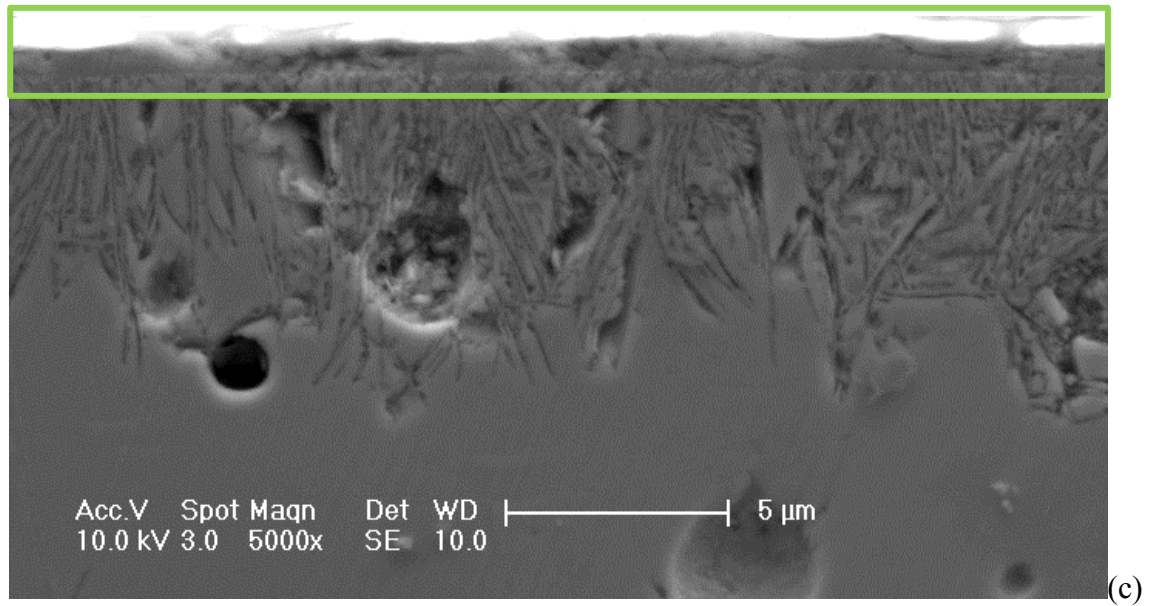
Figure 77. (a) SE image of cross section of C-800°C-1min with a line indicating grain boundary, a frame outlining special phases and the platinum layer indicated. (b) SE image of cross section of C-800°C-1min with arrows indicate a dark phase, a white frame outlining a discontinuous precipitate layer, a red frame outlining plate precipitates and a blue frame outlining chunky precipitates . (c) SE image of cross section of C-800°C-30min. (d) TEM image of one plate in C-800°C-30min.

4.2.8.2 Discussion

4.2.8.2.1 The growth rate of the plates

The average plate-length increased from $0.85 \pm 0.35$ μm to $4 \pm 2$ μm when annealing time was increased from 1 min to 30 min. The growth rate of the plates in $CO_2/N_2$ (9 μm/hr) was higher than that in $N_2$ (1 μm/hr) observed in this study, suggesting $CO_2$ accelerated the growth of the plates. The coverage of the plate-like phase significantly increased with the annealing time.

### 4.2.8.2.2 The dark phase

A Sr-enriched carbonate phase was found adjacent to the plate-like phase in a study by Arnold et al. [16]. The dark phase indicated by arrows in Figure 77 (b) may be the same Sr-enriched carbonate phase because it formed adjacent to the plate-like phase.

## 4.2.9 Chemical composition changes of cross section

### 4.2.9.1 The TEM study

For the following subsections 4.2.9.1.1, 4.2.9.1.2 and 4.2.9.1.4, STEM imaging and EDX analyses were conducted on a FEI Tecnai TF20 TEM. For 4.2.9.1.3, EDX mapping was conducted on FEI Tecnai TF30 FEG TEM.

### 4.2.9.1.1 Co migration

#### *4.2.9.1.1.1 Results*

Figure 78 shows a BF STEM image of a cross section of C-800℃-5min. The blue arrow indicates the original sample surface, which was eroded away during ion beam milling. EDX element mapping was performed in the area indicated by the white frame. Figure 79 shows the map of Co. The element was identified by the characteristic X-ray shown above the map. Figure 79 shows two Co enriched area (indicated by arrows).



Figure 78. STEM image shows the cross section of C-800℃-5min with an arrow indicating original surface, a frame outlining an area of interest and a triangle indicating a denser area.
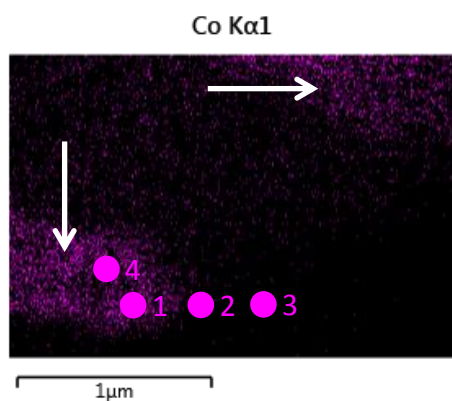
Figure 79. EDX element map of Co of C-800°C-5min in the framed area in Figure 78 with arrows indicating Co enriched areas and numbered spots indicating areas of interest.

EDX spectra were acquired from the points indicated by purple spots in Figure 79 to reveal the composition of the cobalt enriched area and cobalt depleted area. After spectrum quantification, the composition of the areas were obtained and were shown in Table 30, the composition of a fresh BSCF sample is also shown in Table 30. The processing for quantification in Aztec TEM (Oxford Instruments NanoAnalysis, UK) measures the peak counts and estimating the statistical error which contributes to the fractional errors (Ba 1%, Sr 2%, Co 2% and Fe 5%), the peak background is accounted for by a process of "Filtered Least Squares", the statistical error varies when peak overlapping happens [199]. In Table 30, Ba is dramatically enriched in areas 2 and 3 and slightly enriched in areas 1 and 4, compared to the fresh sample composition. Areas 1 and 4 are slightly Sr-deficient, while areas 2 and 3 are Sr-enriched. Areas 1 and 4 are Co-enriched, while areas 2 and 3 are Co-deficient. All areas are Fe-deficient.

Table 30 Atomic concentration of Ba, Sr, Co and Fe from the purple spots in Figure 79 (C-800°C-5min) and a fresh sample

| 1 | $Ba_{0.27}Sr_{0.22}Co_{0.47}Fe_{0.04}O_x$ |
| 2 | $Ba_{0.42}Sr_{0.33}Co_{0.22}Fe_{0.03}O_x$ |
| 3 | $Ba_{0.43}Sr_{0.35}Co_{0.18}Fe_{0.04}O_x$ |
| 4 | $Ba_{0.28}Sr_{0.22}Co_{0.46}Fe_{0.04}O_x$ |
| Fresh sample | $Ba_{0.25}Sr_{0.25}Co_{0.40}Fe_{0.10}O_{3-\delta}$ |

*4.2.9.1.1.2 Discussion*

In a BF STEM image [184], darker contrast suggests higher density when the thickness of all areas are the same. Since the cross section was uniformly thinned by an ion beam, the sample thickness is the same for adjacent areas. The darker contrast indicated by a triangle in Figure 78 suggests a higher density phase than the adjacent areas, suggesting cations from the adjacent areas may have migrated to it. In an EDX map of an element, the pixel intensity is controlled by the X-ray signal intensity of the element of interest [182]. Hence the pixel intensity is proportional to the number of ions present. There are more Co cations in the bright area than in the dark area in Figure 79, suggesting Co migrates in the cross section from the dark area to the bright area. The bright area corresponds to the dark area in the BF STEM image, suggesting Co migrates from adjacent areas to the dark area to enhance the local density.

For Table 30, areas 2 and 3 show a phase that is Ba- and Sr- enriched and Co-deficient compared with BSCF. A similar composition, which was found in another study [17], was ascribed to a mixture of $(Ba, Sr)CO_3$ and Co-deficient $(Ba, Sr)_x(Co, Fe)_yO_z$. The analyses in Table 30 were scaled to set the Co atomic concentration to 100% and are shown in Table 31. The composition of areas 1 and 4 are close to that of $Ba_{0.5}Sr_{0.5}CoO_3$ which is the hexagonal phase identified in previous studies [139, 140]. Thus phases identified in previous studies are present in areas 1-4. Since Co was shown to migrate from areas 2 and 3 to areas 1 and 4, Co may migrate away from the cubic BSCF phase to form the hexagonal phase and the remaining BSCF may consequently transform to a Co-deficient $(Ba, Sr)_x(Co, Fe)_yO_z$ phase. In addition, $(Ba, Sr)CO_3$ may form in areas 2 and 3. This was pointed out for the first time and was summarised in the schematic diagram in Figure 80.

Table 31 Data in Table 30 (C-800°C-5min) were scaled to set Co atomic concentration at 100%

| 1 | $Ba_{0.57}Sr_{0.47}CoFe_{0.09}O_x$ |
|---|---|
| 2 | $Ba_{1.9}Sr_{1.5}CoFe_{0.14}O_x$ |
| 3 | $Ba_{2.4}Sr_{1.9}CoFe_{0.22}O_x$ |
| 4 | $Ba_{0.61}Sr_{0.48}CoFe_{0.09}O_x$ |
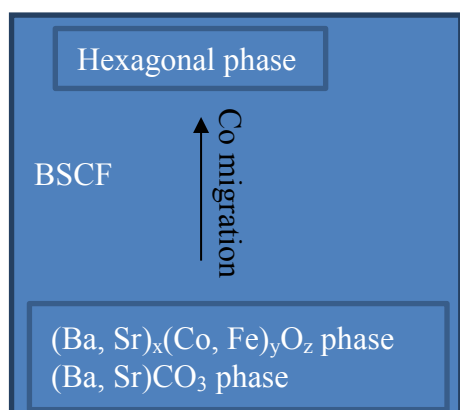
Figure 80. A schematic drawing shows the Co migration in BSCF as a result of decomposition.

4.2.9.1.2 The Ba and Sr migration

*4.2.9.1.2.1 Results*

Figure 81 (a) shows a BF STEM image of a cross-section of the C-800°C-5min. The original surface eroded away by the ion beam milling is indicated by a blue arrow. An EDX linescan was performed along the line shown in the direction indicated by the yellow arrow. Figure 81 (b) shows the atomic concentration variation of Ba, Sr, Co and Fe as a function of scanning distance. The fractional error caused by EDX peak area measurements of each element were 1%, 2%, 2% and 5%, respectively. Three numbered frames can be seen in the figure.

In frame 1, the concentration of Ba varies between 26% and 30% and that of Sr varies between 20% and 25%. Compared to the concentrations in a fresh sample of BSCF, Ba is enriched and Sr is deficient. The concentration of Fe varies between 8% and 13% and that of Co varies between 38% and 43%. These concentrations are changing above and below the corresponding concentrations of a fresh sample.

In frame 2, the concentration of Co is significantly higher than that in a fresh sample of BSCF and the maximum has reached 64%, indicating this area is significantly Co enriched. The concentrations of Ba, Sr and Fe are lower than that in a fresh sample of BSCF and the minimum concentrations of Ba, Sr and Fe have reached 16%, 14% and 5%, respectively, indicating Ba, Sr and Fe have become deficient in this area.

In frame 3, the concentration of Co is lower than that in a fresh sample and the minimum

has reached 34%, indicating this area is Co-deficient. The concentration of Ba and Sr are higher than those in a fresh sample and the maximum concentration of Ba and Sr have reached 32% and 27%, respectively, indicating Ba and Sr are enriched in this area. The Fe concentration varies between 8% and 9%, indicating Fe is slightly deficient in this area.
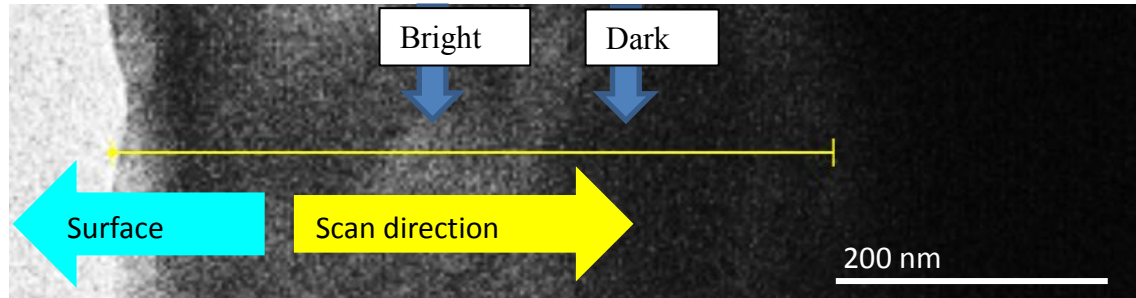


(a)
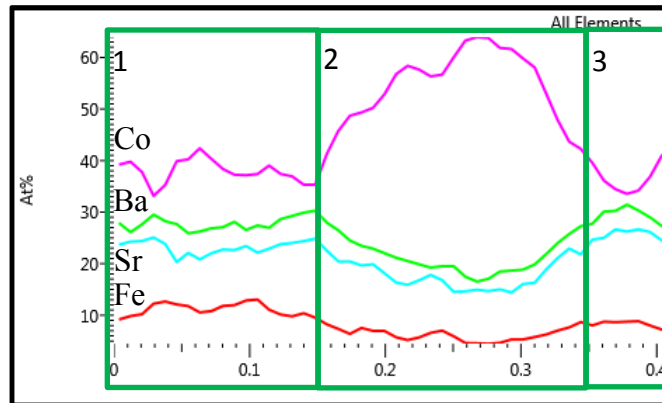


(b)

Figure 81. (a) The BF STEM image shows a cross-section of the C-800°C-5min. The yellow line indicates the EDX linescan pathway. The linescan direction is indicated by the yellow arrow. The original surface is indicated by the blue arrow. (b) EDX Linescan results show atomic concentration (at%) variation of Ba, Sr, Co and Fe as a function of scanned distance.

*4.2.9.1.2.2 Discussion*

In Figure 81 (a), a bright area and a dark area are indicated by arrows. The bright area is associated with the Co enriched area and dark area is associated with frame 3 in Figure 81 (b). In a BF STEM image, a brighter area has lower density than a darker area, providing the thickness and composition are the same [184]. Hence the density of the Co-enriched bright area may be lower than the dark areas, indicating cations may migrate from the bright area to the dark areas. The migration cations may be Ba and Sr because their

concentrations are higher in the dark area. Such behaviour was also observed by another work [17].

### 4.2.9.1.3 EDX element mapping of the plate-like phase

*4.2.9.1.3.1 Results*

Figure 82 shows a HAADF STEM image of a cross-section of the C-800°C-30min. The HAADF detector was chosen for its higher resolution than BF or ADF detectors. The original surface eroded away by the ion beam milling is indicated by an arrow. The white arrows indicate the plate-like phase containing lamellar. EDX element mappings were performed on the area in the frame. The maps of Ba, Sr, Co and Fe are shown in Figure 83 (a), (b), (c) and (d), respectively. The elements were identified by the characteristic X-ray shown above each map.
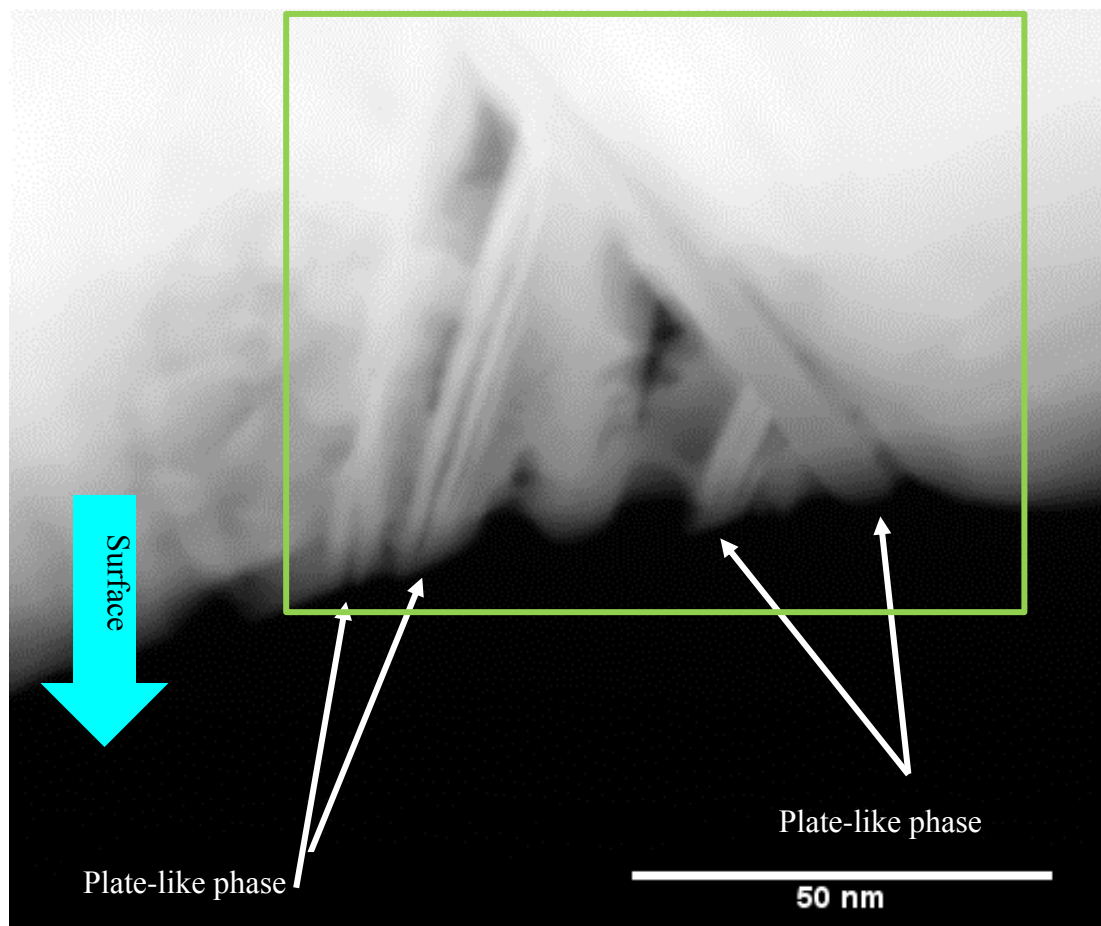


Figure 82. HAADF STEM image shows a cross section of the C-800°C-30min with white arrows indicating plate-like phase, blue arrow indicating original surface and a frame outlining an area of interest.

In Figure 83 (a), the distribution of Ba is nearly uniform except a few dark areas. Ba is deficient in the dark areas. In Figure 83 (b), there are several dark areas indicating Sr deficiency. The dark areas highlighted in the yellow frame are associated with the plate-like phase, indicating the plate-like phase is Sr-deficient. In Figure 83 (c), the areas associated with the plate-like phase are highlighted in the yellow frames. They are bright, indicating they are Co enriched. The areas near the plates are dark, indicating they are Co deficient. In Figure 83 (d), the areas associated with the plate-like phase are highlighted in the yellow frames. They are bright, indicating they are Fe-enriched. The areas near the plates are dark, indicating they are Fe-deficient.

There is an area highlighted by a white frame in Figure 83 (a-d). This area is dark in the Ba, Co and Fe map. But it is bright in the Sr map. It is Ba-, Co- and Fe- deficient and Sr-enriched.
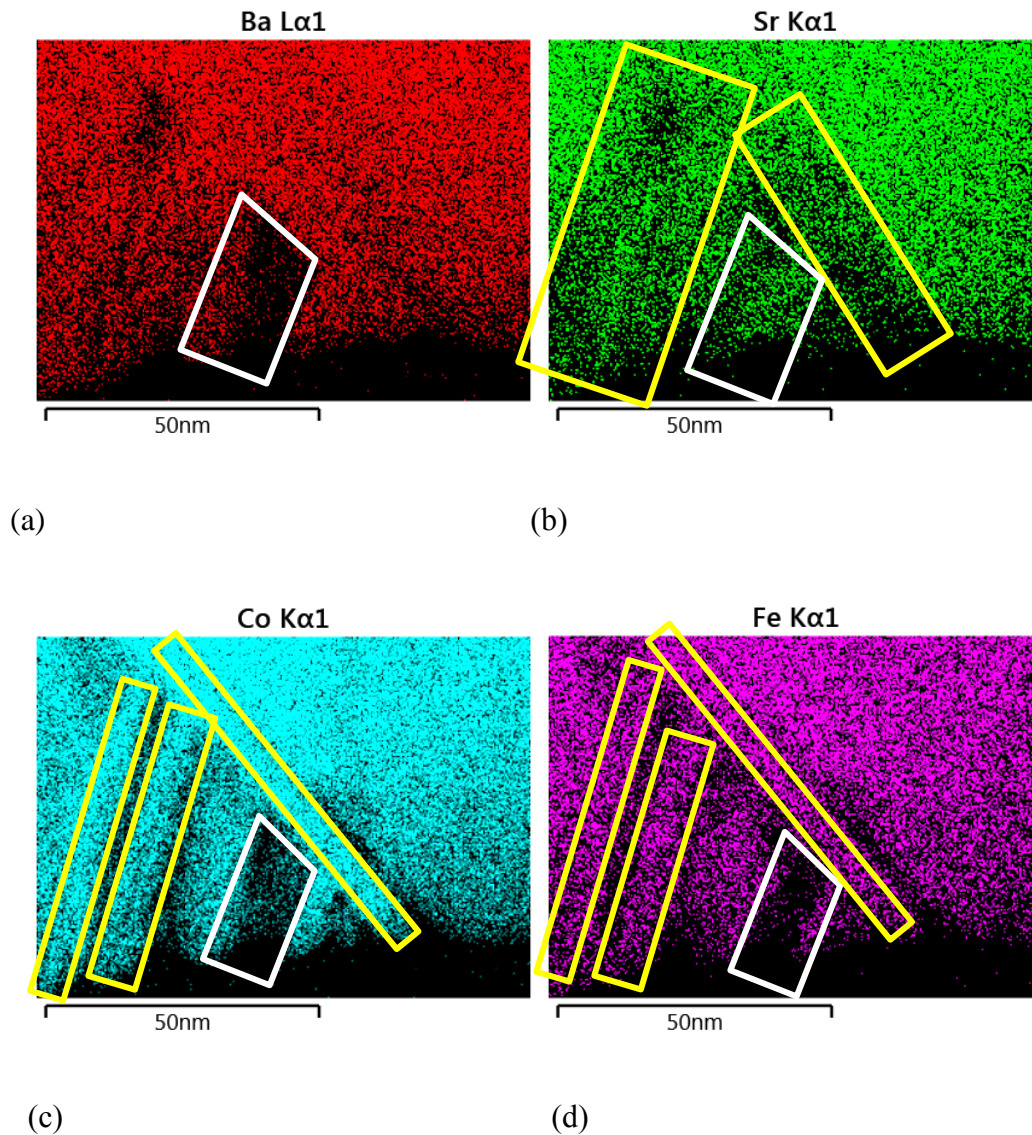
Figure 83. EDX element map of (a) Ba, (b) Sr, (c) Co and (d) Fe with yellow frames indicating lamellar phase and white frame indicating a Sr enriched phase. These were acquired from C-800°C-30min in the framed area in Figure 82.

*4.2.9.1.3.2 Discussion*

The plate-like phase is Sr-deficient and the area in the white frame is Sr-enriched, indicating Sr may migrate from the plate-like phase to this area. In one study, the plate-like phase was found next to a Sr-enriched carbonate phase [16]. Thus the Sr-enriched carbonate phase may be in the Sr-enriched area, suggesting Sr may migrate from the plate-like phase to the carbonate phase. The plate-like phase is Co-enriched and its neighbouring areas are Co-deficient, indicating Co may migrate from the neighbouring areas to the plate-like phase. A secondary phase formation mechanism was obtained: the plate-like phase and the carbonate phase exchanges cations (Co and Sr) to obtain the required

cations and to grow. This mechanism was pointed out for the first time. The Co and Fe enrichment in the plate-like phase was also observed by M. Arnold et al. [16].

### 4.2.9.1.4 The composition of one plate-like phase and its neighbour area

*4.2.9.1.4.1 Results*

The atomic concentration of Ba, Sr, Co and Fe in the plate-like phase and in a neighbour area of one plate were characterised by EDX. A C-800°C-30min sample was studied for this purpose. The fractional error for the concentration of each element were 1%, 2%, 2% and 5%, respectively.

For the plate-like phase, the concentration of the elements were measured from 3 plates and were averaged to obtain $Ba_{0.24}Sr_{0.11}Co_{0.56}Fe_{0.09}O_x$. The errors (Ba ± 0.04, Sr ± 0.02, Co ± 0.04 and Fe ± 0.01) were contributed by the SD of the averaged values. Compared to the composition of BSCF, the plate-like phase was Sr-deficient and Co-enriched. The concentration of Ba of the plate-like phase varied significantly above and below that of BSCF. Fe concentration of the plate-like phase was almost the same as that of BSCF.

For a neighbouring area of a plate, the composition was $Ba_{0.29}Sr_{0.23}Co_{0.37}Fe_{0.10}O_x$. For the corresponding plate, the composition was $Ba_{0.20}Sr_{0.10}Co_{0.59}Fe_{0.10}O_x$. The concentration of Ba and Sr in the plate were lower than those in the neighbour area and the concentration of Co in the plate was significantly higher than that in the neighbouring area. The concentration of Fe in both phases were the same.

*4.2.9.1.4.2 Discussion*

The composition of the plate-like phase is consistent with the EDX element mapping where the plate-like phase is Sr-deficient and Co-enriched. In previous studies [16, 140, 141], the plate-like phase was also found to be Sr-deficient and Co-enriched.

The difference between the composition of the plate and that of the neighbouring area, may arise if Co migrates from the neighbour area to the plate and Ba and Sr migrate from the plate to the neighbour area. This was pointed out for the first time. In another study, the formation of the plate-like phase was ascribed to the high mobility of the cations in BSCF [140]. This reinforces that Ba, Sr and Co migrates.

## 4.2.9.2 The EBSD and EDX study

### 4.2.9.2.1 Results

Figure 84 (a) shows a cross section of the C-800℃-30min sample. Precipitates indicated by triangles and pores indicated by squares are seen. The arrow points in the direction of the original surface, which was damaged due to grinding and polishing. Figure 84 (b) shows an EBSD phase distribution map performed to an area in the frame in Figure 84 (a), the 'C' phase and 'B' phase identified by XRD were assigned to the blue areas and yellow areas, respectively. The 'C' phase was assigned to a portion of the precipitates indicated by triangles, suggesting the 'C' phase was found in the cross section of an annealed sample. The white areas were not mapped because the precipitates protrude from the surface and block the EBSD signal.



(a)                                    (b)
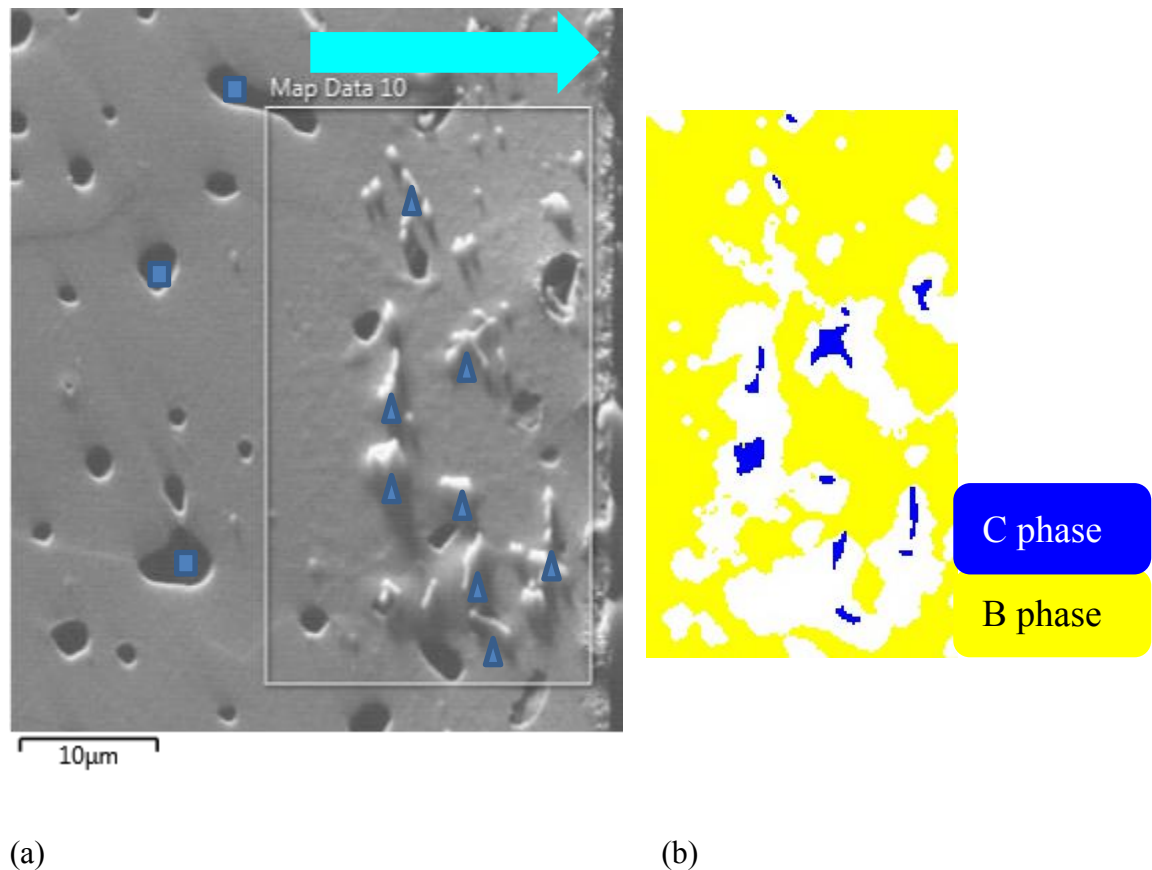
Figure 84. (a) SE image shows the cross section of C-800℃-30min with arrow indicating original surface, triangles indicating precipitates, squares indicating porosity and a frame outlining an area of interest. (b) An EBSD phase map of the area in the frame in (a). The 'C' phase is shown in blue, the 'B' phase is shown in yellow.

Another area (Figure 85) of the C-800°C-30min was studied by both EBSD and EDX to establish the composition of the 'C' phase. The arrow leads to the original sample surface which may be damaged due to polishing and covers several precipitates in a frame. Pores are seen on the top and bottom of the image. The 'C' phase was assigned to the precipitates and the 'B' phase was assigned to the flat areas in the frame, according to an EBSD phase distribution map. EDX element maps of Ba, Sr, Co, Fe and O (Figure 86) were obtained from the framed area. The elements were identified by the characteristic X-ray shown above each map. According to the maps, the 'C' phase precipitates are Ba, Sr and Fe depleted and Co- and O- enriched, suggesting the composition of the precipitates may be CoO.
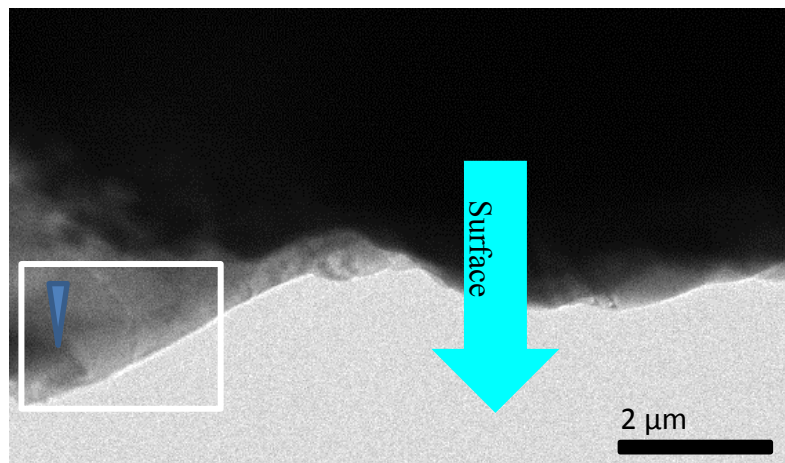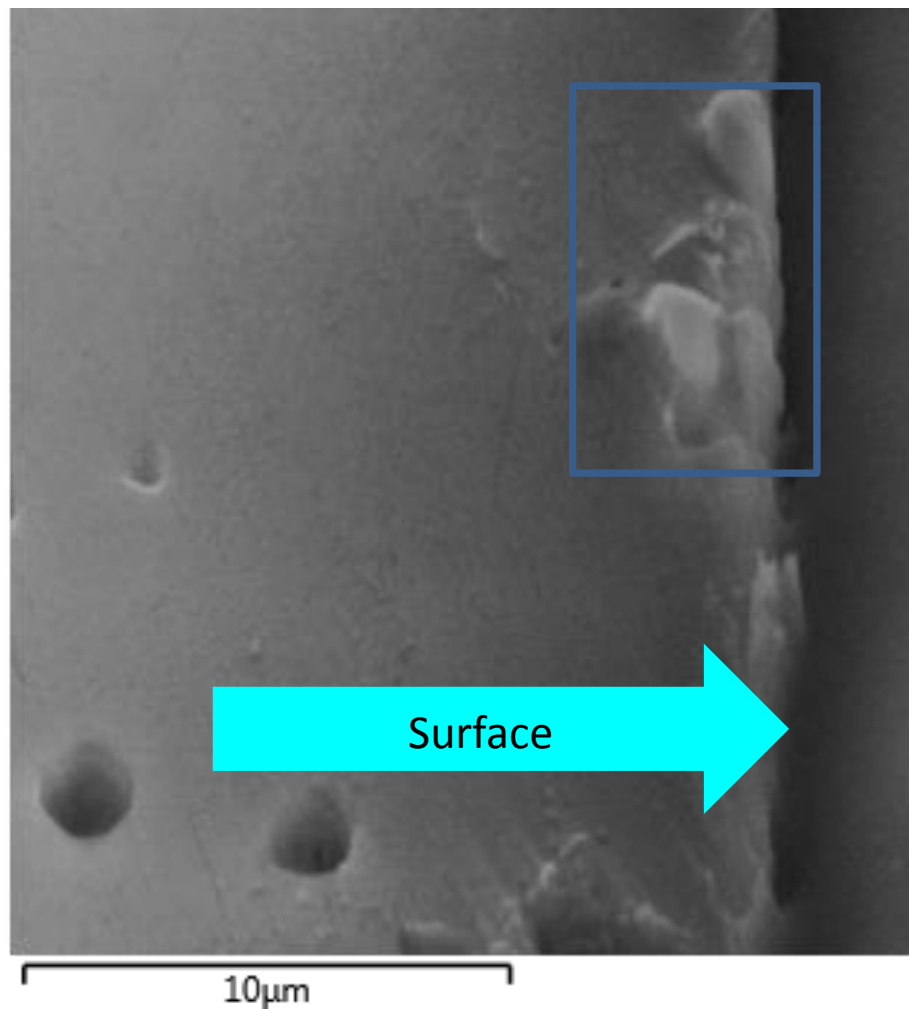


Figure 85. SE image shows the cross section of C-800°C-30min with arrow indicating original surface and frame outlining precipitates.
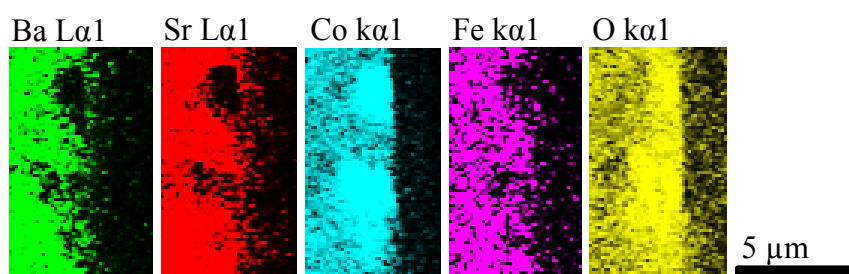
Figure 86. EDX element map of Ba, Sr, Co, Fe and O acquired from C-800°C-30min in the framed area in Figure 85.

## 4.2.9.2.2 Discussion

The observation of the 'C' phase in the cross section explains why this phase was detected by XRD which detects phases from surface and bulk but not by EBSD which detects phases from surface only.

In previous studies [16, 17], crystal structural evidence or chemical compositional information suggested that CoO precipitates were in cross-sections of annealed samples, which supports this study. This study is the first one which offers both crystal structural evidence and chemical compositional evidence to ascribe CoO to precipitates in the cross section.

## 4.2.9.3 The chemical reaction

For the Ba and Sr carbonate phase, the reported Ba/Sr ratio varied significantly in previous studies [16, 17, 133]. It also was found to vary in this study. Hence, a general formula of $(Ba, Sr)CO_3$ was assigned to this phase.

A chemical formula of $Ba_{1-a}Sr_aCo_{2-b}O_{5-\delta}$ was assigned to the plate-like phase in one study [140]. The composition of the plate-like phase in this study can also be described by this formula. Hence the formula was assigned to the plate-like phase in this study.

In another study [17], $(Ba, Sr)_x(Co, Fe)_yO_z$ was assigned to the BSCF the stoichiometry of which was changed. Such BSCF was next to the Co-enriched phases and $(Ba, Sr)_x(Co, Fe)_yO_z$ was Co-deficient [17]. In this study, the BSCF next to the Co-enriched phases was also Co-deficient and changed in stoichiometry, hence $(Ba, Sr)_x(Co, Fe)_yO_z$ was assigned to such BSCF.

The other secondary phases identified in the cross section are a $Ba_{0.5}Sr_{0.5}CoO_3$ phase and a CoO phase.

In summary, a reaction formula (Equation 34) was developed. α, β, γ, ε and θ vary depending on the mass balance of the equation. This was established for the first time.

$$Ba_{0.5}Sr_{0.5}Co_{0.8}Fe_{0.2}O_{3-\delta} + \alpha CO_2$$
$$\rightarrow \alpha(Ba, Sr)CO_3 + \beta Ba_{0.5}Sr_{0.5}CoO_{3-\delta} + \gamma(Ba, Sr)_x (Co, Fe)_y O_z$$
$$+ \varepsilon Ba_{1-a}Sr_aCo_{2-b}Fe_bO_{5-\delta} + \theta CoO_{1-\delta}$$
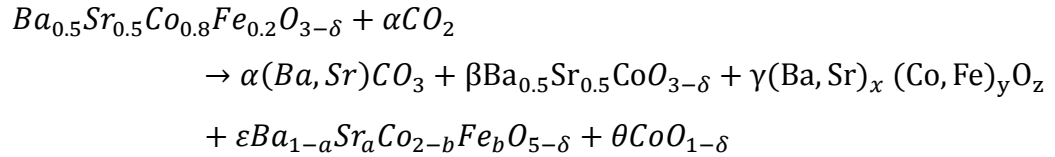
Equation 34

### 4.2.9.4 The secondary phase formation mechanisms

A schematic drawing (Figure 87) of the decomposed cross section was obtained based on the results and shows the secondary phases and corresponding compositions. The fact that the cross section covered by a continuous carbonate layer contains the CoO and plate-like phase is in agreement with previous studies [16, 17, 133].

### 4.2.9.4.1 The carbonate phase formation and the plate-like phase formation

Ba and Sr were uniformly distributed in a BSCF pellet. After decomposition, the plate-like phase is Ba- and Sr- deficient, while the surface precipitate layer contains only Ba and Sr, suggesting Ba and Sr may migrate from the former phase to the latter phase. Evidence in this study shows that Ba and Sr migrate away from the plate-like phase. In one study [17], Ba and Sr were found to diffuse from the bulk to the surface precipitate layer to form carbonates. Hence, the Ba and Sr which migrate away from the plate-like phase may diffuse to the surface precipitate layer to form carbonates, which was pointed out for the first time. In addition to the surface carbonate, a Sr-enriched carbonate phase was tentatively assigned to an area next to the plate-like phase, the Sr cations may also diffuse to this carbonate phase. In another study [140], the Co cation radius in the plate-like phase was found to reduce due to valence increase, evidenced by EELS. The smaller Co cations made the cubic perovskite structure less stable [140]. This may initialise the Ba and Sr diffusion. In addition to the Ba and Sr diffusion, Co was evidenced to migrate to the plate-like phase.

4.2.9.4.2 The CoO phase formation and the $Ba_{0.5}Sr_{0.5}CoO_3$ phase formation

As suggested by Efimov et al. [140], the radius of Co can be reduced at high temperatures, which makes the perovskite structure less stable. As evidenced in this study, Ba and Sr migrate away from certain areas during decomposition. The migration may be a result of the less stable structure. It may produce the CoO phase after Ba and Sr are exhausted in the areas. As evidenced in this study, Co migrates to and enriches in certain areas to form the $Ba_{0.5}Sr_{0.5}CoO_3$ phase. The less stable perovskite structure may also initialise this.
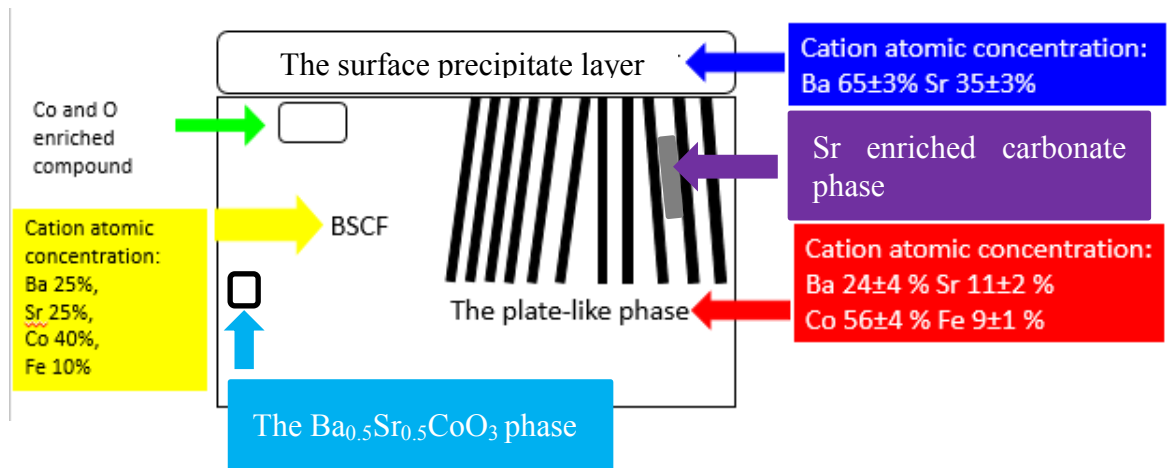


Figure 87. A schematic drawing of the cross section of the C-800°C-30min with the compositions of the phases.

# 4.2.10 The interface study

The interfaces between the plate-like phase and the BSCF in cross-section of C-800°C-5min were studied by HRTEM to obtain crystallographic information to elucidate the decomposition mechanism.

### 4.2.10.1 The interface of the plate-like phase and BSCF

In this and following sections, the plate-like phase was termed the lamellar phase because a lamellar structure was observed within each plate using HRTEM. In each of Figure 88 (a - c), a red line separates the lamellar phase from the cubic BSCF phase. The lamellar phase is above the cubic phase. For image a, the DP on the left was obtained from the lamellar phase, the DP on the bottom was obtained from the entire image. The diffraction spots in the red circles are from the lamellar phase, while the spots in the blue circles belong to the cubic BSCF phase. For image b, each DP was obtained from the area on its left. For image c, the upper DP was obtained from the lamellar phase and the lower DP was obtained from the cubic phase.

Figure 88 (a - c) shows three interfaces with the cubic BSCF in the [011], [001] and [100] orientations, respectively. In Figure 88 (a) and (b) the lamellar phase is indexable using the 15R hexagonal structure with a=b= 5.4489(1) Å (ICSD: 165236), c= 33.8036(7) Å (ICSD: 165236), and space group R-3mH. This structure was first assigned to a lamellar phase by K. Efimov et al. [140, 200]. In these cases the angle between the BSCF 100 g vector and the lamellar is 44 - 45°. The lamellar phase in Figure 88 (c) appears to have a different structure from the 15R variant present in the other images. The pattern in Figure 88 (c) is tentatively assigned to the [210] pattern of $BaFeO_{2.93}$ with rhombohedral structure and lattice parameters of a=b= 5.6915(5) Å (ICSD 167059), c=27.981(1) Å (ICSD 167059) and spacegroup R3m. This phase was assigned to the lamellar phase for the first time. The lattice parameters determined from Figure 88 (c) according to this index are smaller than that of $BaFeO_{2.93}$. The diffraction pattern suggests a large unit cell because the largest d-spacing is 8.61 ± 0.20 Å measured from the diffraction spot indicated by a triangle. In this case there is also a different orientation relationship between the phase and the BSCF: the hexagonal phase 0012 g vector forms a 7° angle with the cubic 001 g vector.

For each of the images shown in Figure 88, Table 32 lists the cubic plane in contact with

the lamellae. For each image, the lamellar segment width measured on DM software (Gatan, UK) is close to a multiple of the d-spacing of the cubic plane (from database) which suggests good crystallographic matching at the interface, as has been reported elsewhere [143].

(b)

Dark chains

Bright spots

5 nm

15R hexagonal structure
[$\bar{1}$10] diffraction pattern

Cubic
[001] diffraction pattern

$11\bar{1}2$
$11\bar{9}$
$00\bar{1}2$
$11\bar{3}$
$00\bar{9}$
$110$
$00\bar{3}$
$113$
$\bar{1}1\bar{1}2$
$\bar{1}1\bar{9}$
$009$
$\bar{1}1\bar{3}$
$003$
$\bar{1}10$
$0012$
$\bar{1}1\bar{3}$
$119$
$\bar{1}112$

$\bar{2}00$
$\bar{1}10$
$110$
$0\bar{2}0$
$020$
$1\bar{1}0$
$110$
$200$
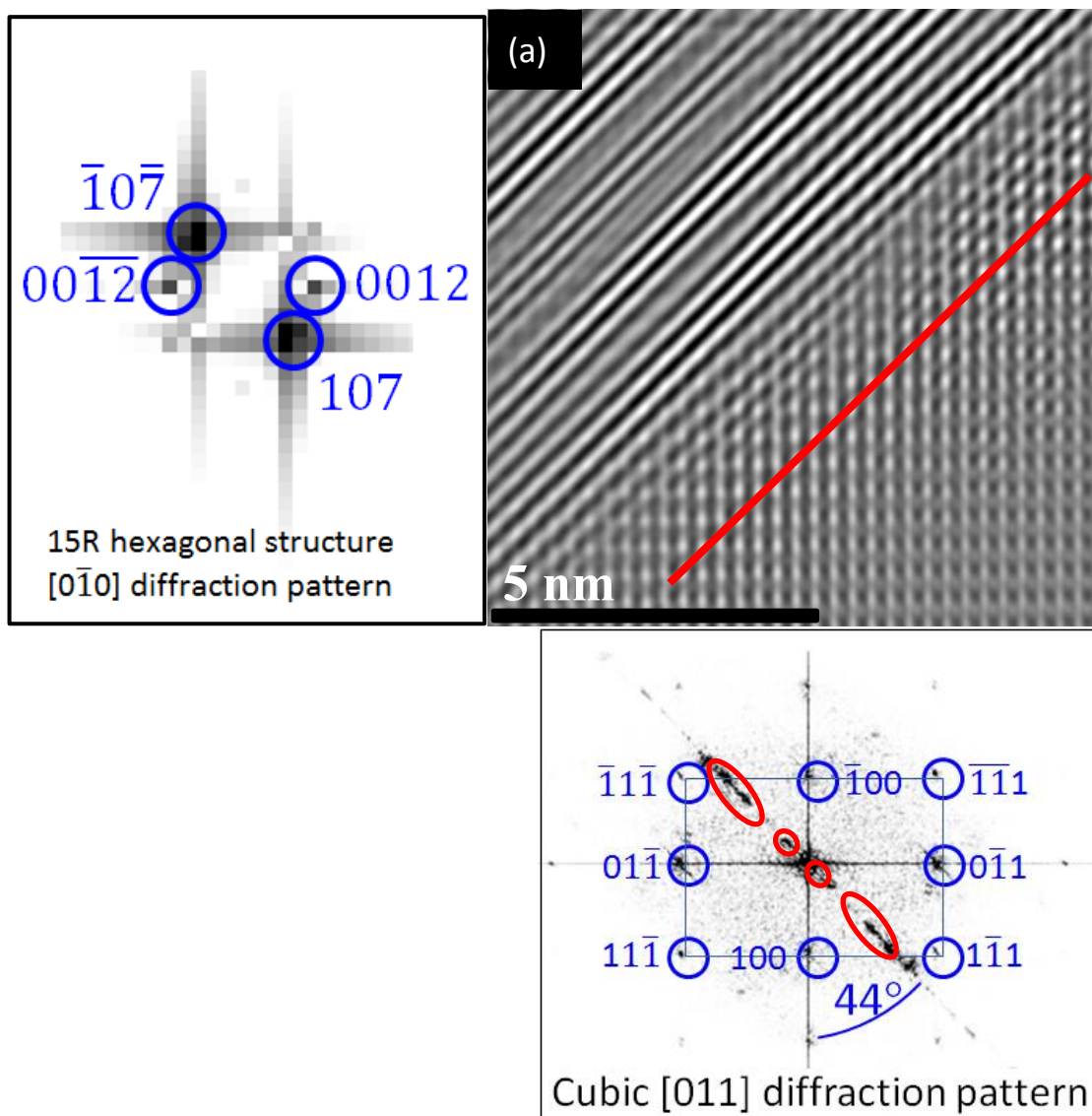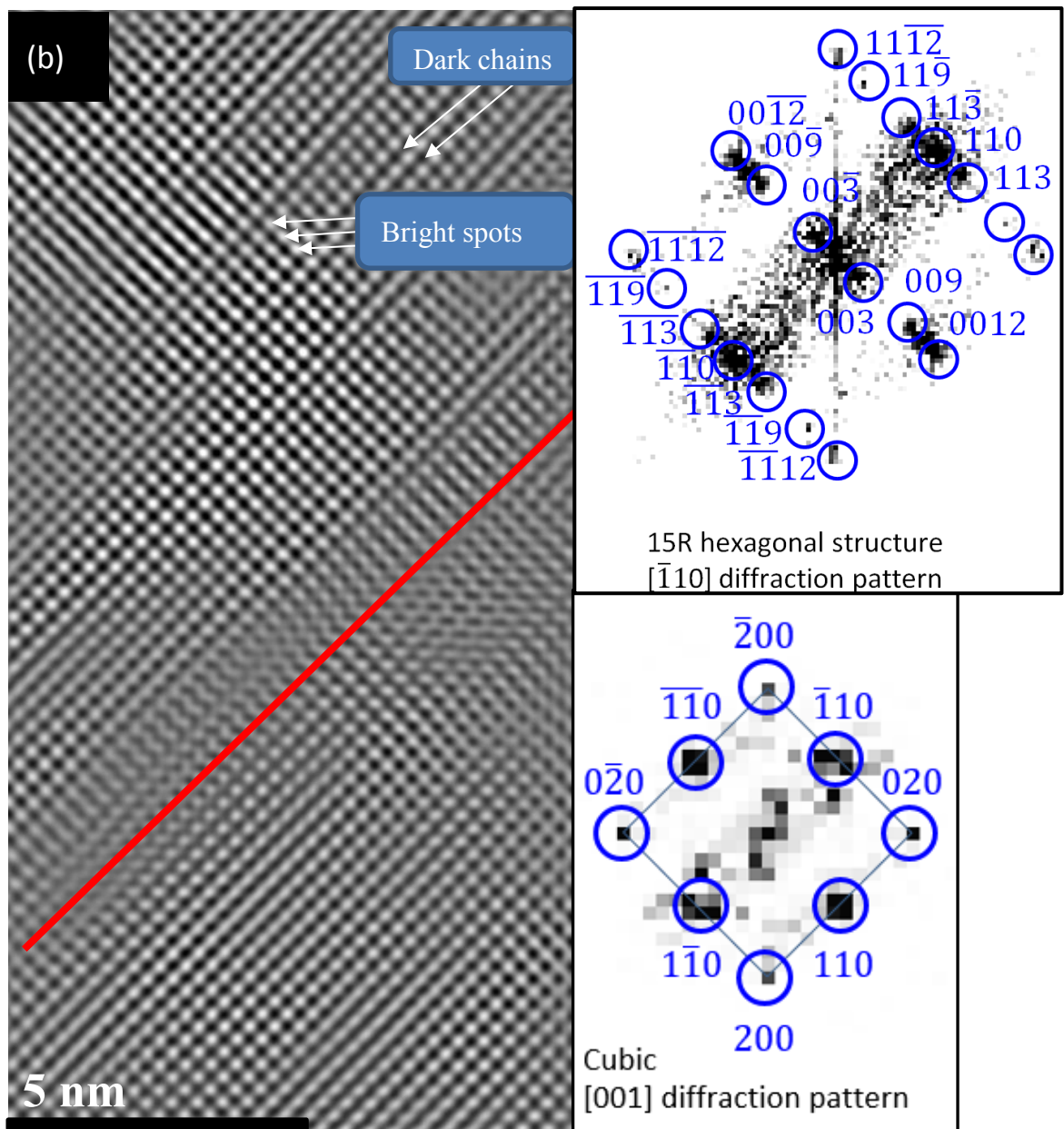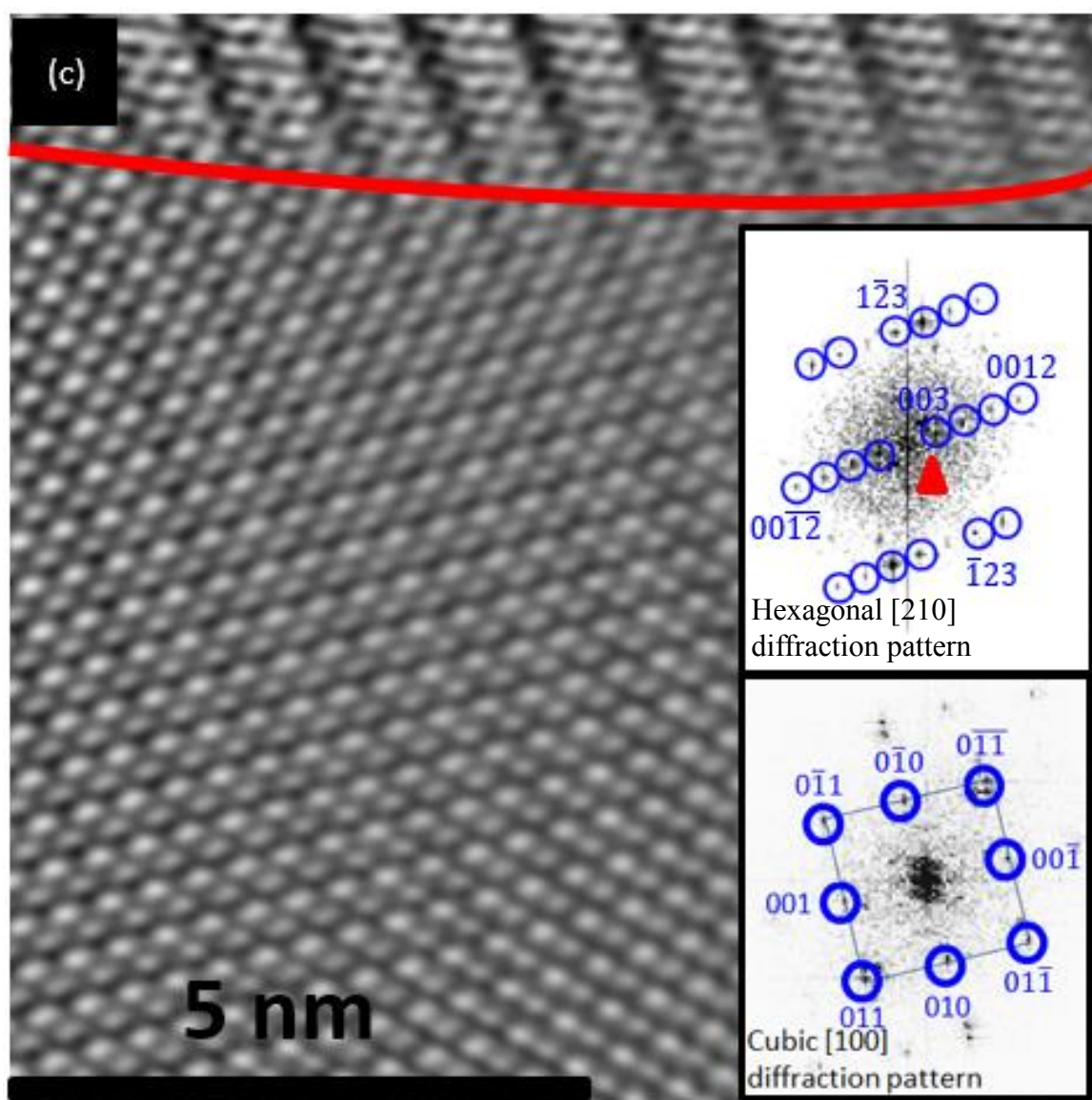
Figure 88. HRTEM images (a-c) shows three lamellae and BSCF interfaces with indexed diffraction patterns given as insets or next to image. These were obtained from C-800℃-5min. The red lines indicate the interfaces. The red circles highlight diffraction spots due to lamellae. Blue arrows indicate morphological characteristics. Red triangle indicates diffraction spot suggesting large unit cell.

Table 32 Crystallographic information at the phase interfaces.

| Image | Cubic contact plane | Cubic plane d-spacing | ICSD code of cubic planes | Lamellae segment width | Structure of lamellae and observing zone axis |
|---|---|---|---|---|---|
| a | (3-22) | 0.9660 Å | 109462 | 3.29 ± 0.01 Å | 15R along [0-10]hex |
| b | (110) | 2.8164 Å | | 12.19 ± 0.03 Å | 15R along [-110]hex |
| c | (08-1) | 0.4940 Å | | 8.61 ± 0.20 Å | R3m along [210]hex |

4.2.10.1.1 The composition of a lamellar phase

For image b, the morphology of the lamellar phase is the same as that of the lamellar phase reported in another study [140]. Both lamellar phases were observed along the same zone axis and they have the same structure. Hence image b may be equivalent to the image shown in that study. In that study [140], the A-site cations (mainly Ba) were assigned to the bright spots indicated by arrows in image b, the dark chains indicated by arrows in image b are A-site vacancies. The B-site cations (mainly Co) were assigned to the chain between two dark chains. The cations were tentatively assigned to the lamellae in image b in the same way. Such a Ba and Co enriched composition is in agreement with the EDX results ($Ba_{0.2}Sr_{0.1}Co_{0.6}Fe_{0.1}O_x$). A schematic diagram of the lamellar phase in the study of Efimov et al. [140] is shown in Figure 89.
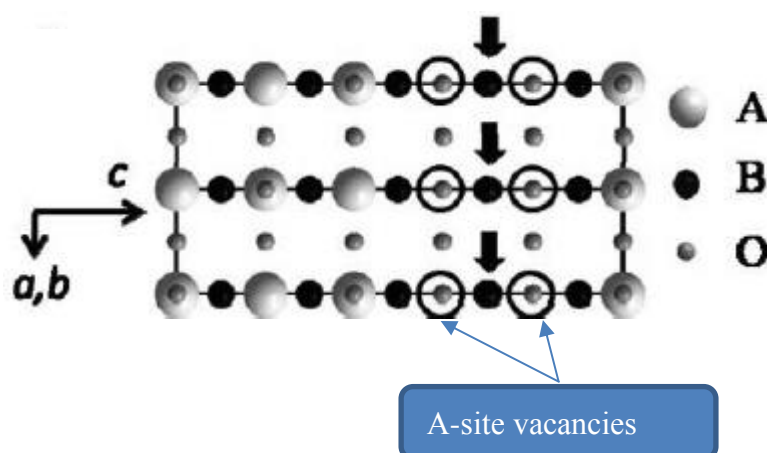


Figure 89. A schematic diagram of the 15R hexagonal structure observed along the [-110] hexagonal zone axis (From Efimov et al. [140]).

### 4.2.10.1.2 The rapid formation of the lamellar phase

The lamellae show similar morphology to that observed by P. Muller et al. [141], which were observed after 100 hours anneal in ambient air, but formed more rapidly in this study. The main differences between the two studies are that $CO_2$ was involved in this study and $CO_2$ reacted with BSCF to produce carbonates. As suggested by this study, the (Ba, Sr)$CO_3$ on the surface formed rapidly and obtained Ba and Sr mainly from the lamellar phase by diffusion. Hence the rapid formation of the lamellae can be a result of the rapid formation of the carbonates. This mechanism was suggested for the first time.

### 4.2.10.1.3 Noise in the DPs

There is a dark and noisy area in the centre of each DP. This is caused by the strong irradiation of the direct beam [184]. The spots which are not circled are noise. Similar noise was also observed in another study [141] and was attributed to beam damage (an accumulation of the microscope beam damage and ion beam milling damage). The damage produced amorphous areas on the sample which produced noise in the DPs. The TEM samples in this study were also prepared by ion beam milling and irradiated by microscope beam hence the noise in DP can also be attributed to beam damage.

### 4.2.10.2 A triple phase area

Figure 90 shows a HRTEM image of a triple junction between three phases (each phase was indicated in the image); a $Ba_2Co_9O_{14}$ rhombohedral phase (BCO) with space group R-3mH and lattice parameters a=b=5.6958(4) Å, c=28.909(4) Å (ICSD: 240500), a $Co_3O_4$ cubic phase with space group Fd-3m and lattice parameters a=b=c=8.0835(6) Å (ICSD: 24210), and cubic BSCF. Diffraction pattern analysis showed that the BCO [241] zone axis, the $Co_3O_4$ [110] zone axis and the BSCF [011] zone axis are parallel.

There is a good plane match at the interfaces between the phases. The BCO (0-14) plane with d-spacing 3.8 ± 0.2 Å is in contact with the BSCF (-100) plane with d-spacing 4.0 ± 0.2 Å. The BCO (0-28) plane with d-spacing 2.1 ± 0.1 Å is in contact with the $Co_3O_4$ (00-4) plane with d-spacing 2.2 ± 0.1 Å. The $Co_3O_4$ (004) plane with d-spacing 2.2 ± 0.1 Å is in contact with the BSCF (-200) plane with d-spacing 2.1 ± 0.1 Å. All d-spacing were measured on DM software (Gatan, UK).

This image was obtained from the cross section of a sample. The top direction leads to the sample surface which was eroded away by ion beam milling. The bottom direction leads to the bulk of sample. Thus, the BCO phase lies closer to the surface than the $Co_3O_4$ phase, which is closer to the bulk, suggesting that the $Co_3O_4$ phase forms below the other decomposition products, and explains its general absence on the surface images.
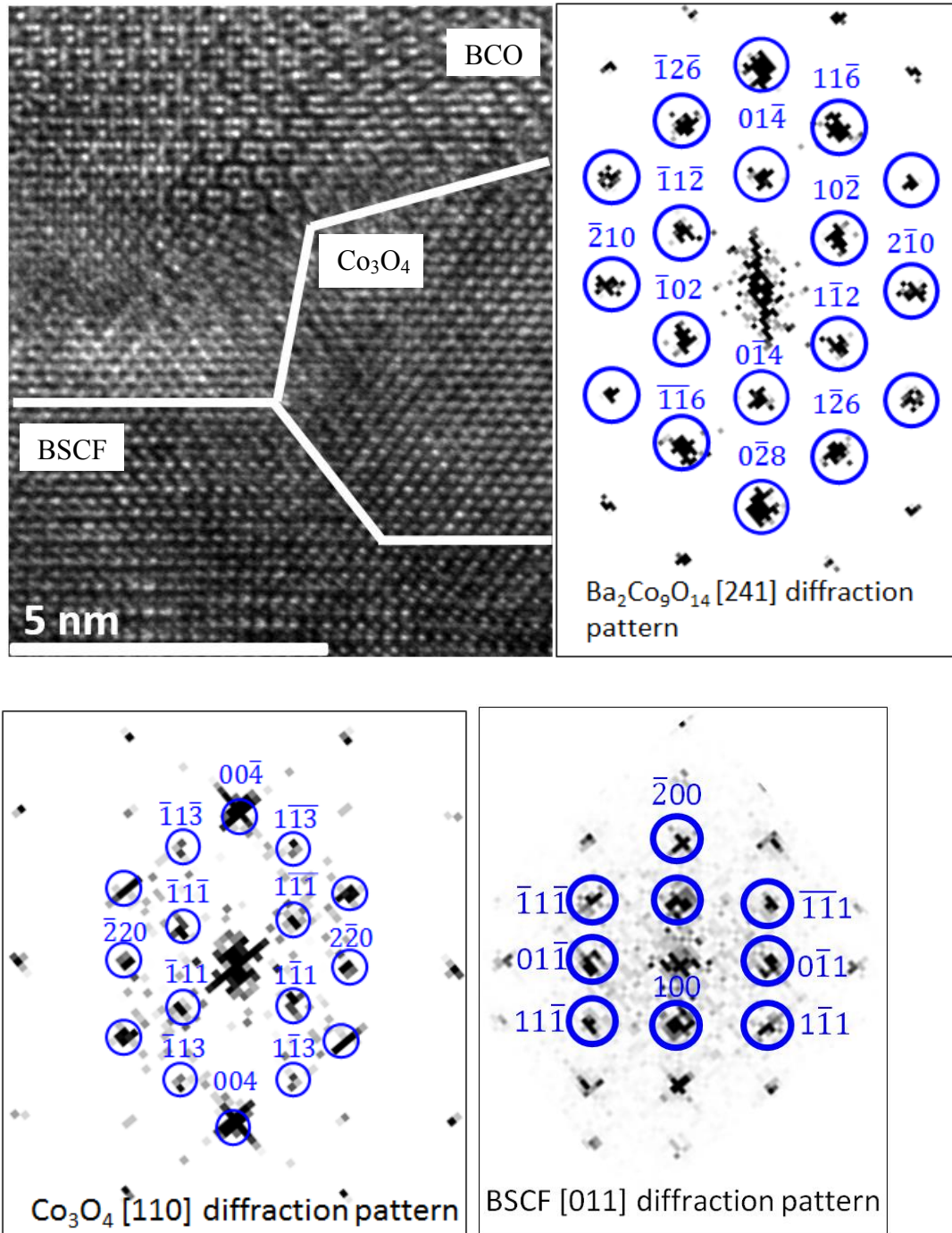


Figure 90. HRTEM image shows a triple phase area observed from a cross section of the

C-800°C-5min. White lines indicate interfaces. The indexed diffraction patterns of different phases are given with zone axis suggested.

As evidenced by this study and another study [17], Ba and Sr diffused from the bulk to the surface to form carbonates. The Ba and Sr cations may locally be exhausted in the bulk, in which case a Co and Fe enriched phase would be formed. This may be the reason for the formation of the $Co_3O_4$ phase in the bulk. This was pointed out for the first time. The $Co_3O_4$ phase was assigned based on diffraction information only. Hence the composition may vary to involve Fe.

### 4.2.10.3 Cubic to lamellae pathways

In previous studies [141, 158], the authors suggested that the hexagonal structure lamellar phase was obtained by moving a portion of the cubic (-111) planes along the cubic [-1-11] direction to change the cubic close pack to the hexagonal close pack, in which case the hexagonal <0001> zone axis is parallel to the cubic <111> zone axis. However, Efimov et al. [140] suggested that this mechanism cannot explain all the orientation relations between the cubic and hexagonal structure observed in their study hence there is more than one pathway. In this study, the hexagonal <0001> zone axis is not parallel to the cubic <111> zone axis at the interfaces, suggesting the lamellae may be formed via other pathways. Hence there is more than one pathway, which is in agreement with Efimov et al. [140].

In one study [70], the authors suggested that the cubic {101} planes are the diffusion path for oxygen, and Co cations can migrate to the high oxygen concentration {101} planes to react with oxygen and form the lamellar phase, which is why the lamellar phase in their study formed parallel to the {101} planes. In image b of this study, the lamellar phase is also parallel to the {101} planes and the Co cation chains in the lamellae are parallel to the {101} planes. Hence, the lamellar formation mechanism suggested by Liang et al. [70] may explain the lamellar formation in image b. This mechanism is different from the cubic {111} plane moving mechanism. Hence, there are at least two mechanisms for the cubic phase to transform to the lamellar phase.

### 4.2.10.3.1 Orientation relations

In one study [140] , the author suggested that crystallographic orientation relation between the plate-like phase and the cubic BSCF is not well defined and showed various

orientation relations (Column 1 Table 33). Three other studies [70, 141, 143] also showed various different relations (Table 33). These results were obtained under similar experimental conditions, suggesting the variation in the orientation relation is not caused by experimental conditions. The orientation relations obtained in this study are summarised in Table 33. Relation 10 and 11 agree with previous studies [140, 141], relations 12 and 13 were observed for the first time. The new relations support the argument of Efimov et al. [140] that the relation is not unique. The various relations can give rise to the various cubic to lamellae pathways

Table 33 The lamellae and BSCF crystallographic orientation relation

| Interface | The cubic BSCF plane is parallel with the lamellae | The cubic BSCF zone axis is parallel with the zone axis on the right | Hexagonal lamellar zone axis | Study |
|---|---|---|---|---|
| 1 | {111} | <011> | <100> | [141] |
| 2 | | | Not mentioned | [140] |
| 3 | | | Not mentioned | [143] |
| 4 | {001} | | [-110] | [140] |
| 5 | | | [-110] | |
| 6 | (3-11) | | Not mentioned | |
| 7 | (2-11) | | Not mentioned | |
| 8 | {011} | <001> | [-110] | |
| 9 | (1-2-1) | [11-1] | [00-1] | [70] |
| 10 | (3-22) | <011> | [0-10] | This study |
| 11 | {011} | <001> | [-110] | |
| 12 | (08-1) | <001> | [210] | |
| 13 | (-100) | <011> | [241] | |

4.2.10.3.2 Structures of the lamellar phase

This study observed a 15R hexagonal structure, a R3m rhombohedral structure and a R-3mH rhombohedral structure. The 15R structure was also observed by Efimov et al. [140] and the R-3mH rhombohedral structure was also observed by Muller et al. [141]. These suggest that the structure of the lamellar phase can vary.

4.2.10.3.3 The preferred zone axes and planes

Table 33 suggests that the low index cubic BSCF zone axes are likely (possibility: may be

larger than 54%) to be parallel with low index lamellar hexagonal zone axes and the low index cubic BSCF planes are likely to become the contact planes (possibility: 62%). Mueller et al. [139] suggested that the hexagonal phase nucleation energy barrier determines the orientation relation between the hexagonal and cubic BSCF. In other words, the relation affects the nucleation energy and the relations with energy lower than the barrier can be formed. Hence the reason why the low index axes and planes were preferred may be that the nucleation energy of them is low.

## 4.2.11 Conclusion on decomposition mechanism

Firstly, a less stable cubic perovskite structure where Co radius was reduced is the trigger for the formation of the lamellae [140]. In a few studies [201-203], Co was replaced by Fe in BSCF, the modified material showed higher stability (fewer lamellae) than BSCF because Fe is less flexible in changing valency, also suggesting Co radius variation is the trigger for the formation of lamellae. Secondly, the lamellae formed via various pathways and formed different orientation relations with BSCF depending on the nucleation energy barrier. The variety was caused by the high cation ion mobility, suggested by Efimov et al. [140]. The high cation mobility was also evidenced in this study by characterising the cation migration. Thirdly, as evidenced in this study, the lamellar phase contributed Ba and Sr to the $(Ba, Sr)CO_3$ phase by diffusion and the formation of the $(Ba, Sr)CO_3$ phase accelerated the formation of the lamellar phase. The crystallographic orientation relation between the carbonate and BSCF is well defined. Fourthly, a CoO phase may form in the bulk after Ba and Sr in the lamellae are exhausted. The decomposition steps are summarised and shown in the flow diagram in Figure 91. This decomposition mechanism was pointed out for the first time.

Co valency changes at high temperatures and cubic perovskite structure is destabilised.

↓

The lamellar phase is formed via various pathways and formed various orientition relation with BSCF.

↓

The Ba and Sr cations diffuse from the lamellar phase to form the BSC phase on the surface and the formation of the BSC phase accelerates the formation of the lamellar phase.

↓

A CoO phase may form after Ba and Sr are locally exhausted.

Figure 91. A schematic flow chart shows the decomposition process.

## 4.3 The interrelation between the cubic BSCF to hexagonal decomposition and the reaction between BSCF and $CO_2$

BSCF decomposed to lamellar phases with different hexagonal structures after long term (longer than 100 hours) heat treatment in air ($CO_2$ deficient environment) at 750 - 800 ℃ [70, 140, 141]. This decomposition may relate to the $CO_2$ enriched decomposition because similar lamellar phases were observed in the $CO_2$ decomposition in this study. To understand the relation, this interrelation study which has two stages was conducted.

In stage one, $CO_2$ effects were removed to observe phase changes and microstructure changes in $CO_2$ free environment. In stage two, $CO_2$ effects were applied to the samples decomposed in stage one to observe phase changes and microstructure changes.

For stage one, an inert gas environment ($N_2$) was chosen. The reason is that the $CO_2$ enriched decomposition during permeation was more significant when $CO_2$ appeared in the permeate side (an inert environment) than the feed side (an oxidising environment) [16].

# 4.3.1 CO$_2$ free slow decomposition (stage 1)

## 4.3.1.1 Secondary phase identification

### 4.3.1.1.1 Results

Figure 92 shows the XRD patterns of BSCF pellet and N-800℃-24hour. In the former pattern, all peaks match the powder diffraction file for a cubic perovskite BSCF phase. In the latter pattern, the peaks labelled by 'H1', 'H2', 'H3', 'H4', 'C' and 'B' match the powder diffraction file for $Ba_{0.9}Sr_{0.1}CoO_3$ (ICSD: 173505), $Ba_{0.5}Sr_{0.5}CoO_3$ (ICSD: 173507), $Ba_{0.3}Sr_{0.7}CoO_3$ (ICSD: 173508), $Ba_{0.2}Sr_{0.8}CoO_3$ (ICSD: 173509), cubic CoO and cubic BSCF, respectively. The peak labelled by 'U' does not match any powder diffraction file. The cubic perovskite BSCF phase has the space group Pm-3m and a lattice parameter of 3.9782 ± 0.0002 Å refined by TOPAS. All these Ba, Sr and Co phases have hexagonal structure and the P6$_3$/mmc space group, the lattice parameters of them are refined by TOPAS and shown in Table 34. The cubic CoO phase has the space group Fm-3m and a lattice parameter of 4.2490 ± 0.0045 Å refined by TOPAS. The crystallographic information was obtained from the powder diffraction files of BSCF (ICSD: 109462) and CoO (ICSD: 9865).

Table 34 Lattice parameters of the hexagonal phases in N-800℃-24hour

| Composition of secondary phase | Lattice parameters |
|---|---|
| $Ba_{0.9}Sr_{0.1}CoO_3$ | a=b=5.7663 ± 0.005 Å, c=4.7113 ± 0.007 Å |
| $Ba_{0.5}Sr_{0.5}CoO_3$ | a=b=5.4612 ± 0.016 Å, c=4.6153 ± 0.017 Å |
| $Ba_{0.3}Sr_{0.7}CoO_3$ | a=b=5.6683 ± 0.012 Å, c=4.1820 ± 0.031 Å |
| $Ba_{0.2}Sr_{0.8}CoO_3$ | a=b=5.4476 ± 0.005 Å, c=4.0985 ± 0.006 Å |
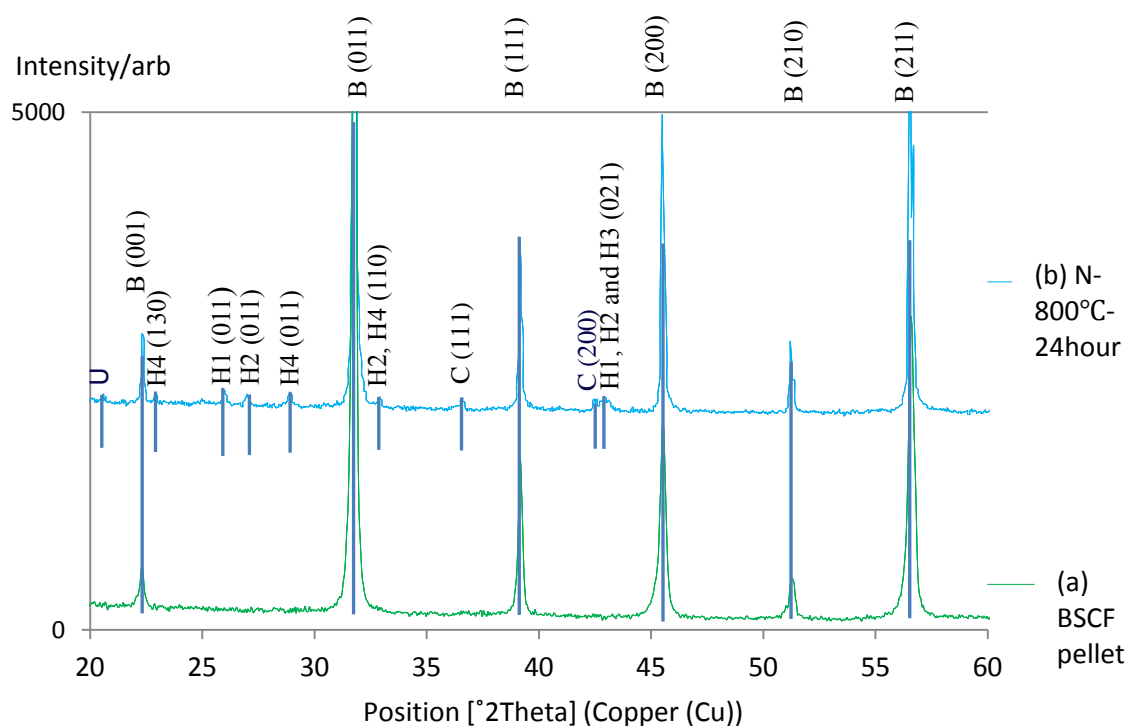
Figure 92. (a) An indexed XRD pattern of a BSCF pellet with peak indicators. (b) An indexed XRD pattern of N-800℃-24hour with peak indicators. B: BSCF. H1: $Ba_{0.9}Sr_{0.1}CoO_3$ phase, H2: $Ba_{0.5}Sr_{0.5}CoO_3$ phase, H3: $Ba_{0.3}Sr_{0.7}CoO_3$ phase, H4: $Ba_{0.2}Sr_{0.8}CoO_3$ phase, C: CoO phase and U: unknown.

The XRD pattern of the N-800℃-1hour is shown in Figure 93, all peaks match the powder diffraction file for the cubic perovskite BSCF phase, and no secondary phase was detected.
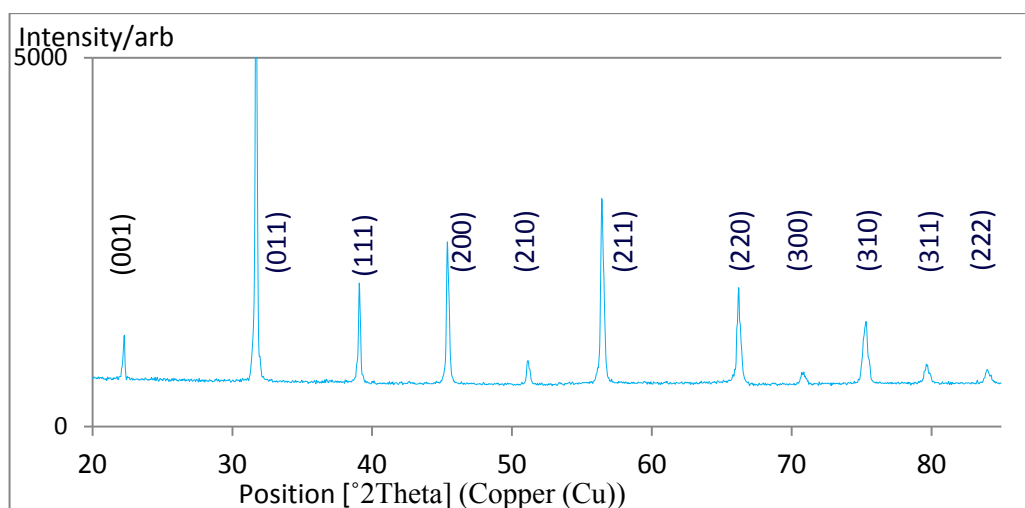


Figure 93. The indexed XRD pattern of the N-800℃-1hour.

4.3.1.1.2 Discussion

*4.3.1.1.2.1 The composition of the secondary phases*
The composition of the secondary phases is not clear at this stage. The secondary phases are temporarily denoted as the 'H1', 'H2', 'H3', 'H4' and 'C' phase.

*4.3.1.1.2.2 The structure of the secondary phases*
The 2H-hexagonal phase observed in a study [139] with $P6_3/mmc$ space group and lattice parameters of a = 5.63 Å and c = 4.38 Å is crystallographically similar to phase H2 and H3. Another hexagonal phase [143] with lattice parameters of a = 5.629 Å and c = 4.361 Å is also similar to the phases H2 and H3. These suggest that the crystallographic structure of phases H2 and H3 is in agreement with previous studies. However the 'H1' and 'H4' phase are reported for the first time.

4.3.1.2 Microstructure changes

4.3.1.2.1 Results
Figure 94 shows the surface of N-800℃-24hour. Precipitates with polygon morphology are seen on grains and grain boundaries, indicated by red and white arrows, respectively. The average radius of the grain precipitates and grain boundary precipitates are 0.26 ± 0.05 μm and 0.30 ± 0.15 μm, respectively. The grains show a maze-like structure the identity of which is not clear and will be addressed in the future.
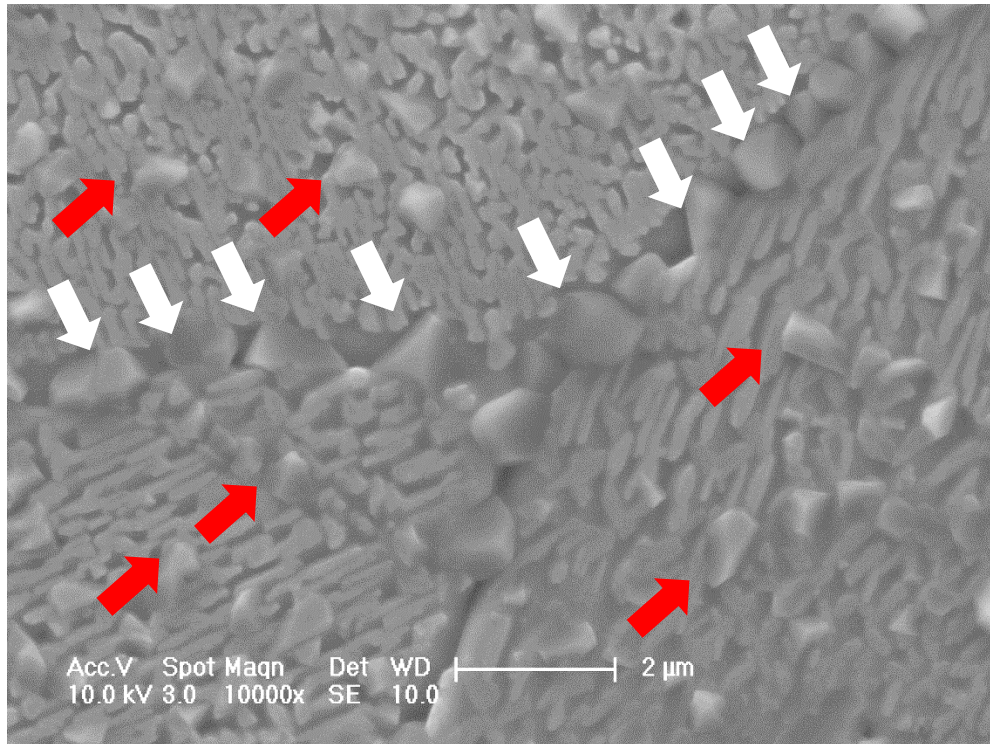
Figure 94. SE image shows the surface of the N-800°C-24hour with red arrows indicating grain precipitates and white arrows indicating grain boundary precipitates.

Figure 95 shows the surface of N-800°C-1hour where precipitates, grains, grain boundaries and pores can be seen. Plate-like precipitates indicated by arrows can be seen on the grain boundaries. A portion of them indicated by the red arrows are parallel to grain boundaries. The others are not parallel to grain boundaries. In the white frames, there are plate-like precipitates on grains. The average radius of the grain precipitates and grain boundary precipitates are $0.10 \pm 0.03$ μm and $0.19 \pm 0.05$ μm, respectively, suggesting the grain boundary precipitates are larger. The precipitate coverage is 0.4%. The plates are Co-enriched and Sr-deficient compared to the composition of BSCF, suggested by EDX linescans conducted in this study.
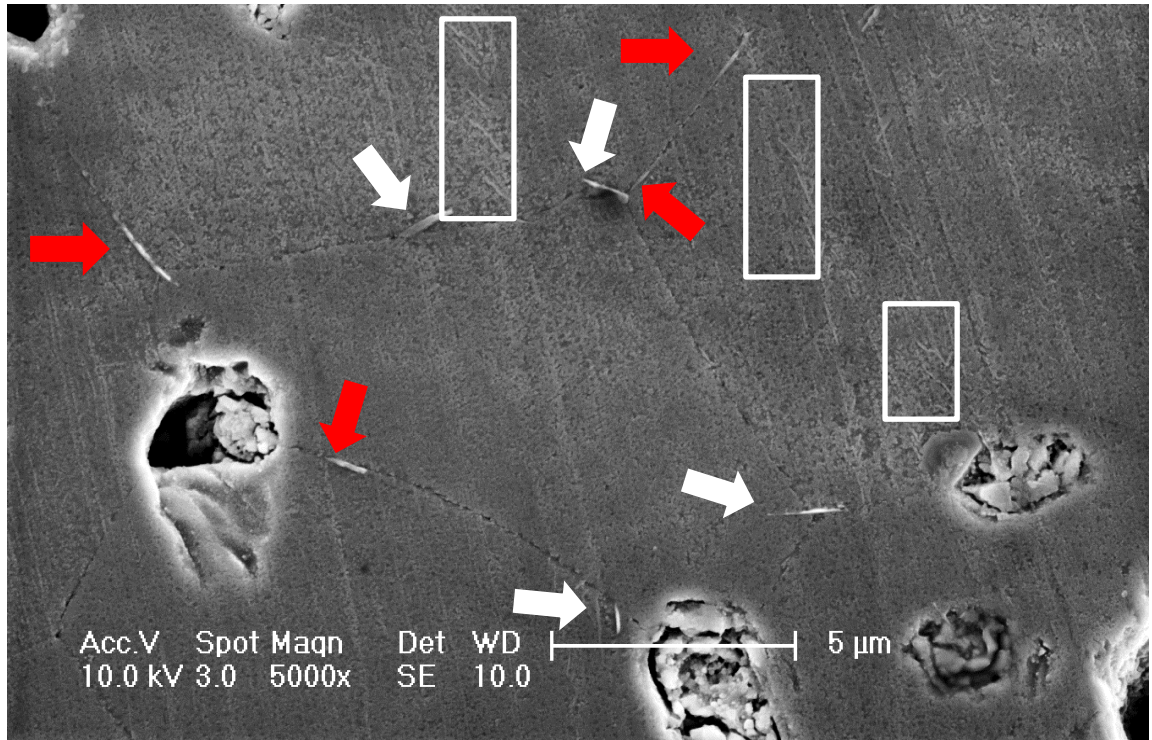
Figure 95. SE image shows the surface of the N-800°C-1hour with arrows indicating plate precipitates on grain boundaries. Red arrows indicate precipitates that are parallel to grain boundaries. Frames outline precipitates on grains.

4.3.1.2.2 Discussion

A series of studies [70, 140, 141, 143] suggested that the plate-like precipitate is Ba- and Co- enriched and Sr- and Fe- deficient, which is in agreement with this study.

Similar plate-like precipitates were also observed in another study of BSCF decomposition [70] in grain boundaries and were also Co-enriched. Co cations tend to migrate to O enriched areas to form such precipitates [70]. Grain boundaries contain more O than grains [70]. This may be why the grain boundary precipitates are larger than the grain precipitates in N-800°C-1hour. The other reason may be that grain boundary diffusion is faster than bulk diffusion [197], in which case the grain boundary precipitates obtain more cations to grow larger. Another reason may be that the heterogeneous nucleation barrier is lower at grain boundaries [204].

4.3.1.3 Annealing gas effects

4.3.1.3.1 Results

*4.3.1.3.1.1 Microstructure*

Figure 96 shows the surface of N-800℃-6hour with pores, precipitates and grain boundaries visible. A few plate-like precipitates indicated by arrows are seen on grain boundaries. One of them is parallel to the grain boundary. Precipitates with sphere morphology are seen on grains and grain boundaries. The average radius of the grain precipitates and grain boundary precipitates are $0.08 \pm 0.03$ μm and $0.155 \pm 0.05$ μm, respectively, suggesting the grain precipitates are smaller than the grain boundary precipitates. The precipitate coverage is 13%.
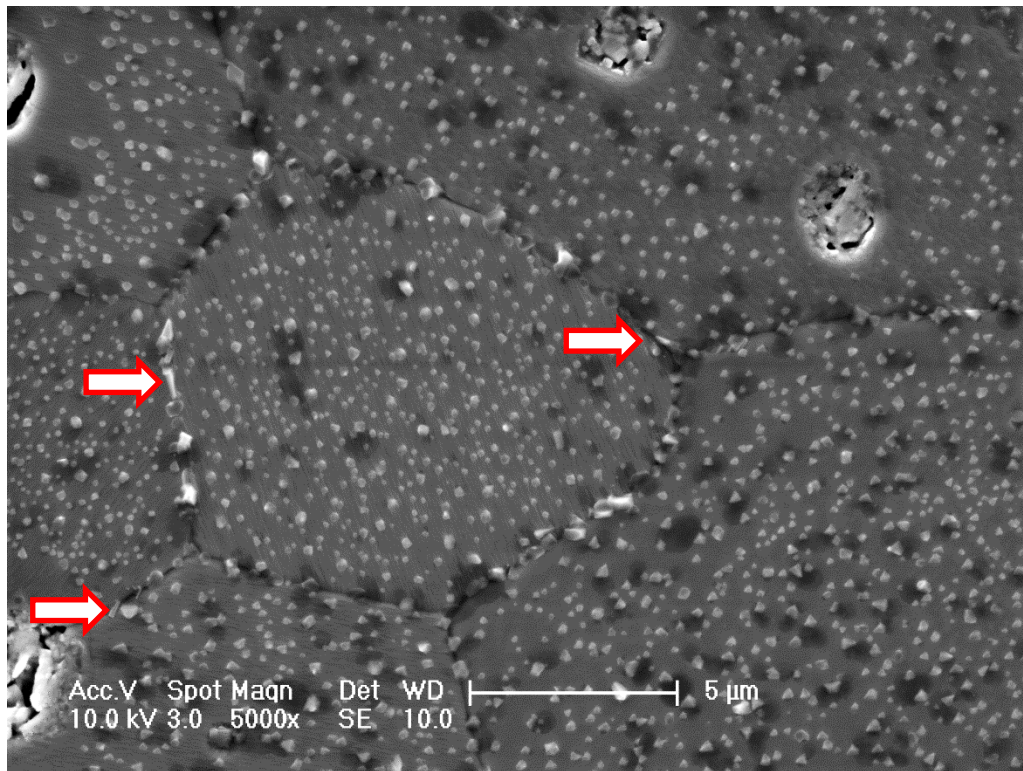


Figure 96. SE image shows the surface of the N-800℃-6hour with arrows indicating plate precipitates.

Figure 97 shows the microstructure of A-800℃-6hour. Polygon precipitates are seen on both grains and grain boundaries, a proportion of them are indicated by white arrows. Plate-like precipitates are seen on grain boundaries, a proportion of them are indicated by red arrows. The average radius of the grain precipitates and the grain boundary precipitates are $0.21 \pm 0.07$ μm and $0.34 \pm 0.18$ μm, respectively, suggesting the precipitates on grains are smaller than those on grain boundaries. The precipitate coverage is 5.6%.
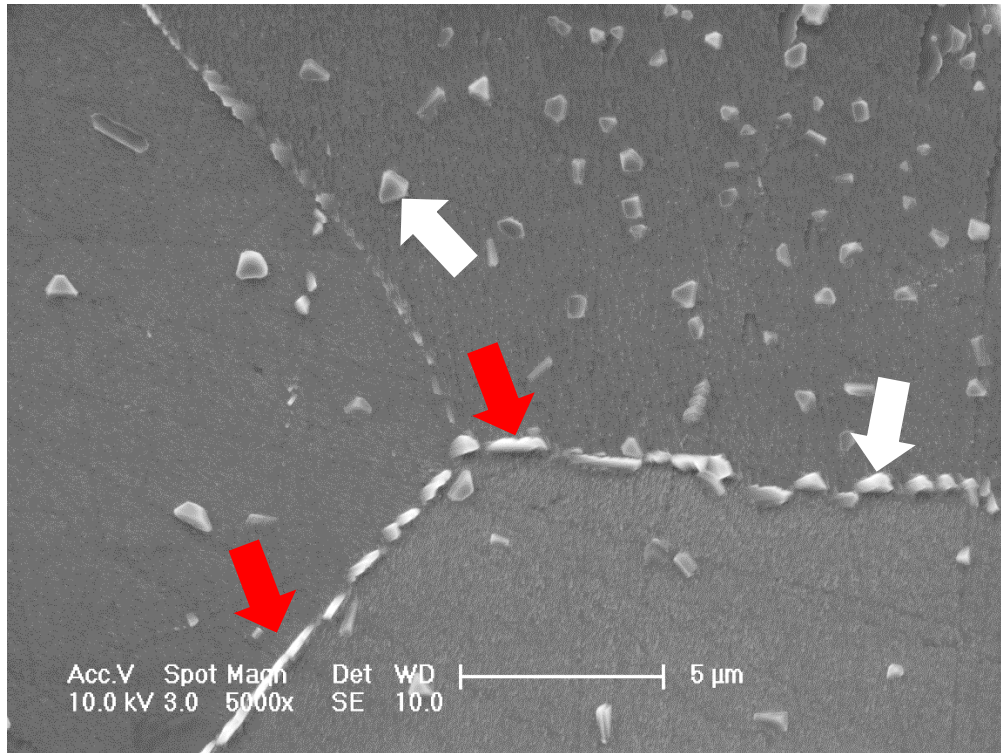


Figure 97. SE image shows the surface of the A-800℃-6hour with white arrows indicating polygon precipitates and red arrows indicating plate precipitates.

*4.3.1.3.1.2 Phase identification*

The XRD pattern of the N-800°C-6hour and the A-800°C-6hour are shown in Figure 98. For each pattern, all peaks match the powder diffraction file peaks for the cubic perovskite BSCF phase. Hence no secondary phase was identified.
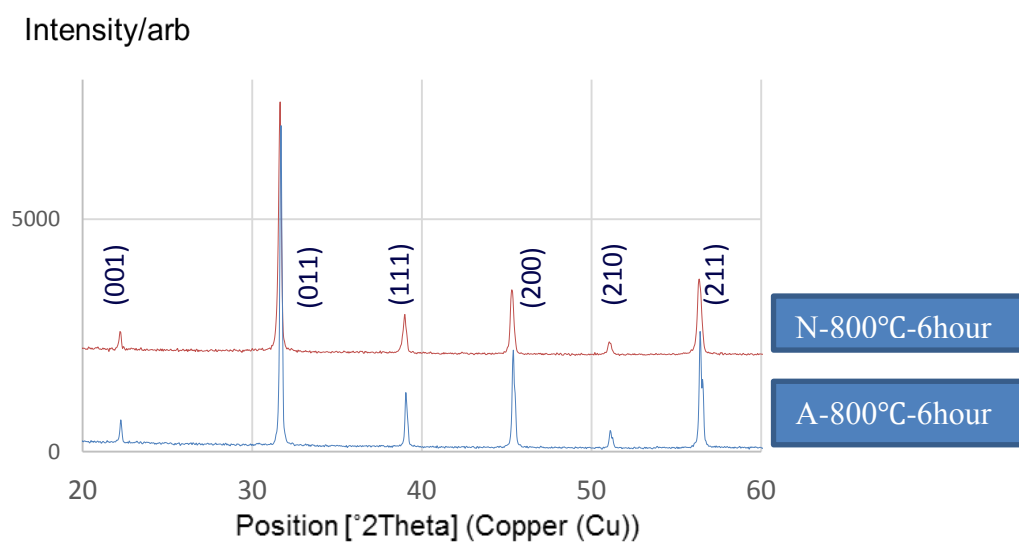


Figure 98. The indexed XRD pattern of the N-800°C-6hour and the A-800°C-6hour.

4.3.1.3.2 Discussion

In another study a BSCF membrane was studied after a permeation experiment [70], the content of a trigonal phase $Ba_{1-x}Sr_xCo_{2-y}Fe_yO_{5-\delta}$ in the feed side (with higher $PO_2$) was significantly lower than the permeate side (with lower $PO_2$). This may suggest that higher $PO_2$ restricts the formation of certain secondary phases. The overall precipitate coverage of the A-800°C-6hour is lower than that of the N-800°C-6hour, which may be attributed to the $PO_2$ effect because the main difference between the two samples is that the $PO_2$ of the former one is higher than the latter one.

For both samples, the grain boundary precipitates are larger than the grain precipitates. One reason may be that the heterogeneous nucleation barrier is lower at grain boundaries [204].

## 4.3.2 Relating two types of decomposition (stage 2)

### 4.3.2.1 Microstructure changes of surface

#### 4.3.2.1.1 A6C2

##### 4.3.2.1.1.1 The new preferred site of the BSC phase
###### 4.3.2.1.1.1.1 Result

Figure 99 (a – c) show the surface of A6C2 where precipitates and pores can be seen. The grain boundaries indicated by lines are covered by grey precipitates. Plate-like precipitates covered by grey precipitates are found on grains. Plate-like precipitates were induced by annealing in air (Figure 97). The grey precipitates were induced by the $CO_2$ annealing because such precipitates were not found after annealing in air (Figure 97). The BSC phase in C-800°C-2min was assigned to the grey precipitates due to their similar morphology and similar annealing condition of C-800°C-2min and A6C2. In addition to grain boundaries, the plate-like precipitates became another preferred site for the BSC phase precipitates because the BSC precipitates on plates are larger (0.14 μm ± 0.04 μm) than those (0.09 μm ± 0.03 μm) on grains and the coverage of the former is higher than the latter. This is the first aspect of the interrelation and was revealed for the first time.

###### 4.3.2.1.1.1.2 Discussion
For precipitate nucleation, the heterogeneous nucleation barrier is lower at boundaries

[204]. There are boundaries between the plate-like precipitates and BSCF grains. This may be the reason why the BSC phase precipitates prefer the plate-like precipitates.

As evidenced in this study, a neighbouring area of a plate-like precipitate is Ba-enriched compared to BSCF and the BSC phase precipitates need Ba and Sr. The neighbouring area may offer Ba more readily to the BSC precipitates than the BSCF grains. This may be another reason why the BSC phase precipitates prefer the plate-like precipitates and grow larger on the plates.

As characterised in this study, the a and b lattice parameters ($5.1397 \pm 0.0070$ Å refined by TOPAS) of the rhombohedral BSC phase is close to that of the hexagonal plate-like phase (Table 34). This may offer good lattice plane match which is the third reason for the preference of the precipitates, if the {110} planes or the {100} planes of both phases are parallel with the interface. An orientation relation study is needed in the future to find the contact planes.

*4.3.2.1.1.2 Plate-like phase affects the morphology of the BSC phase*

*4.3.2.1.1.2.1 Result*

In Figure 99 (a), the BSC precipitates on the grain show a similar morphology. A BSC precipitate on the plate is indicated by a red arrow. Its morphology is different from those on the grain (one of them is highlighted in a green frame), suggesting the plate-like precipitate affects the morphology of the BSC precipitates. This is the subsidiary aspect of the first aspect of the interrelation and was revealed for the first time.

*4.3.2.1.1.2.2 Discussion*

As evidenced in this study, the morphology of the BSC phase precipitates remain the same within a BSCF grain but vary from grain to grain because the precipitate orientation is affected by the BSCF grain orientation. For the BSC precipitates on the plate-like precipitate, their orientation may be affected by the plate-like phase. This is why their morphology is different from those on the grain. An orientation study is needed in the future to prove this.
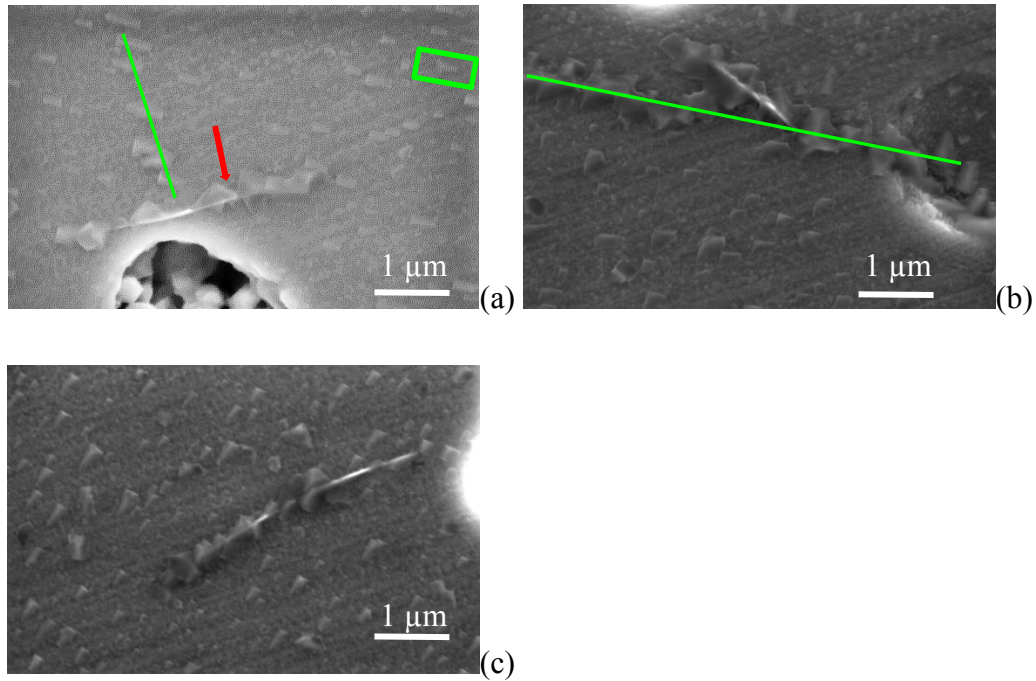
Figure 99. (a - c) SE images show the microstructure of A6C2 with lines indicating grain boundaries, a frame outlining a BSC precipitate and arrow indicating a BSC precipitate with different morphology.

### 4.3.2.1.2 N1C5 and C-800°C-5min

*4.3.2.1.2.1 Results*

Figure 100 (a) shows the surface of the N1C5 sample. Precipitates can be seen on grains and grain boundaries. The BSC phase was assigned to the precipitates due to their similar morphology and similar annealing condition of N1C5 and C-800°C-5min. Pores are also seen in the microstructure. The areas close to the grain boundaries (a portion of them are indicated by white frames) show higher coverage (91 ± 3 %), compared to areas (such as the one indicated by a green frame) away from grain boundaries (59.618 % ± 3 %). Such coverage variation is not observed from C-800°C-5min shown in Figure 100 (b) which shows pores and BSC phase precipitates on grain boundaries and grains. Hence the 1hr $N_2$ annealing may create BSC phase favoured areas along the grain boundaries. N1C5 sample shows a higher average precipitate radius (0.32 ± 0.74 µm), compared to the C-800°C-5min sample (0.15 ± 0.07 µm). This suggests that the N-800°C-1hour sample is more vulnerable to decomposition than a BSCF pellet under $CO_2$ attack.

*4.3.2.1.2.2 Discussion*

Observed in this study, the N-800°C-1hour sample (Figure 95) showed plate-like

precipitates along the grain boundaries. The plates may be covered by BSC phase precipitates after $CO_2$ enriched annealing hence they are not seen in Figure 100 (a). As evidenced in this study, a neighbouring area of a plate-like precipitate is Ba-enriched compared to BSCF and the BSC phase precipitates need Ba and Sr. The neighbour may offer more Ba to the BSC precipitates than BSCF grains. This may be the reason why the BSC phase coverage is higher on the neighbouring areas than the grains. The other reasons may be low heterogeneous nucleation energy barrier at phase boundaries [204] and similar crystal structure and lattice parameters which were suggested earlier.
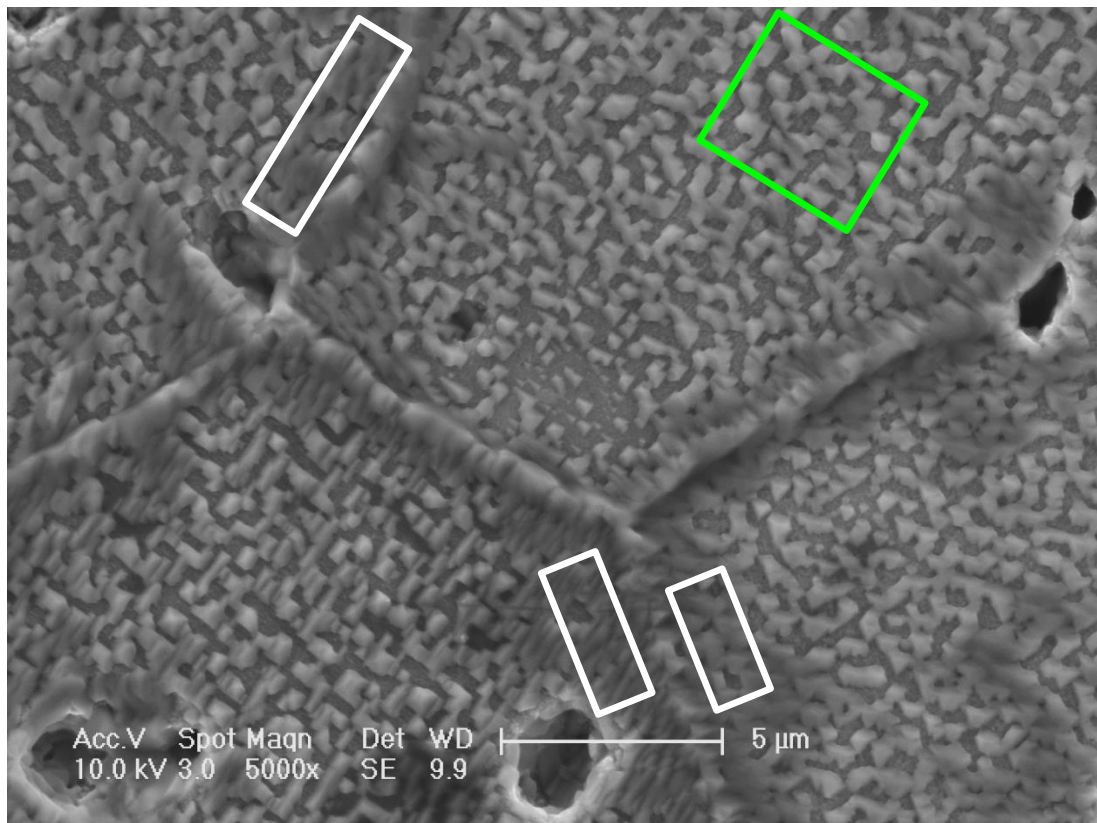


(a)
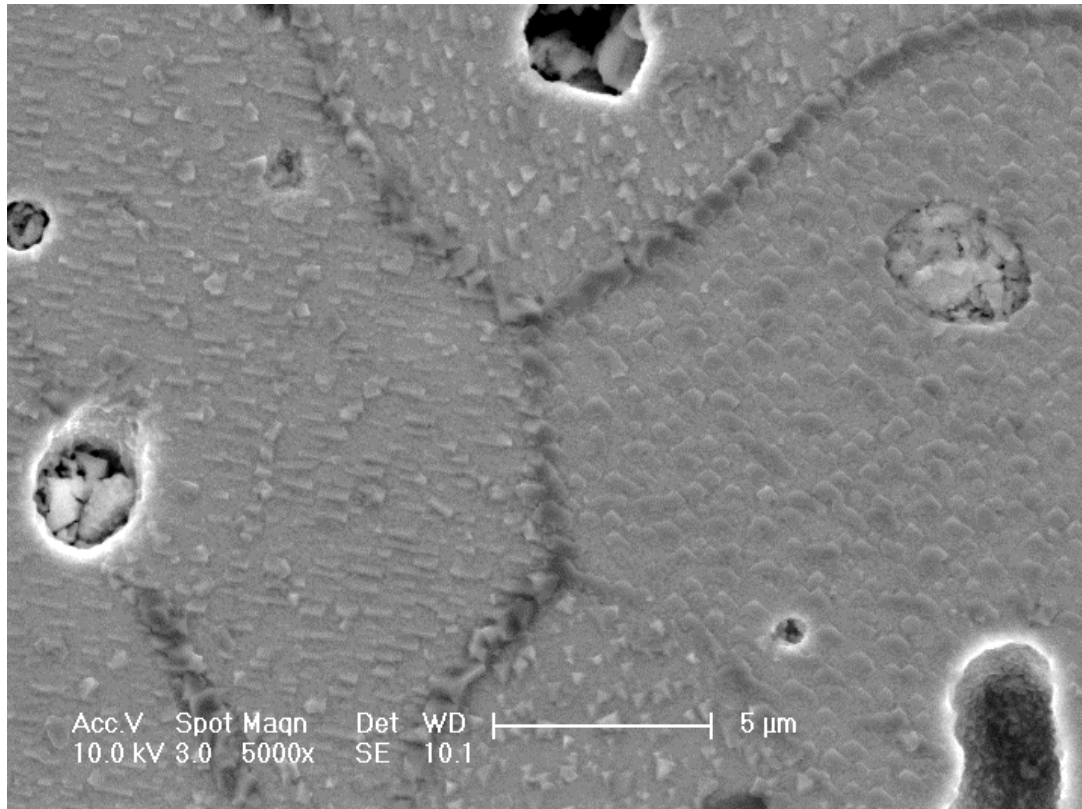
(b)

Figure 100. SE images show (a) the surface of the N1C5 with white frame outlining areas of higher precipitate coverage than area in the green frame and (b) the surface of the C-800°C-5min.

### 4.3.2.1.3 Hot etching effects

The precipitate coverage in N1C5 was higher than that in C-800℃-5min. It was suspected that the hot etching during the annealing in $N_2$ may cause this, instead of the decomposition in the annealing in $N_2$. The microstructure of N6C2 and A6C2 were compared to test this. N6C2 and A6C2 are shown in Figure 101 (a) and (b) respectively. The surface of N6C2 is fully covered by precipitates, while that of A6C2 is partially covered. There are pores on both surfaces. If the high precipitate coverage of N6C2 was caused by hot etching during annealing in $N_2$, the coverage would also be high in A6C2. But, this is not the case. Hence, the high precipitate coverage is not caused by hot etching.



(a)                                             (b)
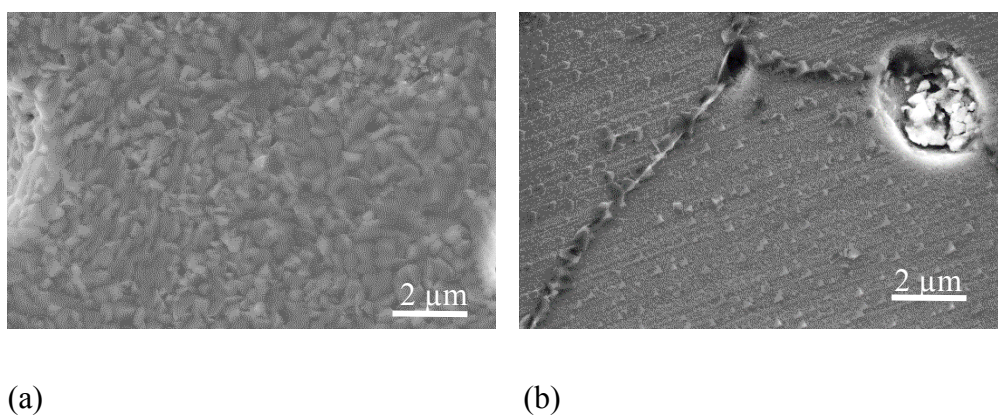
Figure 101. SE image shows microstructure of (a) N6C2 (b) A6C2.

### 4.3.2.2 Secondary phase identification

### 4.3.2.2.1 Results

Figure 102 (a - c) show a XRD pattern of the samples N6C2, A6C2 and C-800℃-2min, respectively. The peaks labelled by 'S' and 'C' match the powder diffraction pattern of the rhombohedral $SrCO_3$ phase (ICSD: 27445) and the cubic CoO phase (ICSD: 9865), respectively. The BSC phase was ascribed to the 'S' phase. Except for the peak labelled by 'U' (an unknown phase), other peaks match the powder diffraction pattern of the cubic BSCF phase (ICSD: 109462). These suggest that the samples have the same secondary phases.

*4.3.2.2.1.1 The amount of the BSC phase*

The Wt% of the BSC is 18.58 ± 1.58 %, 5.22 ± 1.07 % and 8.59 ± 2.94 % in N6C2, A6C2 and C-800℃-2min, respectively. The Wt% was determined by TOPAS. Hence the amount of BSC phase in N6C2 is higher than that in A6C2 and C-800℃-2min.

*4.3.2.2.1.2 The amount of the 'C' phase*

The Wt% of the 'C' phase is 12.34% ± 4.14 %, 0.62 ± 1.46 % and 0.89 ± 0.60 % in N6C2, A6C2 and C-800℃-2min, respectively. The Wt% was determined by TOPAS. Hence the amount of 'C' phase in N6C2 is higher than that in A6C2 and C-800℃-2min.

4.3.2.2.2 Discussion

No secondary phases were identified in the A-800℃-6hour and N-800℃-6hour samples by XRD. However, precipitates were observed in the microstructures of the two samples. Hence the amount of the secondary phases may be too low to be detected by XRD. The secondary phases in N-800℃-24hour sample may be the same as those in N-800℃-6hour. Hence, the 'H1', 'H2', 'H3', 'H4' and 'C' phase were tentatively assigned to the precipitates in N-800℃-6hour. These phases may accelerate the growth of the BSC phase and the 'C' phase. The reason may be that the crystallographic information (crystal structure, lattice parameters) of the 'H' phases is similar to that of the BSC phase. The similarity may make the 'H' phases favoured by the BSC phase. This is the second aspect of the interrelation and was revealed for the first time. Hence it is worth to identify the precipitates in the future to know which phases accelerated the growth of the BSC phase and the 'C' phase.
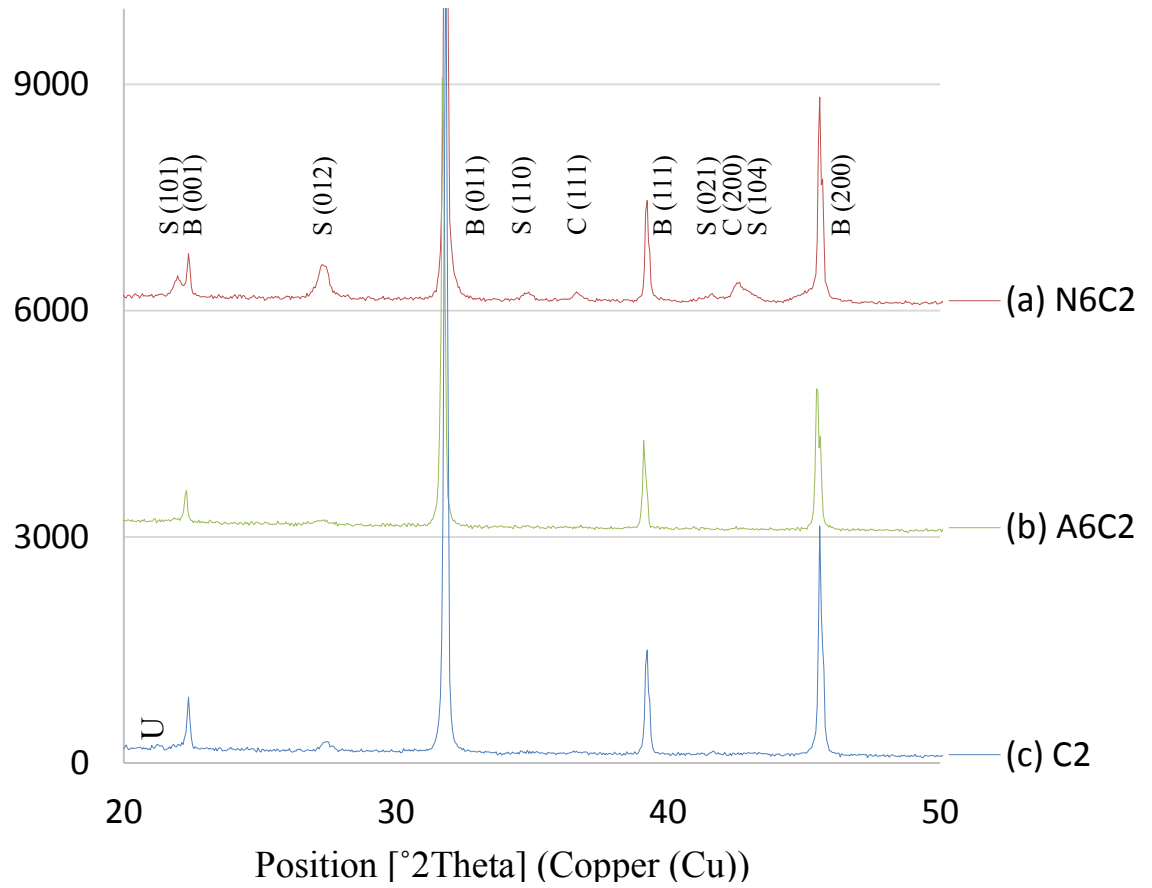
Figure 102. Indexed XRD pattern of (a) N6C2, (b) A6C2 and (c) C2. B: BSCF. S: $SrCO_3$. C: CoO. U: unknown peak.

In one study [16], the sweep side (low $PO_2$) of a BSCF membrane was more vulnerable to $CO_2$ attack than the feed side (high $PO_2$), carbonates formed more quickly on the sweep side to restrict oxygen permeation. The reason can be explained by the new finding in this section that the 'H' phase precipitates induced by annealing in $N_2$ (low $PO_2$) can accelerate the formation of the BSC phase and 'C' phase. It was explained this way for the first time.

In another study where a BSCF membrane was studied after a permeation experiment [70], the content of a trigonal phase $Ba_{1-x}Sr_xCo_{2-y}Fe_yO_{5-\delta}$ in the feed side (with higher $PO_2$) was significantly lower than the permeate side (with lower $PO_2$). It seemed to be restricted in high $PO_2$ gas. This is the lamellar phase which offers Ba and Sr to carbonates in this study. Hence at higher $PO_2$, the Ba and Sr supply from the lamellar phase can be restricted, which reduces the growth of the BSC phase. This may be the reason why the carbonate formation is restricted in high $PO_2$ gas. This reason was revealed for the first time.

## 4.3.3 Conclusions

In summary, two aspects of the interrelation are shown in a schematic diagram in Figure 103. Firstly, the 1 hour $N_2$ annealing ($CO_2$ deficient and inert atmosphere) produced the plate-like precipitates (may be the $Ba_{1-x}Sr_xCo_{2-y}Fe_yO_{5-\delta}$ phase with trigonal structure because of similar morphology) on which the BSC phase precipitates can grow more quickly. Three reasons were addressed. The plate-like phase offers boundaries with lower heterogeneous nucleation barrier [204]. The plate-like phase also offers Ba enriched neighbour area. The crystal structure and lattice parameters of the plate-like phase are similar to those of the BSC phase. The plate-like precipitates affect the orientation of the BSC precipitates. Secondly, the 6 hour $N_2$ annealing ($CO_2$ deficient and inert atmosphere) produced a series of secondary phases (the 'H' phases) which may accelerate the formation of the BSC phase due to similar lattice parameters and crystal structures. The interrelation can explain why BSCF is more vulnerable in a $CO_2$ enriched inert environment (low $PO_2$) because such an environment allows the 'H' phases and the $Ba_{1-x}Sr_xCo_{2-y}Fe_yO_{5-\delta}$ phase to form faster than a $CO_2$ enriched oxidising environment (high $PO_2$).

| 1 hour N₂ annealing | • Plate-like precipitates with trigonal structure formed in this anneal accelerate the growth of the BSC phase and CoO phase and affect the orientation of the BSC phase precipitates. |
| 6 hour N₂ annealing | • A series of hexagonal structured phases formed in this anneal accelerates the growth of the BSC phase and the CoO phase |
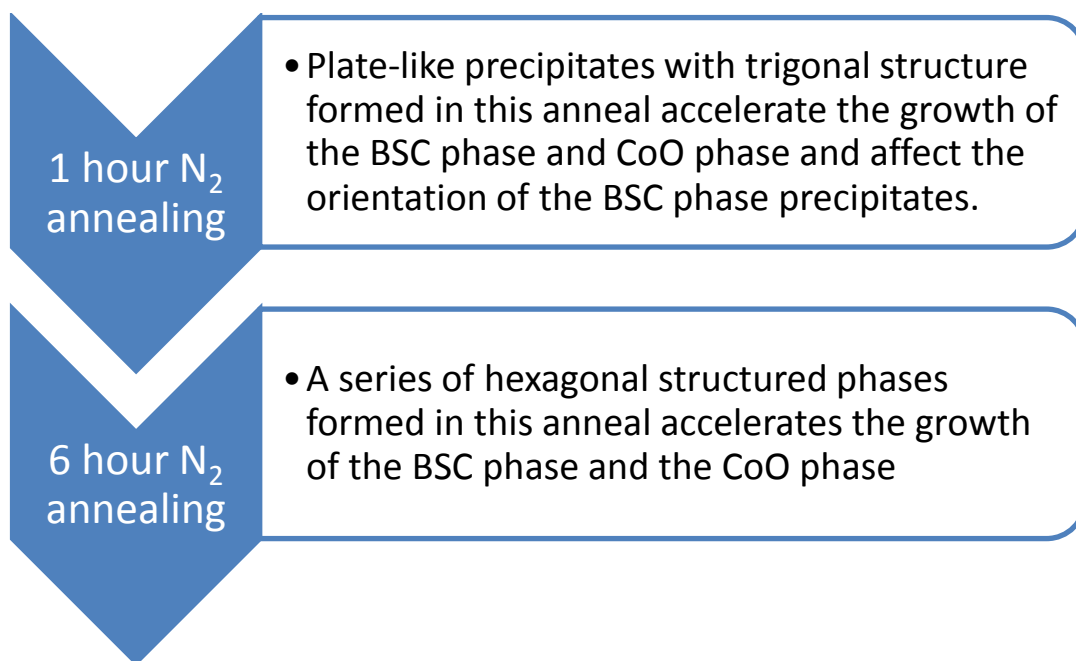
Figure 103. A schematic diagram shows the two aspects of the interrelation between the cubic to hexagonal decomposition and the reaction between BSCF and $CO_2$.

# 4.4 Coating of BSCF

SCFT414 was chosen to coat BSCF, a schematic diagram (Figure 104) shows the intended structure of a BSCF pellet the surface of which is coated by SCFT414 layer to improve the stability of BSCF in $CO_2$ enriched inert atmosphere. SCFT414 was chosen for its relatively high $CO_2$ stability [71]. In one study [71], it was able to permeate oxygen when its permeate side was swept by pure $CO_2$, while BSCF stopped working under the same condition. The TEC of SCFT414 (20 to 22 * $10^{-6}$ $K^{-1}$) [205] is higher than that of BSCF (19.0 to 20.8 * $10^{-6}$ $K^{-1}$) [206] to ensure that the coating layer remains in compression at high temperatures. Otherwise the coating layer can split if the BSCF substrate expands more. SCFT414 has cubic perovskite structure the A site of which is occupied by Sr and the B site of which is occupied by Co, Fe and Ti. The lattice parameter of SCFT414 (3.90 Å) [171] is similar to that of BSCF (3.9782 ± 0.0002 Å refined by TOPAS) to ensure a strong bonding between the two materials which allows good attachment to reduce the chance of spalling. The surface exchange rate is important in selecting the coating material because the oxygen ion conduction is likely to be governed by surface exchange due to low thickness. However, there are no reported studies on SCFT414 or similar materials that measure the surface exchange rate [71, 168, 171, 205].
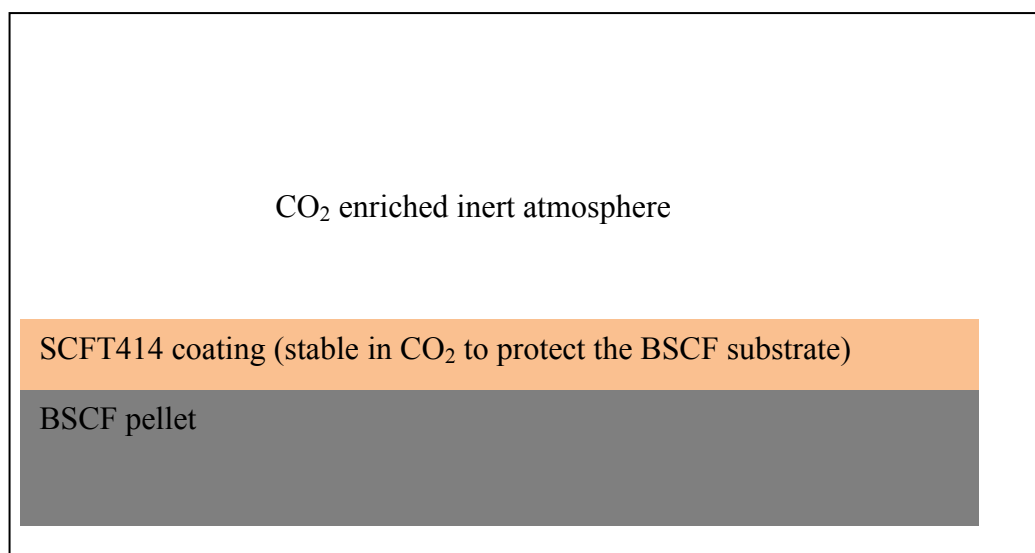
Figure 104. A schematic diagram shows the coated BSCF pellet in $CO_2$ enriched inert atmosphere.

## 4.4.1 The $CO_2$ stability study

### 4.4.1.1 The results

Figure 105 (a) shows the XRD pattern of the SCFTBSCF-CO2 pellet. All peaks match the powder diffraction file peaks for cubic perovskite BSCF (ICSD: 109462), suggesting there is no secondary phase formed hence the SCFT414 coating protected BSCF from $CO_2$ attack.

Figure 105 (b, c) show the XRD pattern of the c-BSCF-CO2 powders and c-BSCF-CO2 pellet. The peaks labelled by 'B', 'S' and 'C' match the powder diffraction file peaks for cubic BSCF (ICSD: 109462), rhombohedral $SrCO_3$ phase (ICSD: 27445) and the cubic CoO phase (ICSD: 9865), respectively. The BSC phase was ascribed to the 'S' phase. This suggests that secondary phases formed on samples without SCFT414 coating after $CO_2$ attack. All the three phases were also identified from C-800℃-1min sample, C-800℃-2min sample, C-800℃-5min sample, C-800℃-15min sample and C-800℃-30min sample, suggesting the changing of BSCF powders did not affect the secondary phases.
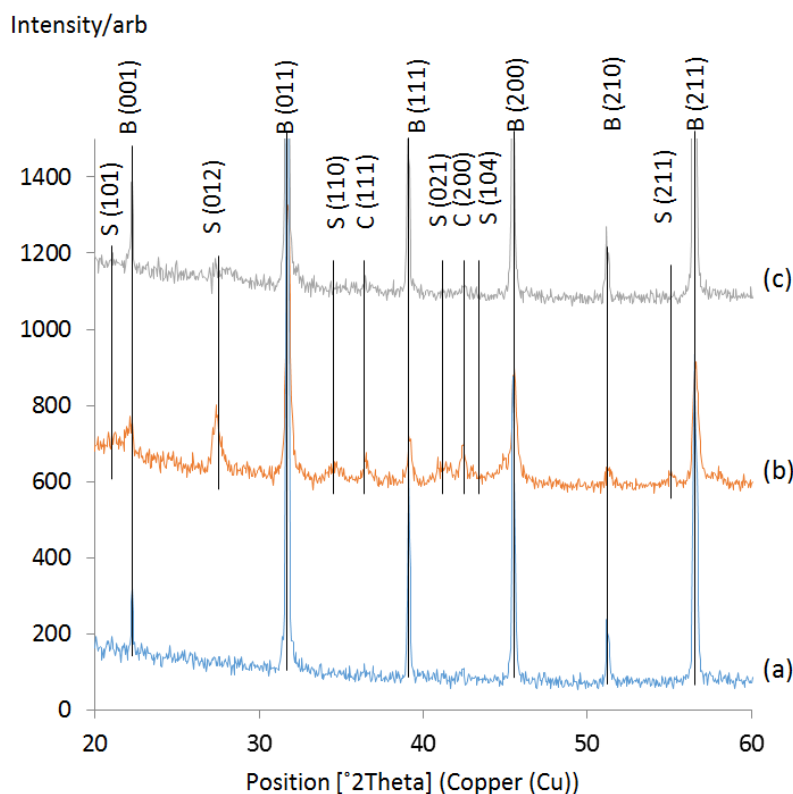
Figure 105. The indexed XRD pattern of the (a) SCFTBSCF-CO2 pellet, (b) c-BSCF-CO2 powders and (c) c-BSCF-CO2 pellet with peak indicators. B: BSCF, S: $SrCO_3$ and C: CoO.

### 4.4.1.2 Discussion

The c-BSCF-CO2 powder showed significantly more BSC phase and 'C' phase than the other samples and the porosity of the powder sample is significantly higher than that of the dense ceramic samples. The higher the porosity, the larger area for BSCF and $CO_2$ to react. A larger reaction area can cause the product to form faster [207]. This may explain why there are more BSC phase and 'C' phase in the powder sample.

## 4.4.2 The oxygen permeability study

### 4.4.2.1 The permeation measurements

In one study [72], the permeation flux of a BSCF pellet (thickness: 0.5 mm) was found to be 91% of that of another BSCF pellet (thickness: 0.3 mm). The other parameters of the pellets were the same and the flux of both pellets were measured under the same conditions. Hence, the permeation flux of the c-BSCF pellet was reduced by 9% to tentatively calculate the flux of a thicker c-BSCF pellet (thickness: 0.5 mm) which can be

compared to the flux of the SCFT coated BSCF pellet.

Figure 106 (a, b) show the oxygen permeation flux of the SCFT coated BSCF pellet and the c-BSCF pellet, respectively. Both curves were plotted as a function of 1/T. The permeation flux of the c-BSCF pellet is in agreement with previous study on BSCF permeation (1.2 ml/cm$^2$.min at 850°C) [13], suggesting the performance of the c-BSCF pellet is comparable with previous works. The permeation flux of the coated pellet is lower than that of the c-BSCF pellet at all temperatures.
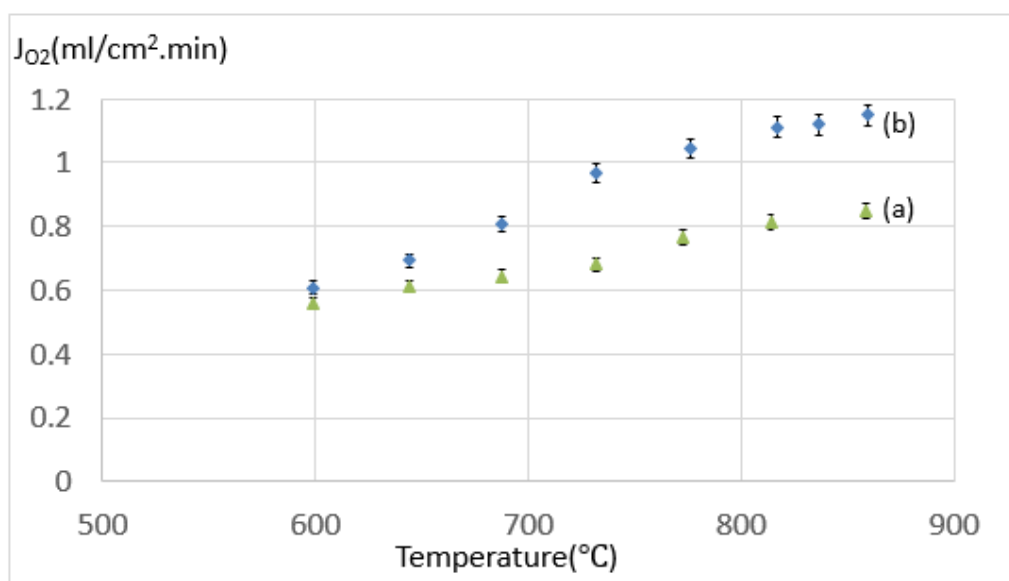


Figure 106. The permeation flux of (a) SCFT coated BSCF pellet and (b) c-BSCF pellet are plotted as a function of temperature.

4.4.2.2 The cross section study of the coated sample

This study was performed to understand the reason for the permeability reduction. Figure 107 shows the cross section of the SCFT coated BSCF pellet, the surface is indicated by an arrow. An EDX spectrum was acquired from the surface and the detected composition are shown in Table 35 with the composition of SCFT414. Ba was detected in the surface which should only have SCFT414, suggesting Ba migrated to the surface after coating and sintering. Ti concentration is significantly lower than SCFT414, suggesting Ti may migrate to the bulk.

The fractional errors (Ba 1.86%, Sr 0.98%, Co 0.67%, Fe 0.19% and Ti 0.20%) were contributed by EDX detector error which was determined by the Gaussian error

propagation [208] from the following errors [209]: statistical errors of peak intensity and background intensity, systematic errors of background calculation, systematic errors of peak/background-ZAF (P/B-ZAF) model and ZAF factors, errors when peak overlaps, errors in absorption calculation especially for low energy lines, errors in measuring time with sample and standard.
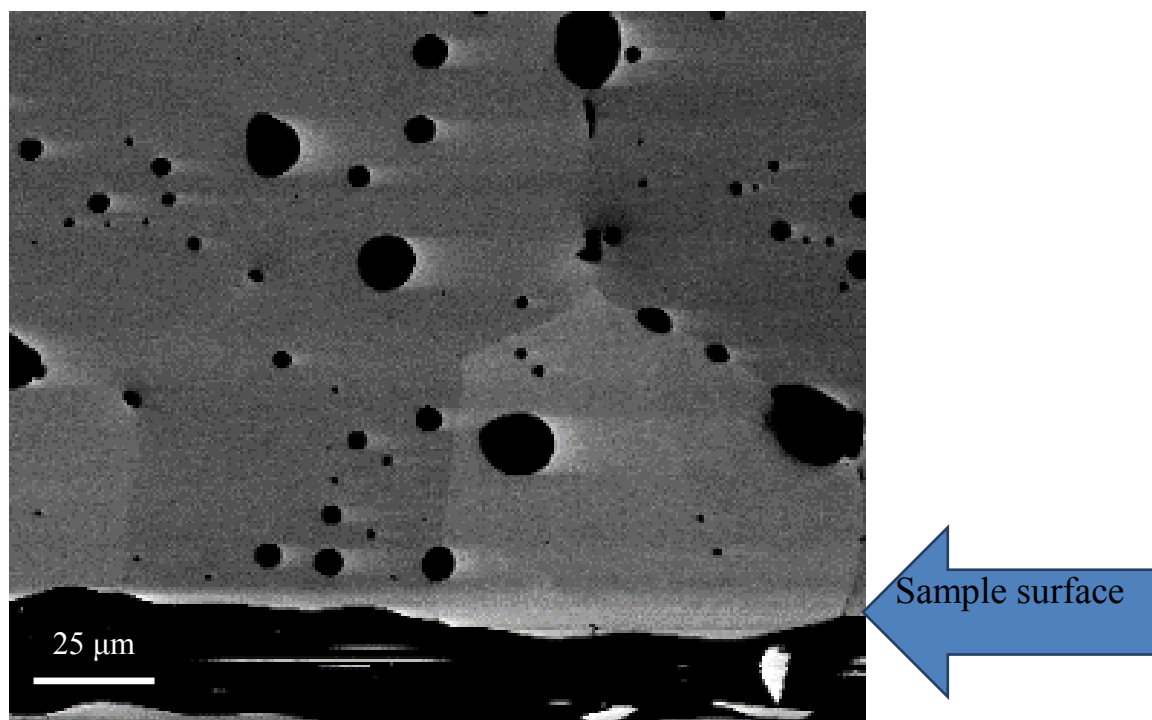


Figure 107. BSE image of the cross section of the SCFT coated BSCF pellet with arrow indicating sample surface.

Table 35 The atomic concentration of each element in SCFT414 and the detected atomic concentration from surface of SCFT coated BSCF pellet and corresponding error

| Detected composition | $Ba_{0.20}Sr_{0.27}Co_{0.40}Fe_{0.10}Ti_{0.04}O_x$ |
|---|---|
| Composition of SCFT414 | $SrCo_{0.48}Fe_{0.12}Ti_{0.4}O_{3-\delta}$ |

### 4.4.2.3 Discussion

The detected composition is close to BSCF hence the lattice parameter may be similar to BSCF. This may explain why a lattice parameter of 3.983 Å (Reference code: 00-055-0563) which is close to BSCF and larger than SCFT414 (3.885 Å [171]) was determined from the XRD pattern of the coated pellet. Another reason may be that the X-ray penetration depth (7 - 17 μm from 20° - 60°) is generally higher than the coating thickness (approximately 2 μm at thin places) which may lead to that most of the X-ray signal was obtained from the BSCF substrate. The detected composition is similar to $Ba_{0.5}Sr_{0.5}(Co_{0.8}Fe_{0.2})_{1-x}Ti_xO_{3-\delta}$. In the study of $Ba_{0.5}Sr_{0.5}(Co_{0.8}Fe_{0.2})_{1-x}Ti_xO_{3-\delta}$ [170], Ti-O bonding was suggested to be stronger than Co-O bonding or Fe-O bonding. $D_V$ of BSCF decreases with B-O bonding energy [119]. This may be the reason why the permeation flux of the coated pellet is lower than the c-BSCF pellet.

## 4.4.3 Conclusions

The coating material SCFT414 has been successfully synthesised and coated on BSCF for the first time. The $CO_2$ stability of the coated pellet was improved. However, the oxygen permeation flux was reduced due to compositional variations of the coating layer caused by cation migration which happened during sintering. An optimised sintering condition will be established in the future. The successfully sintered pellet (with correct coating and substrate compositions) may have improved permeability because the oxygen localisation problem due to the Ti-O bonding is solved and the oxygen interdiffusion at the interface between coating and substrate may be improved due to enhanced oxygen surface exchange which was led by a higher oxygen vacancy concentration [210].

# 5. Conclusions

For the objectives of this study, a thorough understanding of the initial decomposition of BSCF in $CO_2$ enriched environment was achieved. The slow BSCF decomposition and the reaction between BSCF and $CO_2$ were related and valuable information was yielded explaining critical issues in BSCF permeation in $CO_2$. The coating material enhanced the $CO_2$ stability of BSCF, although oxygen permeability was compromised.

BSCF mixed ionic electronic conductors were synthesised using the co-precipitation route developed in another study [18]. A calcination study using different time and temperature combinations optimised the calcination condition to produce single phase BSCF powders.

In the $CO_2$ enriched decomposition study, OPS was found to alter the grain boundaries of BSCF to preferred sites of precipitation, therefore it was not used in sample preparation. Decomposed BSCF samples were prepared to study the early decomposition $(0 - 30$ minutes) which was overlooked in previous studies. Two secondary phases (the BSC phase and the CoO phase) were identified by XRD. The BSC phase was ascribed to the precipitates in the decomposed surface by EBSD phase mapping. The CoO phase was ascribed to the precipitates in the decomposed cross sections by EBSD phase mapping and EDX chemical analysis. The phases were attributed to the precipitates in BSCF by EBSD for the first time.

The composition of the BSC phase was investigated by EDX on a TEM due to small dimension of the precipitates to obtain $Ba_{0.65\pm0.03}Sr_{0.35\pm0.03}CO_3$. A novel TEM sample preparation approach was developed for this chemical analysis due to the conventional method was proved impossible. The equivalency of the two methods was ensured by matching the d-spacing obtained from where the composition was acquired with the d-spacing in the powder diffraction file of the BSC phase.

The growth of the BSC precipitates was found to be a diffusion controlled process, in the early decomposition, suggested by a power law fitting of the precipitate coverage plot (an original method in uncovering the governing process of BSCF precipitation) obtained by an SEM microstructure study. The reaction rate of such process decreases due to the formation of a barrier layer which is the BSC layer in this study, the grain boundary precipitates were generally larger than grain precipitates due to faster grain boundary

diffusion, which improved the understanding of BSCF decomposition.

The trigger for the formations of the various phases was the radius variation of Co at high temperatures which undermined the perovskite structure. In the cross section of the decomposed samples, Ba and Sr diffused from the plate-like lamellar phase to both the surface and neighbouring areas to form the BSC phase or Sr enriched carbonate phase which provided a new insight into the nucleation process. Co migrated from BSCF to the plate-like lamellar phase and other phases, suggested by EDX analysis on a TEM which allowed analysis of sub-micron areas. Both migrations suggested high cation mobility in BSCF during decomposition. The formation mechanisms of the phases were established in terms of the cation migration, which with the trigger constituted the chemical aspect of the novel decomposition mechanism of BSCF in $CO_2$ enriched environments. In addition, the formation of the BSC phase accelerated the formation of the lamellar phase, suggested by SEM microstructure study. A chemical reaction equation was developed based on the phases discovered.

An orientation relation between the BSC precipitates and BSCF was identified by EBSD and was unique and new. The precipitate orientations on a grain or grain boundary can be different, while the relation remained, which was not previously understood. The precipitate morphology was affected by the precipitate orientation which was aligned to the underlying grain, which was studied for the first time. Crystallographic matching and the minimised interfacial energy at the interface between BSC precipitates and BSCF were two of the reasons for this orientation relation, there are other reasons to be discovered.

The decomposition of BSCF was a complex process suggested by a HRTEM study in terms of the various crystal structures of the lamellar phase, the various orientation relations between the lamellar phase and BSCF and the various formation mechanisms of the lamellar phase, which with the BSC and BSCF orientation relation constituted the crystallographic aspect of the decomposition mechanism. The complex process was not a random behaviour because the orientation relations showed preference on high symmetry axes. The preference was caused by the nucleation energy barrier, improving previous understanding which did not suggest an affecting factor.

In the interrelation study, the microstructure changes and secondary phases of BSCF

samples decomposed in $CO_2$ deficient environments were characterised by SEM and XRD, respectively. The plate-like precipitates were found to be favoured by the BSC precipitates in the microstructure due to lower heterogeneous nucleation barrier(s), more Ba readily offered to the BSC precipitates and crystallographic similarity, which provided new insight into the nucleation process. The $CO_2$ deficient low $PO_2$ decomposition created hexagonal phases accelerating the formation of the BSC phase and the CoO phase, suggested by XRD, which improved the understanding on the interrelation. By contrast, higher $PO_2$ environment restricted the amount of the hexagonal precipitates, suggested by SEM observation. BSCF membranes were more vulnerable when the permeate side was swept by $CO_2$ because the low $PO_2$ environment in the permeate side allowed the formation of the various hexagonal phases, which was not previously understood.

The coating material SCFT414 was synthesised by the co-precipitation method, although the sintering condition needed to be further optimised to mitigate over densification to produce intact pellets. BSCF was dip coated by SCFT414 for the first time and showed higher $CO_2$ stability, suggested by the fact that the coated pellet did not show secondary phases after $CO_2$ attack for 30 minutes. However, the permeation flux was reduced due to cation migration between the coating and the substrate to violate the composition of the coating and substrate, suggested by EDX analysis in the pellet cross section. Hence the sintering condition for coating needs to be optimised to prevent cation migration in the future.

# 6. Future work

1. Prepare a TEM sample exposing the interface of the lamellar phase, BSC phase and BSCF to study the orientation relations and composition. Ideally use an aberration corrected STEM with an atomic scale spatial resolution EDX detector to characterise accurate and precise composition of the BSC phase and the lamellar phase and to build atomic model of these phases. This can also yield the crystallographic reason why the BSC precipitates prefer the plate-like lamellar phase (observed in the interrelation study) and may explain how the plate-like phase affects the morphology of the BSC precipitates.

2. Identify the phases in N-800°C-6hour and N-800°C-24hour using XRD with longer scanning time and EBSD phase mapping to discover phases accelerating the formation of the BSC phase and the CoO phase. This can yield the crystallographic reason why the acceleration happened.

3. Characterise the composition of an intact SCFT414 pellet which is sintered under optimised sintering conditions using EDX.

4. Reduce the sintering time of the SCFT414 coated BSCF pellet to mitigate the cation migration. The sintered pellet needs to be characterised in the cross section using EDX to ensure the composition of the coating is correct before permeation measurements and the $CO_2$ stability study.

5. Control the thickness of the coated pellet to ensure the thickness is similar to that of the BSCF pellet before permeation. Hence thickness effects on permeation flux difference can be alleviated.

6. Coat a BSCF pellet by BSCF powder to roughen the surface hence the BSCF coated BSCF pellet and the SCFT414 coated BSCF pellet may have similar surface roughness to take surface roughness effects on permeation into account.

7. Measure the permeability of the SCFT414 coated BSCF pellet and the BSCF coated BSCF pellet to observe any differences. Also study the $CO_2$ stability of these two.

# 7. References

1.  Sunarso, J., Baumann, S., Serra, J.M., Meulenberg, W.A., Liu, S., Lin, Y.S., and da Costa, J.C.D., *Mixed ionic-electronic conducting (MIEC) ceramic-based membranes for oxygen separation.* Journal of Membrane Science, **320**(1-2): p. 13-41 (2008).

2.  Bouwmeester, H.J.M. and Burggraaf, A.J., *Chapter 10 Dense ceramic membranes for oxygen separation*, in *Membrane Science and Technology*. Elsevier. (1996).

3.  Thursfield, A. and Metcalfe, I.S., *The use of dense mixed ionic and electronic conducting membranes for chemical production.* Journal of Materials Chemistry, **14**(16): p. 2475-2485 (2004).

4.  Engels, S., Beggel, F., Modigell, M., and Stadler, H., *Simulation of a membrane unit for oxyfuel power plants under consideration of realistic BSCF membrane properties.* Journal of Membrane Science, **359**(1-2): p. 93-101 (2010).

5.  Shao, Z.P. and Haile, S.M., *A high-performance cathode for the next generation of solid-oxide fuel cells.* Nature, **431**(7005): p. 170-173 (2004).

6.  Stambouli, A.B. and Traversa, E., *Solid oxide fuel cells (SOFCs): a review of an environmentally clean and efficient source of energy.* Renewable & Sustainable Energy Reviews, **6**(5): p. 433-455 (2002).

7.  Chen, C.S., Feng, S.J., Ran, S., Zhu, D.C., Liu, W., and Bouwmeester, H.J.M., *Conversion of methane to syngas by a membrane-based oxidation-reforming process.* Angewandte Chemie-International Edition, **42**(42): p. 5196-5198 (2003).

8.  Manthiram, A., Kim, J.H., Kim, Y.N., and Lee, K.T., *Crystal chemistry and properties of mixed ionic-electronic conductors.* Journal of Electroceramics, **27**(2): p. 93-107 (2011).

9.  Salehi, M., Clemens, F., Pfaff, E.M., Diethelm, S., Leach, C., Graule, T., and Grobety, B., *A case study of the effect of grain size on the oxygen permeation flux of BSCF disk-shaped membrane fabricated by thermoplastic processing.* Journal of Membrane Science, **382**(1-2): p. 186-193 (2011).

10. McIntosh, S., Vente, J.F., Haije, W.G., Blank, D.H.A., and Bouwmeester, H.J.M., *Structure and oxygen stoichiometry of $SrCo_{0.8}Fe_{0.2}O_{3-\delta}$ and $Ba_{0.5}Sr_{0.5}Co_{0.8}Fe_{0.2}O_{3-\delta}$.* Solid State Ionics, **177**(19-25): p. 1737-1742 (2006).

11. Svarcova, S., Wiik, K., Tolchard, J., Bouwmeester, H.J.M., and Grande, T., *Structural instability of cubic perovskite $Ba_xSr_xSr_{1-x}Co_{1-y}Fe_yO_{3-\delta}$.* Solid State Ionics, **178**(35-36): p. 1787-1791 (2008).

12. Van Veen, A.C., Rebeilleau, M., Farrusseng, D., and Mirodatos, C., *Studies on the performance stability of mixed conducting BSCFO membranes in medium temperature oxygen permeation.* Chemical Communications, (1): p. 32-33 (2003).

13. Shao, Z.P., Yang, W.S., Cong, Y., Dong, H., Tong, J.H., and Xiong, G.X., *Investigation of the permeation behavior and stability of a $Ba_{0.5}Sr_{0.5}Co_{0.8}Fe_{0.2}O_{3-\delta}$ oxygen membrane.* Journal of Membrane Science, **172**(1-2): p. 177-188 (2000).

14. Rebeilleau-Dassonneville, M., Rosini, S., van Veen, A.C., Farrusseng, D., and Mirodatos, C., *Oxidative activation of ethane on catalytic modified dense ionic oxygen conducting membranes.* Catalysis Today, **104**(2-4): p. 131-137 (2005).

15. Niedrig, C., Taufall, S., Burriel, M., Menesklou, W., Wagner, S.F., Baumann, S., and Ivers-Tiffee, E., *Thermal stability of the cubic phase in $Ba_{0.5}Sr_{0.5}Co_{0.8}Fe_{0.2}O_{3-\delta}$ (BSCF)1.* Solid State Ionics, **197**(1): p. 25-31 (2011).

16. Arnold, M., Wang, H.H., and Feldhoff, A., *Influence of $CO_2$ on the oxygen permeation performance and the microstructure of perovskite-type $(Ba_{0.5}Sr_{0.5})(Co_{0.8}Fe_{0.2})O_{3-\delta}$ membranes.* Journal of Membrane Science, **293**(1-2): p. 44-52 (2007).

17. Yi, J.X. and Schroeder, M., *High temperature degradation of $Ba_{0.5}Sr_{0.5}Co_{0.8}Fe_{0.2}O_{3-\delta}$ membranes in atmospheres containing concentrated carbon dioxide.* Journal of Membrane Science, **378**(1-2): p. 163-170 (2011).

18. Norman, C.J., *Synthesis and Characterisation of Barium Strontium Cobalt Iron Oxide Mixed Ionic and Electronic Conductors (PhD thesis).* The University of Manchester: Manchester. (2013).

19. Zeng, P.Y., Ran, R., Chen, Z.H., Gu, H.X., Shao, Z.P., da Costa, J.C.D., and Liu, S.M., *Significant effects of sintering temperature on the performance of $La_{0.6}Sr_{0.4}Co_{0.2}Fe_{0.8}O_{3-\delta}$ oxygen selective membranes.* Journal of Membrane Science, **302**(1-2): p. 171-179 (2007).

20. Figueroa, J.D., Fout, T., Plasynski, S., McIlvried, H., and Srivastava, R.D., *Advances in $CO_2$ capture technology—The U.S. Department of Energy's Carbon Sequestration Program.* International Journal of Greenhouse Gas Control, **2**(1): p. 9-20 (2008).

21. Huang, Q.A., Hui, R., Wang, B.W., and Zhang, H.J., *A review of AC impedance modeling and validation in SOFC diagnosis.* Electrochimica Acta, **52**(28): p. 8144-8164 (2007).

22. Li, W., Zhu, X., Cao, Z., Wang, W., and Yang, W., *Mixed ionic-electronic conducting (MIEC) membranes for hydrogen production from water splitting.* International Journal of Hydrogen Energy, **40**(8): p. 3452-3461 (2015).

23. Ursua, A., Gandia, L.M., and Sanchis, P., *Hydrogen Production From Water Electrolysis: Current Status and Future Trends.* Proceedings of the IEEE, **100**(2): p. 410-426 (2012).

24. Ida, S., Yamada, K., Matsuka, M., Hagiwara, H., and Ishihara, T., *Photoelectrochemical hydrogen production from water using p-type and n-type oxide semiconductor electrodes.* Electrochimica Acta, **82**(0): p. 397-401 (2012).

25. Ida, S., Yamada, K., Matsunaga, T., Hagiwara, H., Ishihara, T., Taniguchi, T., Koinuma, M., and Matsumoto, Y., *Photoelectrochemical Hydrogen Production from Water Using p-Type $CaFe_2O_4$ and n-Type ZnO.* Electrochemistry, **79**(10): p. 797-800 (2011).

26. Thursfield, A., Murugan, A., Franca, R., and Metcalfe, I.S., *Chemical looping and oxygen permeable ceramic membranes for hydrogen production - a review.* Energy & Environmental Science, **5**(6): p. 7421-7459 (2012).

27. Chiron, F.-X. and Patience, G.S., *Kinetics of mixed copper–iron based oxygen carriers for hydrogen production by chemical looping water splitting.* International Journal of Hydrogen Energy, **37**(14): p. 10526-10538 (2012).

28. Vincent, T., Gross, M., Dotan, H., and Rothschild, A., *Thermally oxidized iron oxide nanoarchitectures for hydrogen production by solar-induced water splitting.* International Journal of Hydrogen Energy, **37**(9): p. 8102-8109 (2012).

29. Khine, M.S.S., Chen, L.W., Zhang, S., Lin, J.Y., and Jiang, S.P., *Syngas production by catalytic partial oxidation of methane over $La_{0.7}A_{0.3}BO_3$ (A = Ba, Ca, Mg, Sr, and B = Cr or Fe) perovskite oxides for portable fuel cell applications.* International Journal of Hydrogen Energy, **38**(30): p. 13300-13308 (2013).

30. Wender, I., *Synthesis Gas as a Source of Fuels and Chemicals - C-1 Chemistry.* Annual Review of Energy, **11**: p. 295-314 (1986).

31. Kofstad, P., *Nonstoichiometry, Diffusion and Electrical Conductivity in binary Metal Oxides.* Wiley-Interscience: Toronto. (1972).

32. Hodges, J.P., Short, S., Jorgensen, J.D., Xiong, X., Dabrowski, B., Mini, S.M., and Kimball, C.W., *Evolution of Oxygen-Vacancy Ordered Crystal Structures in the Perovskite Series $SrnFe_nO3_{n-1}$ (n=2, 4, 8, and $\infty$), and the Relationship to Electronic and Magnetic Properties.* Journal of Solid State Chemistry, **151**(2): p. 190-209 (2000).

33. Jacobson, A.J., *Materials for Solid Oxide Fuel Cells.* Chemistry of Materials, **22**(3): p. 660-674 (2010).

34. Mizusaki, J., Mima, Y., Yamauchi, S., Fueki, K., and Tagawa, H., *Nonstoichiometry of the perovskite-type oxides $La_{1-x}Sr_xCoO_{3-\delta}$.* Journal of Solid State Chemistry, **80**(1): p. 102-111 (1989).

35. Gryaznov, D., Baumann, S., Kotomin, E.A., and Merkle, R., *Comparison of Permeation Measurements and Hybrid Density-Functional Calculations on Oxygen Vacancy Transport in Complex Perovskite Oxides.* Journal of Physical Chemistry C, **118**(51): p. 29542-29553 (2014).

36. Lee, K.T. and Manthiram, A., *Comparison of $Ln_{0.6}Sr_{0.4}CoO_{3-\delta}$ (Ln = La, Pr, Nd, Sm, and Gd) as cathode materials for intermediate temperature solid oxide fuel cells.* Journal of the Electrochemical Society, **153**(4): p. A794-A798 (2006).

37. Troyanchuk, I.O., Kasper, N.V., Khalyavin, D.D., Szymczak, H., Szymczak, R., and Baran, M., *Magnetic and electrical transport properties of orthocobaltites $R_{0.5}Ba_{0.5}CoO_3$ (R=La,Pr,Nd,Sm,Eu,Gd,Tb,Dy).* Physical Review B, **58**(5): p. 2418-2421 (1998).

38. Petrov, A.N., Kononchuk, O.F., Andreev, A.V., Cherepanov, V.A., and Kofstad, P., *Crystal structure, electrical and magnetic properties of $La_{1-x}Sr_xCoO_{3-y}$.* Solid State Ionics, **80**(3–4): p. 189-199 (1995).

39. Mori, M. and Sammes, N.M., *Sintering and thermal expansion characterization of Al-doped and Co-doped lanthanum strontium chromites synthesized by the Pechini method.* Solid State Ionics, **146**(3–4): p. 301-312 (2002).

40. Heyne, L., *Electrochemistry of mixed ionic–electronic conductors.* Solid Electrolytes, **21**: p. 169-221 (1977).

41. Kingery, W.D., Bowen, H.K., and Uhlmann, D.R., *Introduction to ceramics*. Wiley: New York. (1976).

42. Lee, K.T. and Manthiram, A., *Characterization of $Nd_{1-x}Sr_xCoO_{3-\delta}$ ( $0 \leq x \leq 0.5$ ) Cathode Materials for Intermediate Temperature SOFCs.* Journal of The Electrochemical Society, **152**(1): p. A197-A204 (2005).

43. West, A.R., *Solid State Chemistry and Its Applications*. Wiley. (2013).

44. West, A.R., *Basic solid state chemistry*. John Wiley & Sons: West Sussex. (1999).

45. http://hyperphysics.phy-astr.gsu.edu/hbase/solids/intrin.html. (Accessed 24th Mar 2015).

46. W.D. Kingery, H.K.B., D.R. Uhlmann, *Introduction to Ceramics*. John Wiley & Sons: Toronto. (1976).

47. Teraoka, Y., Zhang, H.-M., Furukawa, S., and Yamazoe, N., *Oxygen permeation through perovskite-type oxides.* Chemistry Letters, **14**(11): p. 1743-1746 (1985).

48. Teraoka, Y., Nobunaga, T., and Yamazoe, N., *Effect of cation substitution on the oxygen semipermeability of perovskite-type oxides.* Chemistry Letters, **17**(3): p. 503-506 (1988).

49. Teraoka, Y., Zhang, H.M., Okamoto, K., and Yamazoe, N., *Mixed ionic-electronic conductivity of $La_{1-x}Sr_xCo_{1-y}Fe_yO_{3-\delta}$ perovskite-type oxides.* Materials Research Bulletin, **23**(1): p. 51-58 (1988).

50. Teraoka, Y., Nobunaga, T., Okamoto, K., Miura, N., and Yamazoe, N., *Influence of constituent metal cations in substituted $LaCoO_3$ on mixed conductivity and oxygen permeability.* Solid State Ionics, **48**(3–4): p. 207-212 (1991).

51. Cook, R.L. and Sammells, A.F., *On the systematic selection of perovskite solid electrolytes for intermediate temperature fuel cells.* Solid State Ionics, **45**(3–4): p. 311-321 (1991).

52. Cook, R.L., Osborne, J.J., White, J.H., MacDuff, R.C., and Sammells, A.F., *Investigations on $BaTh_{0.9}Gd_{0.1}O_3$ as an intermediate temperature fuel cell solid electrolyte.* Journal of The Electrochemical Society, **139**(2): p. L19-L20 (1992).

53. Mogensen, M., Lybye, D., Bonanos, N., Hendriksen, P.V., and Poulsen, F.W., *Factors controlling the oxide ion conductivity of fluorite and perovskite structured oxides.* Solid State Ionics, **174**(1–4): p. 279-286 (2004).

54. Kharton, V.V., Naumovich, E.N., Vecher, A.A., and Nikolaev, A.V., *Oxide-ion conduction in solid-solutions $Ln_{1-x}Sr_xCoO_{3-\delta}$ (Ln=La,Pr,Nd)*. Journal of Solid State Chemistry, **120**(1): p. 128-136 (1995).

55. Itoh, T., Inukai, M., Kitamura, N., Ishida, N., Idemoto, Y., and Yamamoto, T., *Correlation between structure and mixed ionic-electronic conduction mechanism for $La_{1-x}Sr_xCoO_{3-\delta}$ using synchrotron X-ray analysis and first principles calculations*. Journal of Materials Chemistry A, **3**: p. 6943-6953 (2015).

56. Cao, G.Z., *Electrical-conductivity and oxygen semipermeability of terbia and yttria-stabilized zirconia*. Journal of Applied Electrochemistry, **24**(12): p. 1222-1227 (1994).

57. Lin, Y.S., Wang, W.J., and Han, J.H., *Oxygen permeation through thin mixed-conducting solid oxide membranes*. Aiche Journal, **40**(5): p. 786-798 (1994).

58. Dou, S., Masson, C.R., and Pacey, P.D., *Mechanism of oxygen permeation through lime-stabilized zirconia*. Journal of The Electrochemical Society, **132**(8): p. 1843-1849 (1985).

59. Kröger, F.A., *The chemistry of imperfect crystals*. North-Holland Pub. Co.; American Elsevier: Amsterdam, New York,. (1973).

60. Kroger, F.A. and Vink, H.J., *Relations between the concentrations of imperfections in solids*. Journal of Physics and Chemistry of Solids, **5**(3): p. 208-223 (1958).

61. Ishihara, T., *Perovskite oxide for solid oxide fuel cells*. Springer Science & Business Media. (2009).

62. Wang, S., Verma, A., Yang, Y.L., Jacobson, A.J., and Abeles, B., *The effect of the magnitude of the oxygen partial pressure change in electrical conductivity relaxation measurements: oxygen transport kinetics in $La_{0.5}Sr_{0.5}CoO_{3-\delta}$*. Solid State Ionics, **140**(1-2): p. 125-133 (2001).

63. Boehm, E., Bassat, J.M., Steil, M.C., Dordor, P., Mauvy, F., and Grenier, J.C., *Oxygen transport properties of $La_2Ni_{1-x}Cu_xO_{4+\delta}$ mixed conducting oxides*. Solid State Sciences, **5**(7): p. 973-981 (2003).

64. De Souza, R.A., Kilner, J.A., and Walker, J.F., *A SIMS study of oxygen tracer diffusion and surface exchange in $La_{0.8}Sr_{0.2}MnO_{3+\delta}$*. Materials Letters, **43**(1–2): p. 43-52 (2000).

65. Bouwmeester, H.J.M., Kruidhof, H., Burggraaf, A.J., and Gellings, P.J., *Oxygen semipermeability of erbia-stabilized bismuth oxide*. Solid State Ionics, **53**: p. 460-468 (1992).

66. Capoen, E., Steil, M.C., Nowogrocki, G., Malys, M., Pirovano, C., Lofberg, A., Bordes-Richard, E., Bolvin, J.C., Mairesse, G., and Vannier, R.N., *Oxygen permeation in bismuth-based materials. Part I: Sintering and oxygen permeation fluxes*. Solid State Ionics, **177**(5-6): p. 483-488 (2006).

67. Choi, M.B., Jeon, S.Y., Singh, B., Yoo, Y.S., Hwang, J.H., and Song, S.J., *Correlation between defect structure and electrochemical properties of mixed conducting $La_{0.1}Sr_{0.9}Co_{0.8}Fe_{0.2}O_{3-\delta}$*. Acta Materialia, **65**: p. 373-382 (2014).

68. Peters, C., Weber, A., and Ivers-Tiffee, E., *Nanoscaled $La_{0.5}Sr_{0.5}CoO_{3-\delta}$ thin film cathodes for SOFC application at 500 degrees C < T < 700 degrees C*. Journal of the Electrochemical Society, **155**(7): p. B730-B737 (2008).

69. Bouwmeester, H.J.M., Den Otter, M.W., and Boukamp, B.A., *Oxygen transport in $La_{0.6}Sr_{0.4}Co_{1-y}Fe_yO_{3-\delta}$*. Journal of Solid State Electrochemistry, **8**(9): p. 599-605 (2004).

70. Liang, F.Y., Jiang, H.Q., Luo, H.X., Caro, J., and Feldhoff, A., *Phase stability and permeation behavior of a dead-end $Ba_{0.5}Sr_{0.5}Co_{0.8}Fe_{0.2}O_{3-\delta}$ tube membrane in high-purity oxygen production*. Chemistry of Materials, **23**(21): p. 4765-4772 (2011).

71. Schulz, M., Kriegel, R., and Kampfer, A., *Assessment of $CO_2$ stability and oxygen flux of oxygen permeable membranes*. Journal of Membrane Science, **378**(1-2): p. 10-17 (2011).

72. Hong, W.K. and Choi, G.M., *Oxygen permeation of BSCF membrane with varying thickness and surface coating.* Journal of Membrane Science, **346**(2): p. 353-360 (2010).

73. Bouwmeester, H.J.M., Kruidhof, H., and Burggraaf, A.J., *Importance of the surface exchange kinetics as rate-limiting step in oxygen permeation through mixed-conducting oxides.* Solid State Ionics, **72**: p. 185-194 (1994).

74. Baumann, S., Schulze-Kuppers, F., Roitsch, S., Betz, M., Zwick, M., Pfaff, E.M., Meulenberg, W.A., Mayer, J., and Stover, D., *Influence of sintering conditions on microstructure and oxygen permeation of $Ba_{0.5}Sr_{0.5}Co_{0.8}Fe_{0.2}O_{3-\delta}$ (BSCF) oxygen transport membranes.* Journal of Membrane Science, **359**(1-2): p. 102-109 (2010).

75. Baumann, S., Schulze-Kuppers, F., Roitsch, S., Betz, M., Zwick, M., Pfaff, E.M., Meulenberg, W.A., Mayer, J., and Stover, D., *Influence of sintering conditions on microstructure and oxygen permeation of $Ba_{0.5}Sr_{0.5}Co_{0.8}Fe_{0.2}O_{3-\delta}$ (BSCF) oxygen transport membranes.* Journal of Membrane Science, **359**(1-2): p. 102-109 (2010).

76. Zhu, X., Cong, Y., and Yang, W., *Oxygen permeability and structural stability of $BaCe_{0.15}Fe_{0.85}O_{3-\delta}$ membranes.* Journal of Membrane Science, **283**(1–2): p. 38-44 (2006).

77. Tan, X.Y. and Li, K., *Modeling of air separation in a LSCF hollow-fiber membrane module.* Aiche Journal, **48**(7): p. 1469-1477 (2002).

78. Vanhassel, B.A., Kawada, T., Sakai, N., Yokokawa, H., Dokiya, M., and Bouwmeester, H.J.M., *Oxygen Permeation Modeling of Perovskites.* Solid State Ionics, **66**(3-4): p. 295-305 (1993).

79. Chen, C.H., Kruidhof, H., Bouwmeester, H.J.M., and Burggraaf, A.J., *Ionic conductivity of perovskite $LaCoO_3$ measured by oxygen permeation technique.* Journal of Applied Electrochemistry, **27**(1): p. 71-75 (1997).

80. van der Haar, L.M., den Otter, M.W., Morskate, M., Bouwmeester, H.J.M., and Verweij, H., *Chemical diffusion and oxygen surface transfer of $La_{1-x}Sr_xCoO_{3-\delta}$ studied with electrical conductivity relaxation.* Journal of The Electrochemical Society, **149**(3): p. J41-J46 (2002).

81. Yáng, Z., Harvey, A.S., Infortuna, A., and Gauckler, L.J., *Phase relations in the Ba–Sr–Co–Fe–O system at 1273 K in air.* Journal of Applied Crystallography, **42**(2): p. 153-160 (2009).

82. Liu, Z.J. and Huang, X.J., *Factors that affect activation energy for Li diffusion in $LiFePO_4$: A first-principles investigation.* Solid State Ionics, **181**(19-20): p. 907-913 (2010).

83. Kofstad, P., *Nonstoichiometry, diffusion, and electrical conductivity in binary metal oxides.* Wiley-Interscience: New York,. (1972).

84. Kiukkola, K. and Wagner, C., *Measurements on galvanic cells involving solid electrolytes.* Journal of The Electrochemical Society, **104**(6): p. 379-387 (1957).

85. Han, J., Zeng, Y., and Lin, Y.S., *Oxygen permeation through fluorite-type bismuth-yttrium-copper oxide membranes.* Journal of Membrane Science, **132**(2): p. 235-243 (1997).

86. Ten Elshof, J.E., Bouwmeester, H.J.M., and Verweij, H., *Oxidative coupling of methane in a mixed-conducting perovskite membrane reactor.* Applied Catalysis A: General, **130**(2): p. 195-212 (1995).

87. Qiu, L., Lee, T.H., Liu, L.M., Yang, Y.L., and Jacobson, A.J., *Oxygen permeation studies of $SrCo_{0.8}Fe_{0.2}O_{3-\delta}$.* Solid State Ionics, **76**(3–4): p. 321-329 (1995).

88. Wang, H., Cong, Y., and Yang, W., *Oxygen permeation study in a tubular $Ba_{0.5}Sr_{0.5}Co_{0.8}Fe_{0.2}O_{3-\delta}$ oxygen permeable membrane.* Journal of Membrane Science, **210**(2): p. 259-271 (2002).

89. Ten Elshof, J.E., Bouwmeester, H.J.M., and Verweij, H., *Oxygen transport through $La_{1-x}Sr_xFeO_{3-\delta}$ membranes. I. Permeation in air/He gradients.* Solid State Ionics, **81**(1–2): p. 97-109 (1995).

90. Ishihara, T., Yamada, T., Arikawa, H., Nishiguchi, H., and Takita, Y., *Mixed electronic–oxide ionic conductivity and oxygen permeating property of Fe-, Co- or Ni-doped $LaGaO_3$*

*perovskite oxide.* Solid State Ionics, **135**(1–4): p. 631-636 (2000).

91. Kharton, V.V., Yaremchenko, A.A., Kovalevsky, A.V., Viskup, A.P., Naumovich, E.N., and Kerko, P.F., *Perovskite-type oxides for high-temperature oxygen separation membranes.* Journal of Membrane Science, **163**(2): p. 307-317 (1999).

92. Chen, C.S., Boukamp, B.A., Bouwmeester, H.J.M., Cao, G.Z., Kruidhof, H., Winnubst, A.J.A., and Burggraaf, A.J., *Microstructural development, electrical properties and oxygen permeation of zirconia-palladium composites.* Solid State Ionics, **76**(1–2): p. 23-28 (1995).

93. Mazanec, T.J., Cable, T.L., and Frye Jr, J.G., *Electrocatalytic cells for chemical reaction.* Solid State Ionics, **53–56, Part 1**: p. 111-118 (1992).

94. Chen, C.S., Kruidhof, H., Bouwmeester, H.J.M., Verweij, H., and Burggraaf, A.J., *Thickness dependence of oxygen permeation through erbia-stabilized bismuth oxide-silver composites.* Solid State Ionics, **99**(3-4): p. 215-219 (1997).

95. Wu, K., Xie, S., Jiang, G.S., Liu, W., and Chen, C.S., *Oxygen permeation through $(Bi_2O_3)_{0.74}(SrO)_{0.26}$–Ag (40% v/o) composite.* Journal of Membrane Science, **188**(2): p. 189-193 (2001).

96. Hodges, J.P., Short, S., Jorgensen, J.D., Xiong, X., Dabrowski, B., Mini, S.M., and Kimball, C.W., *Evolution of oxygen-vacancy ordered crystal structures in the perovskite series $SrnFe_nO_{3n-1}$ (n=2, 4, 8, and infinity), and the relationship to electronic and magnetic properties.* Journal of Solid State Chemistry, **151**(2): p. 190-209 (2000).

97. Di Felice, L., Middelkoop, V., Anzoletti, V., Snijkers, F., van Sint Annaland, M., and Gallucci, F., *New high temperature sealing technique and permeability data for hollow fiber BSCF perovskite membranes.* Chemical Engineering and Processing: Process Intensification, In press - available on-line; http://dx.doi.org/10.1016/j.cep.2014.12.004 (March 2016).

98. Wang, R., Meng, B., Meng, X., Tan, X., Sunarso, J., Liu, L., and Liu, S., *Highly stable $La_{0.6}Sr_{0.4}Co_{0.2}Fe_{0.8}O_{3-\delta}$ hollow fibre membrane for air separation swept by steam or steam mixture.* Journal of Membrane Science, **479**: p. 232-239 (2015).

99. Zhu, J.W., Liu, Z.K., Guo, S.B., and Jill, W.Q., *Influence of permeation modes on oxygen permeability of the multichannel mixed-conducting hollow fibre membrane.* Chemical Engineering Science, **122**: p. 614-621 (2015).

100. Zhu, J., Guo, S., Zhang, Z., Jiang, X., Liu, Z., and Jin, W., *$CO_2$-tolerant mixed-conducting multichannel hollow fiber membrane for efficient oxygen separation.* Journal of Membrane Science, **485**: p. 79-86 (2015).

101. Ramasamy, D., Shaula, A.L., Gómez-Herrero, A., Kharton, V.V., and Fagg, D.P., *Oxygen permeability of mixed-conducting $Ce_{0.8}Tb_{0.2}O_{2-\delta}$ membranes: Effects of ceramic microstructure and sintering temperature.* Journal of Membrane Science, **475**: p. 414-424 (2015).

102. Kida, T., Ninomiya, S., Tatsushiro, H., Watanabe, K., Yuasa, M., and Shimanoe, K., *Oxygen separation from air using $Ba_{0.95}La_{0.05}FeO_{3-\delta}$ membranes fitted with porous $La_{1-x}Sr_xFeO_{3-\delta}$ layers.* Ceramics International, **41**: p. 7830-7835 (2015).

103. He, B., Ding, D., Ling, Y., Xu, J., and Zhao, L., *Efficient modification for enhancing surface activity of $Ba_{0.5}Sr_{0.5}Co_{0.8}Fe_{0.2}O_{3-\delta}$ oxygen permeation membrane.* Journal of Membrane Science, **477**: p. 7-13 (2015).

104. Kida, T., Ninomiya, S., Watanabe, K., Yamazoe, N., and Shimanoe, K., *High Oxygen Permeation in $Ba_{0.95}La_{0.05}FeO_{3-\delta}$ Membranes with Surface Modification.* ACS Applied Materials & Interfaces, **2**(10): p. 2849-2853 (2010).

105. Bhalla, A.S., Guo, R.Y., and Roy, R., *The perovskite structure - a review of its role in ceramic science and technology.* Materials Research Innovations, **4**(1): p. 3-26 (2000).

106. Tan, L.A., Gu, X.H., Yang, L., Jin, W.Q., Zhang, L.X., and Xu, N.P., *Influence of powder*

*synthesis methods on microstructure and oxygen permeation performance of $Ba_{0.5}Sr_{0.5}Co_{0.8}Fe_{0.2}O_{3-\delta}$ perovskite-type membranes.* Journal of Membrane Science, **212**(1-2): p. 157-165 (2003).

107. Kim, J., Choi, S., Jun, A., Jeong, H.Y., Shin, J., and Kim, G., *Chemically stable perovskites as cathode materials for solid oxide fuel cells: La-Doped $Ba_{0.5}Sr_{0.5}Co_{0.8}Fe_{0.2}O_{3-\delta}$.* Chemsuschem, **7**(6): p. 1669-1675 (2014).

108. Norman, C. and Leach, C., *In situ high temperature X-ray photoelectron spectroscopy study of barium strontium iron cobalt oxide.* Journal of Membrane Science, **382**(1-2): p. 158-165 (2011).

109. Zeljkovic, S., Ivas, T., Vaucher, S., Jelic, D., and Gauckler, L.J., *The changes of $Ba_{0.5}Sr_{0.5}Co_{0.8}Fe_{0.2}O_{3-\delta}$ perovskite oxide on heating in oxygen and carbon dioxide atmospheres.* Journal of the Serbian Chemical Society, **79**(9): p. 1141-1154 (2014).

110. Itoh, T., Shirasaki, S., Ofuchi, H., Hirayama, S., Honma, T., and Nakayama, M., *Oxygen partial pressure dependence of in situ X-ray absorption spectroscopy at the Co and Fe K edges for $La_{0.6}Sr_{0.4}Co_{0.2}Fe_{0.8}O_{3-\delta}$.* Solid State Communications, **152**(4): p. 278-283 (2012).

111. Huang, B., *Thermo-mechanical properties of mixed ion-electron conducting membrane materials (PhD thesis).* RWTH Aachen University: Aachen, Germany. (2010).

112. Mahendiran, R. and Raychaudhuri, A.K., *Magnetoresistance of the spin-state-transition compound $La_{1-x}Sr_xCoO_3$.* Physical Review B, **54**(22): p. 16044-16052 (1996).

113. Kittel, C., *Introduction to Solid State Physics.* Wiley: US. (2004).

114. Huang, B.X., Malzbender, J., Steinbrech, R.W., Grychtol, P., Schneider, C.M., and Singheiser, L., *Anomalies in the thermomechanical behavior of $Ba_{0.5}Sr_{0.5}Co_{0.8}Fe_{0.2}O_{3-\delta}$ ceramic oxygen conductive membranes at intermediate temperatures.* Applied Physics Letters, **95**(5): p. 051901 (2009).

115. Wei, B., Lu, Z., Li, S.Y., Liu, Y.Q., Liu, K.Y., and Su, W.H., *Thermal and electrical properties of new cathode material $Ba_{0.5}Sr_{0.5}Co_{0.8}Fe_{0.2}O_{3-\delta}$ for solid oxide fuel cells.* Electrochemical and Solid State Letters, **8**(8): p. A428-A431 (2005).

116. Tai, L.W., Nasrallah, M.M., Anderson, H.U., Sparlin, D.M., and Sehlin, S.R., *Structure and electrical properties of $La_{1-x}Sr_xCo_{1-y}Fe_yO_3$. Part 1. The system $La_{0.8}Sr_{0.2}Co_{1-y}Fe_yO_3$.* Solid State Ionics, **76**(3–4): p. 259-271 (1995).

117. Kostogloudis, G.C., Fertis, P., and Ftikos, C., *The perovskite oxide system $Pr_{1-x}Sr_xCo_{1-y}Mn_yO_{3-\delta}$: crystal structure and thermal expansion.* Journal of the European Ceramic Society, **18**(14): p. 2209-2215 (1998).

118. Kostogloudis, G.C. and Ftikos, C., *Crystal structure, thermal expansion and electrical conductivity of $Pr_{1-x}Sr_xCo_{0.2}Fe_{0.8}O_{3-\delta}$ $(0 \leqslant x \leqslant 0.5)$.* Solid State Ionics, **135**(1–4): p. 537-541 (2000).

119. Zeng, P., Chen, Z., Zhou, W., Gu, H., Shao, Z., and Liu, S., *Re-evaluation of $Ba_{0.5}Sr_{0.5}Co_{0.8}Fe_{0.2}O_{3-\delta}$ perovskite as oxygen semi-permeable membrane.* Journal of Membrane Science, **291**(1–2): p. 148-156 (2007).

120. Moon, H.J., *Development of thin film inorganic membranes for oxygen separation.* Forschungszentrum, Zentralbibliothek. (2012).

121. Harvey, A.S., Yang, Z., Infortuna, A., Beckel, D., Purton, J.A., and Gauckler, L.J., *Development of electron holes across the temperature-induced semiconductor-metal transition in $Ba_{1-x}Sr_xCo_{1-y}Fe_yO_{3-\delta}$ (x, y=0.2-0.8): a soft x-ray absorption spectroscopy study.* Journal of Physics-Condensed Matter, **21**: p. 1-10 (2009).

122. Berenov, A., Atkinson, A., Kilner, J., Ananyev, M., Eremin, V., Porotnikova, N., Farlenkov, A., Kurumchin, E., Bouwmeester, H.J.M., Bucher, E., and Sitte, W., *Oxygen tracer diffusion and surface exchange kinetics in $Ba_{0.5}Sr_{0.5}Co_{0.8}Fe_{0.2}O_{3-\delta}$.* Solid State Ionics, **268**: p. 102-109

(2014).

123. Bucher, E., Egger, A., Ried, P., Sitte, W., and Holtappels, P., *Oxygen nonstoichiometry and exchange kinetics of $Ba_{0.5}Sr_{0.5}Co_{0.8}Fe_{0.2}O_{3-\delta}$* Solid State Ionics, **179**(21-26): p. 1032-1035 (2008).

124. Chen, D.J. and Shao, Z.P., *Surface exchange and bulk diffusion properties of $Ba_{0.5}Sr_{0.5}Co_{0.8}Fe_{0.2}O_{3-\delta}$ mixed conductor.* International Journal of Hydrogen Energy, **36**(11): p. 6948-6956 (2011).

125. Wang, L., Imashuku, S., Grimaud, A., Lee, D., Mezghani, K., Habib, M.A., and Shao-Horn, Y., *Enhancing oxygen permeation of electronically short-circuited oxygen-ion conductors by decorating with mixed ionic-electronic conducting oxides.* ECS Electrochemistry Letters, **2**(11): p. F77-F81 (2013).

126. Hayamizu, Y., Kato, M., and Takamura, H., *Effects of surface modification on the oxygen permeation of $Ba_{0.5}Sr_{0.5}Co_{0.8}Fe_{0.2}O_{3-\delta}$ membrane.* Journal of Membrane Science, **462**: p. 147-152 (2014).

127. Burriel, M., Niedrig, C., Menesklou, W., Wagner, S.F., Santiso, J., and Ivers-Tiffée, E., *BSCF epitaxial thin films: Electrical transport and oxygen surface exchange.* Solid State Ionics, **181**(13–14): p. 602-608 (2010).

128. Armstrong, E.N., Duncan, K.L., and Wachsman, E.D., *Effect of A and B-site cations on surface exchange coefficient for $ABO_3$ perovskite materials.* Physical Chemistry Chemical Physics, **15**(7): p. 2298-2308 (2013).

129. Ried, P., Holtappels, P., Wichser, A., Ulrich, A., and Graule, T., *Synthesis and characterization of $La_{0.6}Sr_{0.4}Co_{0.2}Fe_{0.8}O_{3-\delta}$ and $Ba_{0.5}Sr_{0.5}Co_{0.8}Fe_{0.2}O_{3-\delta}$* Journal of the Electrochemical Society, **155**(10): p. B1029-B1035 (2008).

130. Mosleh, M., Sogaard, M., and Hendriksen, P.V., *Kinetics and mechanisms of oxygen surface exchange on $La_{0.6}Sr_{0.4}FeO_{3-\delta}$ thin films.* Journal of the Electrochemical Society, **156**(4): p. B441-B457 (2009).

131. Qi, X.W., Lin, Y.S., and Swartz, S.L., *Electric transport and oxygen permeation properties of lanthanum cobaltite membranes synthesized by different methods.* Industrial & Engineering Chemistry Research, **39**(3): p. 646-653 (2000).

132. Wu, Z.L. and Liu, M.L., *Modelling of ambipolar transport properties of composite mixed ionic-electronic conductors.* Solid State Ionics, **93**(1-2): p. 65-84 (1996).

133. Schmale, K., Barthel, J., Bernemann, M., Grunebaum, M., Koops, S., Schmidt, M., Mayer, J., and Wiemhofer, H.D., *AFM investigations on the influence of $CO_2$ exposure on $Ba_{0.5}Sr_{0.5}Co_{0.8}Fe_{0.2}O_{3-\delta}$* Journal of Solid State Electrochemistry, **17**(11): p. 2897-2907 (2013).

134. Engels, S., Markus, T., Modigell, M., and Singheiser, L., *Oxygen permeation and stability investigations on MIEC membrane materials under operating conditions for power plant processes.* Journal of Membrane Science, **370**(1-2): p. 58-69 (2011).

135. Zhen, Q., Yuan, Q., Wang, H.J., Ding, C., Ding, W.Z., and Lu, X.G., *Investigation of chemical stability and oxygen permeability of perovskite-type $Ba_{0.5}Sr_{0.5}Co_{0.8}Fe_{0.2}O_{3-\delta}$ and $BaCo_{0.7}Fe_{0.2}Nb_{0.1}O_{3-\delta}$ ceramic membranes.* Solid State Ionics, **201**(1): p. 101-101 (2011).

136. Yan, A.Y., Bin, L., Dong, Y.L., Tian, Z.J., Wang, D.Z., and Cheng, M.J., *A temperature programmed desorption investigation on the interaction of $Ba_{0.5}Sr_{0.5}Co_{0.8}Fe_{0.2}O_{3-\delta}$ perovskite oxides with $CO_2$ in the absence and presence of $H_2O$ and $O_2$.* Applied Catalysis B-Environmental, **80**(1-2): p. 24-31 (2008).

137. Yan, A.Y., Maragou, V., Arico, A., Cheng, M., and Tsiakaras, P., *Investigation of a $Ba_{0.5}Sr_{0.5}Co_{0.8}Fe_{0.2}O_{3-\delta}$ based cathode SOFCII. The effect of $CO_2$ on the chemical stability.* Applied Catalysis B-Environmental, **76**(3-4): p. 320-327 (2007).

138. Yang, Z., Harvey, A.S., and Gauckler, L.J., *Influence of $CO_2$ on $Ba_{0.2}Sr_{0.8}Co_{0.8}Fe_{0.2}O_{3-\delta}$ at elevated temperatures.* Scripta Materialia, **61**(11): p. 1083-1086 (2009).

139. Mueller, D.N., De Souza, R.A., Weirich, T.E., Roehrens, D., Mayer, J., and Martin, M., *A kinetic study of the decomposition of the cubic perovskite-type oxide $Ba_xSr_{1-x}Co_{0.8}Fe_{0.2}O_{3-\delta}$ (BSCF) (x=0.1 and 0.5).* Physical Chemistry Chemical Physics, **12**(35): p. 10320-10328 (2010).

140. Efimov, K., Xu, Q.A., and Feldhoff, A., *Transmission electron microscopy study of $Ba_{0.5}Sr_{0.5}Co_{0.8}Fe_{0.2}O_{3-\delta}$ perovskite decomposition at intermediate temperatures.* Chemistry of Materials, **22**(21): p. 5866-5875 (2010).

141. Muller, P., Stormer, H., Meffert, M., Dieterle, L., Niedrig, C., Wagner, S.F., Ivers-Tiffee, E., and Gerthsen, D., *Secondary phase formation in $Ba_{0.5}Sr_{0.5}Co_{0.8}Fe_{0.2}O_{3-\delta}$ studied by electron microscopy.* Chemistry of Materials, **25**(4): p. 564-573 (2013).

142. Li, X., Kerstiens, T., and Markus, T., *Oxygen permeability and phase stability of $Ba_{0.5}Sr_{0.5}Co_{0.8}Fe_{0.2}O_{3-\delta}$ perovskite at intermediate temperatures.* Journal of Membrane Science, **438**(0): p. 83-89 (2013).

143. Muller, P., Stormer, H., Dieterle, L., Niedrig, C., Ivers-Tiffee, E., and Gerthsen, D., *Decomposition pathway of cubic $Ba_{0.5}Sr_{0.5}Co_{0.8}Fe_{0.2}O_{3-\delta}$ between 700 degrees C and 1000 degrees C analyzed by electron microscopic techniques.* Solid State Ionics, **206**: p. 57-66 (2012).

144. Ovenstone, J., Jung, J.I., White, J.S., Edwards, D.D., and Misture, S.T., *Phase stability of BSCF in low oxygen partial pressures.* Journal of Solid State Chemistry, **181**(3): p. 576-586 (2008).

145. Tanasescu, S., Yáng, Z., Martynczuk, J., Varazashvili, V., Maxim, F., Teodorescu, F., Botea, A., Totir, N., and Gauckler, L.J., *Effects of A-site composition and oxygen nonstoichiometry on the thermodynamic stability of compounds in the Ba–Sr–Co–Fe–O system.* Journal of Solid State Chemistry, **200**(0): p. 354-362 (2013).

146. Kuklja, M.M., Mastrikov, Y.A., Jansang, B., and Kotomin, E.A., *First principles calculations of (Ba,Sr)(Co,Fe)$O_{3-\delta}$ structural stability.* Solid State Ionics, **230**(0): p. 21-26 (2013).

147. Jung, J.-I. and Edwards, D.D., *Kinetic demixing/decomposition of $Ba_{0.5}Sr_{0.5}Co_xFe_{1-x}O_{3-\delta}$.* Journal of the European Ceramic Society, **32**(14): p. 3733-3743 (2012).

148. Lipinska-Chwalek, M., Schulze-Küppers, F., and Malzbender, J., *Stability aspects of porous $Ba_{0.5}Sr_{0.5}Co_{0.8}Fe_{0.2}O_{3-\delta}$.* Ceramics International, **40**(5): p. 7395-7399 (2014).

149. Buysse, C., Kovalevsky, A., Snijkers, F., Buekenhoudt, A., Mullens, S., Luyten, J., Kretzschmar, J., and Lenaerts, S., *Development, performance and stability of sulfur-free, macrovoid-free BSCF capillaries for high temperature oxygen separation from air.* Journal of Membrane Science, **372**(1–2): p. 239-248 (2011).

150. Arnold, M., Gesing, T.M., Martynczuk, J., and Feldhoff, A., *Correlation of the formation and the decomposition process of the bscf perovskite at intermediate temperatures.* Chemistry of Materials, **20**(18): p. 5851-5858 (2008).

151. Sahini, M.G., Tolchard, J.R., Wiik, K., and Grande, T., *High temperature X-ray diffraction and thermo-gravimetrical analysis of the cubic perovskite $Ba_{0.5}Sr_{0.5}Co_{0.8}Fe_{0.2}O_{3-\delta}$ under different atmospheres.* Dalton Transactions, **44**: p. 10875-10881 (2015).

152. Kuklja, M.M., Mastrikov, Y.A., Jansang, B., and Kotomin, E.A., *The intrinsic defects, disordering, and structural stability of $Ba_xSr_{1-x}Co_yFe_{1-y}O_{3-\delta}$ perovskite solid solutions.* The Journal of Physical Chemistry C, **116**(35): p. 18605-18611 (2012).

153. Kaletsch, A., Pfaff, E.M., and Broeckmann, C., *Effect of aging on microstructure and mechanical strength of reactive air brazed BSCF/AISI 314-Joints.* Advanced Engineering

Materials, **16**(12): p. 1430-1436 (2014).

154. Kuklja, M.M., Mastrikov, Y.A., Rashkeev, S.N., and Kotomin, E.A., *The structural disorder and lattice stability of (Ba,Sr)(Co,Fe)O$_3$ complex perovskites.* Solid Oxide Fuel Cells 12 (Sofc Xii), **35**(1): p. 2077-2084 (2011).

155. Wang, F., Nakamura, T., Yashiro, K., Mizusaki, J., and Amezawa, K., *The crystal structure, oxygen nonstoichiometry and chemical stability of Ba$_{0.5}$Sr$_{0.5}$Co$_{0.8}$Fe$_{0.2}$O$_{3-\delta}$ (BSCF).* Physical Chemistry Chemical Physics, **16**(16): p. 7307-7314 (2014).

156. Lumeij, M., Gille, Bouwmeester, H., Markus, T., Barthel, J., Roitsch, S., Mayer, J., and Dronskowski, R., *Influence of the Ba$^{2+}$/Sr$^{2+}$ content and oxygen vacancies on the stability of cubic Ba$_x$Sr$_{1-x}$Co$_{0.75}$Fe$_{0.25}$O$_{3-\delta}$.* Physical Chemistry Chemical Physics, **16**(4): p. 1333-1338 (2014).

157. Jung, J.-I. and Edwards, D., *X-ray photoelectron study on Ba$_{0.5}$Sr$_{0.5}$Co$_x$Fe$_{1-x}$O$_{3-\delta}$ (BSCF: x = 0.2 and 0.8) ceramics annealed at different temperature and pO$_2$.* Journal of Materials Science, **46**(23): p. 7415-7422 (2011).

158. Mueller, D.N., De Souza, R.A., Yoo, H.-I., and Martin, M., *Phase stability and oxygen nonstoichiometry of highly oxygen-deficient perovskite-type oxides: a case study of (Ba,Sr)(Co,Fe)O$_{3-\delta}$.* Chemistry of Materials, **24**(2): p. 269-274 (2012).

159. Sun, J.L., Yang, M., Li, G.B., Yang, T., Liao, F.H., Wang, Y.X., Xiong, M., and Lin, J.H., *New barium cobaltite series Ba$_{n+1}$Co$_n$O$_{3n+3}$(Co$_8$O$_8$): Intergrowth structure containing perovskite and CdI$_2$-type layers.* Inorganic Chemistry, **45**(23): p. 9151-9153 (2006).

160. Shannon, R., *Revised effective ionic radii and systematic studies of interatomic distances in halides and chalcogenides.* Acta Crystallographica Section A, **32**(5): p. 751-767 (1976).

161. Kim, J.-S., Yeon, D.-H., Jung, D.W., and Kwak, C., *A highly active and long-term stable La-doped Ba$_x$Sr$_{1-x}$Co$_{1-y}$Fe$_y$O$_{3-\delta}$ cathode for solid-oxide fuel cells.* Journal of Power Sources, **249**(0): p. 66-71 (2014).

162. Ravkina, O., Klande, T., and Feldhoff, A., *Investigation of Zr-doped BSCF perovskite membrane for oxygen separation in the intermediate temperature range.* Journal of Solid State Chemistry, **201**: p. 101-106 (2013).

163. Kathiraser, Y., Wang, Z.G., Yang, N.T., Zahid, S., and Kawi, S., *Oxygen permeation and stability study of La$_{0.6}$Sr$_{0.4}$Co$_{0.8}$Ga$_{0.2}$O$_{3-\delta}$ (LSCG) hollow fiber membrane with exposure to CO$_2$, CH$_4$ and He.* Journal of Membrane Science, **427**: p. 240-249 (2013).

164. Czuprat, O., Arnold, M., Schirrmeister, S., Schiestel, T., and Caro, J., *Influence of CO$_2$ on the oxygen permeation performance of perovskite-type BaCo$_x$Fe$_y$Zr$_z$O$_{3-\delta}$ hollow fiber membranes.* Journal of Membrane Science, **364**(1-2): p. 132-137 (2010).

165. Klande, T., Ravkina, O., and Feldhoff, A., *Effect of A-site lanthanum doping on the CO$_2$ tolerance of SrCo$_{0.8}$Fe$_{0.2}$O$_{3-\delta}$ oxygen-transporting membranes.* Journal of Membrane Science, **437**: p. 122-130 (2013).

166. Yi, J.X., Weirich, T.E., and Schroeder, M., *CO$_2$ corrosion and recovery of perovskite-type BaCo$_{1-x-y}$Fe$_x$Nb$_y$O$_{3-\delta}$ membranes.* Journal of Membrane Science, **437**: p. 49-56 (2013).

167. Efimov, K., Klande, T., Juditzki, N., and Feldhoff, A., *Ca-containing CO$_2$-tolerant perovskite materials for oxygen separation.* Journal of Membrane Science, **389**: p. 205-215 (2012).

168. Li, J.L., Zeng, Q., Liu, T., and Chen, C.S., *Oxygen permeability and CO$_2$-tolerance of Sr(Co$_{0.8}$Fe$_{0.2}$)$_{0.8}$Ti$_{0.2}$O$_{3-\delta}$ hollow fiber membrane.* Separation and Purification Technology, **77**(1): p. 76-79 (2011).

169. Lu, H., Kim, J.P., Son, S.H., and Park, J.H., *Novel SrCo$_{1-2x}$(Fe,Nb)$_x$O$_{3-\delta}$ (x=0.05, 0.10) oxides targeting CO$_2$ capture and O$_2$ enrichment: Structural stability and oxygen sorption properties.* Materials Letters, **65**(19-20): p. 2858-2860 (2011).

170. Bi, L., Fabbri, E., and Traversa, E., *Novel $Ba_{0.5}Sr_{0.5}(Co_{0.8}Fe_{0.2})_{1-x}Ti_xO_{3-\delta}$ (x=0, 0.05, and 0.1) cathode materials for proton-conducting solid oxide fuel cells.* Solid State Ionics, **214**: p. 1-5 (2012).

171. Zeng, Q., Zu, Y.B., Fan, C.G., and Chen, C.S., *$CO_2$-tolerant oxygen separation membranes targeting $CO_2$ capture application.* Journal of Membrane Science, **335**(1-2): p. 140-144 (2009).

172. Zhou, W., Liang, F.L., Shao, Z.P., and Zhu, Z.H., *Hierarchical $CO_2$-protective shell for highly efficient oxygen reduction reaction.* Scientific Reports, **2**: p. 1-6 (2012).

173. Kim, J.P., Park, J.H., Magnone, E., and Lee, Y., *Significant improvement of the oxygen permeation flux of tubular $Ba_{0.5}Sr_{0.5}Co_{0.8}Fe_{0.2}O_{3-\delta}$ membranes covered by a thin $La_{0.6}Sr_{0.4}Ti_{0.3}Fe_{0.7}O_{3-\delta}$ layer.* Materials Letters, **65**(14): p. 2168-2170 (2011).

174. Xue, J., Liao, Q., Wei, Y.Y., Li, Z., and Wang, H.H., *A $CO_2$-tolerance oxygen permeable $60Ce_{0.9}Gd_{0.1}O_{2-\delta}$-$40Ba_{0.5}Sr_{0.5}Co_{0.8}Fe_{0.2}O_{3-\delta}$ dual phase membrane.* Journal of Membrane Science, **443**: p. 124-130 (2013).

175. Klande, T., Efimov, K., Cusenza, S., Becker, K.D., and Feldhoff, A., *Effect of doping, microstructure, and $CO_2$ on $La_2NiO_{4+\delta}$ based oxygen-transporting materials.* Journal of Solid State Chemistry, **184**(12): p. 3310-3318 (2011).

176. Wang, H.H., Tablet, C., Feldhoff, A., and Caro, J., *A cobalt-free oxygen-permeable membrane based on the perovskite-type oxide $Ba_{0.5}Sr_{0.5}Zn_{0.2}Fe_{0.8}O_{3-\delta}$.* Advanced Materials, **17**(14): p. 1785-1788 (2005).

177. Zhu, X.F., Wang, H.H., and Yang, W.S., *Novel cobalt-free oxygen permeable membrane.* Chemical Communications, (9): p. 1130-1131 (2004).

178. Whitesell, J.K., *The Merck Index, 12th Edition, CD-ROM (Macintosh): An encyclopedia of chemicals, drugs & biologicals*. Chapman & Hall: New York. (1998).

179. Ghazali Kamardan, M., Hidayah, N., Zaidi, A., Noh Dalimin, M., Mujahid, A., Zaidi, A., Bahrin Jamaludin, S., Mahadi, M., and Jamil, A., *The sintering temperature effect on the shrinkage behavior of cobalt chromium alloy.* American Journal of Applied Sciences, **7**(11): p. 1443-1448 (2010).

180. Fultz, B. and Howe, J.M., *Transmission electron microscopy and diffractometry of materials*. Springer: Berlin ; New York. (2001).

181. Hubbell JH and Seltzer SM, *Tables of X-ray Mass Attenuation coefficients and mass energy-absorption coefficients from 1 keV to 20 MeV for Elements Z=1-92 and 48 Additional Substances of Dosimetric Interest*. National Institute of Standards and Technology, US Department of Commerce: Gaithersburg, MD. (1995).

182. Goodhew, P.J. and Humphreys, F.J., *Electron microscopy and analysis*. Taylor & Francis: London; New York. (1988).

183. RPI/13, *Advanced technical ceramics. Monolithic ceramics. General and textural properties. Determination of density and porosity.* Bsigroup. (1993).

184. Williams, D.B. and Carter, C.B., *Transmission Electron Microscopy: A Textbook for Materials Science*. Springer. (2009).

185. Cliff, G. and Lorimer, G.W. *Quantitative analysis of thin foils using EMMA-4: the ratio technique*. in *Proceedings of the Fifth European Congress on Electron Microscopy*. Institute of Physics: Manchester. (1972).

186. Schwartz, A.J., *Electron backscatter diffraction in materials science*. Springer: New York. (2009).

187. Levenspiel, O., *Tracer Technology: Modeling the Flow of Fluids*. Springer: New York. (2012).

188. RPI/13, *Advanced technical ceramics. Monolithic ceramics. General and textural*

properties. *Determination of grain size and size distribution (characterized by the linear intercept method).* Bsigroup. (2001).

189. Maitra, S., Chakrabarty, N., and Pramanik, J., *Decomposition kinetics of alkaline earth carbonates by integral approximation method.* Cerâmica, **54**(331): p. 268-272 (2008).

190. Voort, G.F.V., *Metallographic Specimen Preparation for Electron Backscattered Diffraction.* Metallurgia Italiana, (11-12): p. 71-79 (2009).

191. Struers, *Active oxide polishing suspensions.* Struers: Denmark. (2013).

192. Maltais, A., Dube, D., Fiset, M., Laroche, G., and Turgeon, S., *Improvements in the metallography of as-cast AZ91 alloy.* Materials Characterization, **52**(2): p. 103-119 (2004).

193. Soustelle, M., *Heterogeneous Kinematics Handbook.* ISTE Ltd and John Wiley & Sons Inc. (2010).

194. Gribble, C.D., *Optical Mineralogy: Principles and Practice.* Springer. (2012).

195. Rapoport, E. and Pistoriu.Cw, *Orthorhombic-Disordered Rhombohedral Transition in $SrCO_3$ and $BaCO_3$ to 40 Kilobars.* Journal of Geophysical Research, **72**(24): p. 6353-& (1967).

196. Beyerlein, A.L., *Reactions in the Solid-State*, in *Comprehensive Chemical-Kinetics*. Elsevier. (1984).

197. Callister, W.D., *Materials Science And Engineering: An Introduction.* John Wiley & Sons. (2007).

198. Zou, H.F., Yang, H.J., Tan, J., and Zhang, Z.F., *Preferential growth and orientation relationship of $Ag_3Sn$ grains formed between molten Sn and (001) Ag single crystal.* Journal of Materials Research, **24**(6): p. 2141-2144 (2009).

199. Instruments, O., *Aztec user manual.* Oxford instruments: Abingdon. (2013).

200. Cussen, E.J., Sloan, J., Vente, J.P., Battle, P.D., and Gibb, T.C., *15R $SrMn_{1-x}Fe_xO_{3-\delta}$ (x approximate to 0.1); A new perovskite stacking sequence.* Inorganic Chemistry, **37**(23): p. 6071-6077 (1998).

201. Efimov, K., Halfer, T., Kuhn, A., Heitjans, P., Caro, J., and Feldhoff, A., *Novel Cobalt-Free Oxygen-Permeable Perovskite-Type Membrane.* Chemistry of Materials, **22**(4): p. 1540-1544 (2010).

202. Martynczuk, J., Efimov, K., Robben, L., and Feldhoff, A., *Performance of zinc-doped perovskite-type membranes at intermediate temperatures for long-term oxygen permeation and under a carbon dioxide atmosphere.* Journal of Membrane Science, **344**(1-2): p. 62-70 (2009).

203. Feldhoff, A., Martynczuk, J., Arnold, M., Myndyk, M., Bergmann, I., Sepelak, V., Gruner, W., Vogt, U., Hahnel, A., and Woltersdorf, J., *Spin-state transition of iron in $(Ba_{0.5}Sr_{0.5})(Fe_{0.8}Zn_{0.2})O_{3-\delta}$ perovskite.* Journal of Solid State Chemistry, **182**(11): p. 2961-2971 (2009).

204. Priester, L., *Grain Boundaries: From Theory to Engineering.* Springer: Netherlands. (2012).

205. Kharton, V.V., Kovalevsky, A.V., Viskup, A.P., Jurado, J.R., Figueiredo, F.M., Naumovich, E.N., and Frade, J.R., *Transport properties and thermal expansion of $Sr_{0.97}Ti_{1-x}Fe_xO_{3-\delta}$ (x=0.2-0.8).* Journal of Solid State Chemistry, **156**(2): p. 437-444 (2001).

206. McIntosh, S., Vente, J.F., Haije, W.G., Blank, D.H.A., and Bouwmeester, H.J.M., *Oxygen stoichiometry and chemical expansion of $Ba_{0.5}Sr_{0.5}Co_{0.8}Fe_{0.2}O_{3-\delta}$ measured by in situ neutron diffraction.* Chemistry of Materials, **18**(8): p. 2187-2193 (2006).

207. Masel, R.I., *Principles of Adsorption and Reaction on Solid Surfaces.* Wiley. (1996).

208. Moseley, H.N.B., *Error Analysis and Propagation in Metabolomics Data Analysis.* Computational and Structural Biotechnology Journal, **4**(5): p. 1 - 12 (2013).

209. GmbH, B.N., *Error bars in Esprit quantified results* Bruker Nano GmbH. (2014).

210.   Gadre, M.J., Lee, Y.L., and Morgan, D., *Cation interdiffusion model for enhanced oxygen kinetics at oxide heterostructure interfaces.* Physical Chemistry Chemical Physics, **14**(8): p. 2606-2616 (2012).